

Copyright  
by  
Vasileios Athanasiou Samaras  
2009

**Simplified Methods of Evaluating the Redundancy of Twin Trapezoidal  
Box Girder Bridges**

**by**

**Vasileios Athanasiou Samaras, DCE**

**Thesis**

Presented to the Faculty of the Graduate School of

The University of Texas at Austin

in Partial Fulfillment

of the Requirements

for the Degree of

**Master of Science in Engineering**

**The University of Texas at Austin**

**August 2009**

**Simplified Methods of Evaluating the Redundancy of Twin Trapezoidal  
Box Girder Bridges**

**Approved by  
Supervising Committee:**

---

**Karl H. Frank**

---

**Eric B. Williamson**

## **Dedication**

To my sister who made me believe this dream

And

To my parents for their love and support

## **Acknowledgements**

I would like to express my gratitude to Dr. Karl Frank and Dr. Eric Williamson for their guidance and support over the past two years. Their personal interest in my progress within and beyond this research, encourage me to improve myself. I am thankful for the opportunity which was given to me to participate in this research project. Those two years full of experiences will be an unforgettable part of my life.

I am grateful and lucky to be on the same team with Bryce Neuman. His personality and patience helped me adjust myself in the lab. His excellent communication skills and his willingness to work hard define him as the best partner. I would like to acknowledge my research partners and lab mates Amy Barret, Arcan Bundur, Jeremiah Fasl, Janghwan Kim, Josh Mouras, Andrew Stam, and Andres Stambuk who helped me the last two years. I want to thank past graduate research students Catherine Hovell, J.P. Sutton, Tim Barnard and Jim Plantes for the information that they provide through their theses.

The staff of Ferguson Engineering Laboratory contributed a lot to this project. I would like to thank Dennis Phillip, Blake Stasney and Eric Schell for their continuous help while I worked at the lab. Barbara Howard, Jessica Hanten, Carrie Billingsley, Andrew Valentine and Mike Wason deserve my thanks for their continual support.

Finally, I am thankful to Texas Department of Transportation and Federal Highway Administration for sponsoring this project.

August, 2009

## **Abstract**

# **Simplified Methods of Evaluating the Redundancy of Twin Trapezoidal Box Girder Bridges**

Vasileios Athanasiou Samaras, M.S.E.

The University of Texas at Austin, 2009

Supervisor: Karl H. Frank

According to the AASHTO Load and Resistance Factor Design (LRFD) Bridge Design Specifications, a bridge is defined to be fracture critical when a failure of a tension component will result in the collapse of the bridge. In the case of a twin box girder bridge, the tension flanges in the positive moment portion of the bridge, as well as the webs, are considered to be fracture critical elements. Due to this classification, those bridges are subjected to stringent inspections at least every two years. Those inspections are crucial for ensuring the safety of the bridge, yet are expensive and time consuming.

Multiple cases of FCBs (Fracture Critical Bridge) that have experienced a fracture in one of their elements without collapse have encouraged owners of those bridges to question the validity of AASHTO's requirements. The Texas Department of Transportation is interested in indentifying when a fracture of an element could lead to a catastrophic collapse of a bridge. A better understanding of fracture critical bridge

behavior may allow TxDOT and other state DOTs to reduce the frequency of the inspections, which could potentially reduce the cost of an otherwise attractive bridge design.

The goal of this research project is to determine the level of redundancy of twin box girder bridges. Simplified analytical methods and guidelines that will conservatively estimate the behavior of such bridges will be presented in this thesis. Those guidelines will be one of the tools that an engineer in practice could use to determine if a bridge is prone to collapse following the failure of a fracture critical component. A full-size bridge has been constructed at the Ferguson Structural Engineering Laboratory to test the response of these systems following a simulated fracture. A series of tests were conducted to determine the response of the bridge in the event of a tension flange fracture. The results provided important information for the development of the simplified methods.

The FSEL test bridge performed extremely well throughout all the testing and supported a load of over four times the AASHTO design truck load. Several elements contributed to create alternative load paths that could sustain the entire applied load with a full-depth fracture of one of its two girders. The large section of the concrete railing above the fractured girder acted as an inverted beam and transmitted a portion of the load back to the supports once the expansion joint closed due to the downward deflection of the bridge. The concrete deck acted as a shear diaphragm and also transferred significant loads in both horizontal directions. Because the performance of the test bridge far exceeded the AASHTO criteria, and because this behavior can be computed using the simplified methods presented in this thesis as well as through detailed finite element models, consideration should be given to revising the current AASHTO specifications and to developing alternate inspection and maintenance requirements that accurately reflect the redundancy available in various types of fracture critical bridges.

## Table of Contents

List of Tables .....	xii
List of Figures .....	xiii
<b>CHAPTER 1</b>	<b>1</b>
Introduction and Research Motivation.....	1
1.1 Introduction.....	1
1.2 Research motivation.....	2
1.3 Previous work and scope of this thesis .....	3
<b>CHAPTER 2</b>	<b>5</b>
Test Results: Test 2.....	5
2.1 Introduction.....	5
2.2 Girder and Concrete Deck Deflection Survey .....	8
2.3 Girders and End Diaphragms Gage Data Analysis.....	12
2.3.1 Instrumentation analysis of intact and fractured girder .....	12
2.3.2 Instrumentation analysis of deck .....	21
2.4 Summary .....	31
<b>CHAPTER 3</b>	<b>32</b>
Simplified Strip Model of Deck Behavior .....	32
3.1 Introduction.....	32
3.2 Initial Strength Checks.....	33
3.3 Development of the Simplified Strip Model.....	46
3.4 Analysis of the Bridge Strips .....	50
3.5 Results of the Simplified Strip Model Analysis .....	53
3.6 Deflection Implementation for Given Loads .....	57
3.7 Summary .....	69



<b>CHAPTER 4</b>	<b>70</b>
Test Results: Test 3 .....	70
4.1 Introduction.....	70
4.2 Girders and End Diaphragms Gage Data Analysis.....	72
4.2.1 Instrumentation analysis of intact and fractured girder .....	72
4.2.2 Analysis of concrete deck strain data.....	86
4.3 Summary .....	95
<b>CHAPTER 5</b>	<b>96</b>
Yield Line Model.....	96
5.1 Introduction.....	96
5.2 Development of the Yield Line Model .....	97
5.2.1 Description of the Yield Line Model analysis procedure .....	99
5.2.2 Yield Line Model analysis results of the FSEL bridge.....	110
5.3 Summary .....	111
<b>CHAPTER 6</b>	<b>112</b>
Conclusions and Recommendations .....	112
6.1 Project Summary.....	112
6.2 FSEL Bridge Behavior During Tests .....	113
6.3 Simplified Models.....	114
6.4 Recommendations.....	114
<b>APPENDIX A</b>	<b>118</b>
Analysis of bridge components.....	118
A.1 Calculation of the Intact Girder’s Moment Diagram .....	118
A.2 Calculation of the Railing’s Moment Diagram.....	124
A.3 Calculation of the Concrete Deck’s Moment Capacity .....	128

<b>APPENDIX B</b>	<b>134</b>
Analysis of the FSEL Test Bridge using the Strip and Yield Line Models .....	134
B.1 Calculation of the Transmitted Load to the Intact Girder .....	134
B.2 Calculation of Maximum Moment on the Bridge .....	135
B.3 Analysis of Composite Section .....	136
B.4 Analysis of Concrete Deck .....	139
B.5 Shear Stud Check .....	144
B.6 Shear Check of the Composite Section at the Supports due to Torsion and Bending .....	146
B.7 Analysis of FSEL Bridge Using the Simplified Strip Model .....	153
B.8 Analysis of FSEL Bridge Using the Yield Line Model .....	157
 <b>APPENDIX C</b>	 <b>165</b>
Analysis of the Woodway Bridge (Span 11) using the simple models .....	165
C.1 Introduction .....	165
C.2 Calculation of the Transmitted Load to the Intact Girder .....	167
C.3 Calculation of Maximum Moment on the Bridge .....	169
C.4 Analysis of Composite Section .....	169
C.5 Analysis of Concrete Deck .....	172
C.6 Shear Stud Check .....	177
C.7 Shear Check of the Composite Section at the Supports due to Torsion and Bending .....	179
 <b>APPENDIX D</b>	 <b>188</b>
Analysis of the Woodway Bridge (span 17 & 18) using the simple models .....	188
D.1 Introduction .....	188
D.2 Calculation of the Transmitted Load to the Intact Girder .....	191
D.3 Calculation of Maximum Moment on the Bridge .....	192
D.4 Analysis of Composite Section .....	193
D.5 Analysis of Concrete Deck .....	198
D.6 Shear Stud Check .....	203

D.7 Shear Check of the Composite Section at the Supports due to Torsion and Bending .....	205
<b>APPENDIX E</b>	<b>217</b>
Instrumentation .....	217
E.1 Glossary of Instrumentation Gages.....	217
E.2 Full-Scale Test 2 .....	221
E.3 Full-Scale Test 3 .....	233
<b>BIBLIOGRAPHY</b>	<b>246</b>
<b>VITA 248</b>	

## List of Tables

Table 4-1: Failures of the bridge elements under different loads during Test 3....	71
Table 4-2: Average shear flow at the intact girder for different loads Test 3.....	82
Table 4-3: Torque in intact girder based on strain gage data Test 3.....	84
Table 4-4: Calculated Torque on Intact Girder from Dead Load of Fractured Girder and Applied Loads .....	84
Table 4-5: Principle stresses of end diaphragms Test 3.....	86
Table A-1: Summary of calculations for the intact girder's moment diagram ....	121
Table A-2: Summary of calculations for the railing's moment diagram .....	126
Table B-1: Eccentricities of loads.....	147
Table B-2: A sample iteration of the Simplified Strip Model .....	154
Table B-3: Basic parameters of the FSEL bridge .....	158
Table B-4: Internal work calculation for FSEL bridge.....	159
Table B-5: External work calculation of the truck load.....	160
Table C-1: General information of bottom and top flange .....	165
Table C-2: Eccentricities of loads.....	180
Table D-1: General information of bottom and top flange .....	188
Table E-1: Glossary of instrumentation codes.....	217
Table E-2: Typical gage models .....	218
Table E-3: Index of instrumentation channels Full-Scale Test 2.....	222
Table E-4: Index of instrumentation channels Full-Scale Test 3.....	234

## List of Figures

Figure 1-1: The Silver Bridge at Point Pleasant. (a) During service, (b) Fractured Eye Bar .....	2
Figure 2-1: The instrumentation plan of the cross-section for Test 2 [Neuman, (2009)] .....	6
Figure 2-2: Plan view of FSEL bridge with significant features [Neuman, (2009)]	7
Figure 2-3: Arrangement of the concrete gages on concrete deck Test 2 [Neuman, (2009)].....	8
Figure 2-4: Intact girder deflection during Test 2 [Neuman, (2009)].....	9
Figure 2-5: Fractured girder deflection during Test 2 [Neuman, (2009)].....	10
Figure 2-6: Concrete deck deflected shape after Test 2 [Neuman, (2009)].....	11
Figure 2-7: Fractured girder's interior top flange separation after Test 2 [Neuman (2009)].....	11
Figure 2-8: Bottom flange strain gages data of the fractured girder during Test 2	13
Figure 2-9: Bottom flange strain gages data of the intact girder during Test 2 .....	13
Figure 2-10: Bottom flange strain gages data of the girders during Test 2 .....	14
Figure 2-11: Bottom flange strain diagram of fractured girder after Test 2 .....	15
Figure 2-12: Bottom flange strain diagram of intact girder after Test 2.....	15
Figure 2-13: Moment diagram of the intact girder after Test 2 .....	16
Figure 2-14: Shear flow of defined intact girder sections during Test 2 .....	18
Figure 2-15: Inner area of the closed section.....	19
Figure 2-16: Torsional moment diagram of the intact girder after Test 2 .....	19
Figure 2-17: Principle stresses orientation at the end diaphragms .....	20
Figure 2-18: Cyclic peak micro-strain along exterior railing during Test 2 .....	22

Figure 2-19: Crushed concrete at the CL exterior railing after Test 2.....	23
Figure 2-20: Railing section used for the moment calculation of the railing .....	23
Figure 2-21: Moment diagram of the exterior railing after Test 2.....	24
Figure 2-22: Shear stud unzipping mode during Test 2 [Neuman, (2009)].....	26
Figure 2-23a: Undeformed shape of the bridge before Test 2 .....	27
Figure 2-23b: Deformed shape of the bridge in double curvature during Test 2 ..	27
Figure 2-23c: Deformed shape of the bridge in single curvature during Test 2 ....	28
Figure 2-24: Strain reversals transverse to bridge span above interior top flange of fractured girder [Neuman, (2009)].....	30
Figure 2-25: Peak compressive strain in exterior railing [Neuman, (2009)] .....	30
Figure 3-1: Bridge divided in strips .....	34
Figure 3-2: Typical deck strip cross section with boundary conditions .....	34
Figure 3-3: Plastic deck mechanism .....	35
Figure 3-4: Shear stud pull out capacity .....	36
Figure 3-5: Variable definition for center of gravity (C.G.).....	39
Figure 3-6: C.G. Location.....	40
Figure 3-7: Deformed shape of the cross section in double curvature .....	46
Figure 3-8: Deformed shape of the cross section in double curvature .....	47
Figure 3-9: Sections based on which moment capacity was calculated .....	49
Figure 3-10: Positive and negative moment capacity in different regions .....	49
Figure 3-11: A typical example of the slope-deflection method .....	51
Figure 3-12 Incremental deflection curves of both girders Test 2.....	52
Figure 3-13: Critical failure locations.....	52
Figure 3-14: Interior top flange of the fracture girder force Test 2 .....	54
Figure 3-15: Typical moment diagram just before a shear stud pulls out .....	55

Figure 3-16: Exterior top flange of the fractured girder force Test 2 .....	55
Figure 3-17: Exterior top flange of the intact girder force Test 2.....	56
Figure 3-18: Moment diagram at the mid-span .....	56
Figure 3-19: Full composite and transformed composite section of the intact girder .....	58
Figure 3-20: Reduced composite and transformed composite section of the intact girder .....	58
Figure 3-21: Inactive length of the railing .....	59
Figure 3-22: Deflection vs. location diagram of the intact girder Test 2.....	60
Figure 3-23: Deflection vs. location diagram of the intact girder Pre-Test 3 .....	61
Figure 3-24: Deflection vs. location diagram of the intact girder Test 3.A .....	61
Figure 3-25: Fractured section .....	62
Figure 3-26: Basic geometry of the Equation 3-3.....	64
Figure 3-27: Deflection vs. location diagram of the fractured girder Test 2 .....	66
Figure 3-28: Deflection vs. location diagram of the fractured girder Pre-Test 3 ..	66
Figure 3-29: Deflection vs. location diagram of the fractured girder Test 3.A .....	67
Figure 4-1: A typical instrumentation plan of a cross-section for Test 3 [Neuman, (2009)].....	71
Figure 4-2: Fracture propagation on the exterior web of the fractured girder .....	73
Figure 4-3: Bottom Flange strain gage data of fractured girder during Test 3 .....	73
Figure 4-4: Top flange strain gages data of fractured girder during Test 3 .....	74
Figure 4-5: Localized shear stud failure .....	75
Figure 4-6: Major shear stud failure .....	76
Figure 4-7: South expansion joints opening Test 3 .....	77
Figure 4-8: Fractured girder's interior and exterior top flange separation Test 3 ..	78

Figure 4-9: Bottom flange strain gages data of intact girder during Test 3 .....	78
Figure 4-10: Bottom flange strain diagram of fractured girder during Test 3 .....	79
Figure 4-11: Bottom flange strain diagram of intact girder during Test 3.....	80
Figure 4-12: Moment diagram of the intact girder during Test 3 .....	81
Figure 4-13: Torsional moment diagram of the intact girder during Test 3 .....	83
Figure 4-14 Total applied load on the intact girder from strain calculations and assumptions.....	85
Figure 4-15: Arrangement of the concrete gages on concrete deck Test 3 [Neuman, (2009)].....	87
Figure 4-16: Top surface of east railing strain gage data during Test 3 .....	88
Figure 4-17: Expansion joint of east railing at centerline during Test 3 .....	88
Figure 4-18: East railing strain gage data along the height during Test 3 .....	89
Figure 4-19: Moment diagram of the exterior railing after Test 3.....	90
Figure 4-20a: Concrete deck longitudinal strain gages at the mid-box of the intact girder during Test 3.....	91
Figure 4-20b: Concrete deck longitudinal strain gages at the mid-width of the bridge during Test 3 .....	92
Figure 4-20c: Concrete deck longitudinal strain gages at the mid-box of the fractured girder during Test 3.....	92
Figure 4-21: Concrete deck gages in the transverse direction during Test 3.....	93
Figure 4-22: Top reinforcement strain gages during Test 3 .....	94
Figure 4-23: Bottom reinforcement strain gages during Test 3 .....	94
Figure 5-1: Overall view of the damaged deck.....	96
Figure 5-2 Hinge line on the concrete deck looking south.....	97
Figure 5-3: Observed yield line pattern .....	98



Figure 5-4: Assumed elastic plate displaced by a virtual displacement $\Delta$ .....	99
Figure 5-5: Parameters of the yield line pattern.....	101
Figure 5-6: Bending moment along a yield line at an angle $\alpha$ [Wight, MacGregor]102	
Figure 5-7: Acting moments on the railing for different cases.....	105
Figure 5-8: Defining the deflection at the load location.....	108
Figure 5-9: Geometric parameters of Equation 5-8.....	110
Figure A-1: Elastic section of the intact girder used for the moment diagram calculation.....	118
Figure A-2: Strain gradient of N1 section of the intact girder.....	119
Figure A-3 Elastic section of the railing - strain & stress gradient.....	124
Figure A-4: Typical sections used for the moment capacity calculation.....	128
Figure A-5: Strain and stress gradients at positive moment regions.....	128
Figure A-6: Strain and stress gradients at negative moment regions.....	130
Figure B-1: Truck load location - Shear and moment diagram due to truck load	136
Figure B-2: Composite section [Sutton,(2007)].....	137
Figure B-3: Plastic neutral axis location.....	138
Figure B-4: Typical one foot wide section of the concrete deck.....	139
Figure B-5: Strain and stress gradients at positive moment regions.....	140
Figure B-6: Strain and stress gradients at negative moment regions.....	141
Figure B-7: Deflected shape and moment diagram before any failure of shear studs .....	143
Figure B-8: Flexural and torsional shear stresses on the composite section.....	152
Figure C-1: Elevation view of Woodway Bridge Span 11.....	166
Figure C-2: Typical cross-section of the Woodway Bridge Span 11.....	166

Figure C-3: Typical cross-section of the steel girder of the Woodway Bridge Span 11 .....	167
Figure C-4: Plastic neutral axis location.....	170
Figure C-5: Actual and modified 1-ft wide section of the concrete deck in the transverse direction .....	172
Figure C-6: Strain and stress gradients at positive moment regions.....	173
Figure C-7: Strain and stress gradients at negative moment regions.....	175
Figure C-8: Deflected shape and moment diagram before any failure of shear studs .....	176
Figure C-9: Flexural and torsional shear stresses on the composite section.....	184
Figure D-1: Elevation view of Woodway Bridge Span 17 & 18.....	189
Figure D-2: Typical cross-section of the Woodway Bridge Span 17 & 18.....	190
Figure D-3: Typical cross-section of the Woodway Bridge Span 17 & 18 steel girder .....	190
Figure D-4: Moment envelope of dead and one truck load on spans 17 and 18 of the Woodway Bridge .....	193
Figure D-5: Plastic neutral axis location.....	194
Figure D-6: Actual and modified 1-ft wide section of the concrete deck in the transverse direction .....	198
Figure D-7: Strain and stress gradients at positive moment regions .....	199
Figure D-8: Strain and stress gradients at negative moment regions.....	200
Figure D-9: Deflected shape and moment diagram before any failure of shear studs .....	202
Figure D-10: Flexural and torsional shear stresses on the composite section .....	210
Figure E-1: Reinforcing bar foil gage locations .....	219

Figure E-2: Shear stud foil gage locations.....	220
Figure E-3: Intact girder rosette orientation Full-Scale Test 2 and 3 .....	221
Figure E-4: End diaphragm rosette orientation Full-Scale Test 2 and 3.....	221
Figure E-5: Typical concrete deck gage locations Full-Scale Test 2 and 3.....	222
Figure E-6: String potentiometer locations between girder bottom flanges and ground Full-Scale Test 3 .....	233

# CHAPTER 1

## Introduction and Research Motivation

### 1.1 INTRODUCTION

Since the late 1950s when the interstate highway system was beginning to be expanded, commuters and transportation companies started depending on the highway system for travel and to distribute goods and services. Highway bridges are a vital component of the US transportation system because they provide a passage over barriers, such as rivers or roadways. The consequences on the economy of any disruption of a highway bridge are several. For instance, the cost to displaced motorists who depend on a bridge that is being inspected has been estimated to be approximately \$400,000 per day [Olson, (2008)].

In the past, collapses of bridges have resulted in major changes to inspection and maintenance procedures in the US. In 1967, just after the collapse of Silver Bridge in Point Pleasant (Figure 1-1), the National Bridge Inspection Program was established. Later failures of the tension elements of bridges raised concerns about these fracture critical components. In response to those concerns, new provisions were established that increased the material toughness and fabrication standards for critical members and required more stringent inspections during construction as well as hands-on inspection during the service life of such bridges. The term ‘fracture critical bridge’ was first used in 1970 to describe a bridge which is expected to collapse if a tension component fractures [AASHTO LRFD].

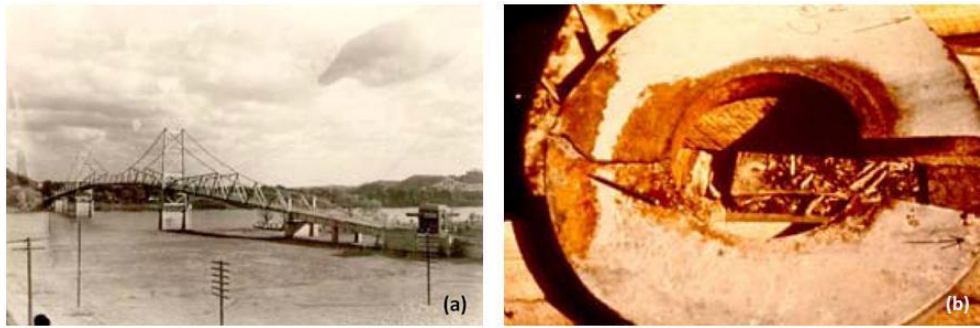


Figure 1-1: The Silver Bridge at Point Pleasant. (a) During service, (b) Fractured Eye Bar

Today, each of the approximately 416 fracture critical bridges in Texas are required to be visually inspected at least once every two years regardless of their expected service life and fatigue performance. One of the most common fracture critical bridges in Texas is the twin box girder bridge. Usually, they are used for highway flyovers due to their slender and aesthetically pleasant profile, which improves the appearance of the elevated interchanges.

The objectives of inspection are to track fatigue cracks in the tension members and to evaluate the remaining life of those fracture critical components of a bridge. Those inspections are important for finding cracks, yet are extremely expensive for the owner.

## 1.2 RESEARCH MOTIVATION

Multiple cases of Fracture Critical Bridges (FCBs) that have experienced a fracture in one of their elements without collapse have made owners of those bridges question the validity of AASHTO's requirements. There is interest among bridge engineers and state Departments of Transportation (DOTs) in indentifying when a fracture of an element could lead to a catastrophic collapse of a fracture critical bridge. A better understanding of the performance of such bridges will potentially allow the Texas Department of Transportation (TxDOT) and other state DOTs to reduce the frequency of the inspections and, to a large extent, reduce the cost of an otherwise attractive bridge design. It is

estimated that TxDOT spends \$26 million a year to inspect its 416 fracture critical bridges. If it is possible to estimate the redundancy level of a bridge and prove that it has enough sufficient capacity to sustain its service loads, then the required inspections could be performed less often.

In order to develop tools that could estimate the redundancy level of twin box girder bridges, TxDOT and the Federal Highway Administration (FHWA) have funded the research project described in this thesis. The main objective of this research project is to develop methods for evaluating the redundancy level of fracture critical bridges. The best way to model such a complex system and obtain detailed results is through finite element modeling. Finite element analysis may provide the most accurate results, yet it requires a substantial amount of work and time. Simplified procedures for initial checks of the bridge redundancy level will be beneficial to engineers in practice. Thus, if the simplified methods are available and are adequate to characterize bridge behavior, then engineers could potentially save a significant amount of time. Otherwise, a more sophisticated finite element analysis can be used to determine the redundancy level of a bridge. For the current study, a set of guidelines was developed to estimate the behavior of a bridge in the event of a fracture. A full-size bridge was constructed at the Ferguson Structural Engineering Laboratory, which was used to evaluate the redundancy of a typical twin box girder bridge in Texas. A series of tests were conducted to determine the response of the bridge in the event of a tension flange fracture. The results provided important information for the development of the simplified analysis methods presented in this thesis.

### **1.3 PREVIOUS WORK AND SCOPE OF THIS THESIS**

One of the goals of Sutton's [Sutton, (2007)] research was to develop a set of simple calculations to predict the behavior of the FSEL test bridge during the fracture test. The simple analysis calculations presented in his thesis showed that the deck and the intact

girder would be able to provide an alternative load path when a full-depth fracture occurs at the mid-span of the fractured girder. An uncertainty in the calculation of the capacity of the shear studs motivated the research team to conduct a series of laboratory tests to determine the tensile capacity of a group of shear studs. Sutton's conclusion was that the haunch played a significant role in the strength and ductility of the shear studs, jeopardizing their ability to carry and to redistribute loads during a fracture event [Sutton, (2007)].

Joshua Mouras extended Sutton's [Sutton, (2007)] research on shear studs [Mouras, (2008)]. Laboratory tests were performed to evaluate the strength and ductility of various stud configurations, including shear studs spaced transversely and longitudinally, different heights of studs in the haunch, and dynamic loading of stud specimens. Mouras [Mouras, (2008)] developed modifications to the existing ACI code equations to represent the findings obtained from the laboratory test program. The proposed strength equations are able to predict the strength of these alternate shear stud configurations and the effect of the haunch.

This thesis will focus on the development of simplified methods and guidelines that will conservatively estimate the behavior of a twin box girder bridge in the event of a fracture of a critical element.

## CHAPTER 2

### Test Results: Test 2

#### 2.1 INTRODUCTION

After reconstructing a full-size twin box girder bridge and using it as a test specimen, the objective of Test 1 was to investigate the behavior of the bridge in the event that a fracture occurred in one of the critical tension flanges. In Test 1, an explosive charge was used to cut the entire thickness of one of the bottom flanges. It was believed that the fracture would propagate to the webs due to the fact that the tension flanges of the twin box-girder bridge were fracture critical members. The bridge was loaded at the mid-span, which was the location of the maximum bending moment, with concrete blocks weighing 75,000 lbs in total. The concrete blocks were positioned on the bridge in a pattern corresponding to the AASHTO-specified design truck load [AASHTO LRFD, (2004)]. Based on the AASHTO Bridge Design Specifications, a total collapse of the bridge was expected after Test 1. However, the FSEL test bridge sustained the total applied load without suffering any significant damage, and the fracture remained confined to the bottom flange of one girder.

Instrumentation data for Test 1 were limited due to a miscommunication, which led to a delay in the start of the data acquisition system. As reported by Neuman [Neuman, (2009)], the system began recording data after the explosion had occurred and the initial pulse had passed. The most significant data of Test 1 were the deflections of the girders during several stages of the test (e.g., after completion of construction, after live load placement, etc.) [Barnard, (2006), Neuman, (2009)].

Many lessons were learned from Test 1. The analysis of the results from the first test helped with the development of a more extensive instrumentation scheme. The instrumentation scheme for Test 2 has been reported by Neuman [Neuman, (2009)]. The gage layout in a typical girder cross section is shown in Figure 2-1.



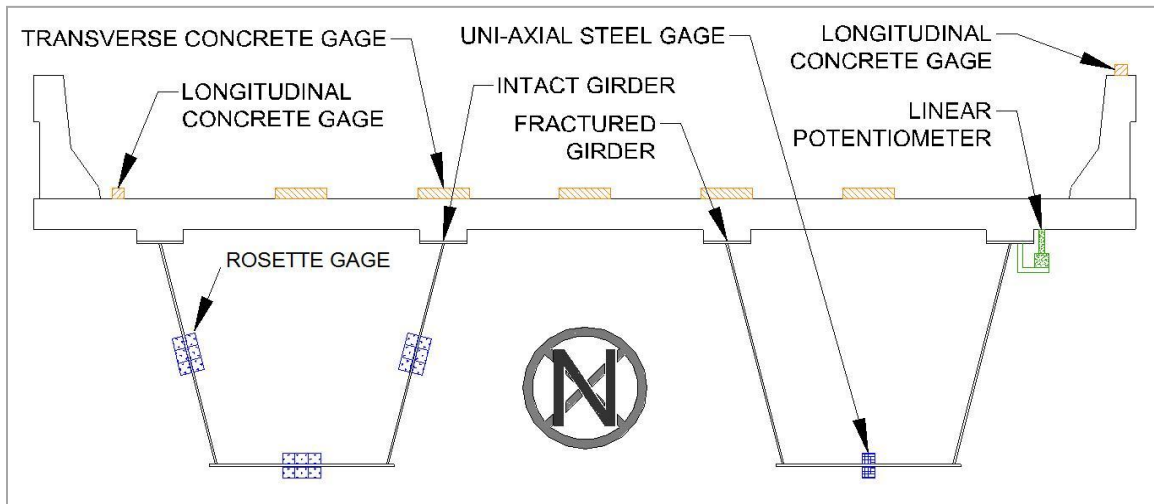


Figure 2-1: The instrumentation plan of the cross-section for Test 2 [Neuman, (2009)]

Longitudinal and transverse concrete strain gages on the deck were installed to capture the behavior of the concrete deck in both directions. Concrete strain gages on the top face of the east railing recorded the strains during Test 2. The strain history of the east railing gave the opportunity to the project team to observe the behavior of an important element that could prevent the collapse of the test bridge. In addition to the concrete deck gages, uniaxial gages on the bottom flange of the fractured girder measured the strain in the longitudinal direction of the bridge. Rosette gages were used on the webs and bottom flanges to determine principal stresses and shear in these components. Linear potentiometers were mounted on the exterior top flange of the fractured girder to measure the separation between fractured girder and concrete deck. The locations of the defined sections that will be discussed throughout this document are illustrated in Figure 2-2. Finally, a plan view of the top surface of the deck is presented in Figure 2-3.

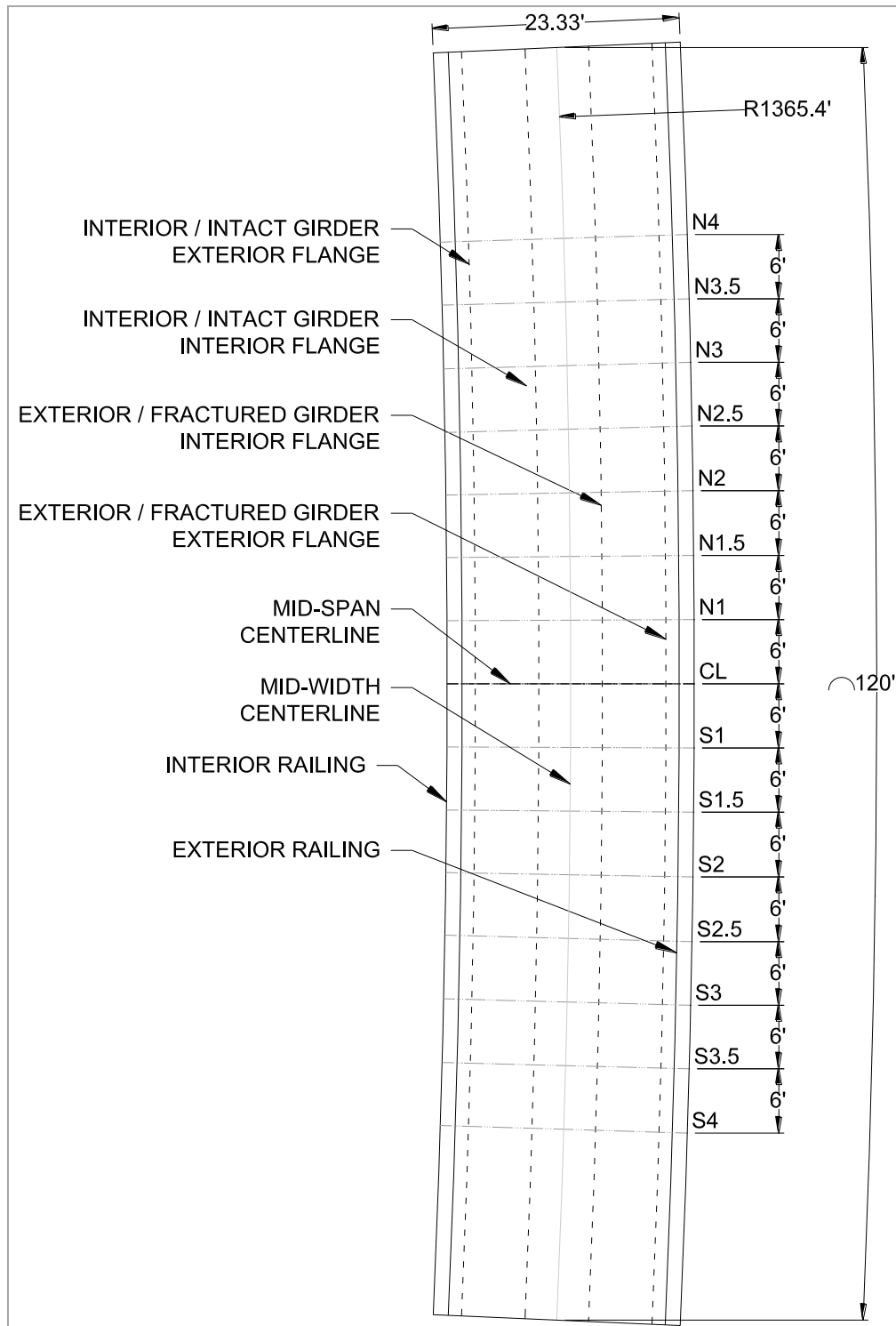


Figure 2-2: Plan view of FSEL bridge with significant features [Neuman, (2009)]

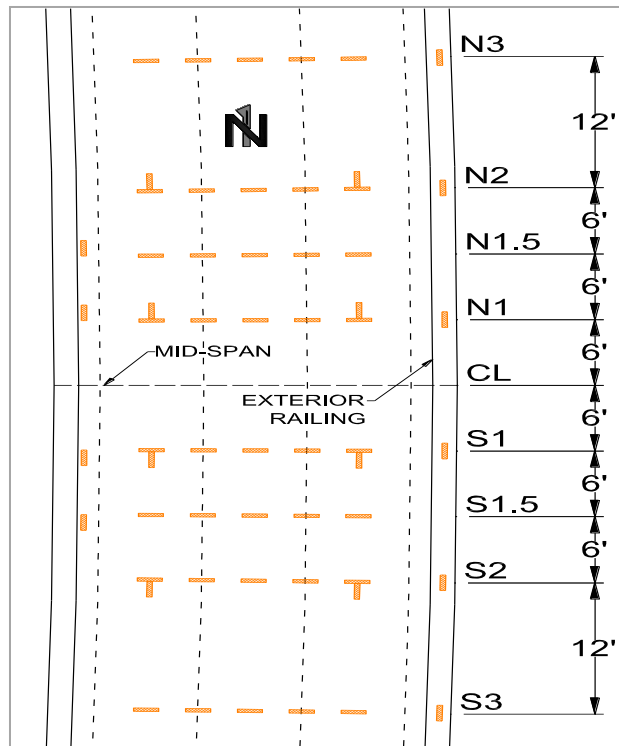


Figure 2-3: Arrangement of the concrete gages on concrete deck Test 2 [Neuman, (2009)]

## 2.2 GIRDER AND CONCRETE DECK DEFLECTION SURVEY

The primary objective of Test 2 was to observe the behavior of the bridge in the case that the fracture would have propagated in Test 1. For this reason, the full depth of the webs was cut, and the same load as in Test 1 was applied to the bridge. A scissor-jack system was used in Test 2 to support the fractured girder while the webs were cut. The scissor-jack was designed so that it was able to instantly release the fractured girder and allow it to deflect as if the fracture occurred in the webs. Based on this fact, the curves of Figures 2-4 and 2-5 “Before Scissor-Jack Release” and “After Scissor-Jack Release” illustrate the deflections of the two girders before and after the test, respectively. Additionally, the curve “After Live Load Release” refers to the deflected shape the girders had after removing the live load (i.e., concrete blocks used to simulate a truck)

that was used during the test. As described by Neuman [Neuman, (2009)], the bottom flanges of both girders were surveyed before and after Test 2, as well as after removing the live load from the bridge. The deflection plots of the intact girder and fractured girder are shown in Figures 2-4 and 2-5.

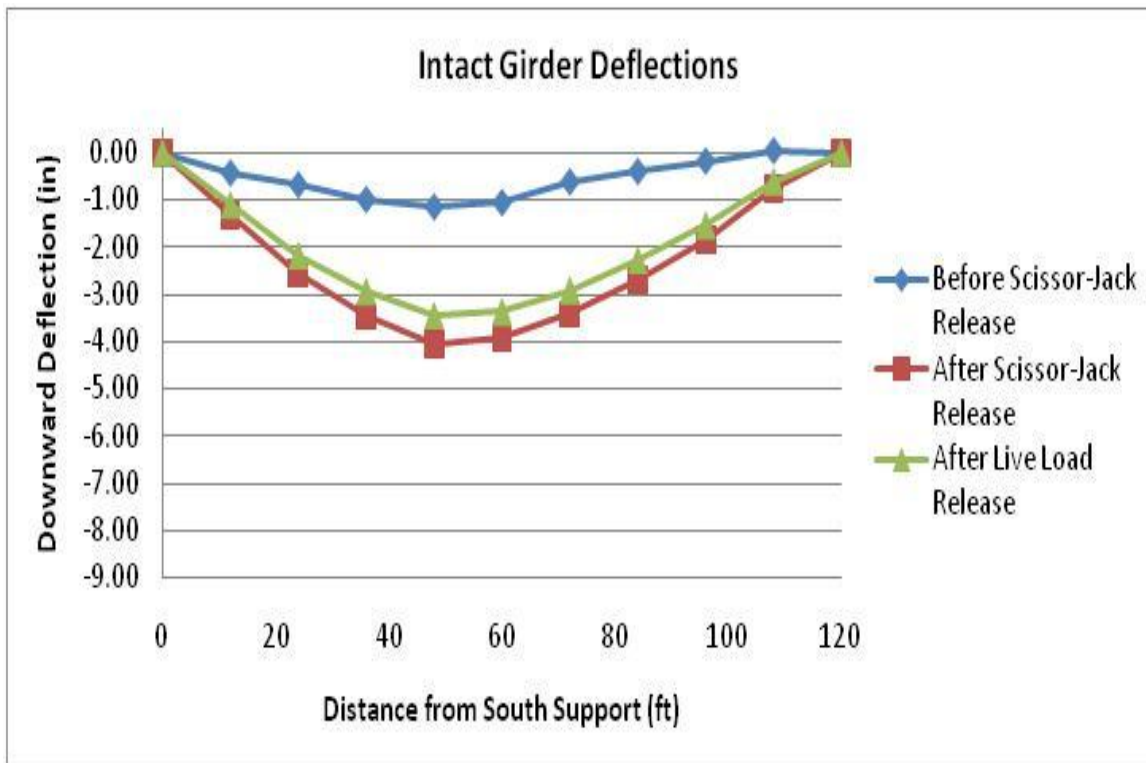


Figure 2-4: Intact girder deflection during Test 2 [Neuman, (2009)]

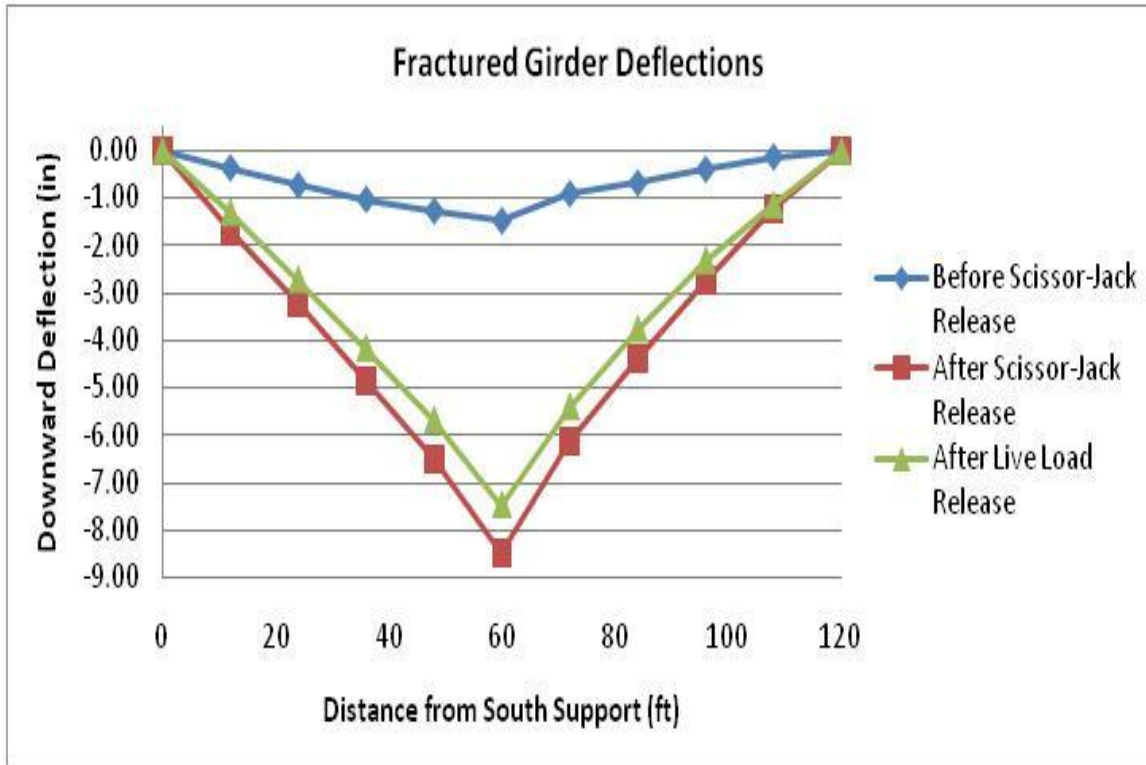


Figure 2-5: Fractured girder deflection during Test 2 [Neuman, (2009)]

In addition to measuring the girder deflections, the top surface of the deck was surveyed after Test 2 to determine its deflected shape. By combining the measurements from the two surveys (deck and girders), it was possible to identify the separation that had occurred at the interior top flange of the fractured girder. The results of direct measurement of the separation between the box girder and the deck and the difference between the deflection of the girders and deck computed from the survey results were essentially the same (Figure 2-7). Based on these observations, the project team was motivated to develop further the Simplified Strip Model, which could predict the pulling out of the studs from the bridge deck. A more detailed description of the Simplified Strip Model will be presented later in this thesis.

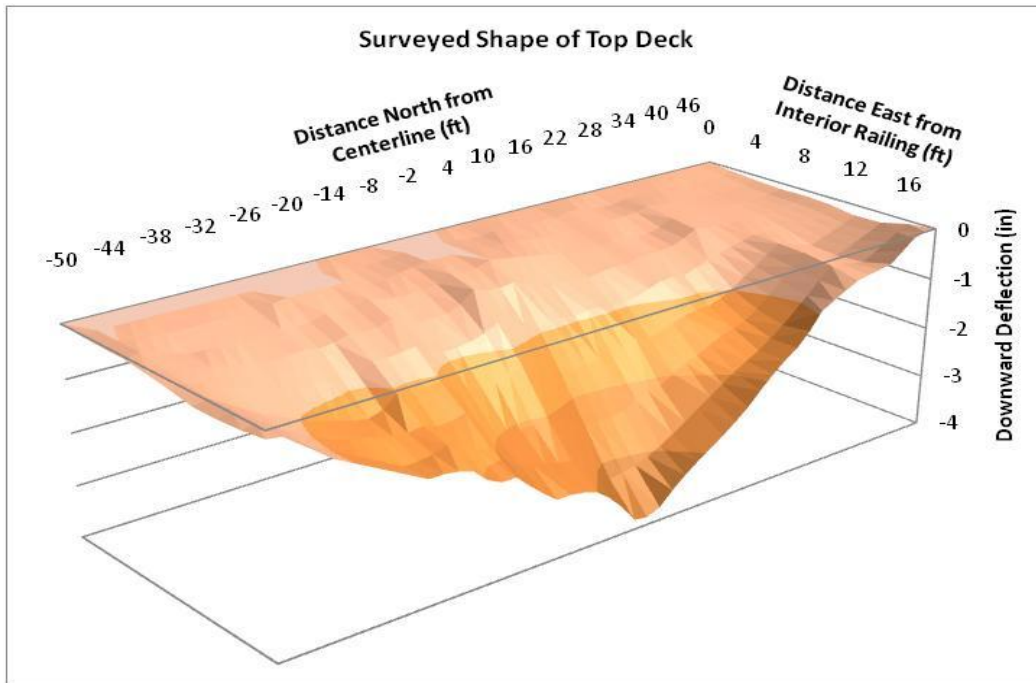


Figure 2-6: Concrete deck deflected shape after Test 2 [Neuman, (2009)]

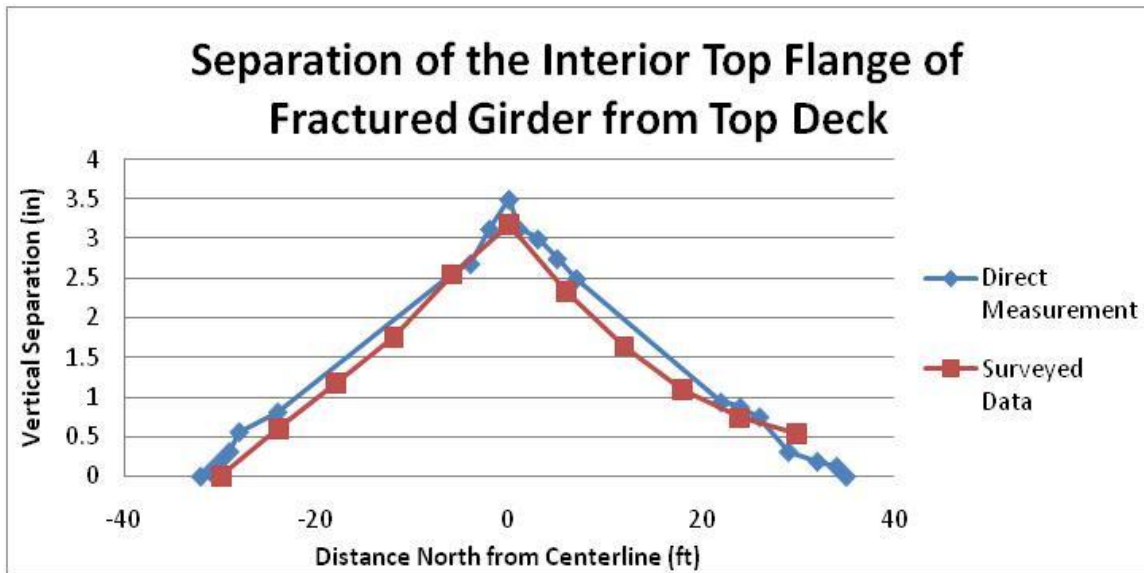


Figure 2-7: Fractured girder's interior top flange separation after Test 2 [Neuman (2009)]

## **2.3 GIRDERS AND END DIAPHRAGMS GAGE DATA ANALYSIS**

### **2.3.1 Instrumentation analysis of intact and fractured girder**

The instrumentation of the two girders was different due to the fact that different behaviors were expected. The fractured girder (FG) was instrumented with uniaxial strain gages on the bottom flange because the torsion and vertical shear in the webs was expected to be small, while rosette gages were installed on the intact girder (IG) because torsional and flexural behavior was expected to be important. During the test, the bottom flange of the fractured girder was in compression along the whole span, which has been well captured by the uniaxial gages (Figure 2-8). Moreover, all the strain values of the monitored locations were in the elastic range. The compressive state of the bottom flange was consistent with the deflected shape of the fractured girder, which was similar to two beams cantilevered from the supports (Figure 2-5). It is worthwhile to mention that the first couple of seconds were the most interesting period of time, and for this reason, all the strain plots focus on this period.

The intact girder was one of the critical members of the bridge because it had to sustain the entire dead load of the bridge and live load of the simulated truck. The deflected shape of the intact girder shown in Figure 2-4 suggests that the bottom flange should be in tension. This observation was verified by the gage data shown in Figure 2-9. The strain values were in the elastic range, and their magnitude was higher than the gages on the bottom flange of the fractured girder. The fractured girder deflected under its own weight, whereas the intact girder deflected under the total load.

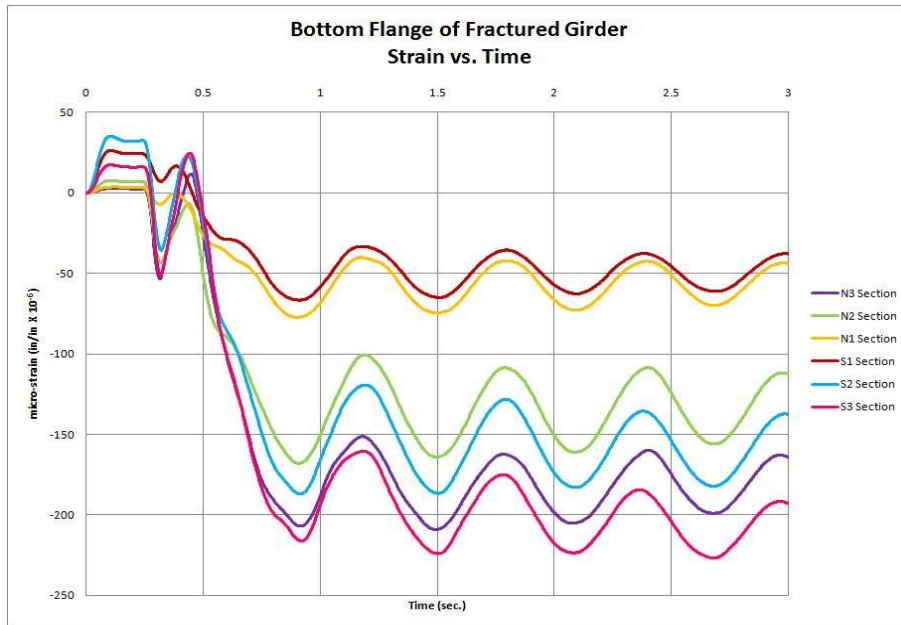


Figure 2-8: Bottom flange strain gages data of the fractured girder during Test 2

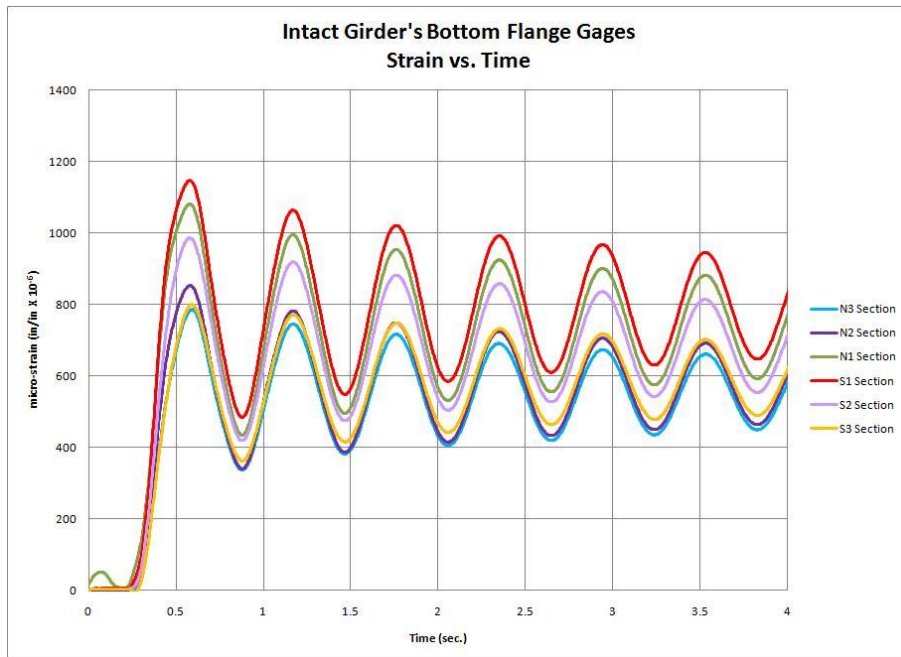


Figure 2-9: Bottom flange strain gages data of the intact girder during Test 2



A combined plot of all the gages located on both bottom flanges (Figure 2-10) gives an overall view of the different behavior of the girders. The initial pulse from the release of the jack and the damped oscillations of the structural system are clearly shown in Figure 2-10. A dynamic load could have a significantly larger effect than a static load of the same magnitude due to the structure's inability to respond quickly to the loading. The increase in the effect of a dynamic load was given by the dynamic amplification factor (DAF), which could be computed as the ratio of  $u_{max}/u_{static}$ . As it was reported by Neuman [Neuman, (2009)], a dynamic amplification factor of 1.3 has been observed in the output of the strain gages used during Test 2.

The strain in the bottom flange of both girders is shown in Figures 2-11 and 2-12. All the values shown in these figures are the static values captured by the strain gages after the end of Test 2 with the exception of the data corresponding to the end points, which have been extrapolated by data from S2, S3, N2 and N3 sections.

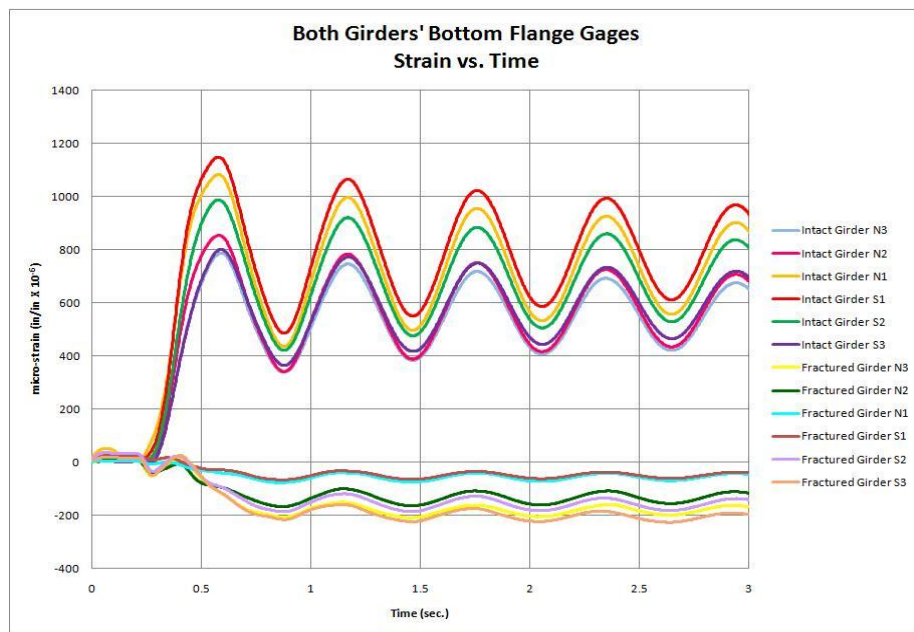


Figure 2-10: Bottom flange strain gages data of the girders during Test 2

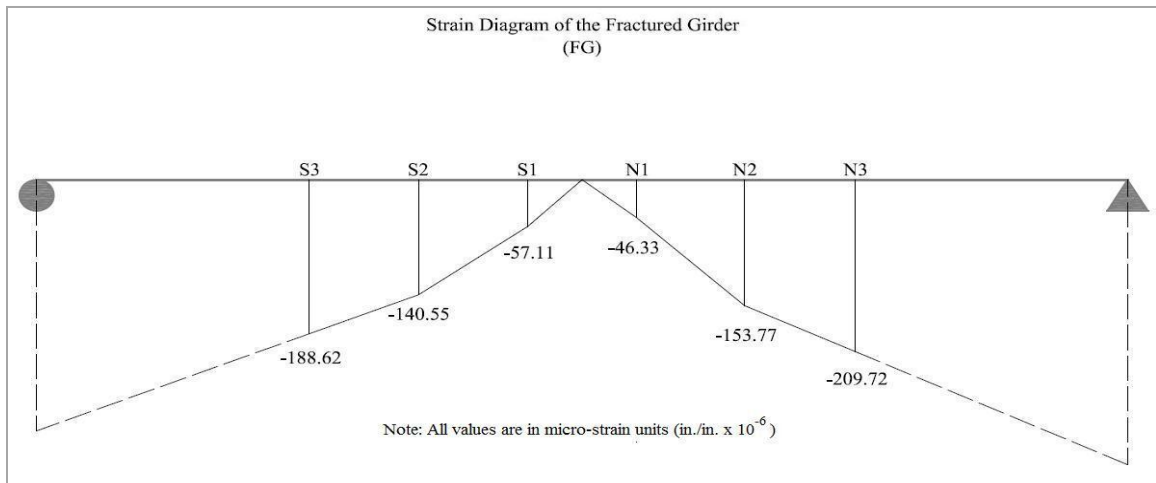


Figure 2-11: Bottom flange strain diagram of fractured girder after Test 2

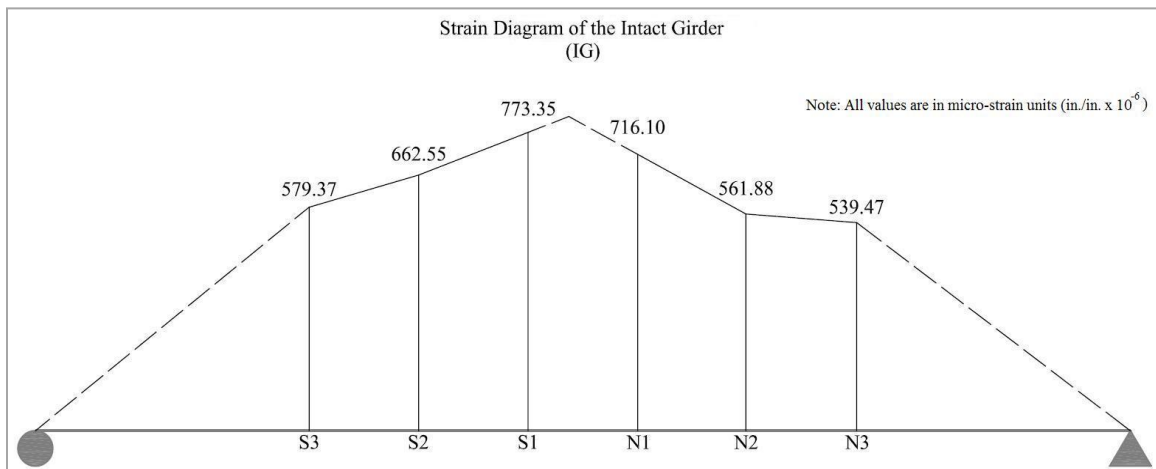


Figure 2-12: Bottom flange strain diagram of intact girder after Test 2

The moment diagram for the intact girder (Figure 2-13) was constructed using the static values of the strains recorded from the gages on the bottom flange of the intact girder and on the top surface of the deck. The strains of the extreme fibers of the elastic composite cross section were used to construct the strain gradient. By converting the strain gradient to stresses, the internal forces, which acted on different parts of the elastic

section, could be calculated. Then, the moment was calculated by adding the moments of the forces acting at various parts of the section about the bottom flange of the girder. It was assumed that the elastic section for the calculation of the bending moment along the length of the bridge was based on a section that consists of the steel box of the intact girder, the concrete deck, and the railing. Half of the width of the deck was assumed to be the effective width of the elastic section. The details of the calculations are given in Appendix A.

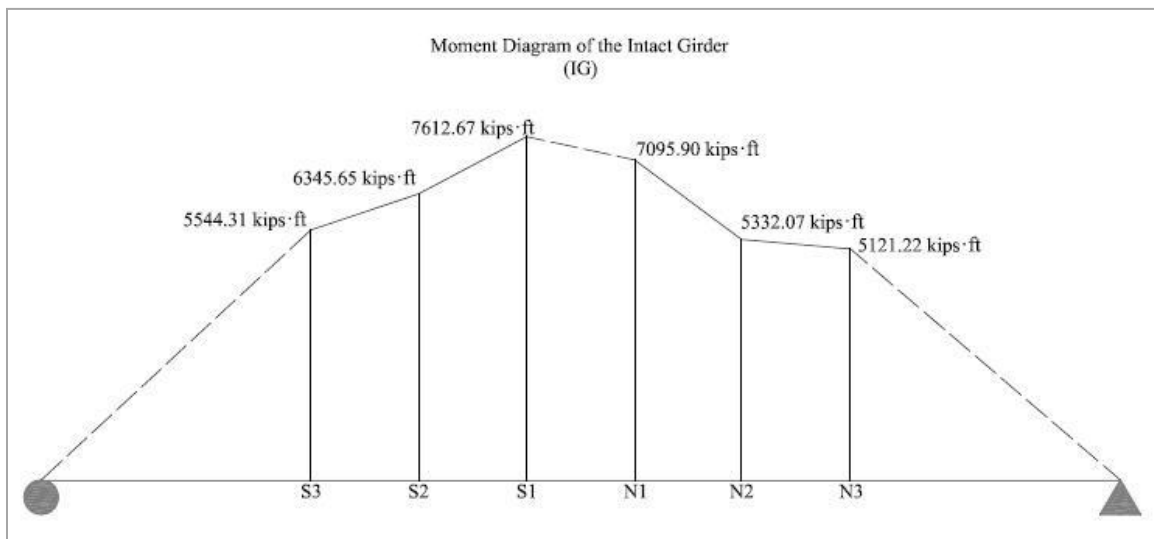


Figure 2-13: Moment diagram of the intact girder after Test 2

The shear flow at the defined sections was calculated by analyzing the different components of the rosette gages on the intact girder. From the rosette gage on the bottom flange, the torsional shear could be readily calculated because the bending in the bottom flange was almost zero. The torsional shear multiplied with the thickness of the bottom flange gives the shear flow of the bottom flange. The shear in the webs contains two components, the torsional shear and the bending shear. After separating the two

components of the shear, the shear flow was equal, as above, with the product of the torsional shear times the thickness of the web. Figure 2-14 shows that the calculated shear flow in the webs was the same as at the bottom flange, which was expected. The curves of two defined sections (N1 and S2) are missing due to the fact that some of the components of the rosettes did not capture the data properly.

If the composite section of the intact girder was treated as a closed section where the shear flow in the deck was assumed to be the same as in the webs and the bottom flange, then it was possible to calculate the torque that was applied on the intact girder by the live truck load and the dead load of the bridge that the fractured girder could not support. The torsion at each section was equal to:

$$T=2\cdot A\cdot q \quad \text{(Equation 2-1)}$$

where  $A$  was the inner area of the closed section ( $A= 26.74 \text{ ft}^2$ ), and  $q$  was the shear flow value at each section. The magnitudes of the shear flow at N3, N2, S1 and S3 were -14.98 kips/ft (-1.25 kips/in), -10.36 kips/ft (-0.86 kips/in), 1.60 kips/ft (0.13 kips/in), 14.60 kips/ft (1.22 kips/in), respectively. All the values were calculated from the static strain values. The torsional moment diagram (Figure 2-16) was constructed by inserting all these values into Equation 2-1. The applied distributed torque was equal to the slope of the line shown in Figure 2-16. The distributed load which was transferred to the intact girder could be calculated as the distributed torque divided by the distance between the centerline of the girders. The calculated distributed torque was equal to 26.59 kips·ft/ft, whereas the distributed torque produced by half of the dead load (weight of the fractured girder plus half the weight of the deck) was 23.19 kips·ft/ft. In this comparison, the three concentrated torques produced by the front and the two rear axles of truck, which were  $8.18\cdot 9.89=80.90$  kips·ft and  $33.92\cdot 9.89=335.47$  kips·ft, respectively, should be taken into account. The total calculated load that was transferred to the intact girder was 265.87 kips. Considering that a portion of the simulated truck load was being transferred to the

supports by the action of the concrete deck and railing, the value of the total applied load from the strain data was relatively close with the assumed total applied load being supported by the fractured girder. Realizing that the strain gage data may contain small errors, this load was relatively close to the load of 307.89 kips, which represents half the bridge dead load plus the truck load.

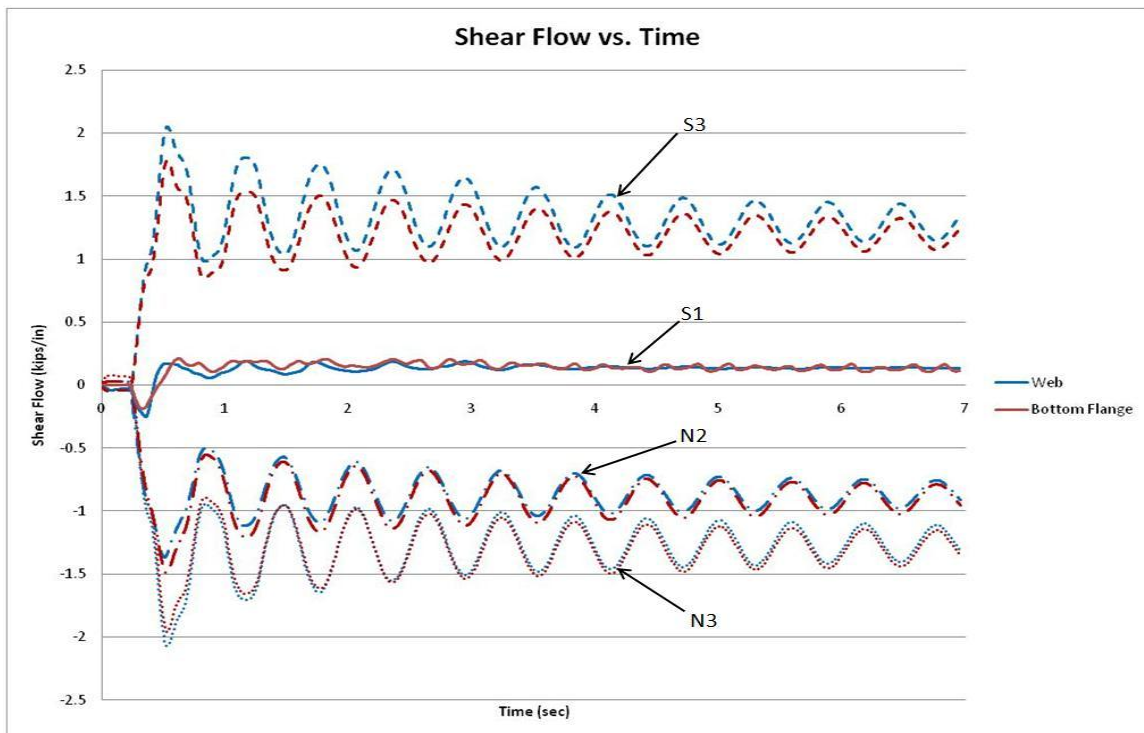


Figure 2-14: Shear flow of defined intact girder sections during Test 2

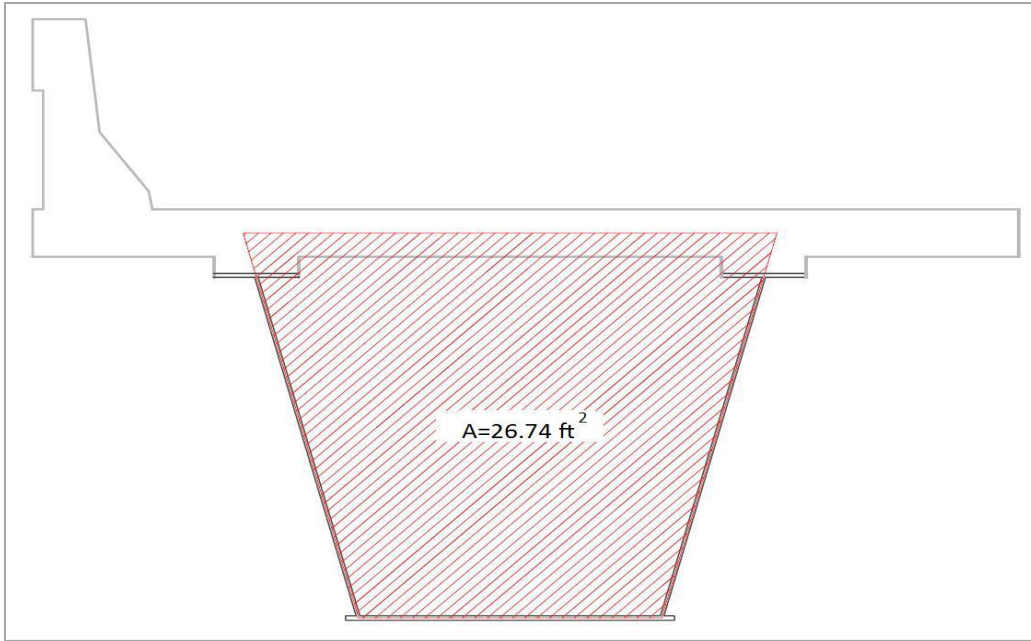


Figure 2-15: Inner area of the closed section

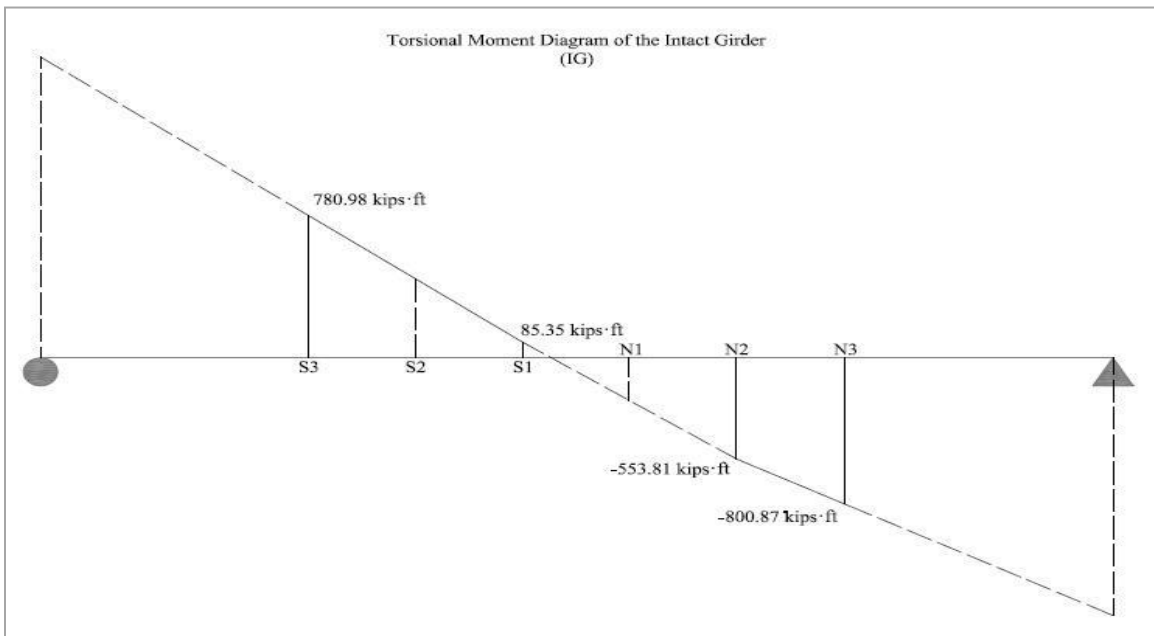


Figure 2-16: Torsional moment diagram of the intact girder after Test 2

The overall behavior of the bridge after Test 2 was more than satisfactory. The fractured girder's deflections were small under its own dead load, and the intact girder was able to hold the entire dead load of the bridge and the simulated truck live load. The end diaphragms played a significant role in providing torsional moment restraint at the ends of the intact girder. A lack of torsional restraint would have resulted in larger rotations and deflections than those that were measured. The angle from the horizontal axis "x" ( $\varphi^\circ$ ) and the magnitude of the principle stresses ( $\sigma_1$ ,  $\sigma_2$ ) was calculated [VISHAY Micro-Measurements, (2008)] for both end diaphragms by using data that the rosette gages captured during Test 2 (Figure 2-17). At the north end diaphragm, it was found that  $\sigma_1 = 4.29$  ksi,  $\sigma_2 = -5.68$  ksi,  $\tau_{max} = 4.99$  ksi and  $\varphi = 45.02^\circ$ , whereas at the south end diaphragm,  $\sigma_1 = 8.05$  ksi,  $\sigma_2 = -3.77$  ksi,  $\tau_{max} = 5.91$  ksi and  $\varphi = 48.61^\circ$ . The fact that the principle axes were oriented at almost  $45^\circ$  indicates a pure shear stress state at both end diaphragms. The rosette was not able to capture any out-of-plane behavior, and for this reason, all the results were only for in-plane behavior.

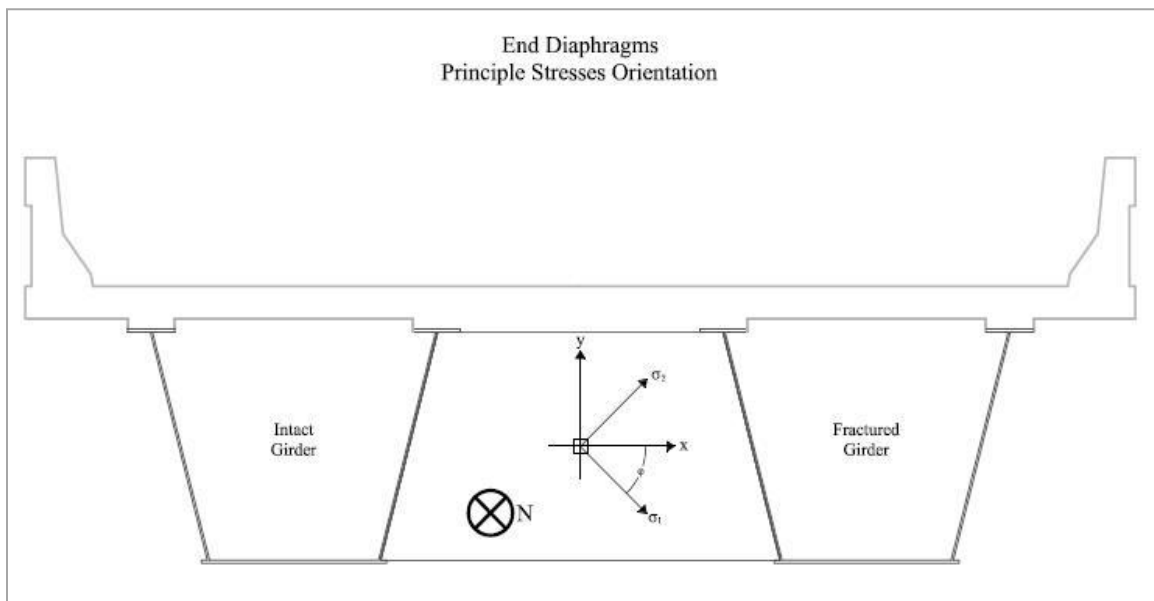


Figure 2-17: Principle stresses orientation at the end diaphragms

### **2.3.2 Instrumentation analysis of deck**

The bridge deck and the end diaphragms were the two elements that connect the two girders, and they were the only elements of the bridge that could transfer loads from the fractured girder to the intact girder. For this reason, it was decided to instrument the top surface of the deck as well as the east railing (Figure 2-3). Additionally, some of the reinforcing steel in the deck and the shear studs were instrumented during construction of the bridge.

After Test 2, it was recognized that the exterior (or east) railing was acting as an inverted beam, and it was able to carry a part of the load that the fractured girder was not able to support. Moreover, the behavior of the deck, which acted as a shear diaphragm, provided a load path to transfer the loads from the fractured girder to the intact girder and back to the supports. Figure 2-18 shows the strain data history of the gages located at the exterior railing. At no location was the concrete strain close to crushing. Strain gages were not installed at the centerline expansion joint, so no data point was obtained at this location. For this reason, the strain values for the centerline expansion joint were extrapolated from measured data points. The extrapolation showed that the concrete strain might be at a range of 300 micro-strains, which was 1/10 of the crushing strain (0.003 in/in). During Test 2, a thin layer of concrete at the centerline expansion joint spalled (Figure 2-19). The spall was produced by the localized contact strain caused by the engagement of the railing at the expansion joint. The strain through the height of the centerline expansion joint away from the areas of contact was small. The strain values at the north and the south expansion joints were close to zero due to the fact that there was no continuity of the railing at the open expansion joints.



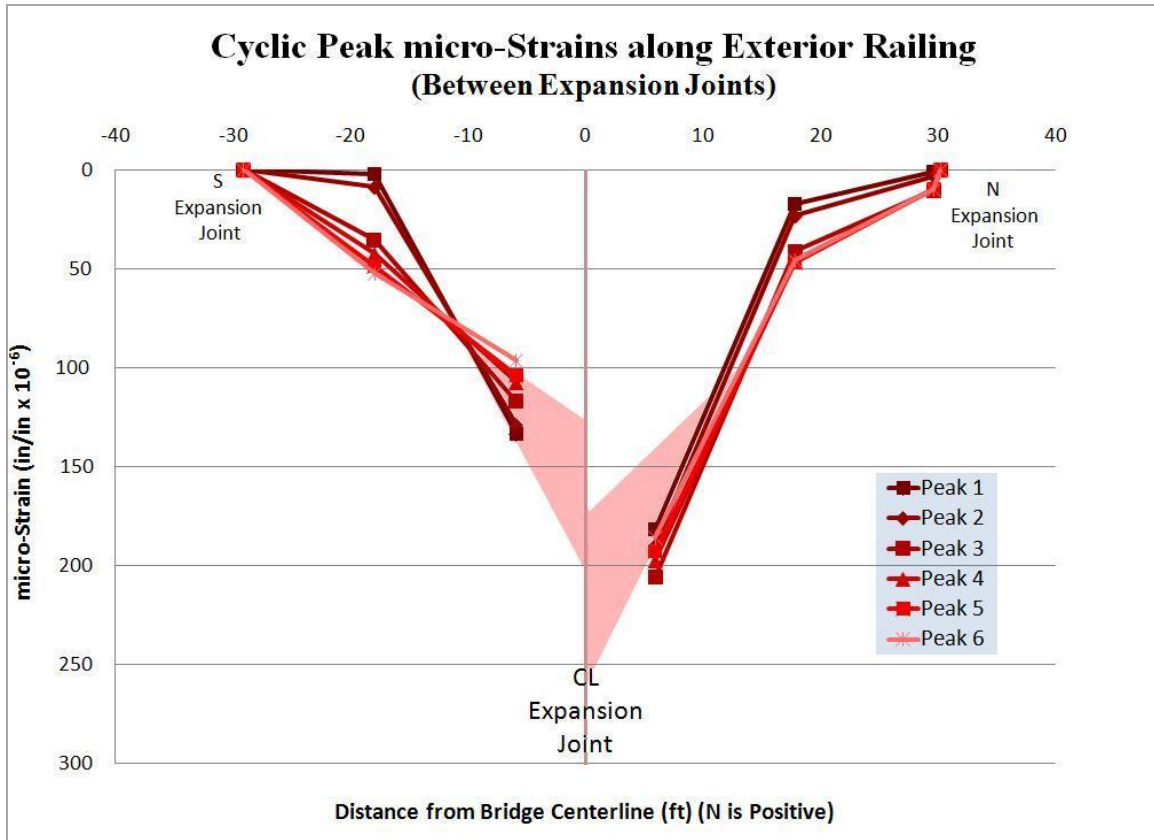


Figure 2-18: Cyclic peak micro-strain along exterior railing during Test 2

The moment diagram of the exterior railing depicted in Figure 2-21 was constructed using static strain values from the gages that were attached on the top face of the east railing. The section that was used to calculate the moments from the strains consists of the typical T501 traffic rail and a part of the bridge deck (Figure 2-20). More detailed calculations of the moment diagram are given in Appendix A.

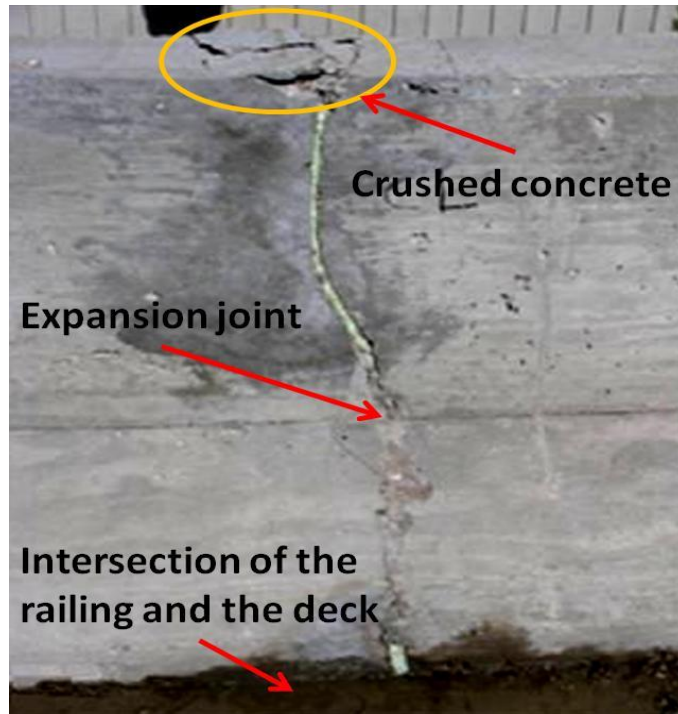


Figure 2-19: Crushed concrete at the CL exterior railing after Test 2

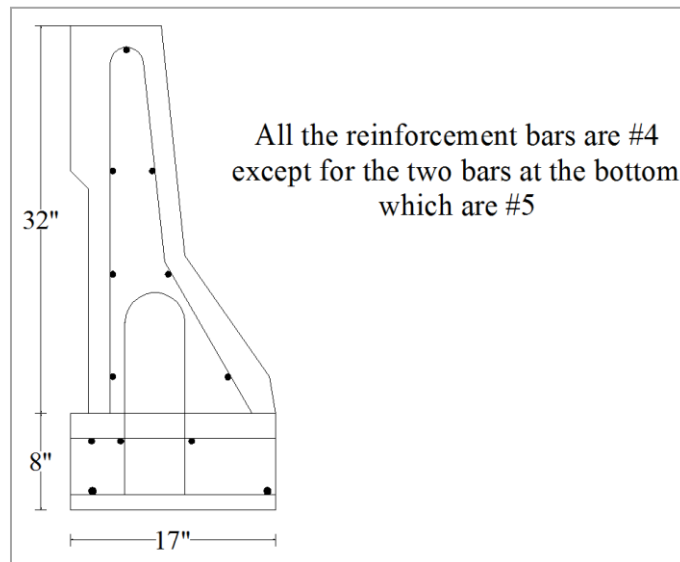


Figure 2-20: Railing section used for the moment calculation of the railing

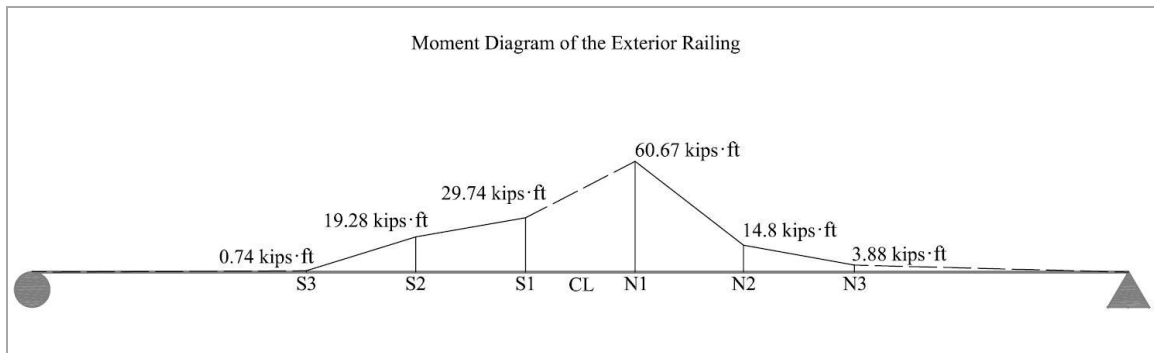


Figure 2-21: Moment diagram of the exterior railing after Test 2

After Test 2, initial observations appeared to show an intact bridge, though these observations were in contrast to the computations of the finite element model as well as the results from the Simplified Strip Model. Both analyses indicated that the interior top flange of the fractured girder and the concrete deck should have been separated. As reported by Neuman [Neuman, (2009)], only after a closer inspection, it became apparent that the interior top flange was not connected to the deck. The separation occurred in an unzipping mode, depicted in Figure 2-22, which started from the centerline and extended almost 30 ft. to each side. Each group of shear studs of the interior top flange, starting from the centerline, was loaded up to its tensile capacity due to double curvature bending of the deck. The unzipping mode occurred because once the tensile capacity of the shear stud was reached, it pulled out of the deck. The double curvature bending of the deck across the width and between the two girders was the result of the downward deflection of the fractured girder after the fracture had been propagated. The connection of the shear studs with the deck played a significant role in the deformed shape of the deck. The cross-section, in which the connection of the shear studs with the concrete deck was intact, deflects in double curvature bending (Figure 2-23b). For sections where the shear studs are no longer attached, the deck deflects across its width in single curvature. Therefore, the deflected shape of the deck was dependent upon the existence (or lack thereof) of the force transmitted from the deck to the interior top flange of the fractured

girder through the shear studs in tension. Under this state, the extreme fiber of the top surface of the deck located above the interior top flange of the fractured girder was under compression. After the tensile capacity of the shear stud connection was reached, the group of shear studs was pulled out of the concrete deck, releasing the reacting force on the deck. The loss of the downward force affects the deformed shape of the cross-section. As a result of this change, the deformed shape of the cross-section will be changed from double curvature to single curvature (Figure 2-23b, c).

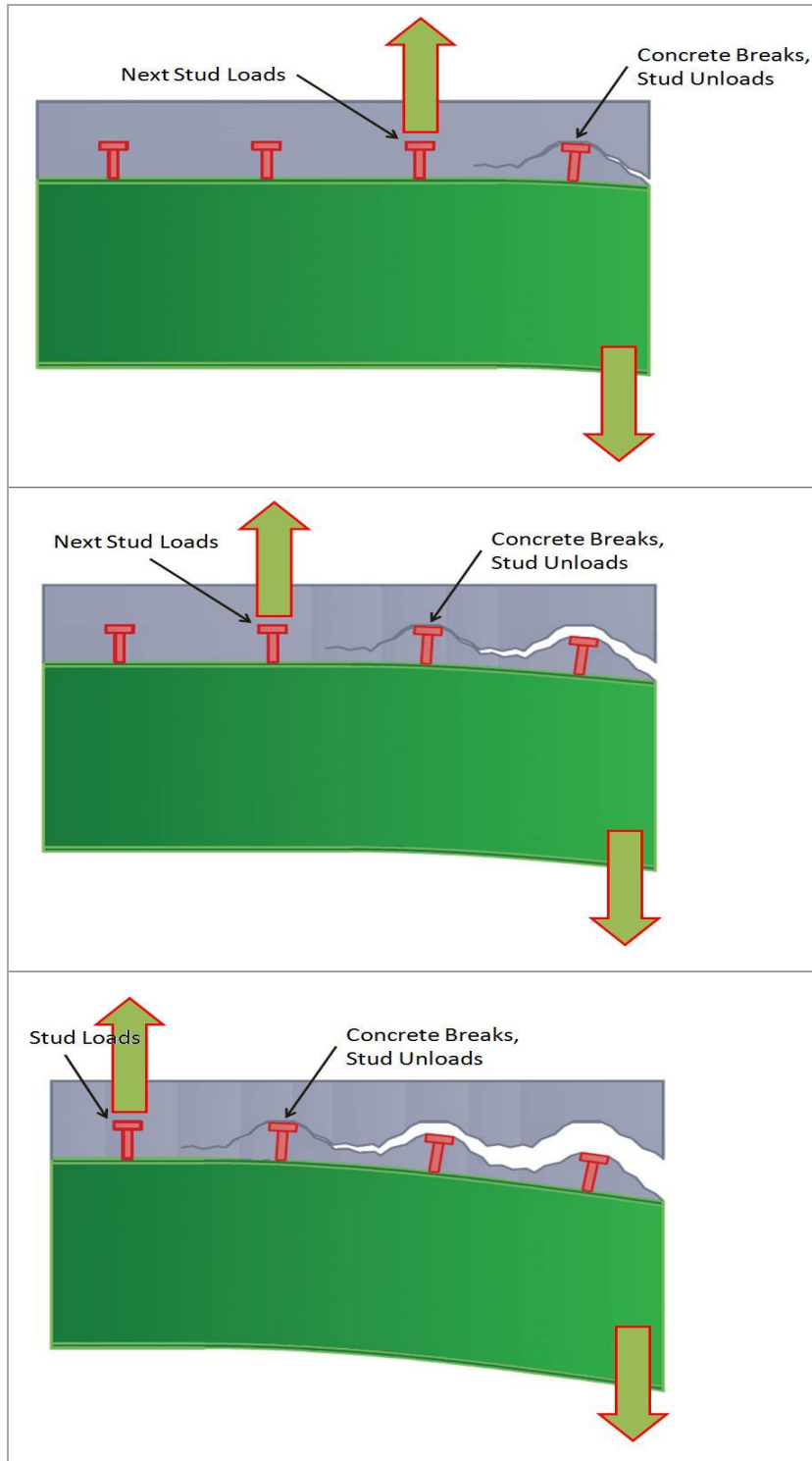


Figure 2-22: Shear stud unzipping mode during Test 2 [Neuman, (2009)]

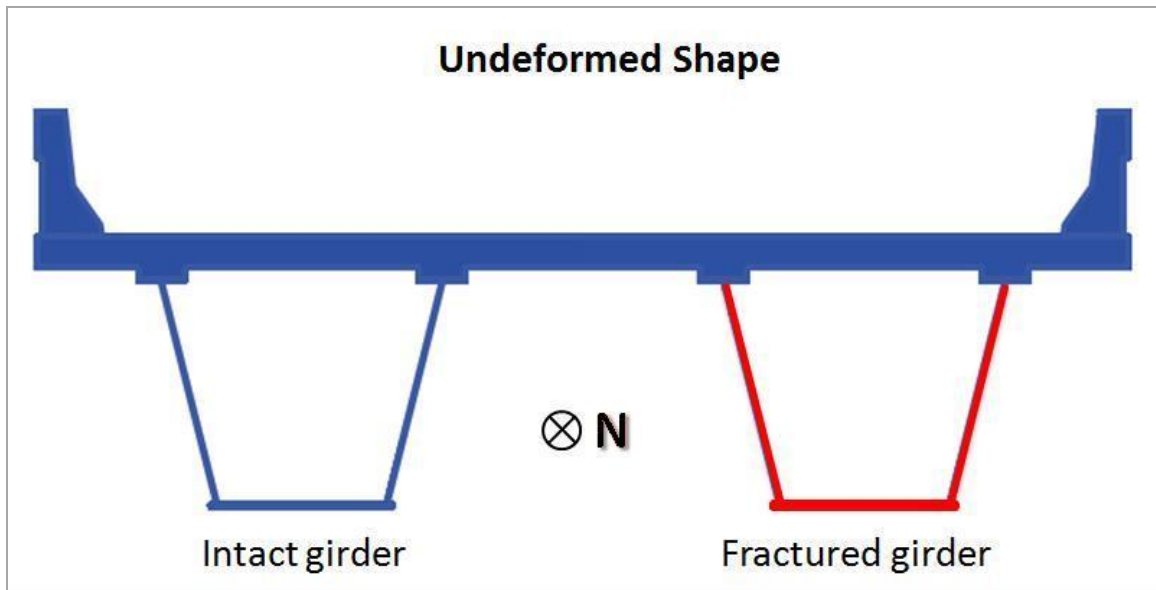


Figure 2-23a: Undeformed shape of the bridge before Test 2

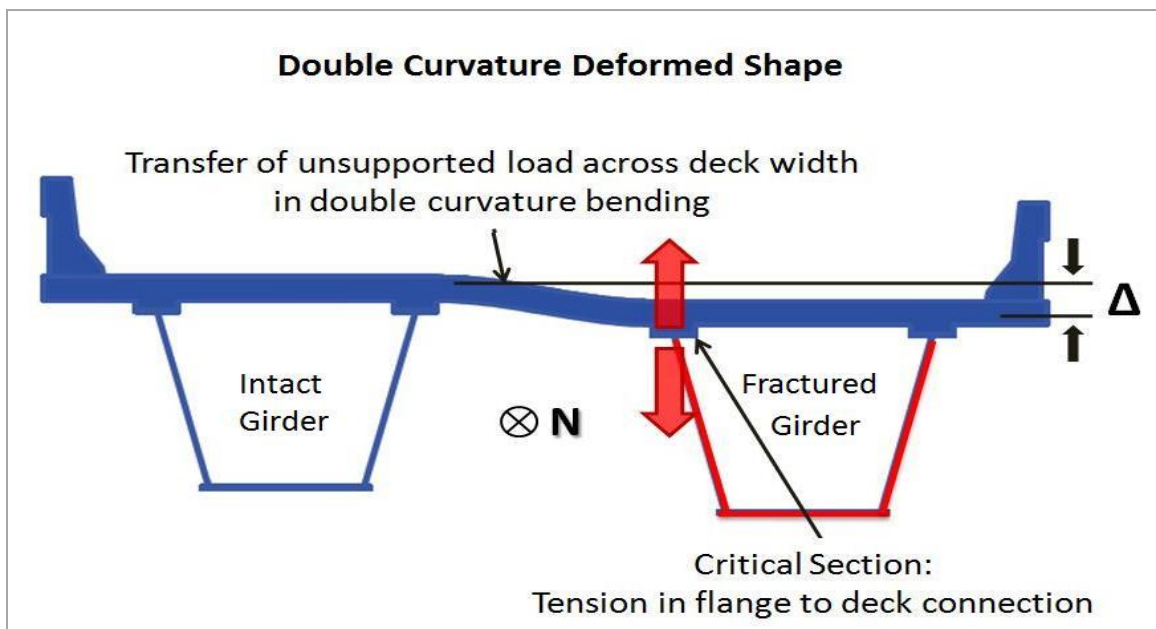


Figure 2-23b: Deformed shape of the bridge in double curvature during Test 2

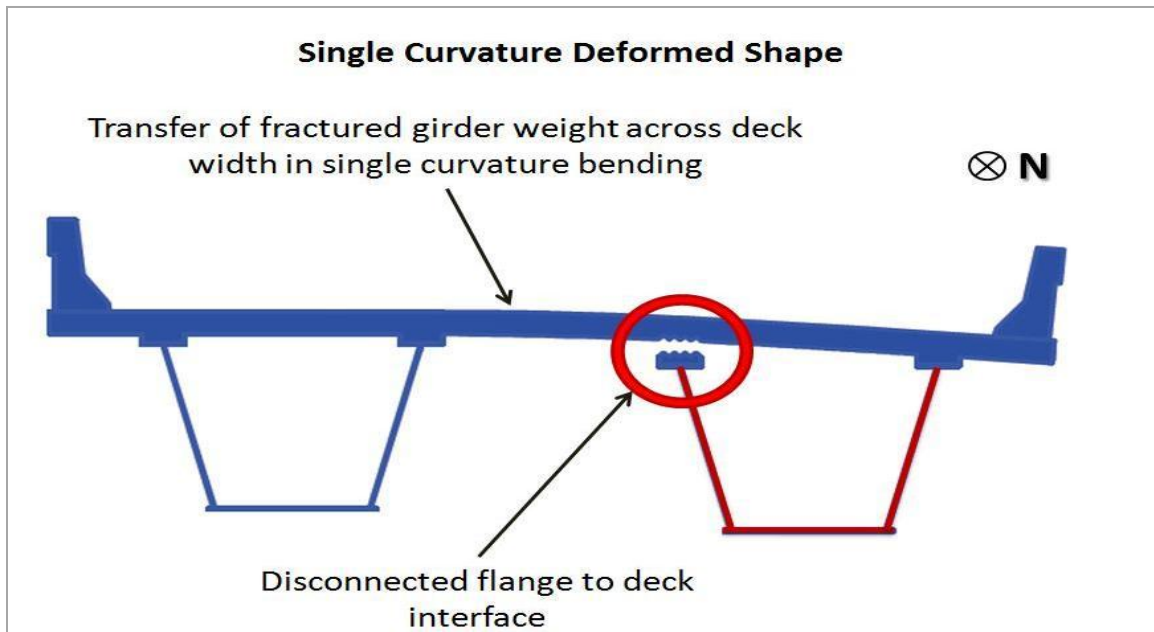


Figure 2-23c: Deformed shape of the bridge in single curvature during Test 2

The unzipping of the shear studs was captured from the strains that were measured on the top surface of the deck, which were recorded from the transverse concrete gages located immediately above the interior top flange of the fractured girder (Figure 2-24). Figure 2-24 shows the strain data history for the first 0.6 second of response. All the curves in Figure 2-24 show the strain reversals of the extreme fiber on the top surface of the concrete deck located above the interior top flange at the fracture location. The blue curves represent the strain transverse to the span of the bridge above the interior top flange of the fractured girder at the N1 and S1 sections, which are located 6 ft. away from the centerline. The red curves show similar strain data for the N1.5 and S1.5 sections, which are 12 ft. from the centerline. The green curves are the plot of the strain readings taken at the N2 and S2 sections, which are 18 ft. from the centerline. The last two purple curves represent strain data from the gages at N3 and S3, which are 30 ft. from the mid-span. The presence of strain reversals indicates that the curvature of the deck changed at a given location from double to single curvature. The strain reverses from compression to

tension, which indicates that the top surface of the deck initially deformed in a double curvature shape; once the unzipping of the shear studs started, it changed to single curvature. Just after the release of the scissor-jack, the gages 6 ft., 12 ft., and 18 ft. away from the fracture captured sudden strain reversals. The behavior captured by those strain gages were in good agreement with the change in deck curvature described above. Moreover, the strain reversals at equal distances from the centerline occurred approximately at the same time, illustrating the symmetric behavior of the bridge about the fracture location. The strain gages located at the N3 and S3 sections, which are 30 ft. from the mid-span, do not indicate a change in curvature, thereby indicating that studs did not continue to pull out at these locations.

Figure 2-25 shows the strain behavior of gages that were installed longitudinally to the bridge span, on the top surface of the railing and 6 ft. away from the centerline, relative to the strain reversals of the deck gages described above. The progressive unzipping of the shear studs from the deck extended beyond 18 ft. from the centerline, but once the exterior railing engaged and started picking up load, pullout of the shear studs was arrested somewhere before reaching 30 ft. from mid-span. The reason why the railing started picking up forces later was due to the closing of the  $\frac{3}{4}$ -in. expansion joint, which was not closed before the bridge deflected. After the scissor-jack was released, the compressive strain at the railing increased, indicating that the expansion joint at mid-span was starting to close. The railing strain reached its peak 0.33 second after the beginning of the test. As reported by Neuman [Neuman, (2009)], the peak compressive strain of the railing and the maximum dynamic displacement of the fractured girder happened in a time period where the strain of the extreme fiber of the top surface of the deck above the interior top flange of the fractured girder at the N2 and S2 sections showed sudden reversals. Inside the same time frame, the compressive strains at the top surface of the deck for similar positions at the N3 and S3 sections reached their maximum values, but they did not undergo reversals. These data indicate that, as the fractured girder deflected under its own weight, the shear stud connection was progressively failing until the point that the joints in



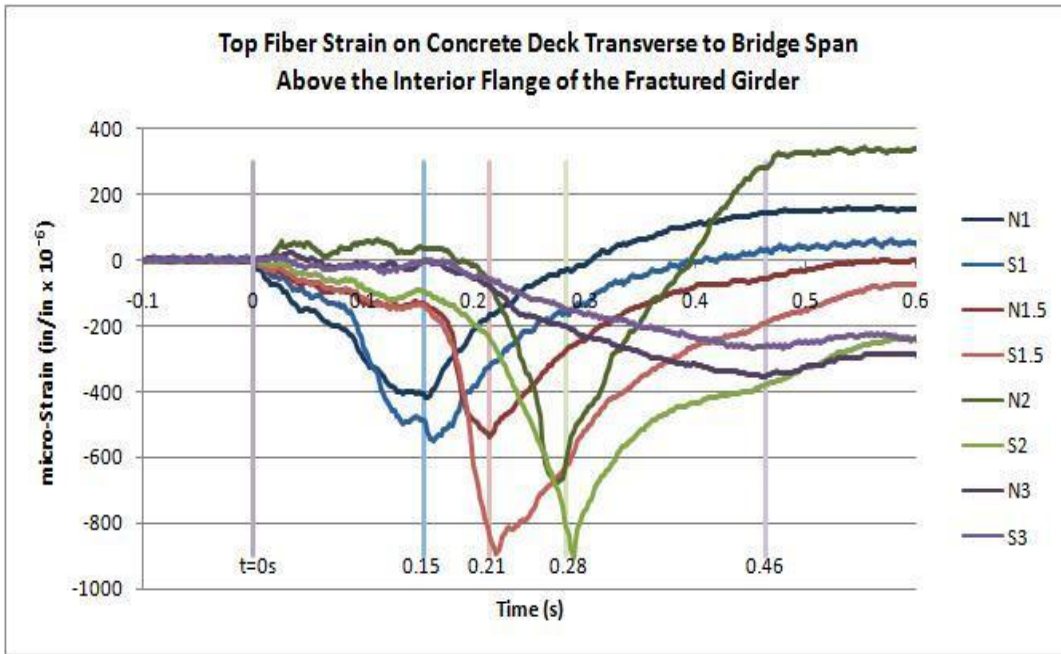


Figure 2-24: Strain reversals transverse to bridge span above interior top flange of fractured girder [Neuman, (2009)]

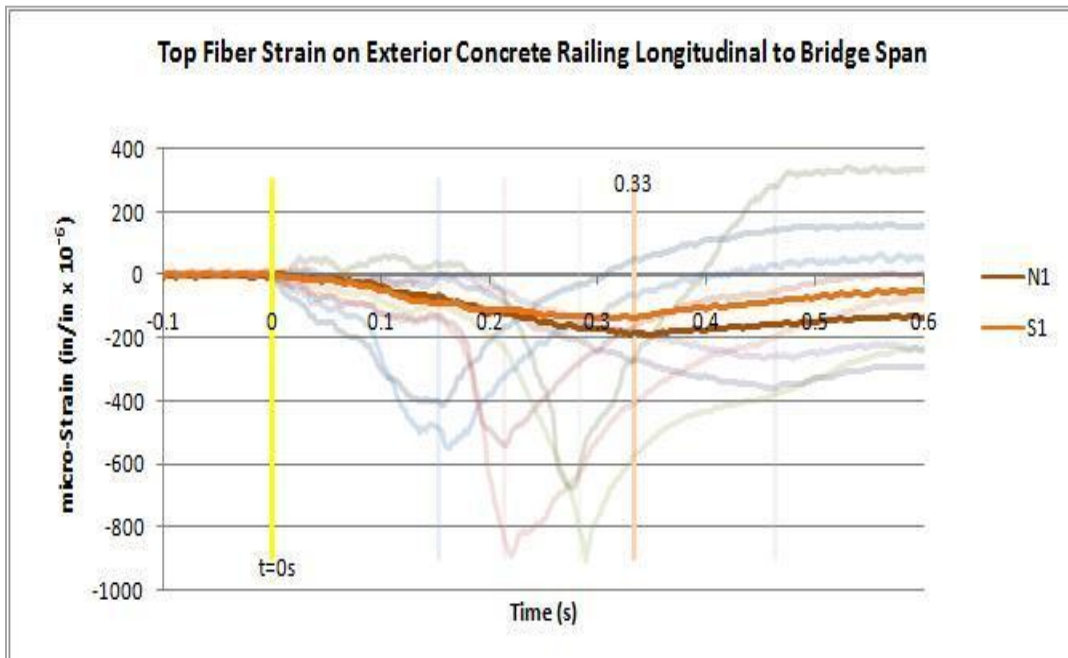


Figure 2-25: Peak compressive strain in exterior railing [Neuman, (2009)]

the rail closed and the rail began to take a portion of the load. The length of the separation which was predicted by the strain reversals was in agreement with the measured separation between the interior top flange of the fractured girder and the concrete deck (Figure 2-7).

## **2.4 SUMMARY**

Many lessons were learned after Test 2. Despite the significant displacements and damage of the fractured girder, the FSEL test bridge resisted collapse while sustaining the large truck load positioned directly above the fracture location. Alternative load paths through several elements including the railing, the concrete deck and the end diaphragms were engaged. The role of these elements was important for the performance of the bridge. Based on the method that was used to identify the separation of the fractured girder's interior top flange, the Simplified Strip Model was developed. The Simplified Strip Model will be described in the next chapter.

## CHAPTER 3

### Simplified Strip Model of Deck Behavior

#### 3.1 INTRODUCTION

The behavior of a complex structural system can often be analyzed with the assistance of a finite element program. Although finite element programs may produce the most accurate results, consideration must also be given to the amount of time and work that is required to model and analyze a structural system. The main goal of this thesis is to provide engineers simplified methods to check the redundancy level of twin box girder bridges before investing time and effort in developing a sophisticated and complex finite element model. Depending on the results from the simplified analytical modeling methods, an engineer can decide if a finite element model is needed. Thus, if the results from the simplified modeling methods show that a bridge has adequate redundancy, then the effort and the cost of a more detailed analysis will have been saved.

The Simplified Strip Model is developed to predict the tensile failure of shear studs from the bridge deck. The tensile strength of shear studs is one of the initial checks that an engineer needs to perform to evaluate the redundancy level of twin box girder bridges. The initial checks, which will be described in the next section, are focused on determining the ability of the concrete deck connecting the two girders to transmit the load from a fractured girder to the intact girder, and the ability of the intact girder to carry the entire load. The critical elements are the shear stud tensile capacity, the transverse moment capacity of the deck, the shear and moment capacity of the intact girder, and the flexural strength of the railing. These components of a twin box girder bridge play a significant role in the behavior of the bridge after fracture of one of the girders occurs. Several assumptions are made in order to simplify the analyses. The assumptions used to develop the Simplified Strip Model are presented in following sections.

Depending on the results of the initial checks, a yield line analysis may be needed to be implemented. The Yield Line Model is presented in Chapter 5. The initial checks and

the Yield Line Model are a set of simple modeling methods that can help an engineer to conservatively predict the redundancy level of twin box girder bridges.

### **3.2 INITIAL STRENGTH CHECKS**

Consistent with the experimental testing program, it is proposed that evaluations of bridge redundancy be performed for the case in which a single HS-20 truck is positioned on the bridge deck above the presumed fracture location so as to cause the most severe internal stresses to develop. Thus, on an in-service bridge, this worst-case scenario would occur when the design truck load was passing across the bridge at the location that induced the maximum internal bending moment at the same instant that a fracture event occurred at that point of maximum moment. Under these conditions, initial strength checks are performed to determine if there is sufficient strength in the intact girder to support the weight of the bridge and the factored truck load and to evaluate if the deck has sufficient strength to transmit the load carried by the fractured girder to the intact girder. If the bridge under consideration does not satisfy these initial strength checks, a three-dimensional finite element model may developed to provide a more accurate estimate of the bridge's performance.

An initial check should determine if the concrete deck has adequate flexural and shear capacity to transfer all the unsupported loads of the fractured girder to the intact girder (e.g., dead load of the fractured girder plus any truck live loads). Analysis of the test results has shown that the fractured girder is capable of sustaining a portion of its load; however, to obtain a conservative solution, it was assumed that the total load was transferred to the intact girder. The deck capacity can be calculated using a strip model of the deck (Figure 3-1) with a width equal to shear stud spacing. The deck strip should be analyzed as a continuous beam with roller connections at the location of top flanges (Figure 3-2).

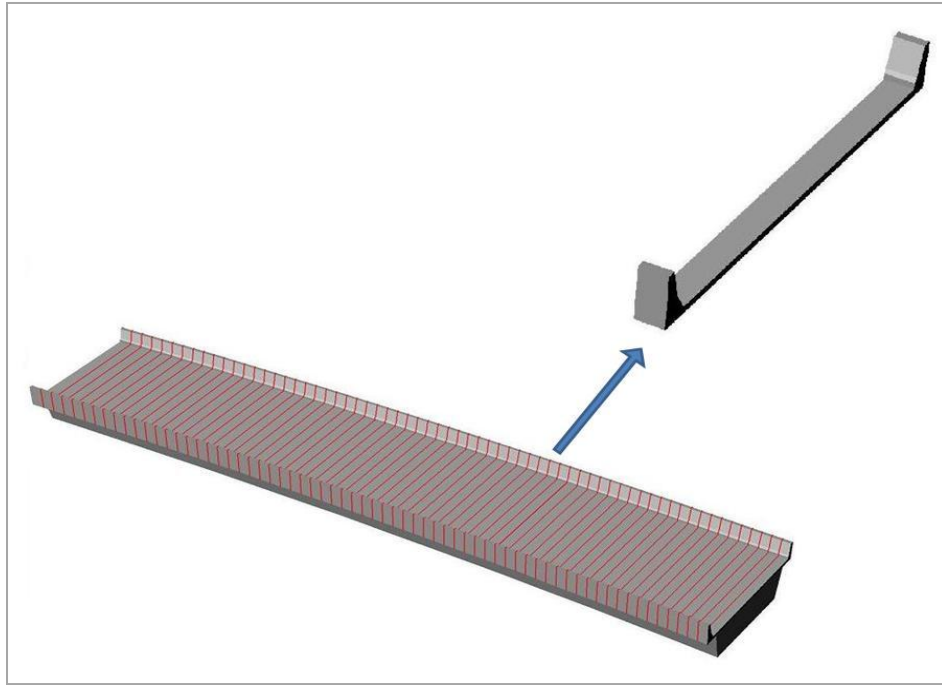


Figure 3-1: Bridge divided in strips

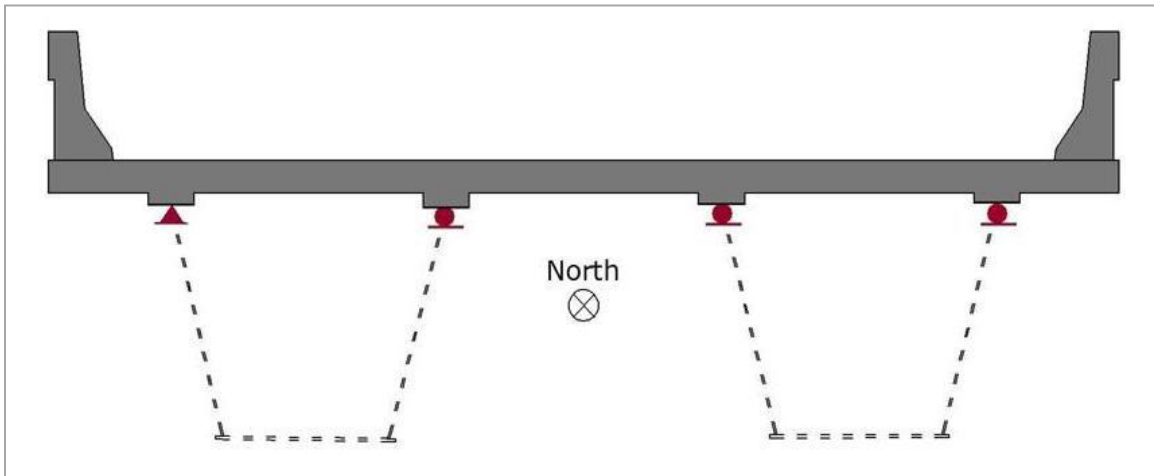


Figure 3-2: Typical deck strip cross section with boundary conditions

First, the bridge deck shear capacity should be greater than the transferred shear. The shear capacity is the sum of the capacity of the individual deck strips. The transferred shear is assumed to be equal to the entire dead load carried by the fractured girder plus the factored truck load. The unsupported load must be transferred to the intact girder, and therefore the deck shear capacity should be adequate. The maximum shear capacity is taken as the smaller of the shear corresponding to a plastic moment mechanism in the deck and the shear capacity of the deck,  $V_{Deck}$ . The shear developed from the plastic moment deck mechanism shown in Figure 3-3 is given by (Equation 3-1)

$$V = \frac{M_1 + M_2}{S} \leq V_{Deck} \quad \text{(Equation 3-1)}$$

where  $M_1$  and  $M_2$  are the positive and negative moment capacity of the deck, and  $S$  is the distance between the mid-width of the fractured girder's interior top flange and the edge of the interior top flange of the intact girder (Figure 3-3).

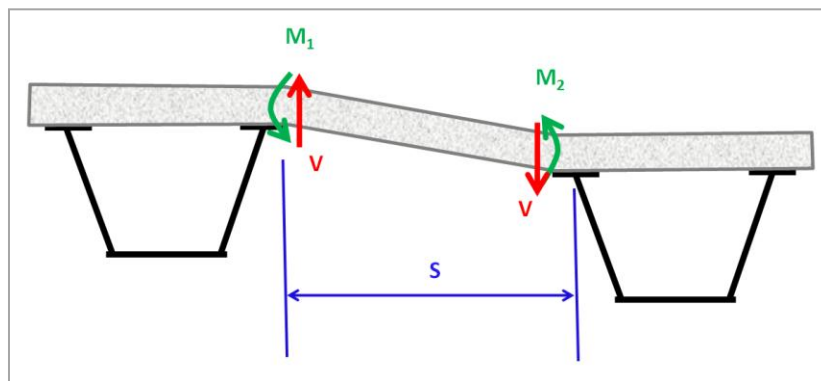


Figure 3-3: Plastic deck mechanism

The shear studs connecting the deck to the fractured girder must have sufficient tension capacity to develop the plastic beam mechanism in the bridge deck. The required shear stud tensile capacity can be estimated using the model of the bridge deck shown in Figure 3-4. The required tension capacity of the group of shear studs included in the strip can be calculated using (Equation 3-2.

$$T \geq \frac{M_2}{b} + V \quad (\text{Equation 3-2})$$

where  $T$  is the tensile capacity of the shear stud group in the strip,  $M_2$  is the positive moment capacity of the deck strip,  $b$  is the distance between the mid-width of the top flanges of the fractured girder, and  $V$  is the shear from the plastic deck mechanism. The tensile capacity of the shear studs group can be estimated by using the modified ACI equations developed in this research and detailed in the report “The Tensile Capacity of Welded Shear Studs” (FHWA/TX-08/9-5498-R2).

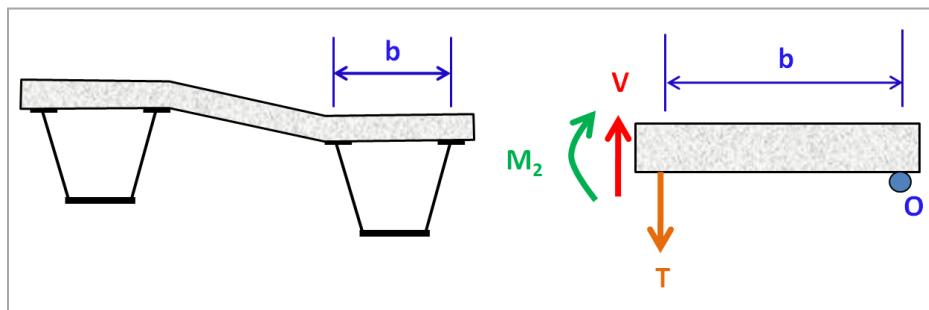


Figure 3-4: Shear stud pull out capacity

Moreover, a check of the flexural, shear and torsional capacity of the intact girder should be undertaken to make sure that it can support the dead and live loads on the bridge, including those transferred from the fractured girder. The bending moment produced by the loading should not exceed the plastic positive moment capacity at the

critical positive moment location of the span, nor should it exceed the plastic negative moment capacity at the interior pier. A failure of the intact girder would lead to a catastrophic collapse of the whole bridge.

The torsional capacity and stiffness of the intact girder is an important factor in the ability of the bridge to carry load after a fracture. The closed composite box sections are torsionally stiff. A large torque acts on the intact girder through the concrete deck by the live load and dead load carried by the fractured girder. The shear of the end panels of the intact girder should be checked to ensure that the webs have adequate capacity. The end panel's shear is limited to its buckling capacity, and the capacity of an interior support is equal to its tension field strength. The shear in the girder due to the torsion and vertical loads transferred from fractured girder need to be included in the strength check. Results from the test program on the full-scale test bridge indicated that the torsion introduced into the intact girder was nearly symmetrical (Figure 2-16); therefore, it is assumed that the intact girder has symmetrical torsional boundary conditions. It is further assumed that the live load and dead load is uniformly distributed. The torques of the dead load and live load are given in Equations 3-3 and 3-4, respectively:

$$T_{DL} = w_{0.5DL} \cdot e_{DL} \quad \text{(Equation 3-3)}$$

where:

$w_{0.5DL}$  = weight of fractured girder plus the weight of one railing and 1/2 the concrete deck

$e_{DL}$  = centerline distance between the two girders for straight girders or calculated eccentricity using Equation 3-19 for curved girders

and



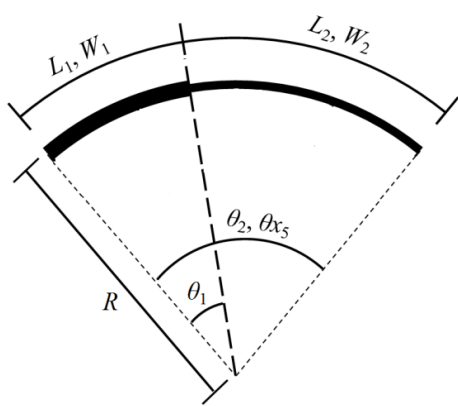
$$T_{TL} = w_{TL} \cdot e_{TL} \quad (\text{Equation 3-4})$$

where:

$w_{TL}$  = truck load

$e_{TL}$  = distance between intact girder's center and truck center, or calculated eccentricity (Equation 3-19)

The FSEL test bridge had a large radius of curvature, allowing the eccentricity for the torque calculation to be approximated as the distance between the two girders or the distance between the intact girder's center and the truck center. In-service twin box-girder bridges, however, may be designed with a significantly smaller radius of curvature than that of the test bridge. A decrease in the radius of curvature increases the torsion on the bridge, which must be resisted by the intact girder in the event of a fracture of a critical tension flange. Under such conditions, the eccentricity should not be taken as the distance between the centerlines of the girders; it should be computed as the distance from the center of gravity of the loads to the line of the intact girder interior supports. The center of gravity for non-prismatic girders can be determined by using equations developed by Stith (2010), modified for the case of box-girders. In the equations presented below, polar coordinates are used, and the origin of the coordinate system is located at the center of radius of the girder. Figure 3-5 provides a schematic of a curved girder with a definition for all the variables needed for the derivation.



- $L_1$ : Length of Section 1
- $L_2$ : Length of Section 2
- $W_1$ : Weight per Unit Length of Section 1
- $W_2$ : Weight per Unit Length of Section 2
- $\theta_0 = 0$
- $\theta_1$ : Internal Angle from the Beginning of the Girder to the End of Section 1
- $\theta_2$ : Internal Angle from the Beginning of the Girder to the End of Section 2
- $R$ : Radius of Curvature of the Girder

Figure 3-1: Variable definition for center of gravity (C.G.)

where  $\theta_1$  and  $\theta_2$  are given in (Equation 3-5 and 3-6:

$$\theta_1 = \frac{L_1}{R} \quad (\text{Equation 3-5})$$

$$\theta_2 = \frac{L_2}{R} + \theta_1 \quad (\text{Equation 3-6})$$

The weight of the girder in Figure 3-5 can be defined as follows:

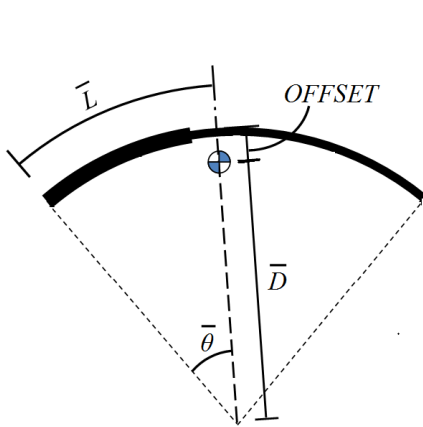
$$\text{Total Girder Weight} = \int_{\theta_0}^{\theta_1} W_1 R d\theta + \int_{\theta_1}^{\theta_2} W_2 R d\theta \quad (\text{Equation 3-7})$$

$$= W_1 R(\theta_1 - \theta_0) + W_2 R(\theta_2 - \theta_1) \quad (\text{Equation 3-8})$$

The generalized form of the total girder weight equation is provided in Equations 3-9 and 3-10, where  $n$  is the number of the different cross sections along the length of the bridge under consideration:

$$\text{Total Girder Weight} = \sum_i^n \int_{\theta_{i-1}}^{\theta_i} W_i R d\theta \quad (\text{Equation 3-9})$$

$$= R \sum_i^n W_i (\theta_i - \theta_{i-1}) \quad (\text{Equation 3-10})$$



: Center of Gravity

$\bar{\theta}$ : Angular Distance to C.G.

$\bar{L}$ : Length along Girder to C.G.

$\bar{D}$ : Radial Distance to C.G.

$t_T$ : Top Flange Thickness

*OFFSET*: Radial Distance of

C.G. from the Girder Centerline

Figure 3-2: C.G. Location

The angular distance from the beginning of the girder to the center of gravity is determined by taking a weighted average of each segment's centroid, which is located at the angular center of each cross-section. For the girder shown in Figure 3-6, the angular distance is given by Equations 3-11 through 3-13:

$$\bar{\theta} = \frac{\frac{\theta_1 + \theta_0}{2} \int_{\theta_0}^{\theta_1} W_1 R d\theta + \frac{\theta_2 + \theta_1}{2} \int_{\theta_1}^{\theta_2} W_2 R d\theta}{\int_{\theta_0}^{\theta_1} W_1 R d\theta + \int_{\theta_1}^{\theta_2} W_2 R d\theta} \quad (\text{Equation 3-11})$$

$$\bar{\theta} = \frac{W_1 R \frac{(\theta_1 + \theta_0)(\theta_1 - \theta_0)}{2} + W_2 R \frac{(\theta_2 + \theta_1)(\theta_2 - \theta_1)}{2}}{W_1 R(\theta_1 - \theta_0) + W_2 R(\theta_2 - \theta_1)} \quad (\text{Equation 3-12})$$

$$\bar{\theta} = \frac{\frac{W_1 R(\theta_1^2 - \theta_0^2) + W_2 R(\theta_2^2 - \theta_1^2)}{2}}{W_1 R(\theta_1 - \theta_0) + W_2 R(\theta_2 - \theta_1)} \quad (\text{Equation 3-13})$$

The generalized form of the equation for determining the angular distance to the center of gravity is

$$\bar{\theta} = \frac{R \sum_i^n W_i (\theta_i^2 - \theta_{i-1}^2)}{R \sum_i^n W_i (\theta_i - \theta_{i-1})} \quad (\text{Equation 3-14})$$

The following equation determines the location along the length of the girders to center of gravity:

$$\bar{L} = \bar{\theta} R \quad (\text{Equation 3-15})$$

The radial distance to the center of gravity is determined by taking the weighted average of the girder projected onto the  $\bar{\theta}$  radial line. This distance is show schematically in Figure 3-6, and it can be computed using Equations 3-16 and 3-17:

$$\bar{D} = \frac{\int_{\theta_0}^{\theta_1} W_1 R \cos(\theta - \bar{\theta}) R d\theta + \int_{\theta_1}^{\theta_2} W_2 R \cos(\theta - \bar{\theta}) R d\theta}{\int_{\theta_0}^{\theta_1} W_1 R d\theta + \int_{\theta_1}^{\theta_2} W_2 R d\theta} \quad (\text{Equation 3-16})$$

$$\bar{D} = \frac{W_1 R^2 [\sin(\theta_1 - \bar{\theta}) - \sin(\theta_0 - \bar{\theta})] + W_2 R^2 [\sin(\theta_2 - \bar{\theta}) - \sin(\theta_1 - \bar{\theta})]}{W_1 R(\theta_1 - \theta_0) + W_2 R(\theta_2 - \theta_1)} \quad (\text{Equation 3-17})$$

The generalized equation to compute the radial distance to the center of gravity for a girder with multiple cross-sections is given by can be determined by the generalized form of Equation 3-18:

$$\bar{D} = \frac{R^2 \sum_i^n W_i [\sin(\theta_i - \bar{\theta}) - \sin(\theta_{i-1} - \bar{\theta})]}{R \sum_i^n W_i (\theta_i - \theta_{i-1})} \quad (\text{Equation 3-18})$$

Equation 3-18 should be used two times to compute  $\bar{D}$ —once for the fractured girder and once for the intact girder. Because the line of rotation of the bridge passes through the supports of the intact girder, each girder's offset from the center of gravity to the line of rotation is given by Equation 3-19:

$$e_i = \bar{D}_i - R_{INT} \cdot \cos(\phi/2) \quad (\text{Equation 3-19})$$

where:

$R_{INT}$  = Radius of curvature at the location of the interior intact girder's supports

$\phi = L_{INT} / R_{INT}$

$L_{INT}$  = Arc length at the location of the interior intact girder's supports

Equations 3-5 through 3-19 can be used to calculate the eccentricities of each girder. When multiplied by the dead load of each girder and the truck load, the torque applied on the end sections of the intact girder can be computed.

Assuming that half of the calculated torque is applied to each end of the intact girder, the shear flow of the closed section can be determined by Equation 3-20.

$$q = \frac{1}{2 \cdot A} \cdot \frac{(T_{DL} + T_{TL})}{2} \quad (\text{Equation 3-20})$$

where:

$T_{DL}$  = torque due to dead load, which is equal to the dead load multiplied by the eccentricity to the chord of the intact girder supports

$T_{TL}$  = torque due to truck load, which is equal to the dead load multiplied by the eccentricity to the chord of the intact girder supports

$A$  = area enclosed by the mid-thickness of the composite box-girder section

Note that the calculated torques are divided by two, because it is assumed that the end torques are equal.

The concrete deck forms the top flange of the closed box section and should be checked to ensure that it has adequate capacity to resist the shear force due to torsion. According to ACI 318-08, the shear capacity of reinforced concrete is given Equation 3-21. Equation 3-21 should always be greater than the shear due to torsion ( $V_{TORSION} = q \cdot b$ )

$$V_S = A_t \cdot f_{yt} \cdot b \cdot \cot(\theta) / s \quad (\text{Equation 3-21})$$

where:

$b$  = width of the concrete deck between the top flanges

$A_t$  = area of a reinforcement bar in the transverse direction

$s$  = spacing between the reinforcement bars

$\theta$  = angle of the crack with the horizontal (ACI 318-08 recommends  $45^\circ$ )

The shear stress developed in the webs due to torsion must be added to the shear stress due to bending of the girders using the following procedure:

- i. Calculate the shear stress in the webs due to torsion using Equation 3-22.

$$\tau_{TORSION\ WEB} = q/t_{WEB} \quad (\text{Equation 3-22})$$

where  $t_{WEB}$  = thickness of the web

- ii. Calculate the shear stress due to bending at webs through Equation 3-23.

$$\tau_{FLEXURAL\ WEB} = V / (2 \cdot d_{WEB} \cdot t_{WEB} \cdot \cos(\beta)) \quad (\text{Equation 3-23})$$

where:

$d_{WEB}$  = height of the web

$\beta$  = angle of web inclination

$V$  = one-half of the total factored load on the span

- iii. Ensure that the summation of the shear due to torsion and bending is less than or equal to the shear buckling stress as given below:

$$\tau_n = C \cdot 0.58 \cdot f_{yw} \geq \tau_{TORSION\ WEB} + \tau_{FLEXURAL\ WEB} \quad (\text{Equation 3-24})$$

where:

$C$  = ratio of shear-buckling resistance to the shear yield strength (AASHTO Sec. 6.10.9.3.2)

The larger tension field shear capacity can be used to check the shear at interior supports.

- iv. The bottom flange at the pier should be checked for combined shear and compression (AASHTO Sec. 6.11.8.2.2)
- v. The end diaphragm and its connection to both girders needs to be checked to ensure that it has adequate resistance to the torque applied to the intact girder. This applied torque is resisted by a couple generated by the bearings of the two girders (i.e., bearing reactions). The reaction at the bearing of the fractured girder is equal to the torque applied to the intact girder divided by the distance between the bearings of the two girders. In the case of a continuous girder, the interior support is not as critical as the end support because some of the applied torque is resisted by the continuous girder. Thus, it is always critical to check the end diaphragm of the end support.

Following the steps outlined above, the redundancy level of a twin steel box-girder bridge can be evaluated. If the bridge under investigation satisfies the following conditions, the bridge has sufficient strength to sustain load without collapsing:

- i. Intact Girder has adequate shear and moment capacity
- ii. Deck has adequate shear capacity
- iii. Shear studs have adequate tension capacity



If the bridge satisfies only the first two conditions, it is still possible that it can sustain load without collapsing. Under these conditions, a yield line analysis—described in Chapter 5—can be used to evaluate the ability of the deck to transmit load to the intact girder without the shear studs connecting the deck to the fractured girder. In the event that the capacity predicted from the yield line analysis is not adequate, a more refined analysis can be performed.

### 3.3 DEVELOPMENT OF THE SIMPLIFIED STRIP MODEL

Preliminary studies before Test 1 assumed the concrete deck would deflect in double curvature across its width (Figure 3-7) due to the downward deflection of the fractured girder. The model estimates the capacity of the bridge deck bending moment and the shear stud tension capacity to transfer the load that was carried by the fractured girder to the intact girder [Sutton, (2007)]. In these analyses, the critical elements of the load path were the flexural and shear capacity of the concrete deck as well as the shear stud tensile capacity.

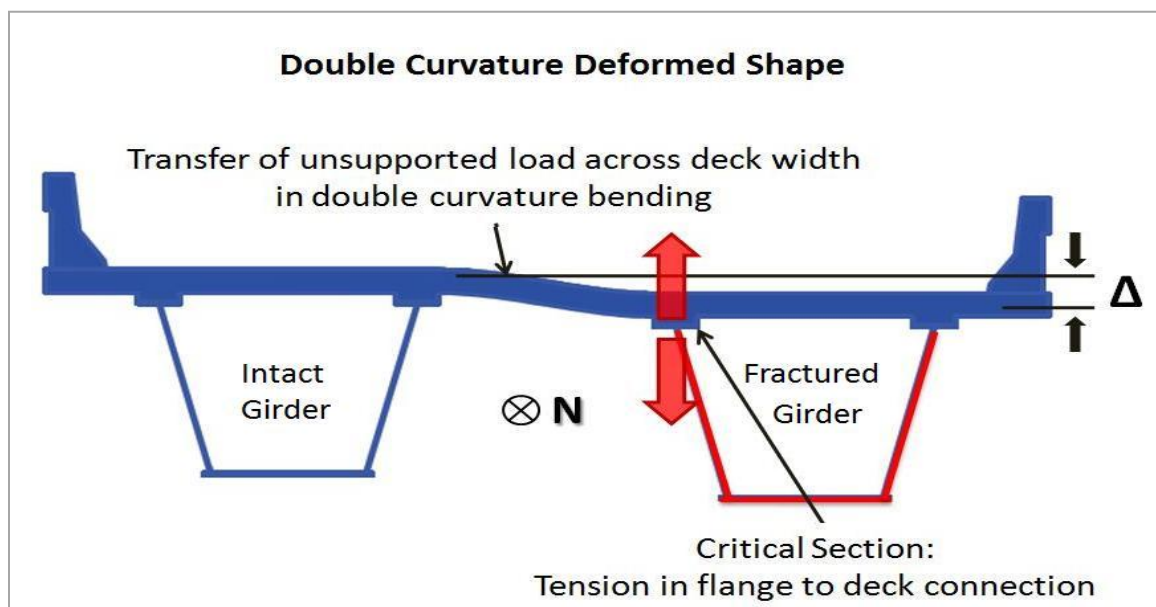


Figure 3-7: Deformed shape of the cross section in double curvature

After Test 2, it was recognized that the deflected shape of the bridge deck depended upon the magnitude of the tensile force of the shear studs located at the interior top flange of the fractured girder. Once the tensile capacity of the shear studs was reached, a brittle tensile failure occurred, causing a separation of the interior top flange and the deck. After the pull out of the shear studs, the deck would deflect in a single curvature as discussed in Chapter 2 and shown in Figure 3-8.

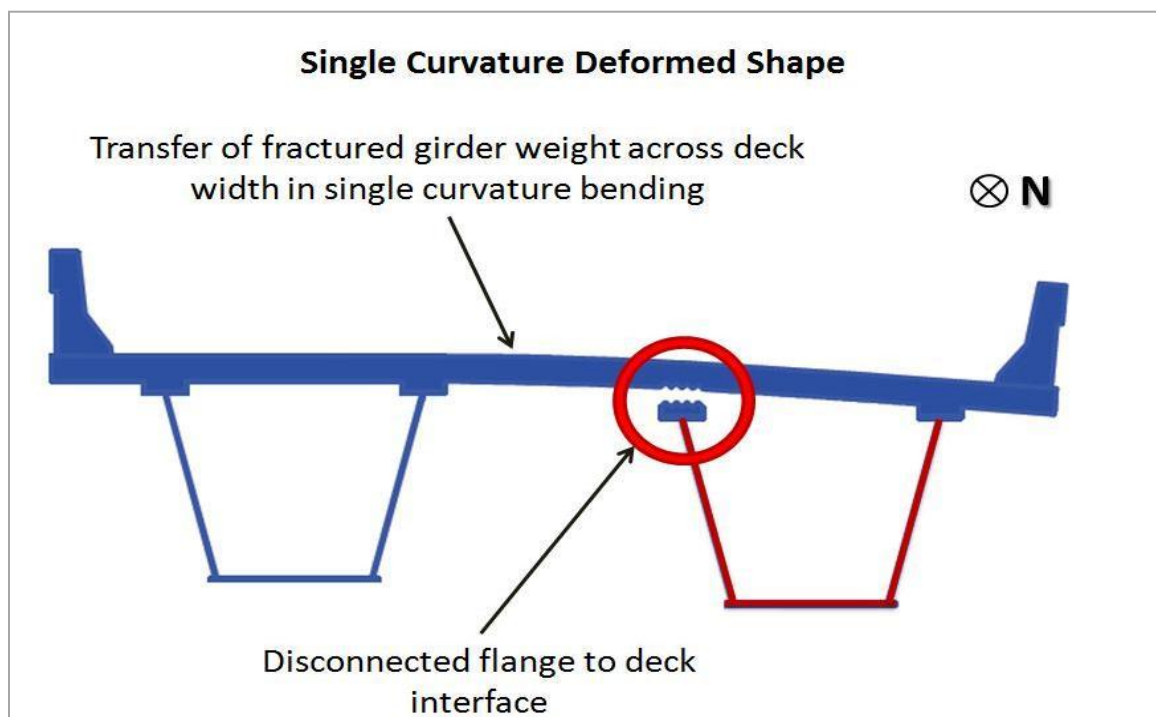


Figure 3-8: Deformed shape of the cross section in double curvature

As discussed above, a simple strip model of the deck was used to estimate the forces in the shear studs. The deck was sub-divided into strips with a width equal to the shear stud spacing. The strips were analyzed as a three-span beam (Figure 3-2) with supports corresponding to the top flanges of the girders. Due to the symmetrical layout of the

girders, the lengths of the end spans in the model was equal to the top width of the trapezoidal box sections, and the middle span was equal to the distance between the two interior top flanges. After defining the section properties, the strips forming the continuous beam were subjected to support settlements that were equal to the displacements measured after Test 2. From the imposed deformations, the internal forces and the moments of the beam could be calculated.

From the imposed deformations, the internal forces and the moments of the beam could be calculated. The rows of shear studs in the bridge were spaced longitudinally in approximately equal increments of 22 in. Thus, the bridge deck was divided in 22-in. wide strips as shown in Figure 3-1, with each strip containing one row of shear studs. The section properties of the strip in the transverse direction were calculated based on the uncracked section. Moreover, it was assumed that the concrete deck stiffness remained constant until the plastic moment capacity was reached, and the additional stiffness of the haunch was ignored. The analysis of the concrete deck strips assumed that the deck behaved as an elastic-perfectly-plastic material. Accordingly, the deck was treated as a linear-elastic material below the plastic moment capacity ( $M_p$ ), and beyond  $M_p$  it was assumed that the concrete deck could sustain the plastic moment  $M_p$ . Figure 3-9 shows the typical sections from which the moment capacities were calculated. As reported by Barnard [Barnard, (2006)], the average as-built height of the haunches above the flanges was 3 in. at all the haunch locations except for the interior haunch of the intact girder, which was 3.8 in. The moment capacity of the haunch area was calculated assuming a 3.8-in. tall haunch because the negative moment was developed at the interior haunch of the intact girder as the fractured girder deflected downward in Test 2. It should be emphasized that the negative moment capacity in the haunch area was bigger than in the rest of the concrete deck due to the deeper section. Figure 3-10 illustrates both the negative and the positive moment capacity in different regions. The concrete and reinforcement strength used in all the calculations were 6.26 ksi and 60 ksi, respectively, based on lab tests. Appendix A contains detailed calculations of the moment capacity calculations.

The tensile capacity of shear stud groups was investigated in laboratory tests performed by J.P. Sutton [Sutton, (2007)] and J.M. Mouras [Mouras, (2008)]. The shear stud group configuration used in the test bridge included three 5-in. tall shear studs installed transversely to the span direction. The tensile capacity of this configuration was found to be 17.3 kips. Accordingly, when the reaction of the strip at the girder flange was equal to this value, the reaction was released for subsequent load steps.

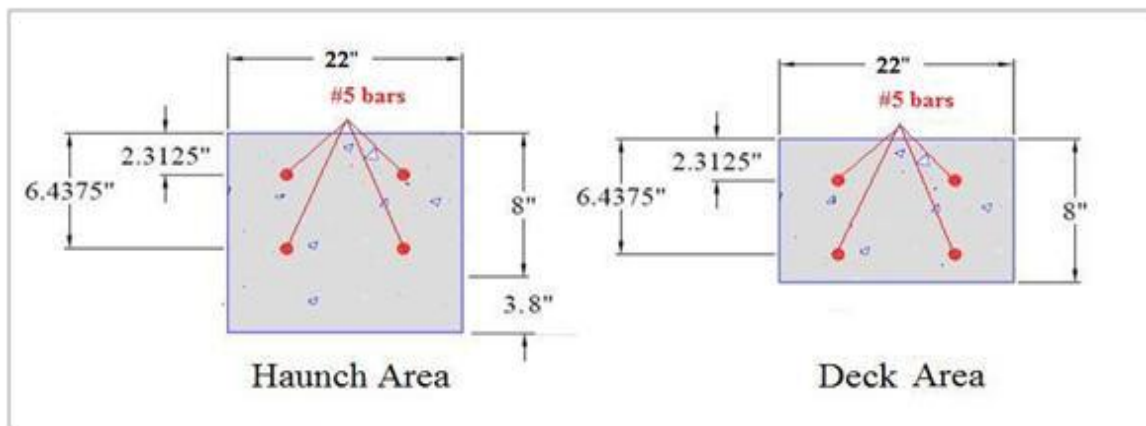


Figure 3-9: Sections based on which moment capacity was calculated

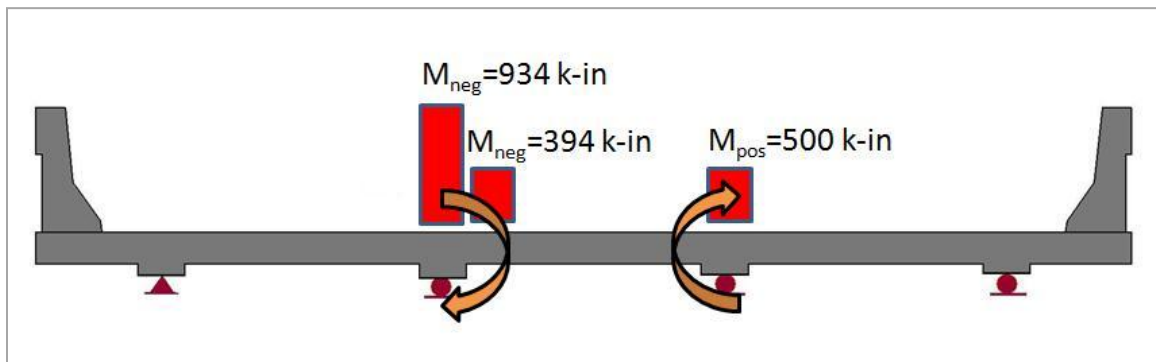


Figure 3-10: Positive and negative moment capacity in different regions

### 3.4 ANALYSIS OF THE BRIDGE STRIPS

After defining all the section and material properties, the internal forces and moments of the three-span continuous beam formed by the 22-in wide strips of the concrete deck could be calculated by using the measured deflections and classical structural analysis methods. For this research, the slope-deflection method was used. The following fundamental equations were derived using the moment-area theorems [Norris, Charles H., Wilbur, John B., (1960)].

$$M_{AB} = \frac{2EI}{L} \cdot (2\theta_A + \theta_B - 3\psi_{AB}) + \frac{2}{L} [(M_0)_A - 2 \cdot (M_0)_B] \quad (\text{Equation 3-25})$$

$$M_{BA} = \frac{2EI}{L} \cdot (2\theta_B + \theta_A - 3\psi_{AB}) + \frac{2}{L} [2 \cdot (M_0)_A - (M_0)_B] \quad (\text{Equation 3-26})$$

where  $M_{AB}$  and  $M_{BA}$  are the moments that are developed at the  $A$  and  $B$  ends, respectively, of a flexural member. By definition,  $\theta_A$  and  $\theta_B$  are the rotations of the tangent to the elastic curve at the respective ends of the element measured from the original position of the element, and the values are taken as positive when the tangent has rotated in the clockwise direction relative to the initial direction. The rotation of the chord (Figure 3-11) connecting the two ends of the elastic curve of the member ( $\psi_{AB}$ ) is taken as positive when this chord has rotated clockwise relative to the original direction. If the member has fixed ends, then  $\theta_A$ ,  $\theta_B$  and  $\psi_{AB}$  are equal to zero, and the last two terms of Equations 3-25 and 3-26 are equal to the so called fixed end moments. The fixed end moments could be easily calculated for any given load.

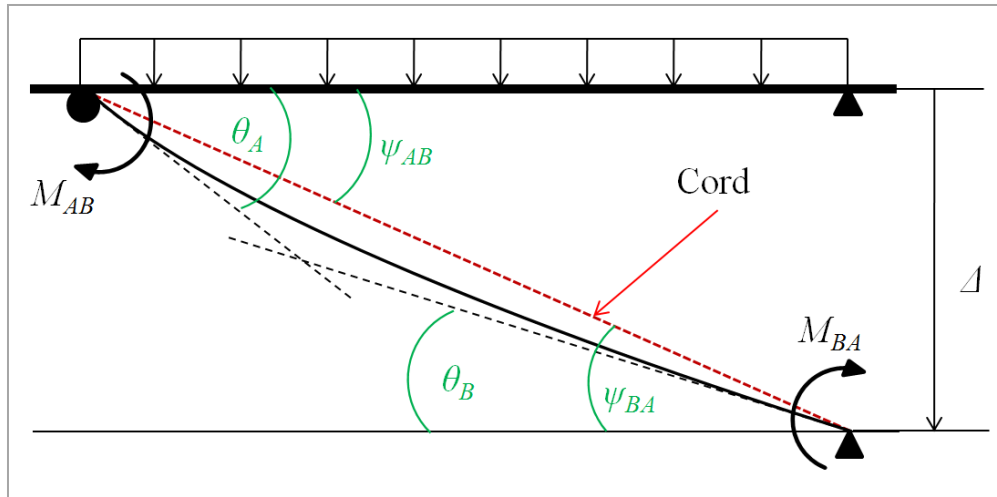


Figure 3-11: A typical example of the slope-deflection method

The measured deflections of the intact and the fractured girder after Test 2 were divided into 50 displacement increments, which were then applied to the beam model. This procedure was adopted to investigate the behavior of each strip and to compute the tension forces in the shear studs as the girders deflected (Figure 3-12). To determine the deflections of the strips which were located between the survey points, additional data points were interpolated from the survey locations.

At each increment, after calculating all the reactions and moments using the slope deflection equations, the moments and reactions were checked at the critical locations to determine if they exceeded the allowable capacities. Figure 3-13 illustrates all the possible critical failure locations. If a failure occurred, the structural model was revised to match the new boundary conditions. For instance, if a shear stud has pulled out in region 1, then at the next step the support of this location was removed. If the applied moment exceeded the moment capacity of a section, a hinge was inserted at the location. The analysis was performed on a spreadsheet constructed by the author.

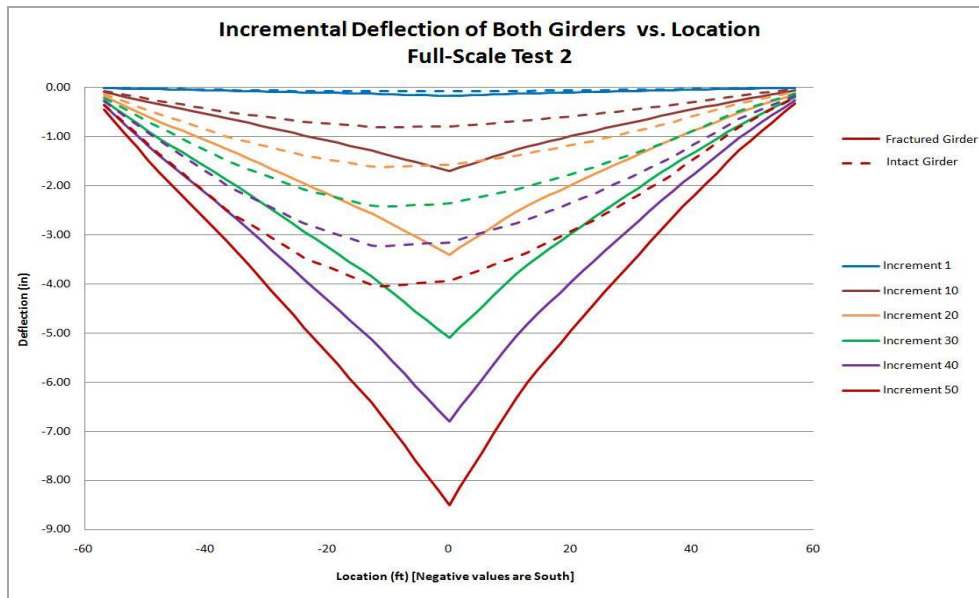


Figure 3-12 Incremental deflection curves of both girders Test 2

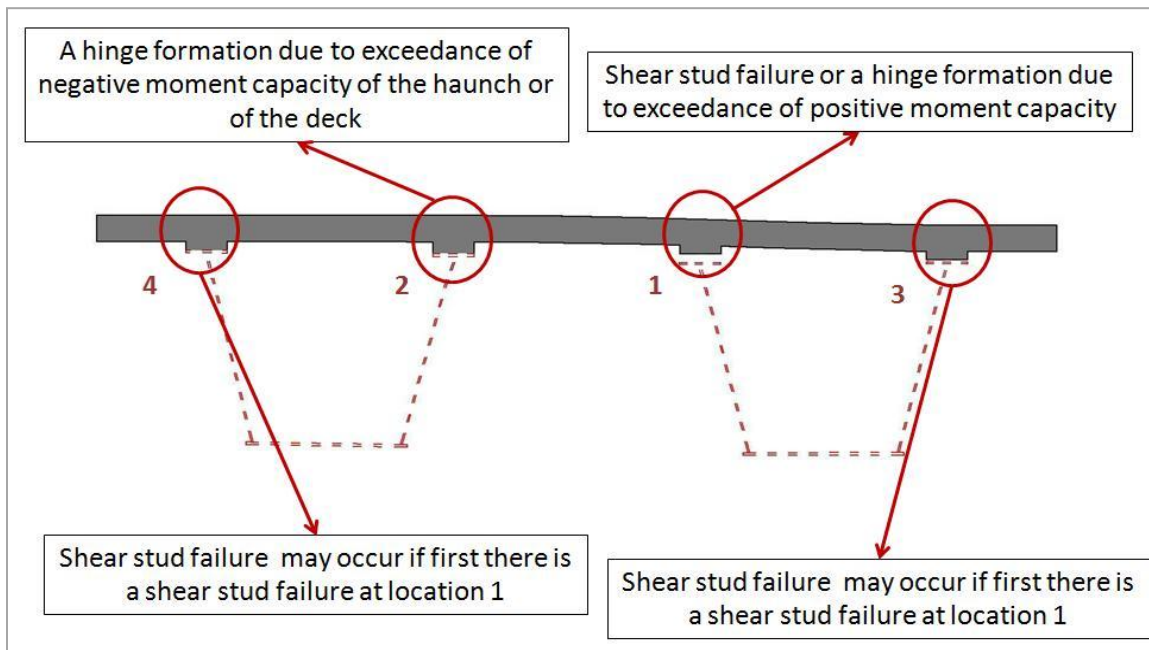


Figure 3-13: Critical failure locations

In the next section, the results of several analyses are presented and compared with observations from the actual test. Additional detailed calculations of the Simplified Strip Model iterations are presented in Appendix B.

### **3.5 RESULTS OF THE SIMPLIFIED STRIP MODEL ANALYSIS**

Test 2 was the starting point for development of the Simplified Strip Model. This test was used to evaluate and to calibrate the model. The results of the analysis were in good agreement with the observations from the test.

The analysis showed that all the connections of the interior top flange of the fractured girder to the deck had failed over a length of 62.33 ft. A close inspection of the interior top flange of the fractured girder found that the shear studs had pulled out over a length of 60 ft (Figure 2-7), which was within 2 feet of the length predicted using the Simplified Strip Model. Figure 3-14 shows the forces of the shear studs of the interior top flange of the fractured girder along the span. The shear studs were in compression close to both ends. This behavior was not expected and appears to be due to an initial differential deflection between the top flanges of the fractured girder near the ends.



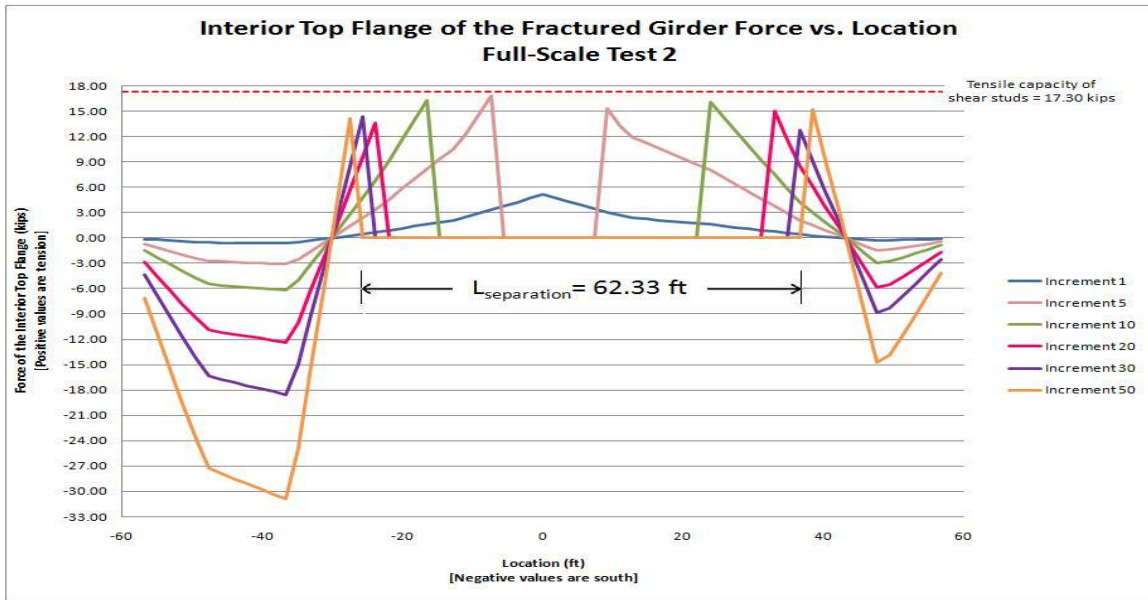


Figure 3-14: Interior top flange of the fracture girder force Test 2

Figure 3-15 illustrates an interesting behavior observed during the analysis. It was found that the shear stud group located above the interior top flange of the fractured girder pulls out just before the positive moment capacity at the same location was reached. Once a shear stud that was located at the interior top flange of the fractured girder pulls out, the force of the exterior top flange of the same girder changes from compressive to tensile. Figure 3-16 shows clearly the reversal of the force from compression to tension over the region that a shear stud failure has occurred. Although both exterior top flanges were in tension, their forces never reach the tensile capacity of the shear stud group connection (Figure 3-16, 3-17). A plastic hinge formed in the concrete deck above the interior top flange of the intact girder and expanded as the shear studs on the interior top flange of the fractured girder pulled out of the deck. Figure 3-18 shows how the moment diagram at the mid-span changes during the analysis. The first shear stud pulls out in increment 5. The increase in moment at increments 10 and 15 were due to pull out of the studs from adjacent strips. The moment in increment 19 was zero throughout the width of the bridge due to the hinge that has formed at the interior top

flange of the intact girder. At the end of the analysis, the total length of the plastic hinge in the deck was computed to be 14.67 ft. After Test 2, major cracking of the concrete deck was observed at the same location as captured in the Simplified Strip Model, indicating that a hinge line was formed.

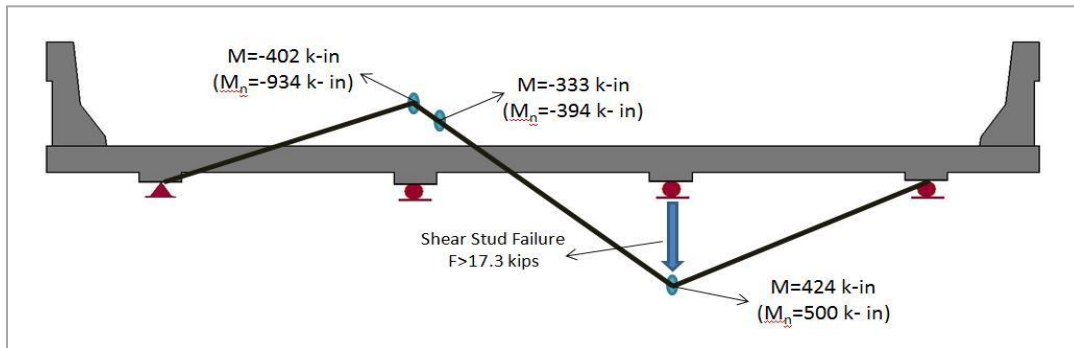


Figure 3-15: Typical moment diagram just before a shear stud pulls out

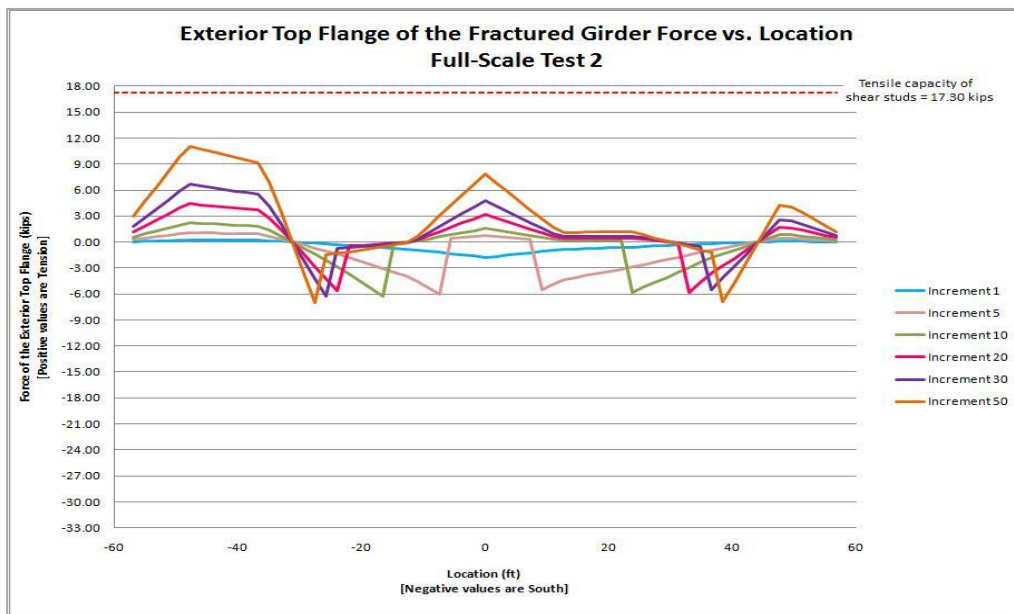


Figure 3-16: Exterior top flange of the fractured girder force Test 2

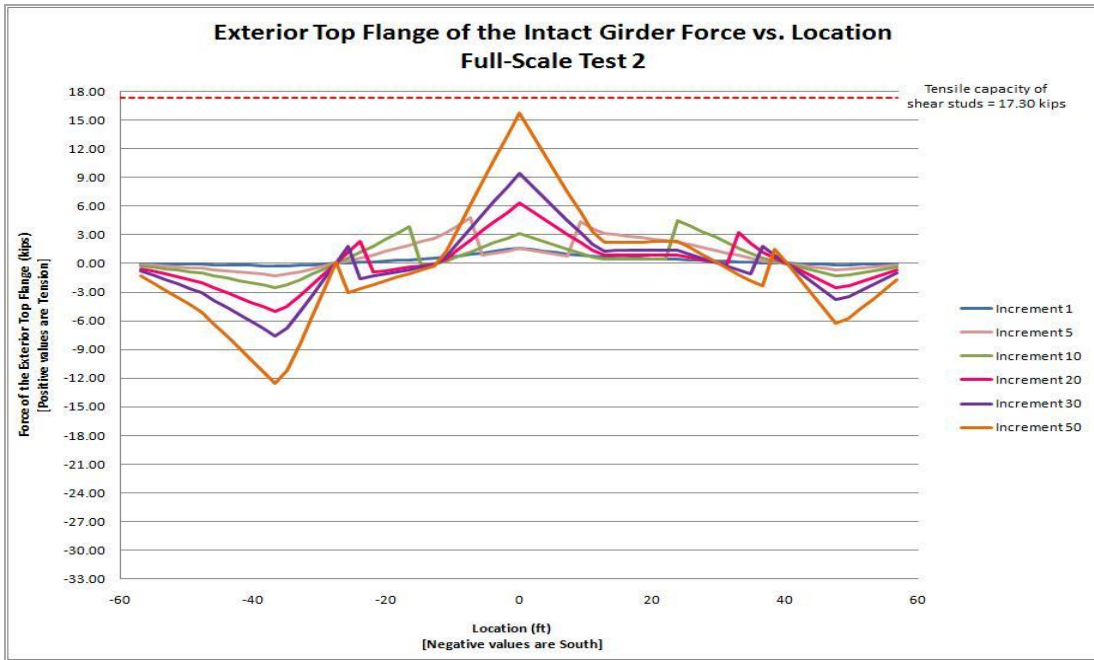


Figure 3-17: Exterior top flange of the intact girder force Test 2

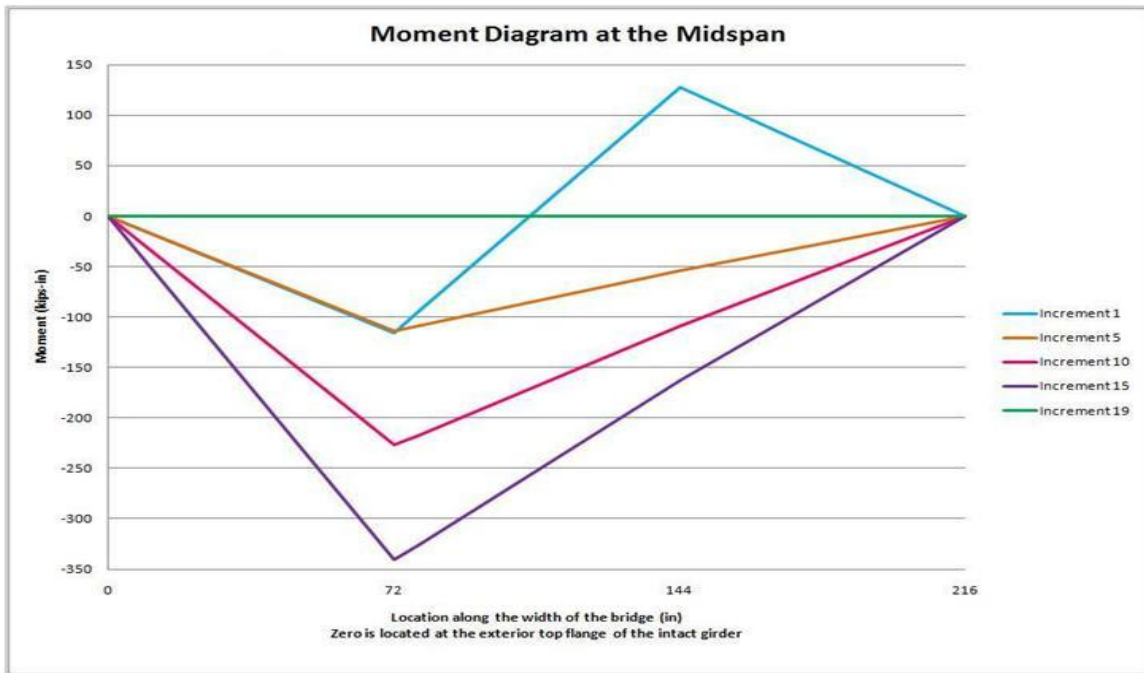


Figure 3-18: Moment diagram at the mid-span

### 3.6 DEFLECTION IMPLEMENTATION FOR GIVEN LOADS

After validating the model with the results of the test, the extension of the model to a bridge where the displacement was not known *a priori* was developed. Assuming that a fracture has occurred in one of the bottom flanges of the girders, an engineer needs to be able to calculate the deflections of the girders for a given load acting on the bridge being analyzed. Accordingly, a procedure was developed using an estimate of the girders' deflections.

In the first step, the bridge was divided along the mid-width of the concrete deck into two parts, which represent the intact girder and the fractured girder composite sections. Each part was analyzed individually to calculate the deflections of each girder, which would be inserted into the Simplified Strip Model. The intact girder was analyzed based on the boundary conditions of each bridge. For this project, the FSEL bridge was a single span and simply supported. According to this layout, both the intact and the fractured girders were analyzed as simply supported beams. The moment of inertia used for the intact girder was assumed to be the whole composite section calculated about the centroid of the elastic transformed composite steel section (Figure 3-19). At the locations of the expansion joints in the rail, a reduced moment of inertia was calculated neglecting the rail (Figure 3-20). The reduced moment of inertia was used over a length of one foot to each side of the rail expansion joint. The length of one foot was equal to the distance between the mid-points of the first and second stirrups connecting the railing to the concrete deck on each side of the expansion joint (Figure 3-21).

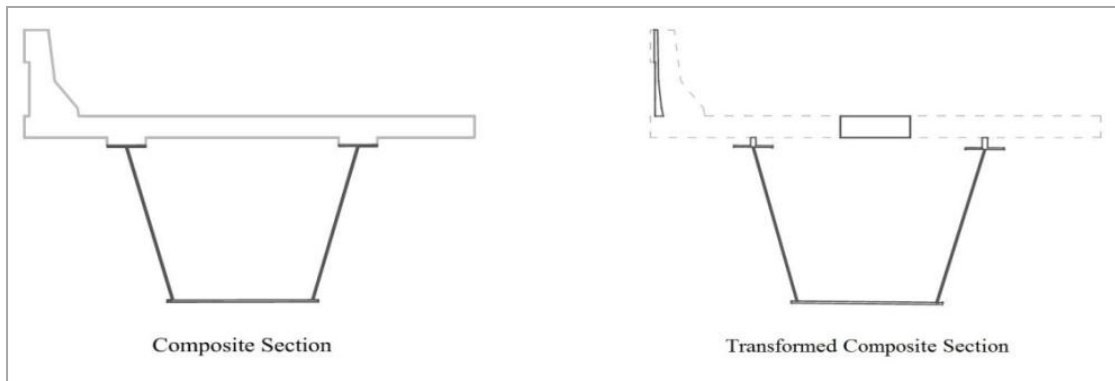


Figure 3-19: Full composite and transformed composite section of the intact girder

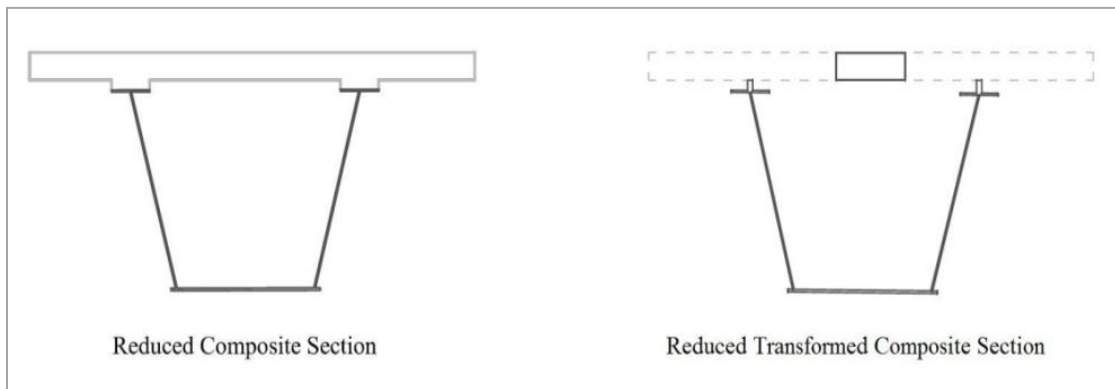


Figure 3-20: Reduced composite and transformed composite section of the intact girder

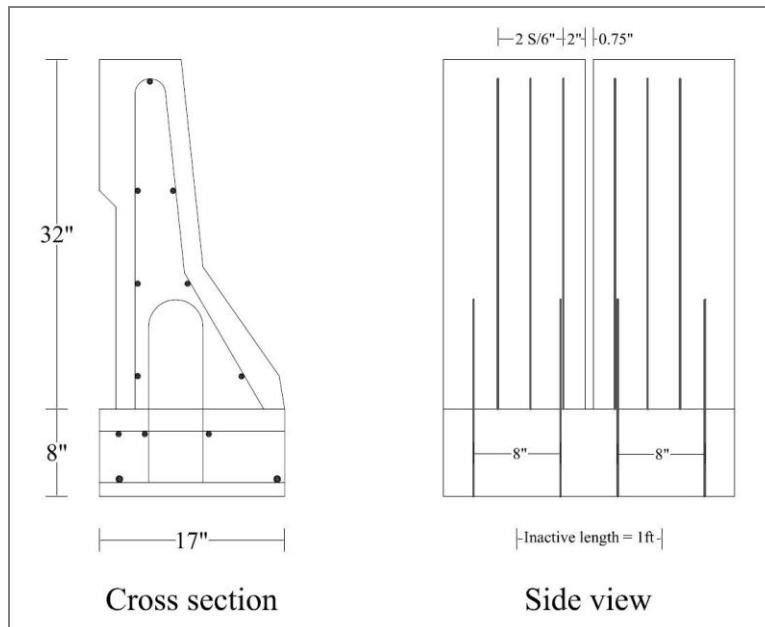


Figure 3-21: Inactive length of the railing

Parametric studies for the influence of including the railing were carried out and are presented in Figures 3-22 through 3-24. It could easily be observed that the railing plays a significant role in the behavior of the bridge.

The next step should be the identification of the loading combinations for which the intact girder would be analyzed. As mentioned before, to obtain a conservative solution, it was assumed that the total load would be carried by the intact girder, even if a portion of it was carried by the railing above the fractured girder. Based on this assumption, the intact girder should be loaded with a distributed load equal to the whole dead load of the bridge (two girders, concrete deck and railing) and the truck live load as concentrated point loads at the same longitudinal distances as it would be positioned above the fractured girder. The torsional effects due to the eccentricity of the truck relative to the intact girder were neglected in the analysis to estimate deflections. A torsional check should be included in the preliminary analysis of every bridge. Detailed calculations are

given in Appendices B, C and D. The deflections produced from this analysis were compared with the actual measurements during different stages in Figures 3-22 to 3-24. In those graphs, it can be observed that the best correlation between the estimated and the actual deflections was when the bridge was analyzed with the railing (with or without expansion joints). Several analyses indicated that it was more conservative to model the bridge with expansion joints than without because the estimated failure region was more extensive when expansion joints were present. As will be discussed below, the fractured girder deflections were in better agreement with the actual deflections when the expansion joints were included in the analysis. For these reasons, it was concluded that an engineer should include the expansion joints in the analysis to estimate the deflections of the girders.

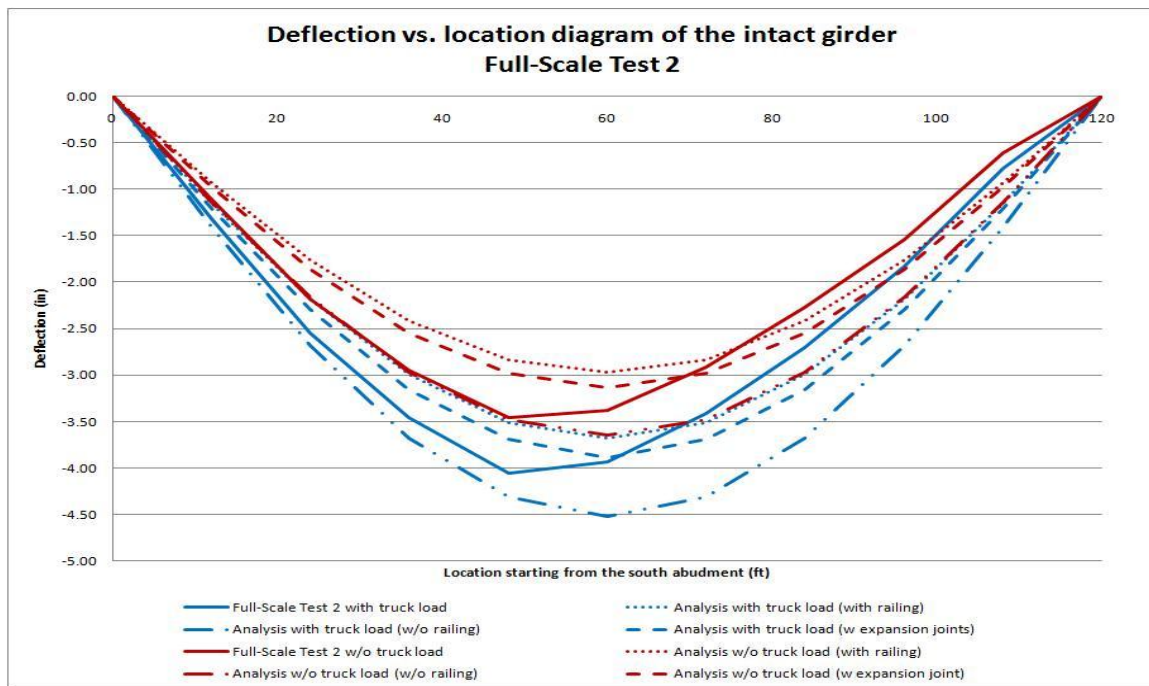


Figure 3-22: Deflection vs. location diagram of the intact girder Test 2

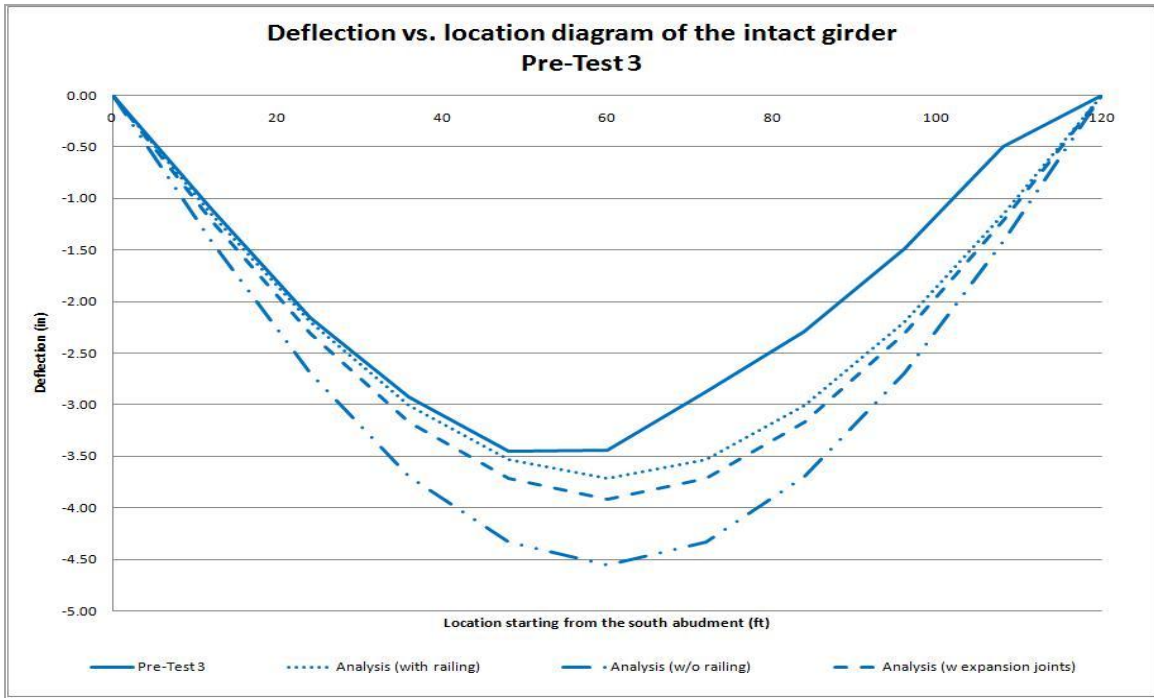


Figure 3-23: Deflection vs. location diagram of the intact girder Pre-Test 3

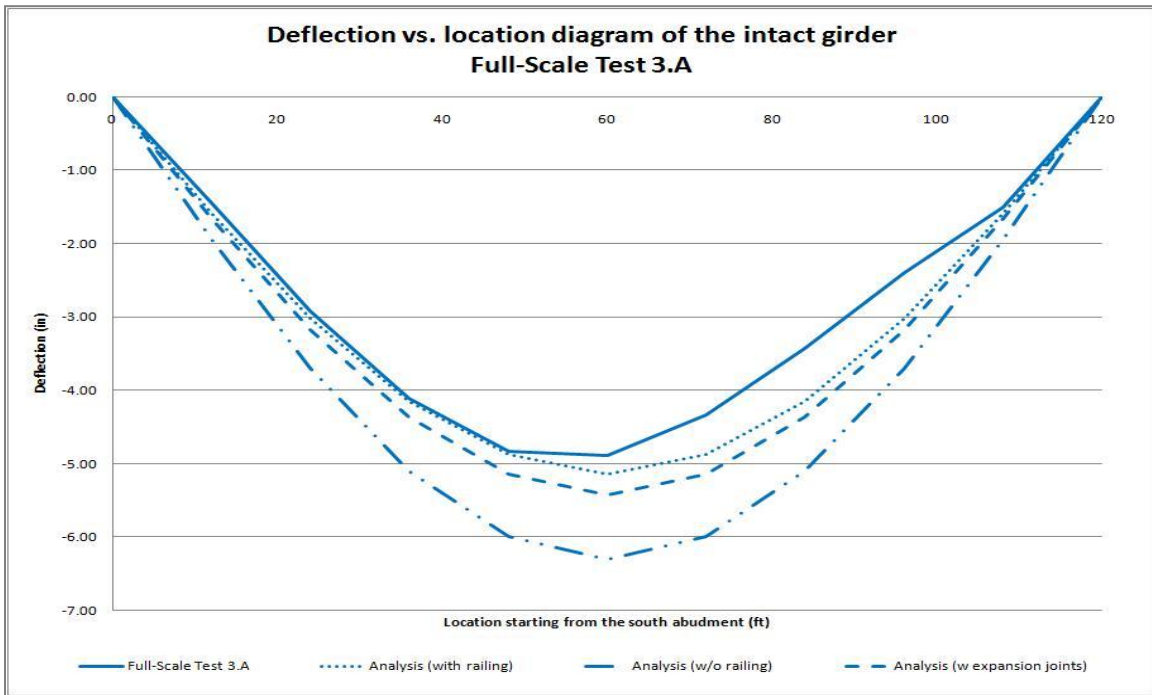


Figure 3-24: Deflection vs. location diagram of the intact girder Test 3.A



The procedure to obtain the deflection profile of the fractured girder was essentially the same as that for the intact girder. The only difference was the insertion of a section without a bottom flange and webs at the fracture location. Figure 3-25 shows the fractured section, which only includes the railing, the concrete deck and the haunch. The moment of inertia of the fractured section was calculated about the centroid of the section. The expansion joint in the rail was ignored. The railing was included in the calculation of the moment of inertia because the gap in the railing closes as the bridge deflects. The initial deflection to close the gap in the rail should be included in the total deflection of the fractured girder. The deflection could be calculated using Equation 3-27. Because the shear stud groups were spaced equally every 22 in., it was decided to assign the fractured section properties over a length of 22 in. in which the midpoint of the fractured section coincides with the centerline.

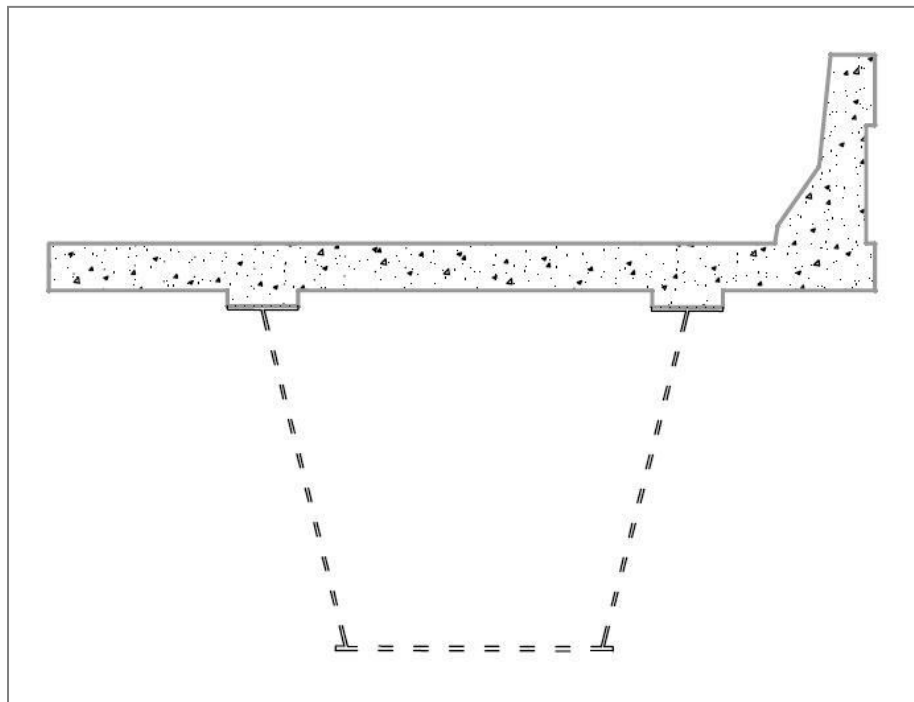


Figure 3-25: Fractured section

The fractured girder should be loaded with a distributed load equal to half the dead load of the bridge (one girder, half of the concrete deck and one railing) and the entire truck live load. The middle axle of the truck should be positioned at the point of the maximum moment obtained from the dead load, which is the location that the fracture was assumed to occur. For the FSEL bridge, this point corresponds to the centerline. The HS-20 truck load with all the axles spaced 14 ft. apart was used in the analysis to produce the largest moment. The calculated deflection at the fracture location was used to define the deflected shape of the fractured girder. The downward deflection at the fracture location for the FSEL bridge was calculated as 3.21 in. It is worthwhile to be mentioned that the loads used in the analysis of the bridge girders were assumed

Even if the truck and some portions of the concrete deck were included in the deflection calculations of both girders; their contribution to the total deflection was based on the following assumptions. It was assumed that the fracture girder was not able to sustain any load, and the entire load was transferred to the intact girder. In other words, the fractured girder was analyzed with half the dead load and the entire truck load in order to estimate its deflections which would be used in the Simplified Strip Model. The intact girder's deflections were calculated with the entire load in order to be consistent with the assumption that the entire load was carried by the intact girder.

Initially, the railing at the centerline was assumed not to be in contact due to the gap in the expansion joint. After the fracture of the girder, it was assumed that the bridge would deflect downward until the gap in the railing closed and the railing becomes effective. Figure 3-26 illustrates that the width of the expansion joint decreases by an amount  $z_1+z_2$ , when the bridge deflects downward by  $\Delta$ , where  $z_1$  and  $z_2$  are the horizontal displacements of each segment of the railing. Due to the downward deflection, each segment of the railing rotates by an angle  $\theta_1$  and  $\theta_2$ , respectively. For small angles  $\theta_1$  and  $\theta_2$ , the horizontal displacements  $z_1$ ,  $z_2$  could be determined as  $z_1/h=\tan(\theta_1)$  and  $z_2/h=\tan(\theta_2)$ , where  $h$  was the distance from the top of the railing to the bottom of the haunch, which was assumed to be the center of rotation. Moreover,  $\Delta/L_1=\tan(\theta_1)$  and  $\Delta/L_2=\tan(\theta_2)$ , where  $L_1$  and  $L_2$  were the lengths of the two girder segments that span

from the nearest supports to the fracture location. Knowing that the total width of the expansion joint  $z$  was equal to  $z = z_1 + z_2$ , Equation 3-27, which gives the initial deflection, could be derived.

$$\Delta_{initial} = z \cdot (L_1 \cdot L_2) / (h \cdot (L_1 + L_2)) \quad (\text{Equation 3-27})$$

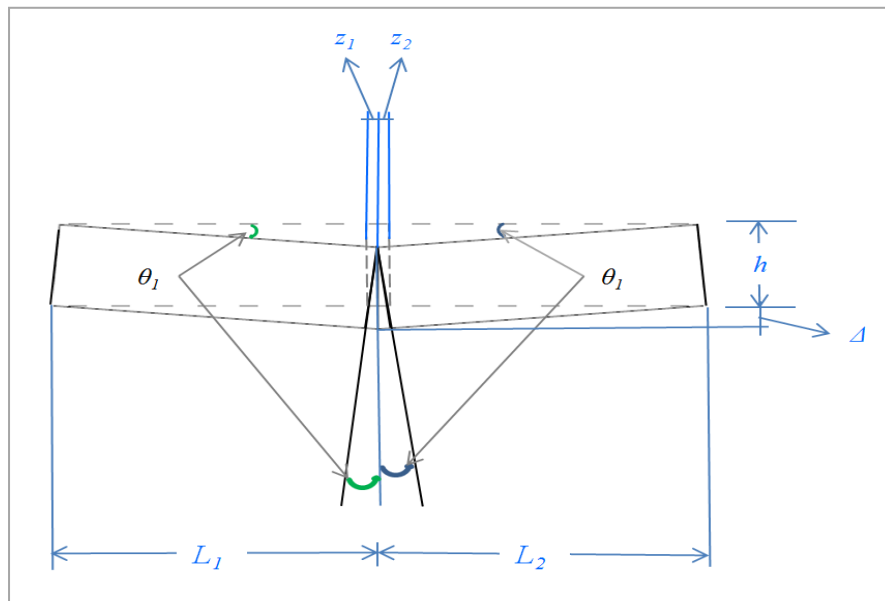


Figure 3-26: Basic geometry of the Equation 3-3

In the case of the FSEL test bridge, the fracture was at the centerline, so  $L_1 = L_2 = 60$  ft (or 720 in.). The width of the expansion joints were 0.75 in. During Test 2, the webs of the bridge had been cut up to 8 in. from the top flange. Using an  $h$  equal to 43 in. ( $h_{RAILING} + h_{HAUNCH} + h_{UNCUTTED\ WEB} = 32 + 3 + 8 = 43$  in.) because the center of rotation was 8 in. below the haunch, the initial deflection was calculated as 5.60 in. As a result, the total deflection at the centerline of the FSEL test bridge (8.81 in.) was the summation of the initial deflection (5.6 in.) and the elastic deflection (3.21 in.), which was estimated from the analysis.

Based on the deflected shapes from the actual measurements, a formula to estimate the deflections of the fractured girder was investigated. It was found that the best curve to replicate the deflections of the fractured girder measured at different stages of the tests was a sine curve. According to this fact, it was assumed that the sine curves given in Equations 3-28 and 3-29 would be used to estimate the deflections of the fractured girder. Equation 3-28 represents the sine curve that was used to estimate the deflected shape of the segment of the fractured girder between the simple support and the fracture location. The range of the angle  $\varphi$  is limited between  $0^\circ$  and  $50^\circ$  because this range provides the best deflection estimate.

$$Y(\varphi) = W \cdot \sin(\varphi) - W \cdot \sin(50^\circ), 0^\circ \leq \varphi \leq 50^\circ \quad (\text{Equation 3-28})$$

where  $W = (\Delta_{initial} + \Delta_{analysis}) / \sin(50^\circ) = \Delta_{total \text{ at the fracture location}} / \sin(50^\circ)$ . It should be mentioned that  $Y(0^\circ)$  is the deflection at the fracture location and  $Y(50^\circ) = 0$  is the deflection at the simple support. Figures 3-27 to 3-29 illustrate that the deflections produced by Equation 3-28 are in good agreement with the deflections of the fractured girder that were measured during different stages of Tests 2 and 3.

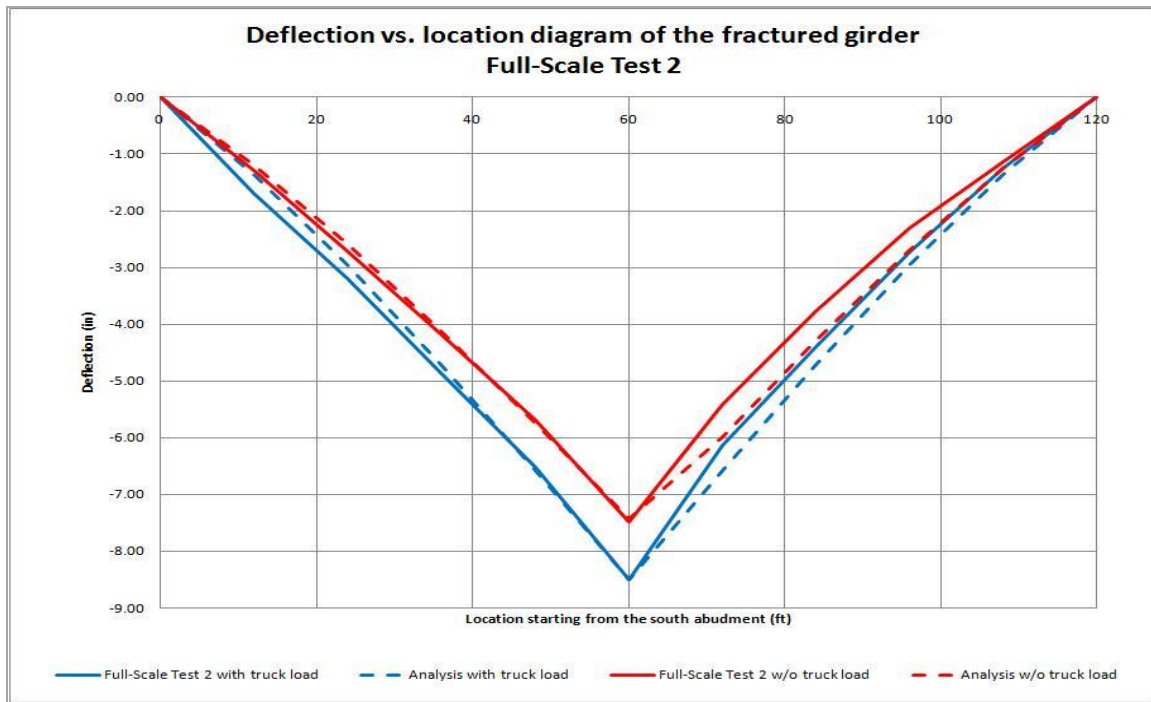


Figure 3-27: Deflection vs. location diagram of the fractured girder Test 2

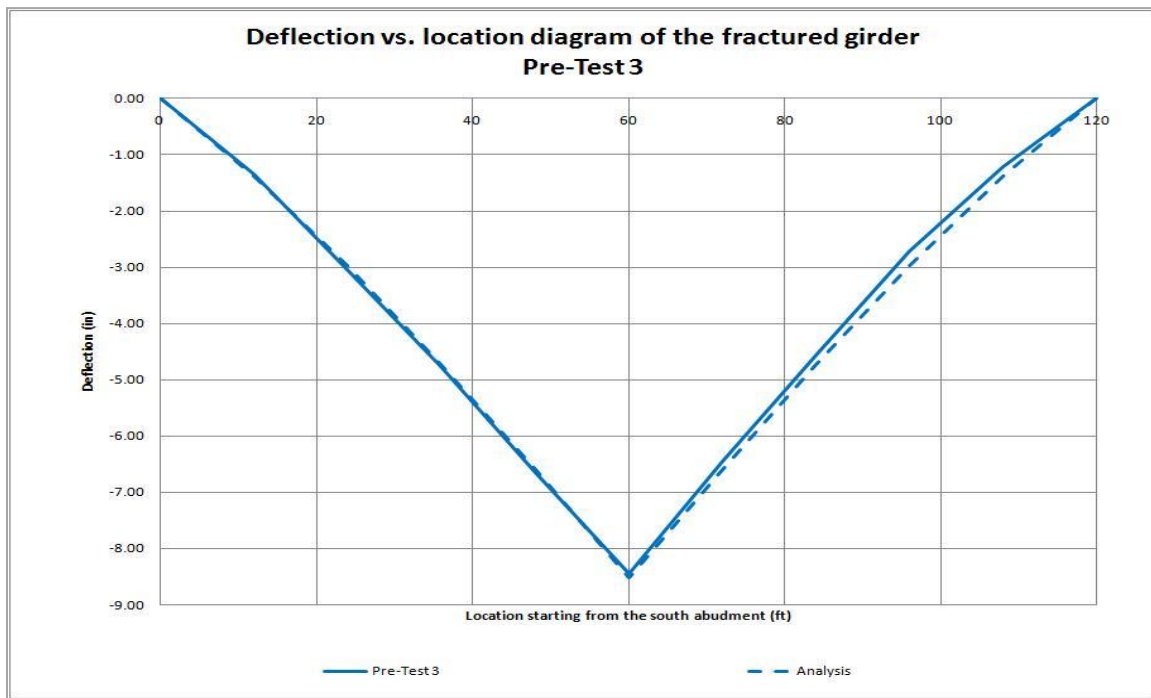


Figure 3-28: Deflection vs. location diagram of the fractured girder Pre-Test 3

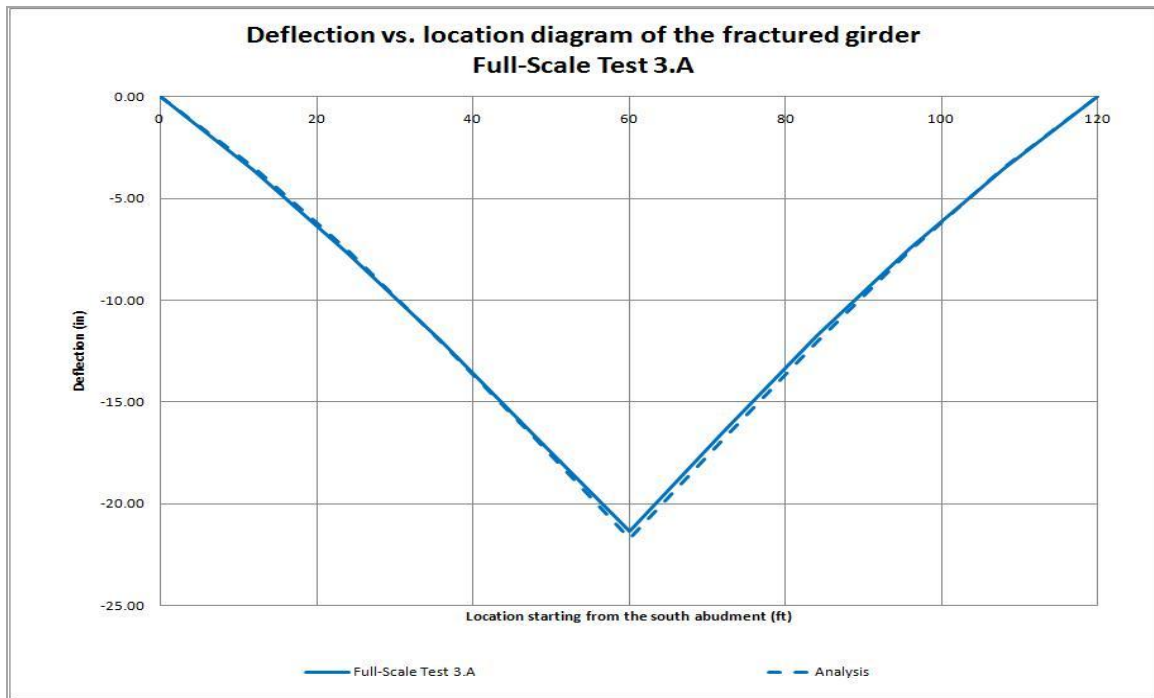


Figure 3-29: Deflection vs. location diagram of the fractured girder Test 3.A

It is important to note that the maximum deflection at the centerline in Figure 3-29 was obtained by assigning the fractured section over a larger length of the span than was considered for the previous figures. This assumption is reasonable if it is taken into account that the shear stud connections at the exterior top flange of the fractured girder had failed almost 30 ft. on each side of the centerline after Test 3.A. Thus, in order to obtain a good estimate of the deflections, at each increment of the load, the length of the fractured girder which had lost the shear stud connections in both top flanges should be estimated from the Simplified Strip Model. The reduced stiffness fractured section should be assigned to the length equal to the length that the shear studs have pulled out.

In the case of a continuous bridge, the segment between the fracture and the interior support should deflect according to Equation 3-29. Parametric studies indicated that the

range of angle  $\varphi$  should be between  $15^\circ$  and  $75^\circ$  for this case. Therefore, for continuous bridges,

$$Y(\varphi) = W \cdot \sin(\varphi) - W \cdot \sin(75^\circ), \quad 15^\circ \leq \varphi \leq 75^\circ \quad (\text{Equation 3-29})$$

where  $W = (\Delta_{initial} + \Delta_{analysis}) / (\sin(15^\circ) - \sin(75^\circ)) = \Delta_{total \text{ at the fracture location}} / (\sin(15^\circ) - \sin(75^\circ))$ . In addition,  $Y(15^\circ)$  is the deflection at the fracture location and  $Y(75^\circ) = 0$  is the deflection at the interior support. It should be mentioned that Equations 3-28 and 3-29 were based on a sine curve. It would be beneficial if other types of curves to estimate the deflections would be investigated. Moreover, Equation 3-29 was not verified with any test results because the FSEL bridge was a simply supported bridge. Equation 3-29 was based on results of computational analyses of fractured girders on continuous bridges.

After establishing the Simplified Strip Model, the ultimate load that the FSEL test bridge could sustain was estimated to be 126.4 kips. This estimation was compared with the results obtained from Test 3. As will be discussed in Chapter 4, the bridge actually collapsed at a much higher load (363.75 kips) than that predicted by the Simplified Strip Model. This large deviation between the estimated and the actual ultimate load was due to the fact that the Simplified Strip Model does not take into account the behavior of the concrete deck in the two horizontal dimensions. The Yield Line Model, which will be described later on in this thesis, provides a better estimation of the ultimate load than the Simplified Strip Model. It is worthwhile to mention that the Simplified Strip Model should be used initially to check if the shear studs are expected to fail. In the event that the shear studs do not fail and hinge lines are formed at the interior top flanges of the concrete deck, then the Simplified Strip Model would provide a good estimation of the ultimate load. In contrast, if shear stud failure occurs, then the Yield Line Model should be used to estimate the ultimate load that a bridge could sustain.

All the deflections from the various tests (Test 2, Pre-Test 3, etc.) were the average of the measured deflection of the two edges of each bottom flange. As reported by Neuman

[Neuman, (2009)], the twist of both girders was negligible. Only after the shear stud connections of the fractured girder pulled out over the entire length of the bridge did the twist of the intact girder become significant. Based on this observation, it was assumed that both girders would not twist as they deflect downward so that girder deflections could be estimated at both ends of the bottom flange for use in the Simplified Strip Model.

Detailed calculations of how to analyze the FSEL bridge and two other bridges with the simple methods presented in this chapter are given in Appendices B, C and D.

### **3.7 SUMMARY**

The Simplified Strip Model provides a quick and easy way to predict the length of shear stud failure and the formation of hinge lines at the interior top flanges of twin box girder bridges with a fracture. This simple method is very beneficial for an engineer who wants to evaluate the redundancy level of a twin box girder bridge. Because the FSEL test bridge results are the only information available to verify this model, future evaluation of the simplified model may be needed. A comparison between the results of the strip model and other test or finite element model results will be beneficial in order to refine the Simplified Strip Model. Because the Simplified Strip Model was developed before Test 3, it was used to estimate the ultimate load of Test 3. Further discussion of the estimation is given in the next chapter.



## CHAPTER 4

### Test Results: Test 3

#### 4.1 INTRODUCTION

After Test 2, the bridge was damaged, but still able to sustain the applied loads. In order to determine the maximum load that the FSEL bridge could sustain and to determine the failure sequence, it was decided to perform an additional test. The bridge was tested to failure in Test 3. Test 3 was not a single test but rather a series of tests. The series of tests included in Test 3 are Pre-Test 3, Test 3.A, Test 3.B and Test 3.C. In Pre-Test 3, the bridge was loaded with concrete blocks that were placed to form the perimeter of a rectangular (40 ft × 8 ft) bin. The rectangle was symmetrically placed about the bridge centerline in the longitudinal direction in order to maximize the bending moment on the bridge. In the transverse direction, the bin was located 2 ft. from the railing over the fractured girder. Inside the rectangular bin, road base material was poured during Test 3. The static loading procedure relied on a crane to place increments of load on the bridge. The bridge had a full-depth fracture on one of the girders, and there was no external system to support the fractured girder. By loading the bridge with increments of loads in excess of the design truck load (HS-20), the ultimate strength of the bridge with both webs fractured and a fractured bottom flange was determined. Table 4-1 summarizes significant events during Test 3 and under what load they occurred. Due to the fact that the loading was in increments rather than continuous, all the strain data in this chapter are presented as step plots. Because the total applied load changed constantly, all the data are presented as load versus strain plots. It is worthwhile to note that all the residual strains after unloading the bridge at the end of Test 2 have been included in several strain plots presented in this chapter. The residual stresses were only added in the instrumentation of the steel girders and reinforcement bars and only at the locations where strain gages existed in Test 2.

Table 4-1: Failures of the bridge elements under different loads during Test 3

Load (kips)	Element Failure Event
34.23	Fracture at the exterior web of the fractured girder propagated all the way to top flange
107.6	Initiation of shear stud failure at the centerline of the exterior top flange of the fractured girder
161.52	Shear stud of exterior top flange of fractured girder pulled out instantaneously over a length of 60 ft. and arrested at south and north expansion joint
363.75	Total collapse of the bridge

Following the end of Test 2, the instrumentation of the bridge was repaired, and new strain gages and displacement transducers were installed at several new locations. Overall, the new instrumentation scheme was similar to Test 2 except for few small changes. Figure 4-1 presents a typical instrumented cross-section for Test 3. All the instruments used in Test 3 have been reported by Neuman [Neuman, (2009)].

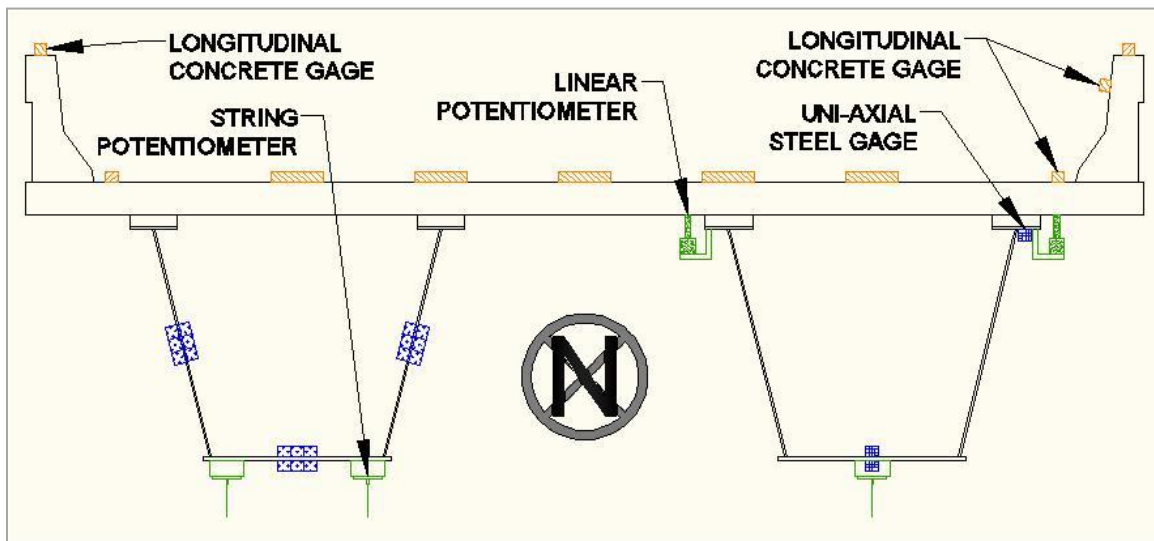


Figure 4-1: A typical instrumentation plan of a cross-section for Test 3 [Neuman, (2009)]

## **4.2 GIRDERS AND END DIAPHRAGMS GAGE DATA ANALYSIS**

### **4.2.1 Instrumentation analysis of intact and fractured girder**

Although there were a few small changes, the instrumentation of the two girders for Test 3 was similar to the instrumentation employed in Test 2. The fractured girder (FG) was instrumented with uniaxial strain gages on the bottom flange, except the N1 and S1 uniaxial gages were removed because the strains of these locations were almost zero. In addition, several more uniaxial gages were installed on both top flanges of the fractured girder for Test 3. It was assumed that the top flange, as the extreme top fiber of the fractured girder, would develop a tensile force to resist the cantilever-like deflected shape of the fractured girder.

In Test 3, the bridge behaved in a similar way as in Test 2. Thus, the bottom flange of the FG was in compression along the whole span, which was well captured by the uniaxial gages (Figure 4-3). Moreover, all the strain values of the monitored locations were in the elastic range. In Figures 4-3 and 4-4, several significant stages of the bridge behavior are depicted. During Pre-Test 3 and at the point that the total load on the bridge was 34.23 kips, the fracture on the exterior web of the fractured girder propagated all the way up to the top flange (Figure 4-2).

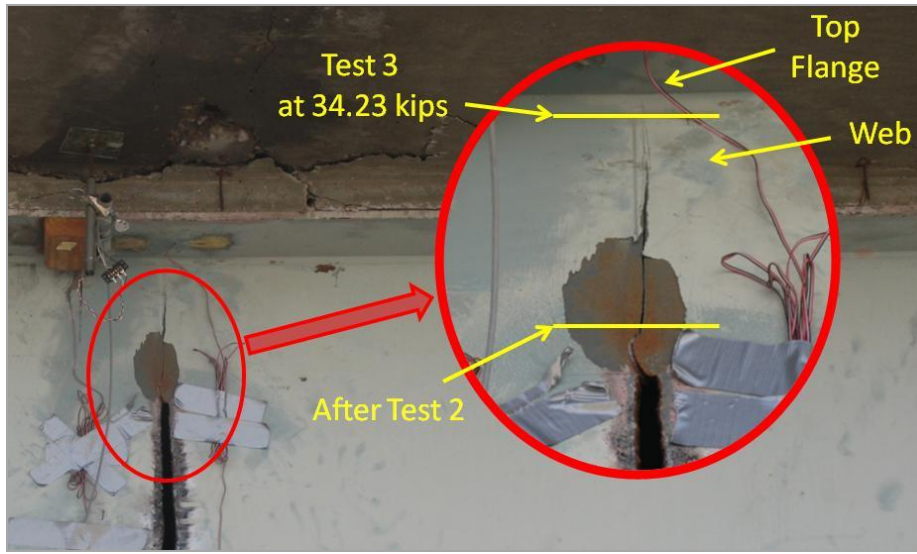


Figure 4-2: Fracture propagation on the exterior web of the fractured girder

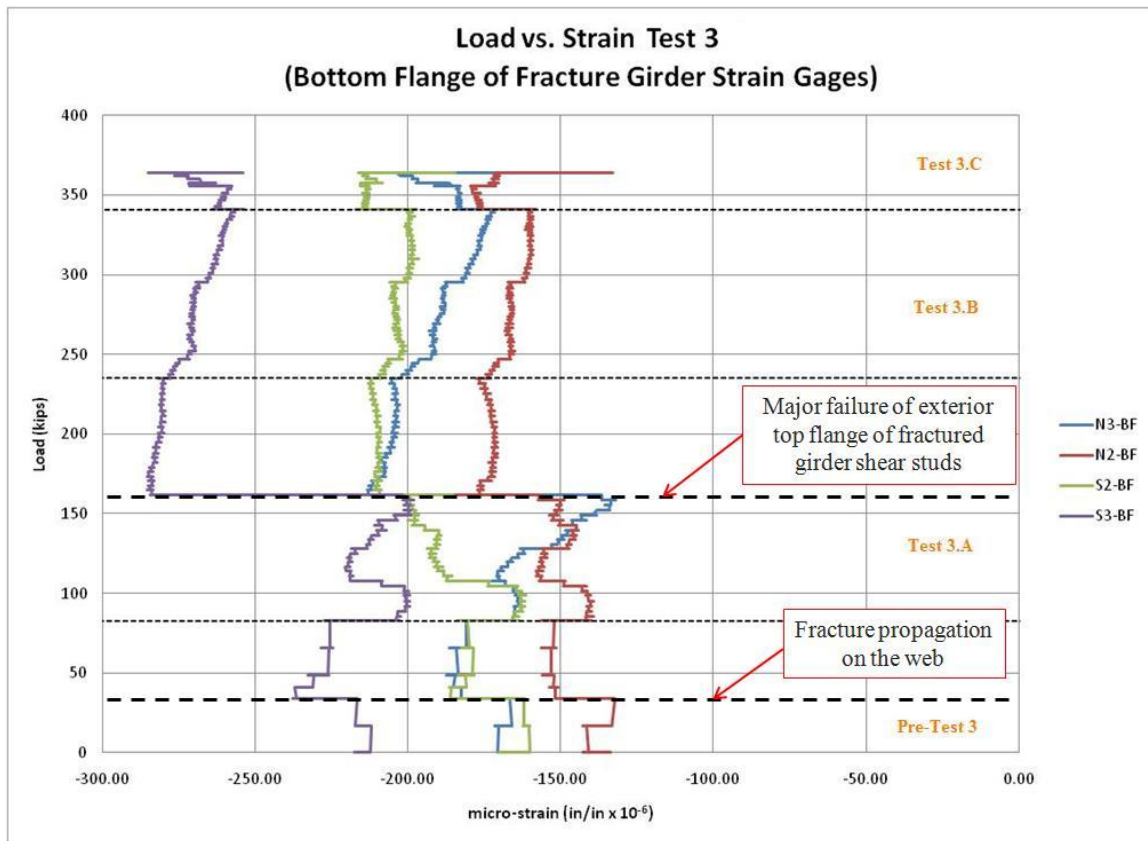


Figure 4-3: Bottom Flange strain gage data of fractured girder during Test 3

Due to the propagation of the fracture, the fractured girder deflected downward, forcing the bottom flange to bend in a cantilever-like shape. As illustrated in Figure 4-3, the strains had a large increase at the load level of 34.23 kips when the fracture propagated. A similar increase in strain was recorded in the uniaxial gages installed on the top flange at the centerline of the fractured girder as shown in Figure 4-4. The fracture propagated at a lower load than the load applied in Test 2. The lower temperature of the steel may have contributed to this behavior. Test 2 took place on a hot summer day (6/6/2008) when the temperature had risen to 93° F, whereas Pre-Test 3 took place during a cold day when the temperature was 45° F.

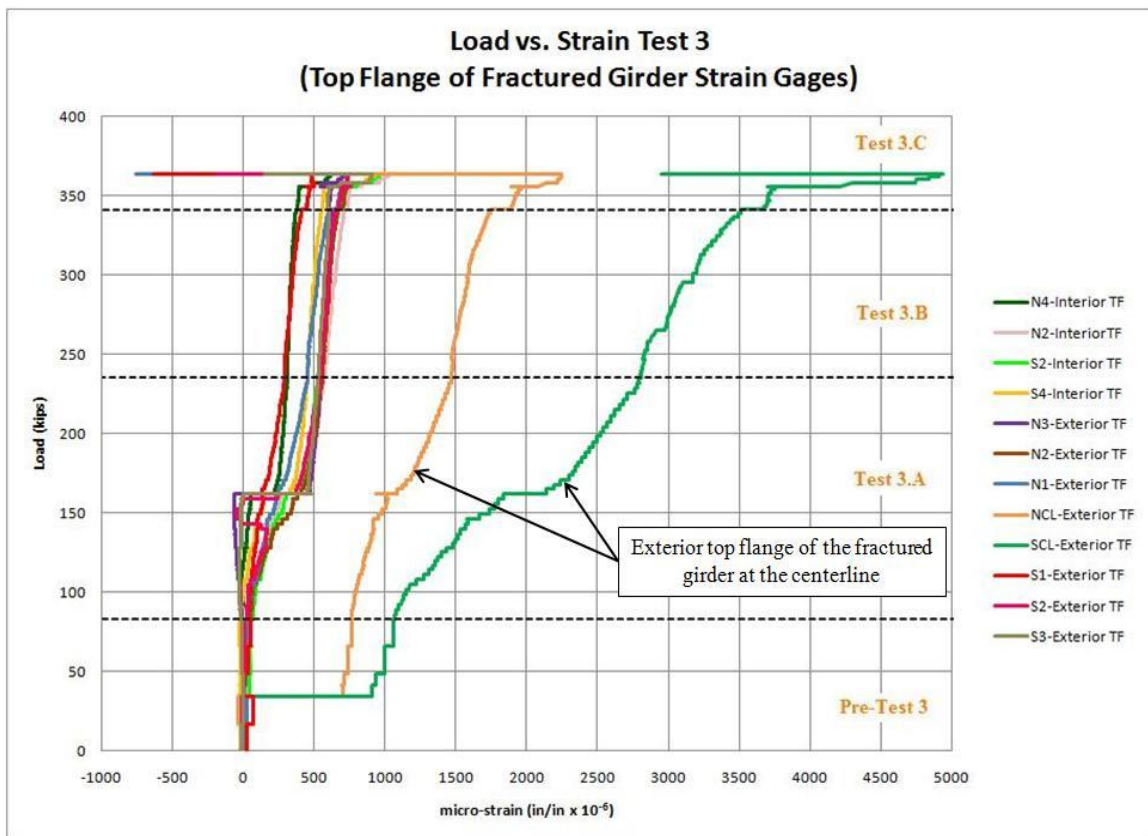


Figure 4-4: Top flange strain gages data of fractured girder during Test 3

Following Pre-Test 3, the bridge was incrementally loaded with road base material (Test 3.A through 3.C). During Test 3.A, the shear stud connections began failing as the load was increased. The first significant loss of shear studs was localized around the centerline of the exterior top flange of the fractured girder, and it occurred when the total load was 107.6 kips as shown in Figure 4-5. The strain in the bottom flange in Figure 4-3 shows a large increase of strain at an applied load of 107.6 kips. However, in Figure 4-4, the slope of the exterior top flange of the fractured girder at the centerline curve changes at the same load. The most significant loss of shear studs shown in Figure 4-6 happened suddenly at a load of 161.52 kips. The shear studs in the exterior flange pulled out almost instantaneously over a length of 60 ft., and the pullout of the studs arrested approximately at the locations of the south and north expansion joints in the railing. The discontinuity of the railings led to the opening of the south and north expansions joints of the east railing as the fractured girder deflected from the sudden loss of shear studs at the exterior top flange of the fractured girder. This event is illustrated in Figure 4-7. The linear potentiometer, which was installed at the south expansion joint, captured the opening



Figure 4-5: Localized shear stud failure

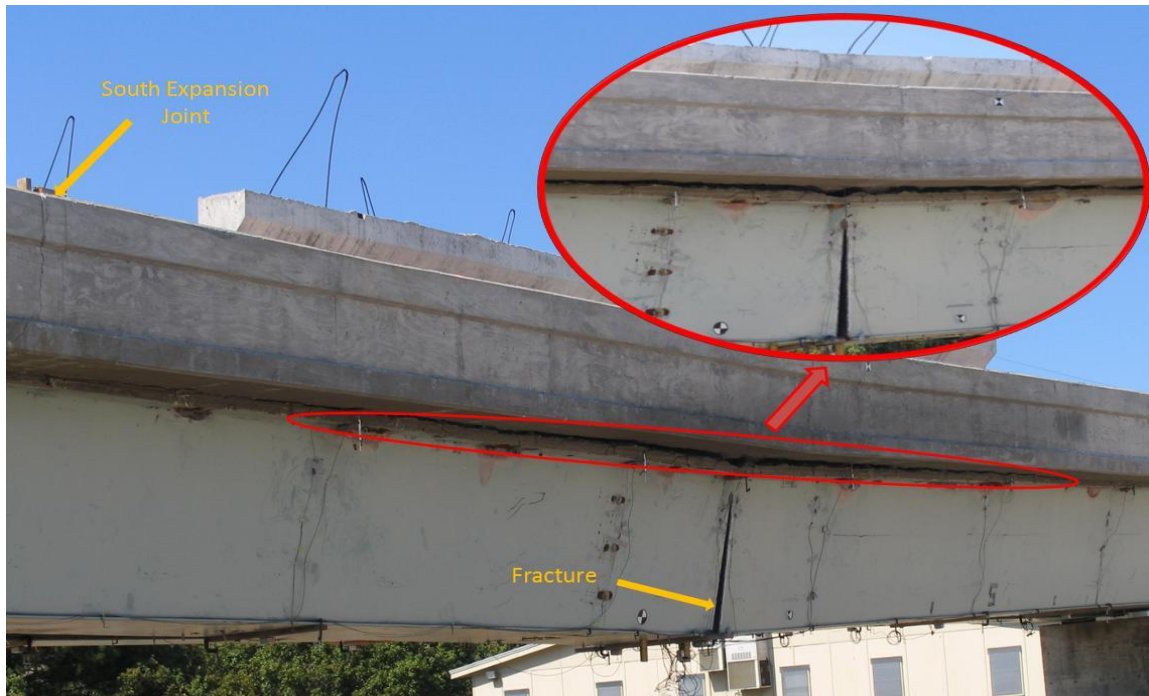


Figure 4-6: Major shear stud failure

and closing of the expansion joint as the bridge was responding from the sudden pull out of shear studs. Following the sudden loss of shear studs that took place at an applied load of 161.52 kips, no data were captured by this potentiometer because it had reached its stroke capacity. Furthermore, as shown in Figure 4-8, the separation at the centerline of the exterior top flange was over 3 in. In the same figure, the overall separation between the bridge deck and the top flanges on each side of the fractured girder is plotted. The plot stops after Test 3.A because all the instruments were at their stroke length, producing the vertical line in the plot. The shear studs of the interior top flange of the fractured girder had been pulled out over a length of 60 ft. during Test 2, so all the values of separation of the interior top flange in Figure 4-8 are the additional separation following Test 2. Because all the instrumented shear studs on the fractured girder were damaged in the previous tests, no information on the forces in the shear studs was available.

Extensive finite element analysis [Kim, (In progress)] of the bridge indicated high stresses in the bottom flange of the intact girder at the centerline. To verify the computational predictions, two longitudinal uniaxial strain gages were installed on the inside and outside of the bottom flange of the intact girder at the centerline. The ability of the intact girder to sustain the entire dead load of the bridge and truck live load was necessary to prevent collapse of the bridge. Figure 4-9 indicates that all the strain values were in the elastic range, and their magnitude was much larger than the strains in the bottom flange of fractured girder. No spalling of paint was observed on the intact girder, further indicating that the girder remained elastic.

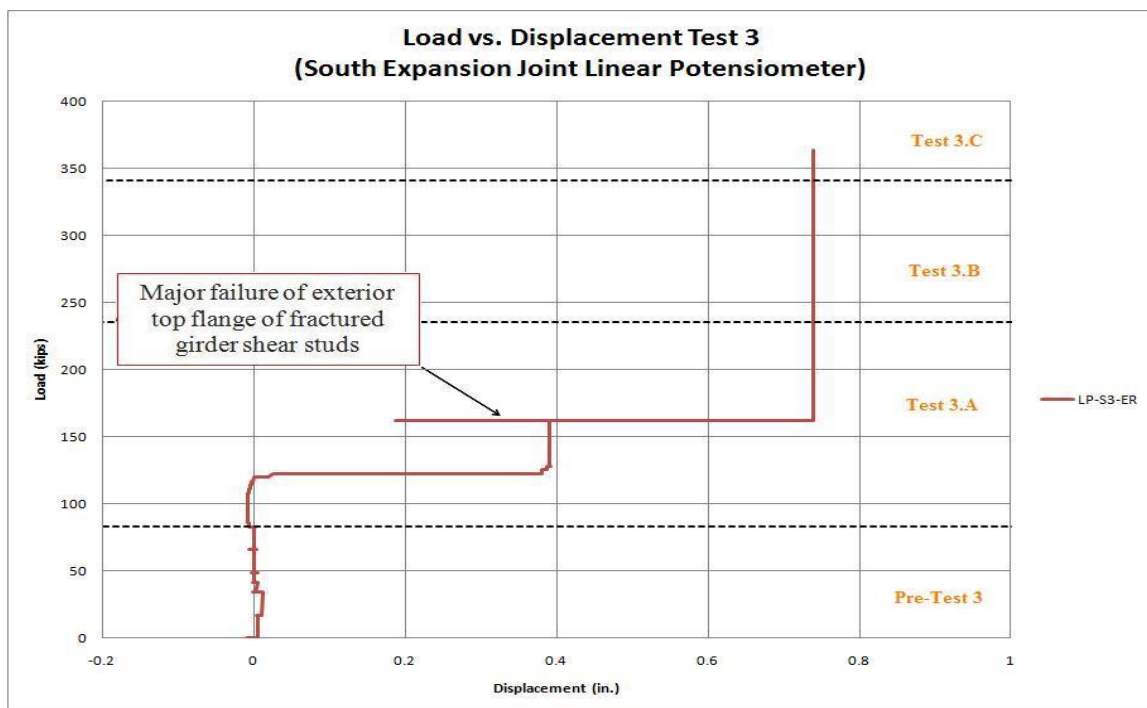


Figure 4-7: South expansion joints opening Test 3



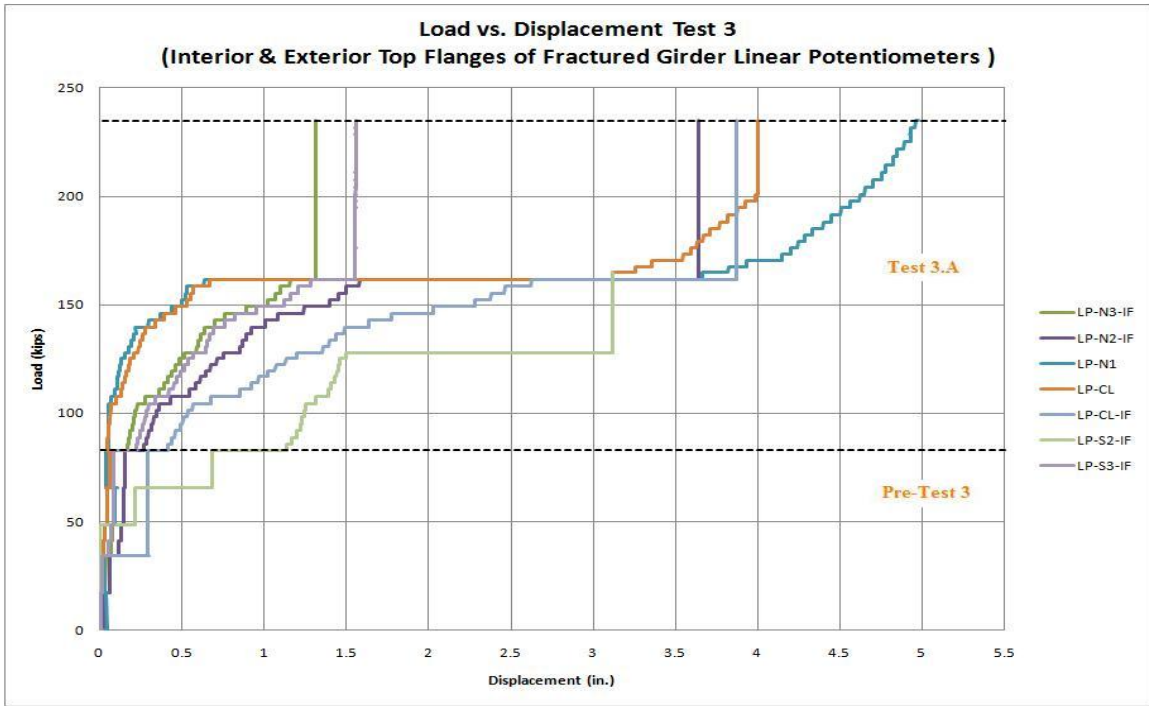


Figure 4-8: Fractured girder's interior and exterior top flange separation Test 3

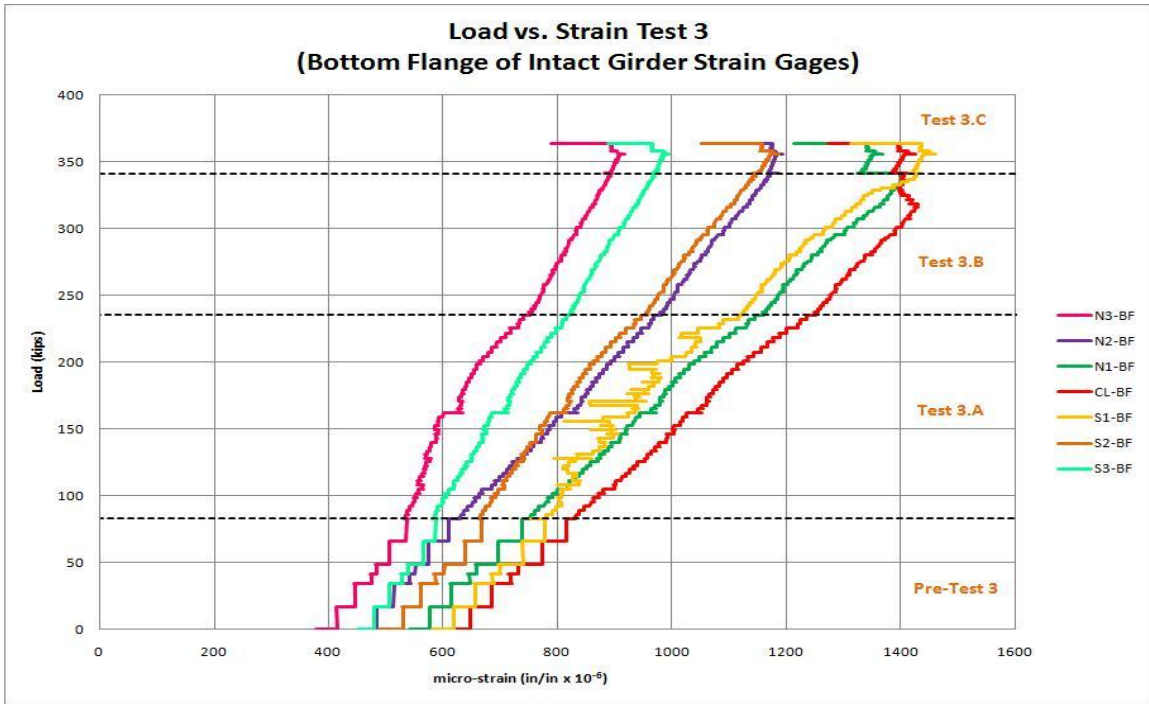


Figure 4-9: Bottom flange strain gages data of intact girder during Test 3

Figures 4-10 and 4-11 show the strains measured in the bottom flange of the girders. After the major failure of shear studs, the strain in the bottom flange of the fractured girder did not change with application of the load to the bridge because the fractured girder was only supporting its own self weight. The strain at the end of the girders was estimated by extrapolating the data at S2, S3, N2 and N3 sections. The extrapolation is shown by the dashed lines in the figures.

Figure 4-11 illustrates the increase of the strain in the intact girder's bottom flange as the load was increasing. The increase in strain was expected because the intact girder was carrying most of the applied load and was the member that prevented the collapse of the bridge.

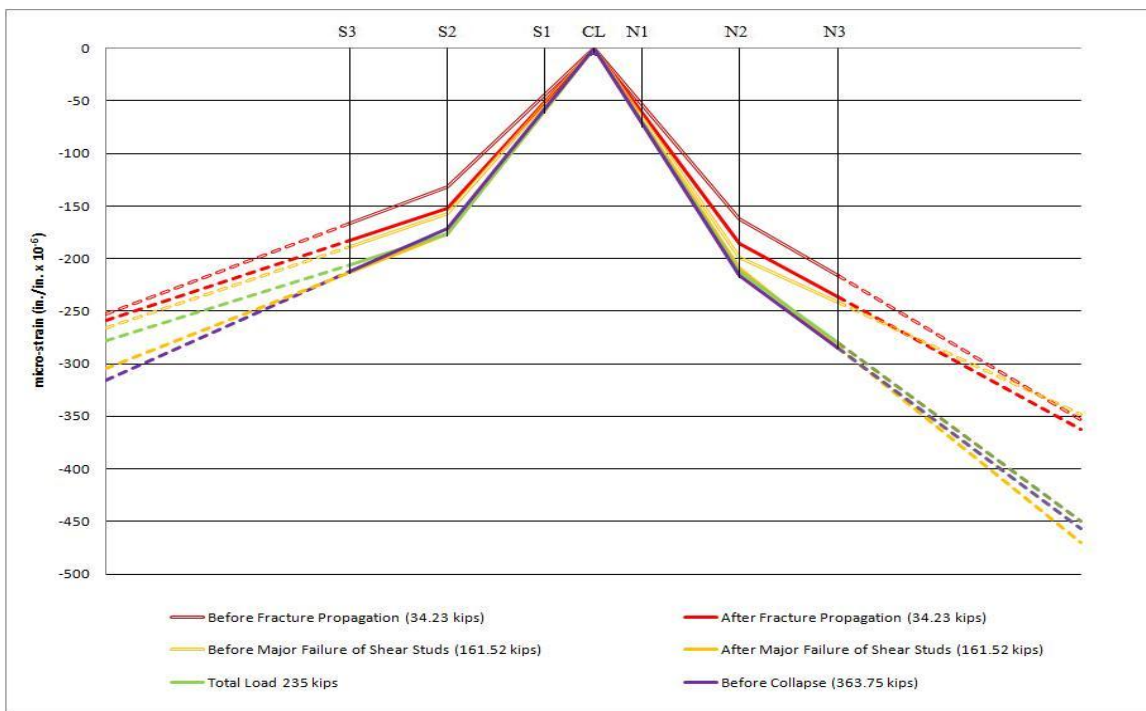


Figure 4-10: Bottom flange strain diagram of fractured girder during Test 3

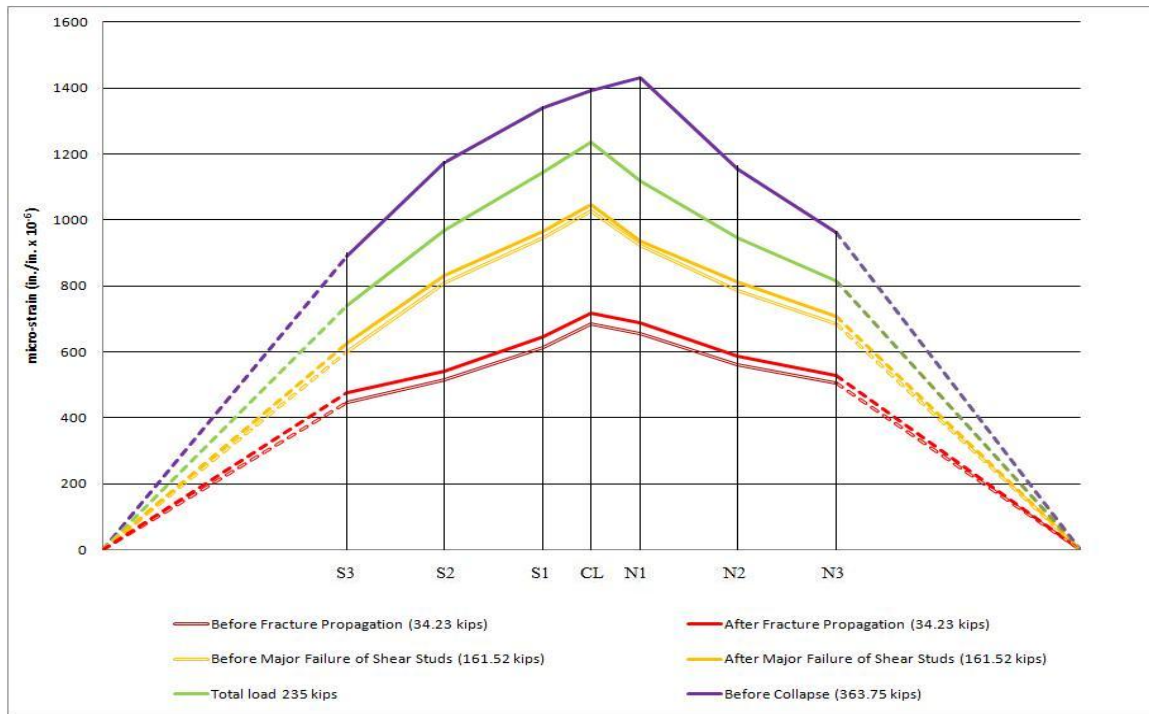


Figure 4-11: Bottom flange strain diagram of intact girder during Test 3

The moment diagram for the intact girder (Figure 4-12) was constructed using the strain values from the gages on the bottom flange of the intact girder and the longitudinal concrete gages on the deck. The procedure described in Chapter 2 was followed. The strains of the extreme fibers of the elastic composite cross section were used to construct the strain gradient. By converting the strain gradient to stresses, the internal forces that act on different parts of the elastic section could be calculated. The internal moment was calculated by adding the moments of the calculated forces acting at various parts of the section about a defined axis. As before, the section behaved elastically based on strain data. The section consisted of the steel box of the intact girder, the concrete deck and the railing. Half of the width of the deck was assumed to be the effective width of the elastic section. The details of the calculations are given in Appendix A.

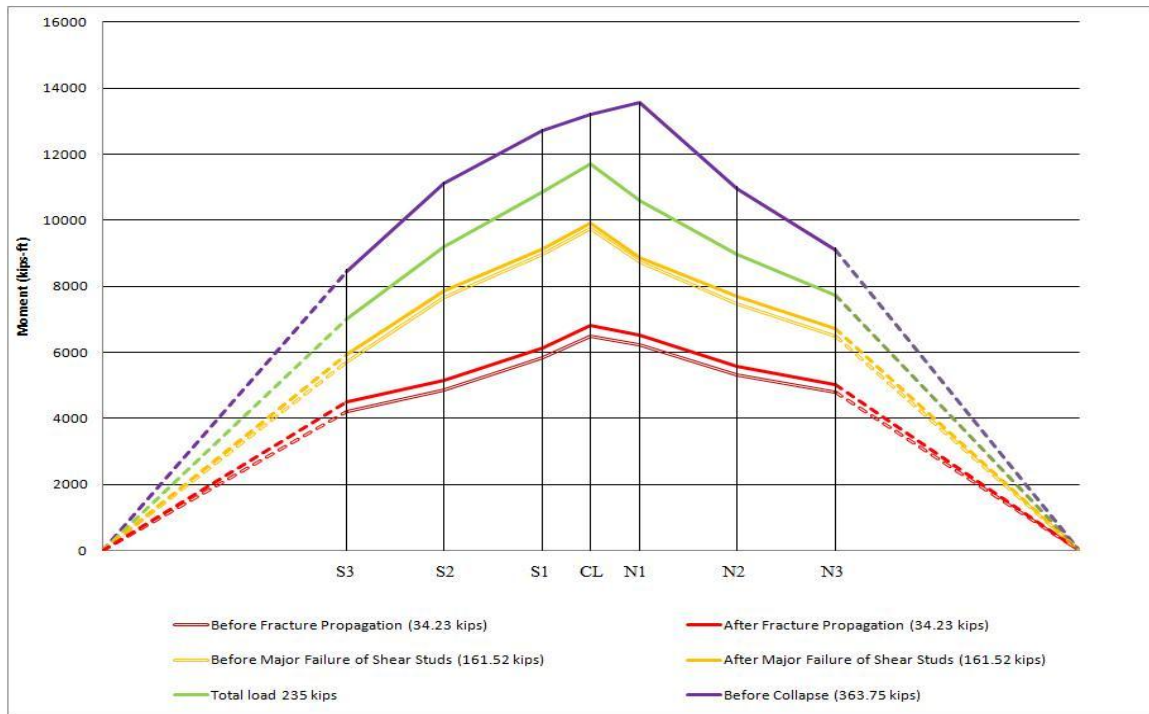


Figure 4-12: Moment diagram of the intact girder during Test 3

Following the procedure described in Chapter 2, the shear flow at the defined sections was calculated using strain data from different load levels. The torsional moment diagram provides an overall view of how the load was transferred to the intact girder for each stage of loading.

If the composite section of the intact girder was treated as a closed section where the shear flow in the deck was the same as in the webs and the bottom flange, it was possible to calculate the torque that was acting on the intact girder due to the truck live load and the dead load of the bridge that the fractured girder could not support by using Equation 2-1. As before,  $A$  was the inner area of the closed section ( $A= 26.74 \text{ ft}^2$ ), and  $q$  was the shear flow value at each section. The shear flow values ( $q$ ) at each section used to calculate the torsional moments are listed in Table 4-2. It should be mentioned that for sections N3 and S3, the shear flow of the bottom flange was used whereas for sections

N1, S1 and S2 the shear flow of the webs was used. This choice was based on the fact that the rosette gauges on the other locations did not record the data properly.

Table 4-2: Average shear flow at the intact girder for different loads Test 3

<b>Applied Test Load</b>	<b>N3</b>	<b>N2</b>	<b>N1</b>	<b>S1</b>	<b>S2</b>	<b>S3</b>
<b>(kips)</b>	<b>(kips/in)</b>	<b>(kips/in)</b>	<b>(kips/in)</b>	<b>(kips/in)</b>	<b>(kips/in)</b>	<b>(kips/in)</b>
<b>34.23</b>	-1.13	-0.7	-0.06	-0.03	0.57	1.02
<b>34.23</b>	-1.13	-0.7	-0.06	-0.03	0.58	1.03
<b>161.52</b>	-1.57	-1.1	0.13	0.04	1.1	1.57
<b>161.52</b>	-1.66	-1.08	0.09	0.04	1.12	1.71
<b>235</b>	-1.92	-1.27	0.13	0.21	1.27	1.92
<b>363.75</b>	-2.06	-1.34	-0.06	0.47	1.29	2.01

Figure 4-13 shows the calculated torsional moment diagram for different loads. A uniformly distributed torque could be determined for each load level by computing the slope of each line show in Figure 4-13. The distributed load that was transferred to the intact girder could be estimated as the distributed torque divided by the distance between the centerline of the girders (12 ft). Table 4-3 presents the calculated distributed torque from the strain data. Table 4-4 shows the calculated distributed torque produced by half of the dead load (weight of the fractured girder plus half the weight of the deck) and the simulated truck load. The contribution of dead load was included in the values of Table 4-3. The self weight of the concrete and one girder was 1.56 kips/ft and 0.37 kips/ft, respectively. The values of the applied load in Tables 4-3 and 4-4 should be compared at the same load level. Taking into account that a portion of the simulated truck load was being transferred to the supports by the remaining intact segment of the fractured girder, concrete deck and railing, the values of the total applied load from the strain data were relatively close with the assumed total applied load until the point that the applied load on the bridge was 235 kips. As shown in Figure 4-14, above the load of 235 kips, load in the

girder estimated from the applied load exceeds that calculated from the strain data. This result was probably caused by the release of the steel girder weight due to the pull out of the shear studs and the transfer of load into the railing.

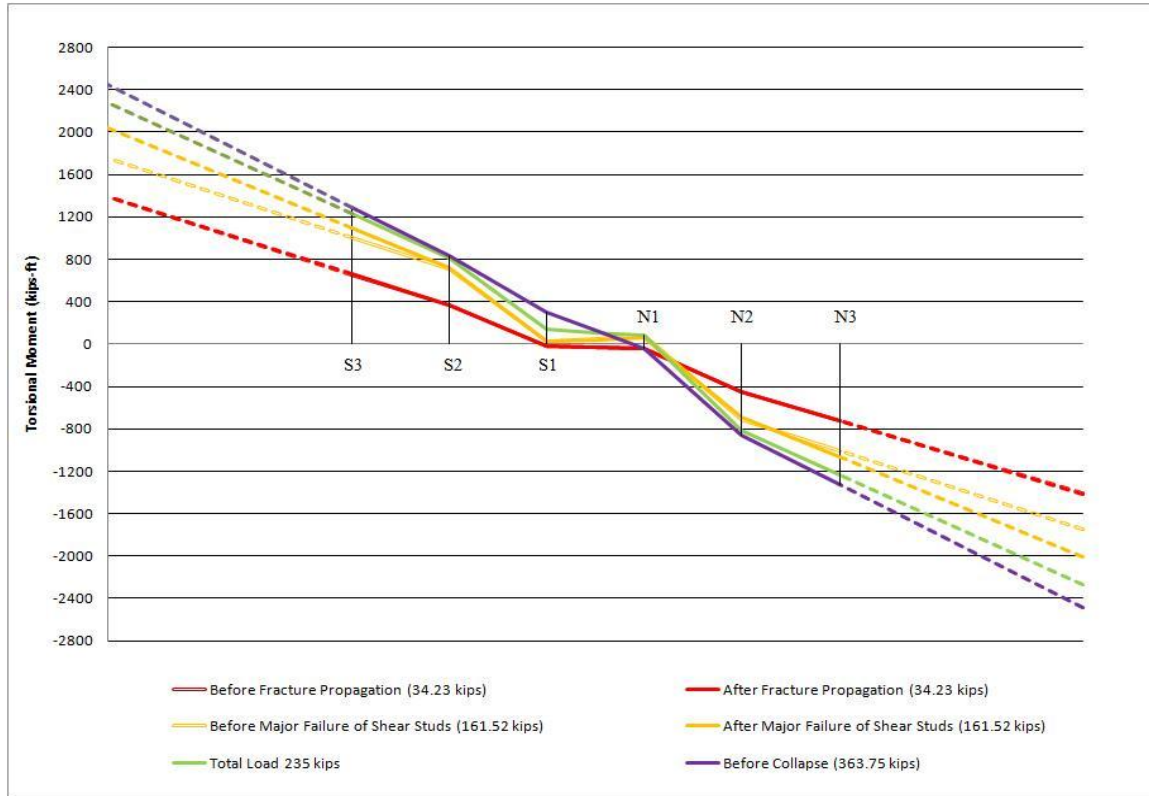


Figure 4-13: Torsional moment diagram of the intact girder during Test 3

Table 4-3: Torque in intact girder based on strain gage data Test 3

Applied Test load	Applied distributed torque	Distributed load transferred to the intact girder	Vertical load on intact girder from torque
(kips)	(kips·ft/ft)	(kips/ft)	(kips)
34.23	22.29	1.86	222.93
34.23	22.46	1.87	224.58
161.52	33.91	2.83	339.08
161.52	35.74	2.98	357.44
235.00	41.10	3.43	411.01
363.75	44.04	3.67	440.35

Table 4-4: Calculated Torque on Intact Girder from Dead Load of Fractured Girder and Applied Loads

Load	Distributed Load	Applied distributed torque	Length of distributed torque	Total vertical load applied to intact girder
(kips)	(kips/ft)	(kips·ft/ft)	(ft)	(kips)
Dead Load	1.93	23.19	120	231.88
34.23	0.86	34.48	40	266.11
161.52	4.04	56.58	40	393.40
235	5.88	71.77	40	466.88
363.75	9.09	98.39	40	595.63

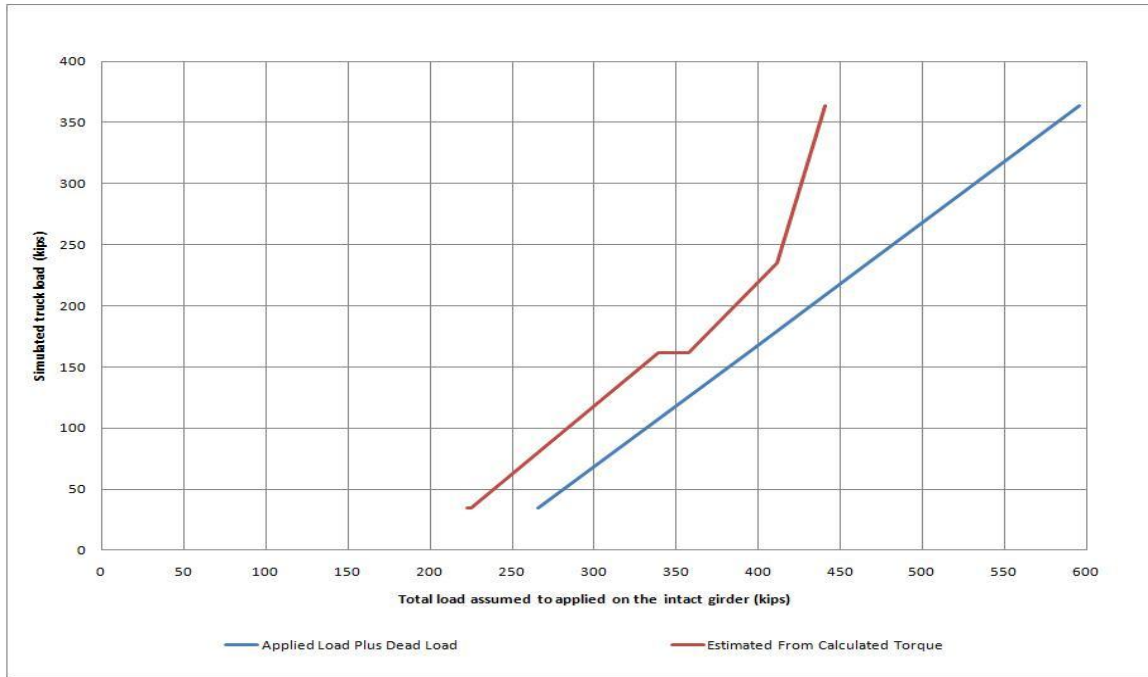


Figure 4-14 Total applied load on the intact girder from strain calculations and assumptions

Similarly to Test 2, the end diaphragms played a significant role in providing torsional moment restraint at the ends of the intact girder. A lack of torsional restraint would have resulted in larger rotations and deflections than were measured during the test. The orientation and the magnitude of the principle stresses was calculated for both end diaphragms by using data that the rosette gages captured during Test 3 (Figure 2-17). The results of the principle stress calculations are summarized in Table 4-5. Because the angle  $\phi$ , which was the angle of the principle axes from the horizontal, was relatively close to  $45^\circ$ , it could be concluded that the stress state at the end diaphragms was nearly pure shear.



Table 4-5: Principle stresses of end diaphragms Test 3

Load	North End Diaphragm				South End Diaphragm			
	$\sigma_1$ (ksi)	$\sigma_2$ (ksi)	$\tau_{max}$ (ksi)	$\phi$ (degrees)	$\sigma_1$ (ksi)	$\sigma_2$ (ksi)	$\tau_{max}$ (ksi)	$\phi$ (degrees)
Before 34.23kips	5.65	-4.81	5.23	48.70	8.11	-3.40	5.76	50.11
After 34.23kips	5.63	-5.28	5.46	49.12	8.04	-3.21	5.63	49.23
Before 161.52 kips	7.04	-4.70	5.87	45.42	8.27	-2.27	5.27	56.02
After 161.52kips	7.04	-4.43	5.74	43.52	8.30	-1.61	4.96	53.83
235 kips	7.53	-4.70	6.12	41.65	8.25	-0.54	4.40	46.00
363.75 kips	7.44	-4.34	5.89	39.02	6.99	2.16	2.42	49.09

#### 4.2.2 Analysis of concrete deck strain data

The top surface of the concrete deck and both railings were instrumented as shown in Figure 4-15. Finite element analyses by Kim [Kim, (In progress)] indicated high stresses in various locations that were instrumented with concrete strain gages. As reported by Neuman [Neuman, (2009)], new concrete strain gages were installed on the top surface of the deck and on the east and west railings to monitor the response of the bridge.

During Test 3, the collected test data and visual observations indicated that the exterior railing was acting as an inverted beam and was carrying a portion of the applied load. Figure 4-16 shows the strain data history of the gages located at the top surface of the exterior railing. At all of the monitored locations, the concrete strain was not close to crushing. Localized crushing occurred at the centerline after Test 3.A. The strain gages at this location did not record strains close to crushing. Instead, tensile strains were captured during Test 3 because a thin layer of concrete on which the strain gage was installed spalled off while the railing was crushing (Figure 4-17). The complete failure of the east railing at the centerline occurred just before the collapse of the bridge. With the exception of the top surface of the east railing, gages were installed along the height of the railing at the same locations as the strain gages on the top surface of the east railing sections to quantify its strain profile. Figure 4-18 illustrates the way that the strain along the height of the railing at different locations changed during Test 3. It should be mentioned that for

sections N2, N1, S1 and S2, the strain gage was located at the mid-height of the section, whereas for the CL section, the strain at 6 in. from the top surface was captured. As the applied load increased, the strains in all the monitored sections also increased. An interesting observation was that after the major failure of the shear studs occurred, the strain values dropped off; however, they started building back up as the applied load increased.

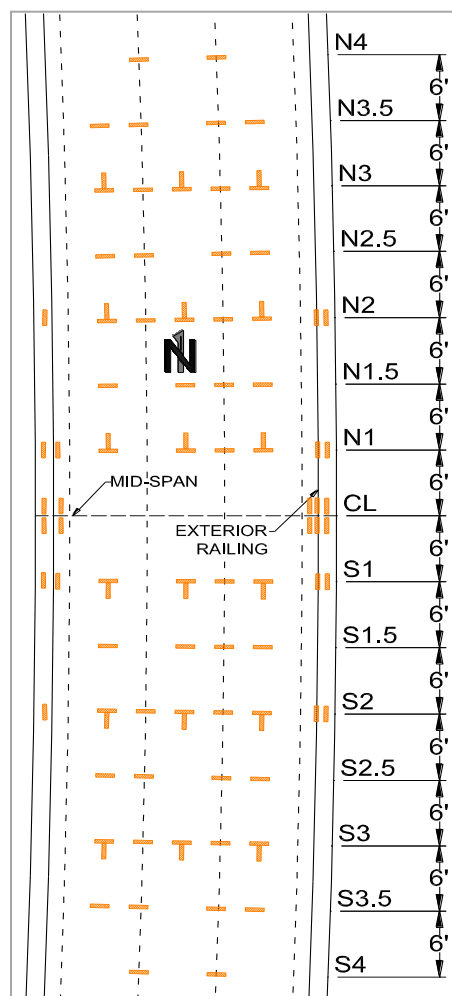


Figure 4-15: Arrangement of the concrete gages on concrete deck Test 3 [Neuman, (2009)]

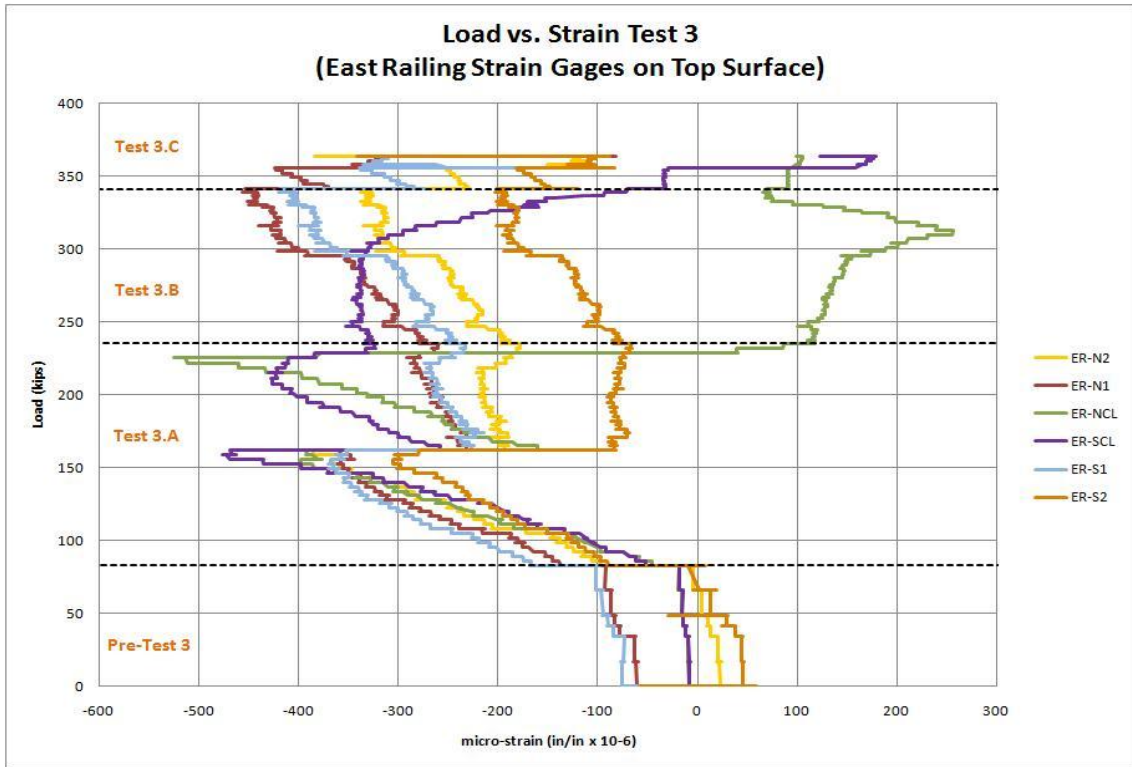


Figure 4-16: Top surface of east railing strain gage data during Test 3

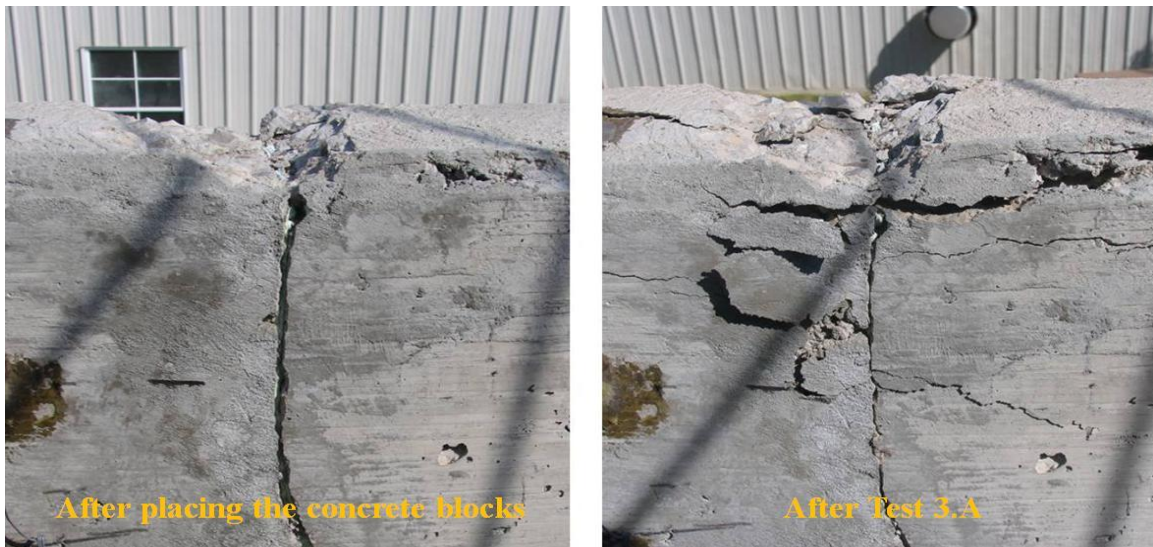


Figure 4-17: Expansion joint of east railing at centerline during Test 3

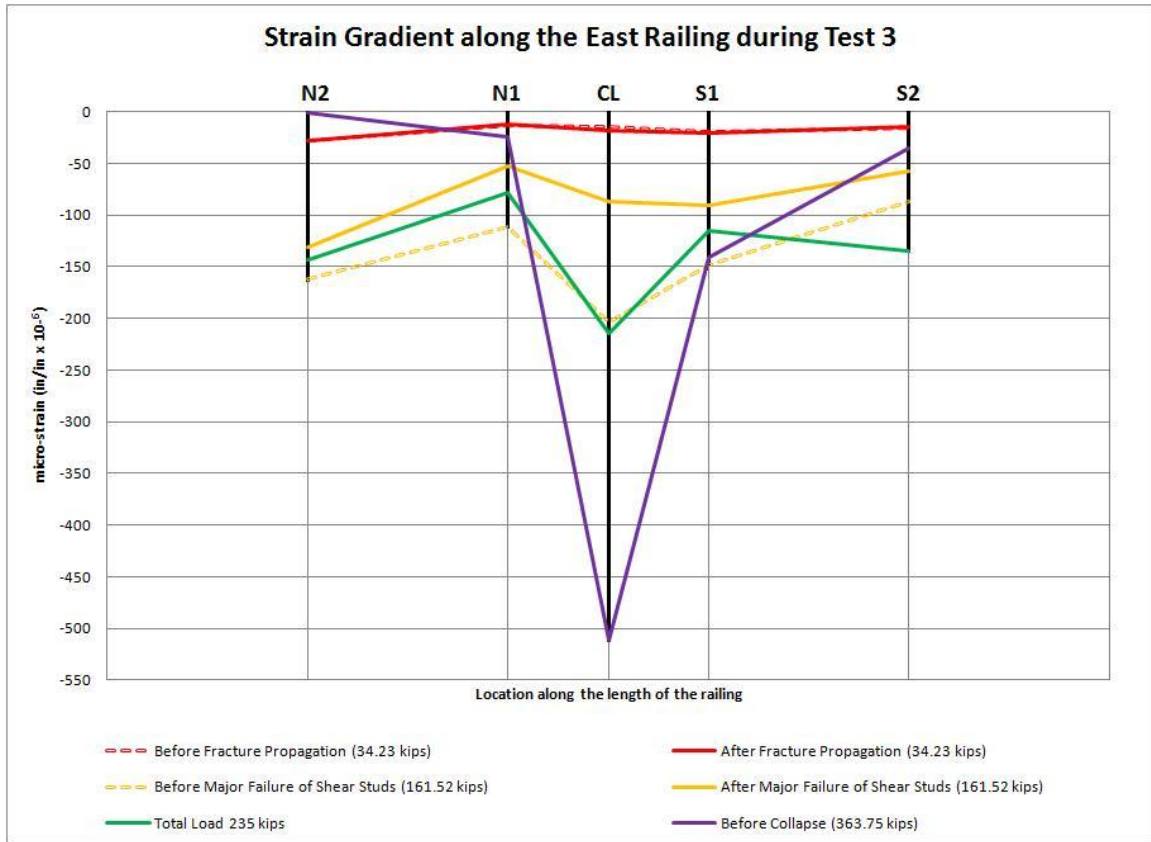


Figure 4-18: East railing strain gage data along the height during Test 3

The moment diagram of the exterior railing (Figure 4-19) was constructed using strain values from the gages that were attached on the top face of the east railing. The section that was used to calculate the moments from the strains consisted of the T501 traffic rail and a part of the concrete deck. Detailed calculations of the moment diagram are given in Appendix A. The calculated moment in the railing decreases after the failure of shear studs because the self weight of the fractured girder was no longer being carried by the concrete deck due to the fact the fractured girder has been disconnected from it. Thus, a decrease of the load leads to a decrease of the moment developed at the railing. A similar reduction occurred in the calculated torsional moment transmitted to the intact girder.

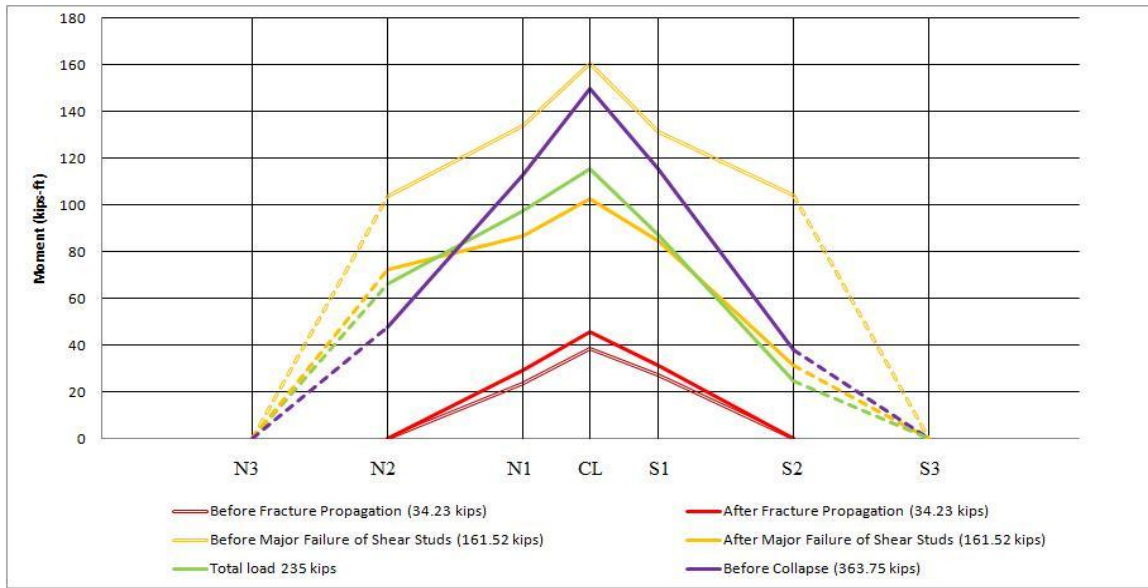


Figure 4-19: Moment diagram of the exterior railing after Test 3

The length over which failure of the shear studs was observed along the fractured girder did not change significantly after the first major failure occurred (161.52 kips). However, at the onset of bridge collapse when the failure of the railing at the centerline and the formation of a hinge line in the concrete deck occurred, the shear studs of both flanges of the fractured girder pulled out over the whole span. This observation illustrates the significant role of the railing and the concrete deck.

Figures 4-20a, b and c illustrate the strain data from the concrete longitudinal gages located between the top flanges of the intact girder, mid-width of the bridge and between the top flanges of the fractured girder, respectively. All the strains were in the compression range, which was expected due to the bending of the bridge. The gages closer to the centerline have higher strain values than the gages located further away from the centerline.

In the transverse direction, many gages were damaged due to extensive cracking. Figure 4-21 presents all the undamaged gages. The main purpose of this figure is to show

the change of the strain in the transverse direction of every section. TC1 was located midway between the flanges of the intact girder, TC2 was located above the interior top flange of the intact girder, TC3 was at the mid-width of the bridge, and TC4 and TC5 were at the interior top flange and middle of the fractured girder, respectively. The hinge line observed during the testing initiated above the interior top flange of the intact girder as the concrete deck was bending transversely to the span. Cracks formed at location TC2. High strain values were also observed at TC1. As the intact girder was trying to resist the applied torque, high bending stresses were developed in the concrete deck above the intact girder.

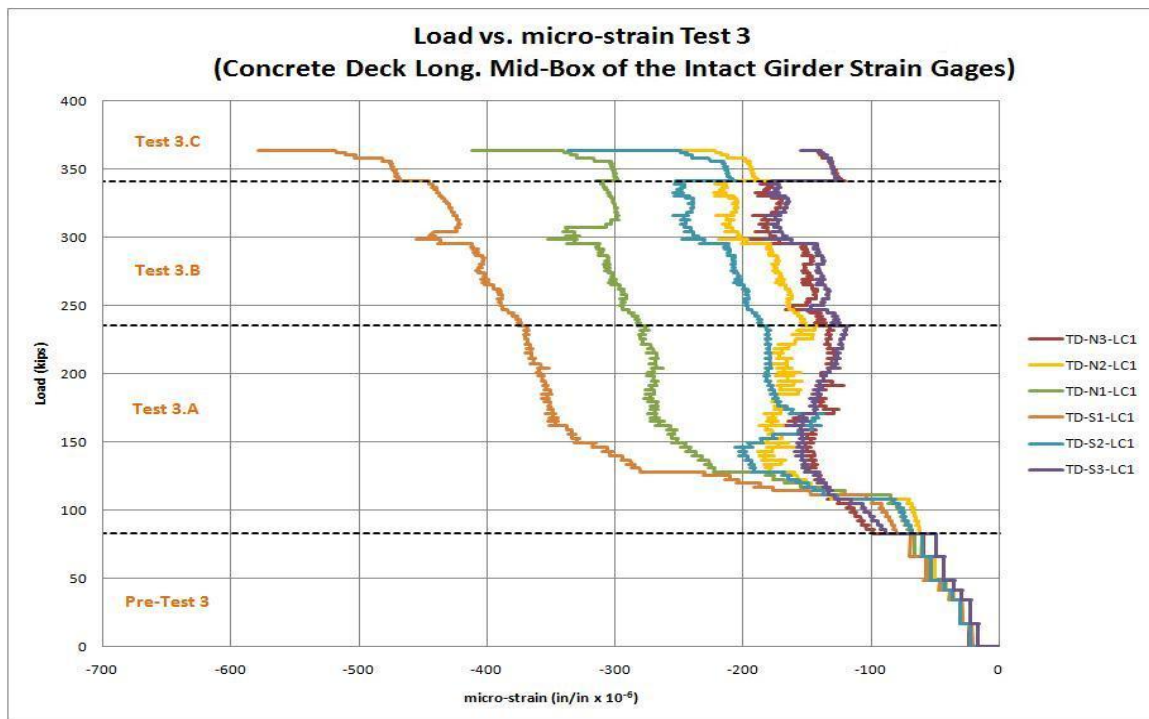


Figure 4-20a: Concrete deck longitudinal strain gages at the mid-box of the intact girder during Test 3

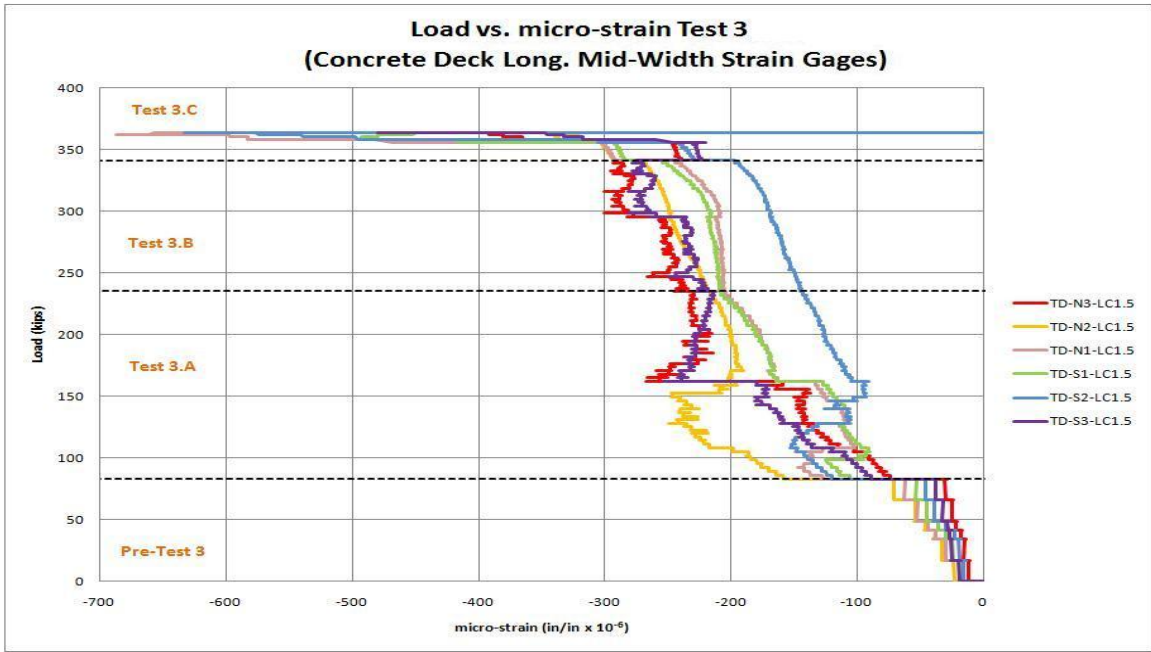


Figure 4-20b: Concrete deck longitudinal strain gages at the mid-width of the bridge during Test 3

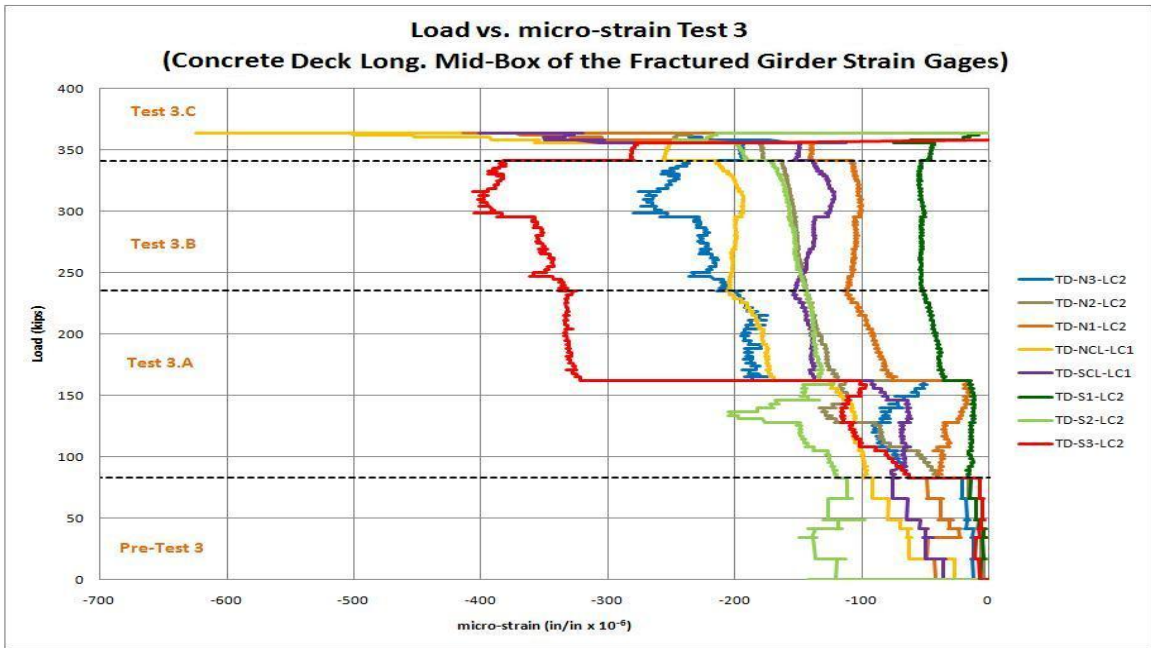


Figure 4-20c: Concrete deck longitudinal strain gages at the mid-box of the fractured girder during Test 3

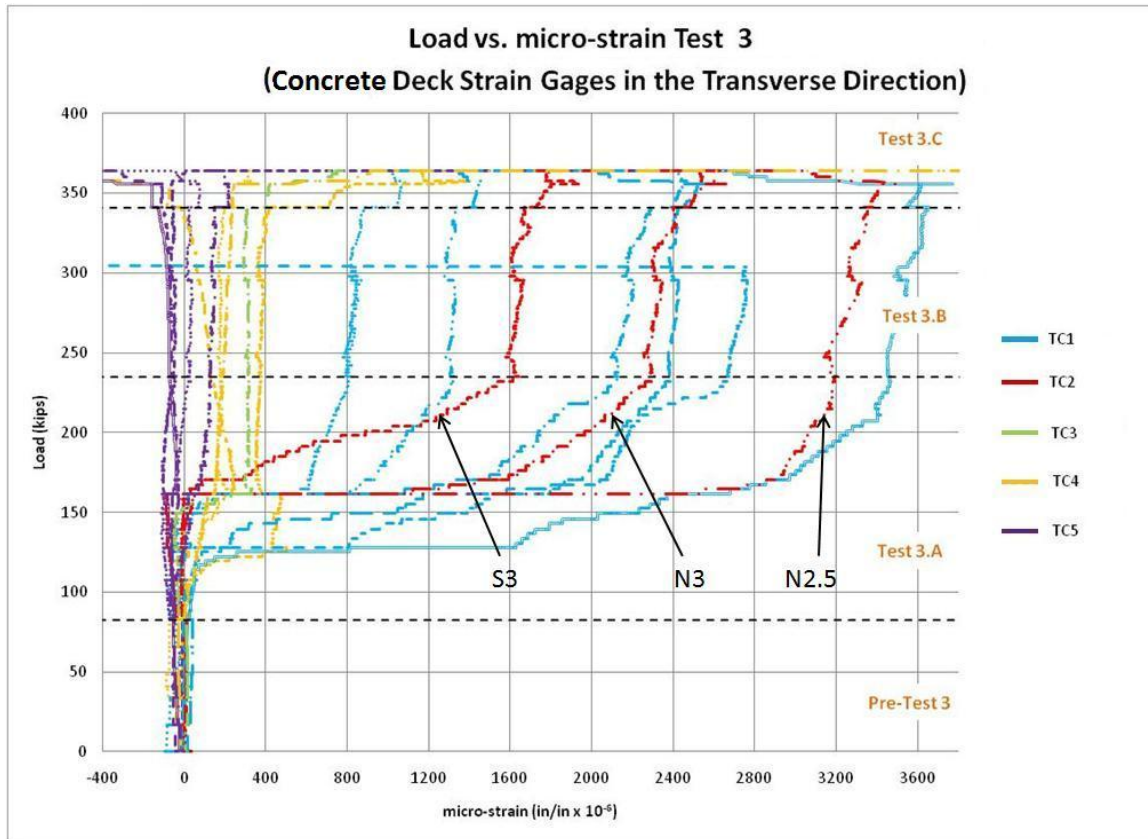


Figure 4-21: Concrete deck gages in the transverse direction during Test 3

The last two figures in this chapter (Figures 4-22 and 4-23) present strain values from the top and bottom reinforcement located at the interior top flanges of the girders. Due to the single curvature bending of the concrete deck across the width of the bridge (i.e., transversely to the bridge span), tension forces were expected to develop in the top mat reinforcement. High strain values were captured from the gages that were installed on the reinforcing bars at the location where the hinge formed (e.g., FR9 and FR10). This result was an indication that the reinforcement bars at these locations passed their yield limit.



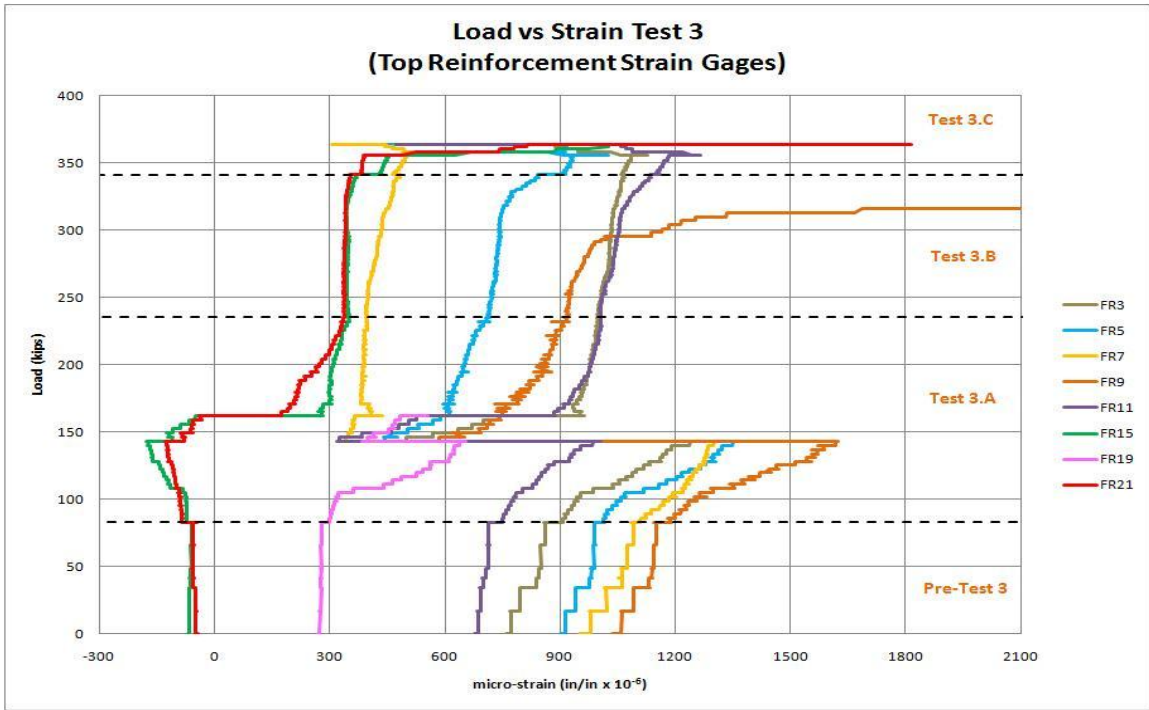


Figure 4-22: Top reinforcement strain gages during Test 3

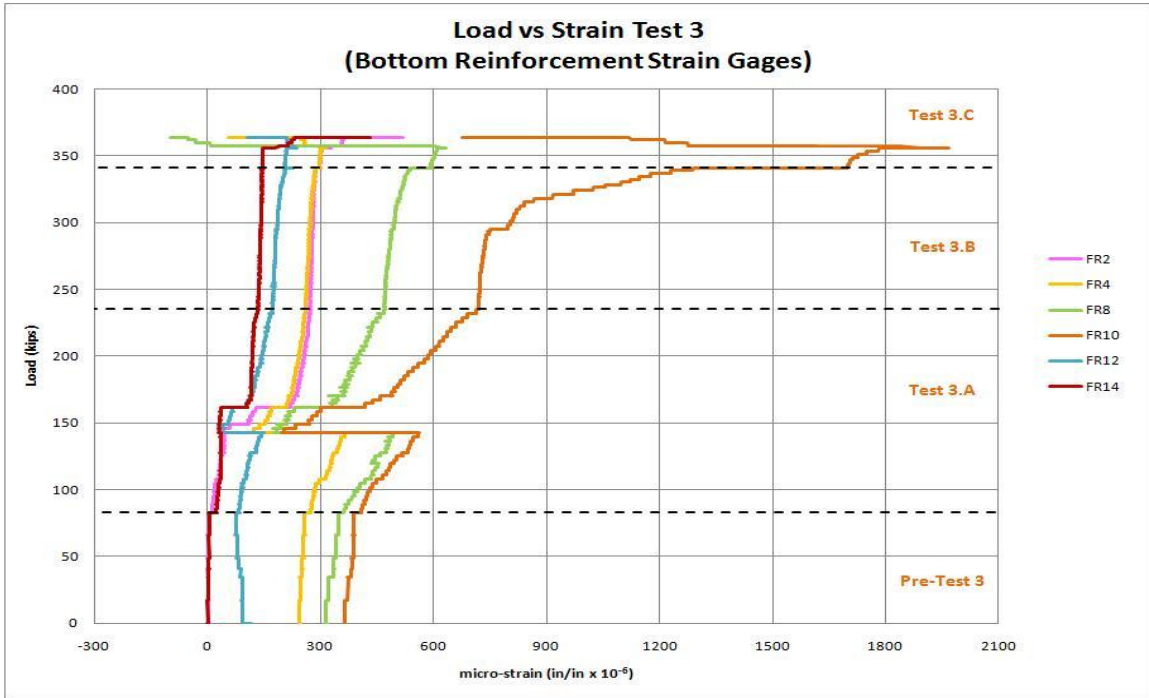


Figure 4-23: Bottom reinforcement strain gages during Test 3

### 4.3 SUMMARY

In this chapter, several observations from Test 3 were documented. A detailed analysis of the strain data has been presented in order to have an overall view of the bridge behavior and to identify the elements that resisted the applied loads.

The bridge was successfully loaded to collapse during Test 3. The loading procedure, which consisted of over 100 loading increments, added a total load of 363.75 kips or over 4.5 times the AASHTO design truck load to the already damaged bridge. The bridge was able to sustain this load before it collapsed. The east railing and the concrete deck provided a redundant load path that sustained the entire load, and the bridge collapsed after these members failed.

Once the railing at the centerline started to crush, the bridge began deflecting at a faster rate than it had prior to the crushing of the rail. The ultimate load carried by the bridge was reached after the railing section exhausted its moment capacity. A hinge line was initiated at the centerline of the span above the interior top flange of the intact girder and curved to the south and north expansion joints. The Yield Line Model was based on this hinge line shape to estimate the ultimate load that any bridge could sustain. The Yield Line Model is presented in the next chapter.

## CHAPTER 5

### Yield Line Model

#### 5.1 INTRODUCTION

Preliminary analysis of the bridge with the Simplified Strip Model indicated that the bridge would have failed at a lower load (126.4 kips) than the total applied load at the end of Test 3 (363.75 kips). After removing the road base material and the concrete blocks from the surface of the bridge, the cracking pattern of the concrete deck was revealed. Figure 5-1 shows an overall view of the damaged deck after Test 3. A hinge line formed over the interior flange of the intact girder at the centerline, and from that location, it curved and ended at the north and south expansion joints of the east railing (Figure 5-2). A simple yield line model was developed that captured the response observed from the test. The Yield Line Model developed is introduced later in this chapter.



Figure 5-1: Overall view of the damaged deck

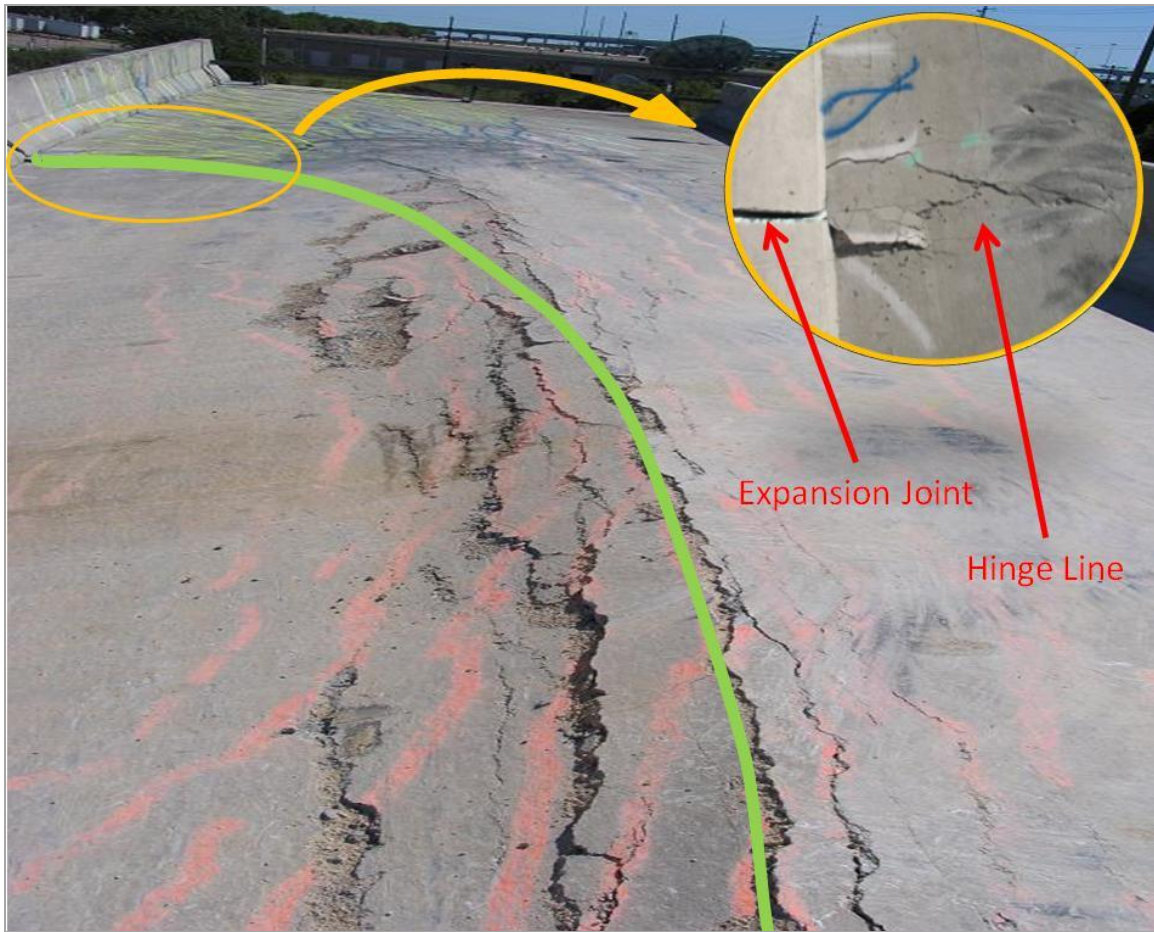


Figure 5-2 Hinge line on the concrete deck looking south

## 5.2 DEVELOPMENT OF THE YIELD LINE MODEL

The Simplified Strip Model does not take into account the three-dimensional action of the concrete deck. Based on observations during and after Test 3, it was decided to investigate whether a yield model would provide a more realistic estimate of the bridge behavior than the Simplified Strip Model when the shear studs do not have adequate tension capacity.

The development of the yield line model was initiated after completion of the tests on the FSEL test bridge. A detailed survey of the deck's top surface indicated that the failure in the deck followed the shape of a half-ellipse (Figure 5-3). A yield line pattern was developed using a combination of straight lines that provided a similar failure shape to the one observed on the test bridge. After investigating different yield line patterns to calculate the ultimate load, it was found that the optimum shape (Figures 5-4) consisted of straight lines lying on the perimeter of an ellipse along with two diagonals along diagonal interior fold lines. The results of the yield line analysis were in good agreement with the observed hinge locations in the deck. Thus, it was concluded that the assumed yield line shape could be used to estimate the ultimate load of the bridge.

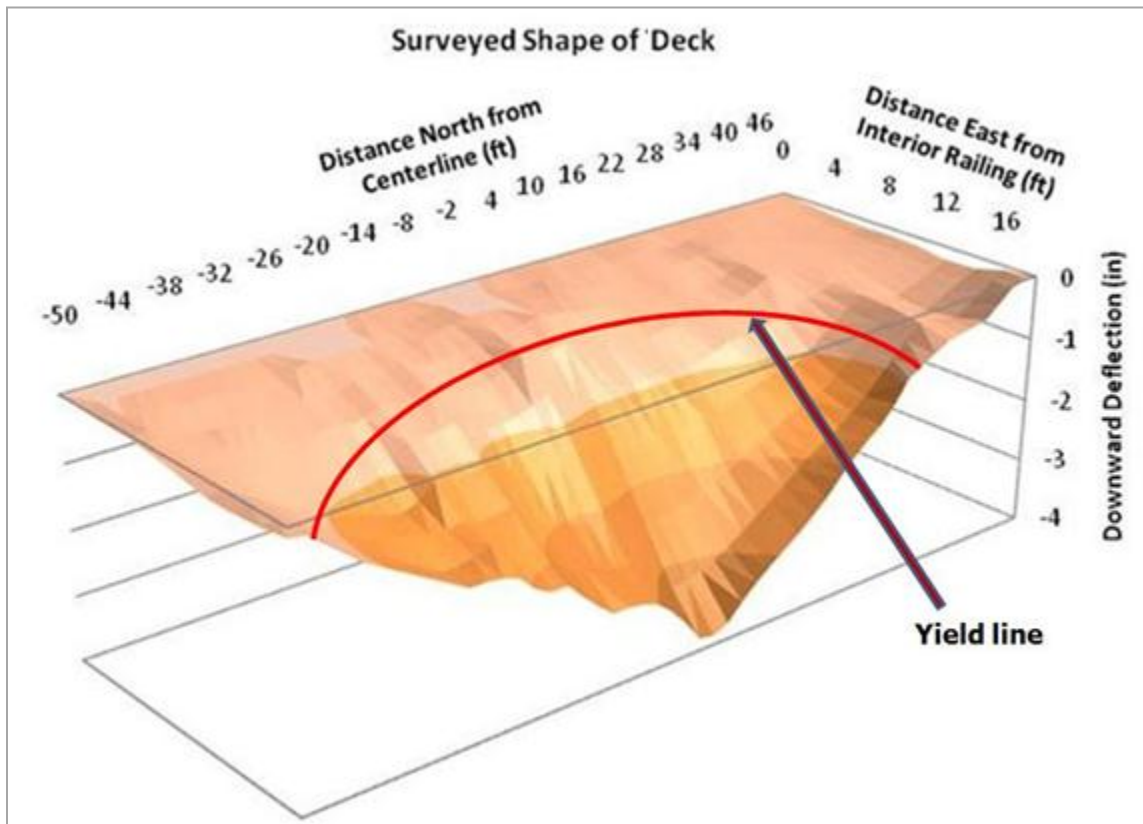


Figure 5-3: Observed yield line pattern

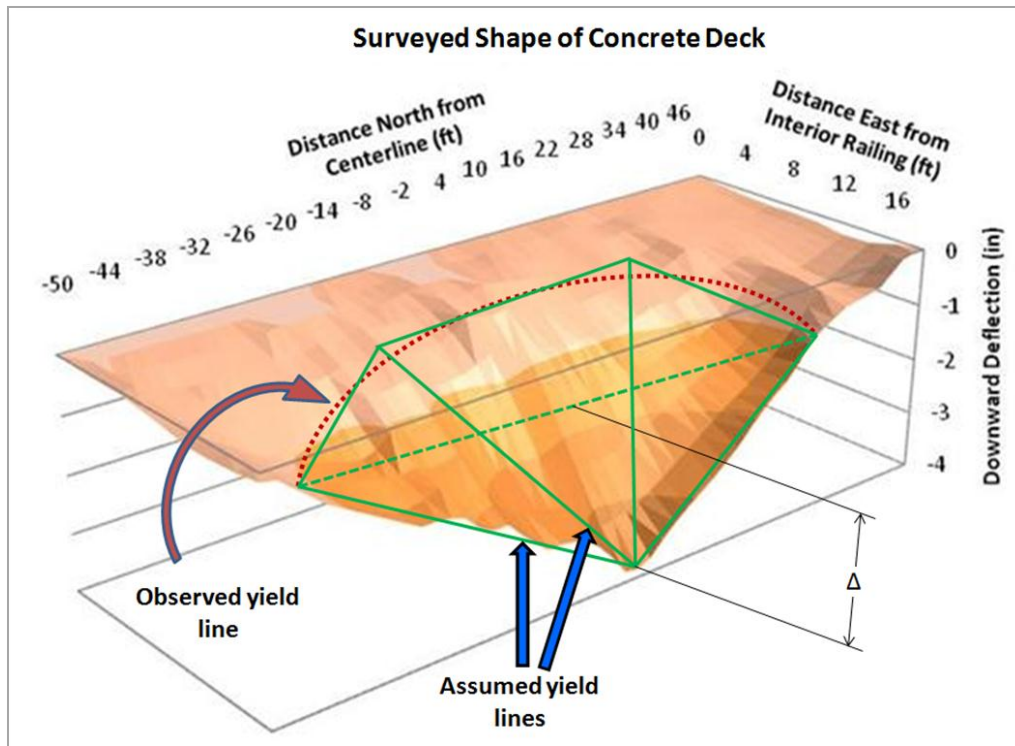


Figure 5-4: Assumed elastic plate displaced by a virtual displacement  $\Delta$

### 5.2.1 Description of the Yield Line Model analysis procedure

When a slab fails in flexure under overload conditions, the reinforcement at a region of high moment will yield first, and then a plastic hinge will form at this location in the slab. When that occurs, the slab is only able to sustain the hinging moment. The hinging region will rotate plastically with an increase of the load, and the moments associated with the additional load will be distributed to adjacent sections, eventually causing them to yield.

A yield line analysis was performed using virtual work principles which yielded an upper-bound solution to the problem. To implement the procedure, a yield line pattern was chosen, and a virtual displacement was introduced at the edge of the deck above the fracture in the girder (Figure 5-4). The principle of virtual work requires that the external

virtual work done by the external forces must be equal to the internal virtual work done by the internal forces of each element of a structure. The external virtual work is computed from the summation of the product of the externally applied forces multiplied by the virtual displacement at the load position, which was a function of the assumed virtual displacement. The total internal virtual work due to the virtual displacement is equal to the summation of the product of the bending moment developed at the segment of the yield line times the hinging rotation of each segment. The elastic moment and rotations were ignored with this approach, which was a reasonable assumption based on relative magnitude of the terms.

All the geometric parameters of the yield line pattern have to be defined before calculating the internal virtual work. It was assumed that a straight yield line would always initiate at the interior top flange of the intact girder, and it would extend to intersect with the inner diagonal yield lines (Figure 5-5). The yield line pattern was completed with two outer yield lines that started at the intersection of the straight line with the inner diagonal and extended diagonally to the edge of the concrete deck above the fractured girder (Figure 5-5). A series of parametric studies suggested that a minimum load solution resulted when the angle  $\varphi$  between the inner diagonal and the vertical axis was held constant and equal to  $55^\circ$ . The length  $a$ , which is the horizontal distance from point A or D to the origin, was determined by finding the value that produced the minimum truck load. It should be noted that the length  $a$  and the magnitude of the truck load are mutually dependant. Accordingly, one of these variables should be fixed to obtain the other one. It is recommended that the live load magnitude corresponding to the number of trucks be selected first; with this value set, the length  $a$  for the given load magnitude can be obtained. If a valid solution for the length  $a$  is computed, the given truck load is a possible failure loading. In subsequent iterations, the truck load should be decreased until a valid solution for  $a$  no longer exists. The minimum truck load is the last one that gave a physically admissible solution for the length  $a$ . In contrast, if the initially chosen truck load does not provide a physically admissible solution for the length  $a$ , then the truck load needs to be increased in subsequent iterations. Once the length  $a$  has been

determined, all the coordinates of the yield line end points can be defined to calculate the variables used to compute the virtual work. These coordinates were calculated by applying fundamental trigonometric relationships. In the case of a bridge with significant horizontal curvature, the coordinates of points A and B would be affected. Adjustments should be made to account for the angle  $\theta$  (Figure 5-5).

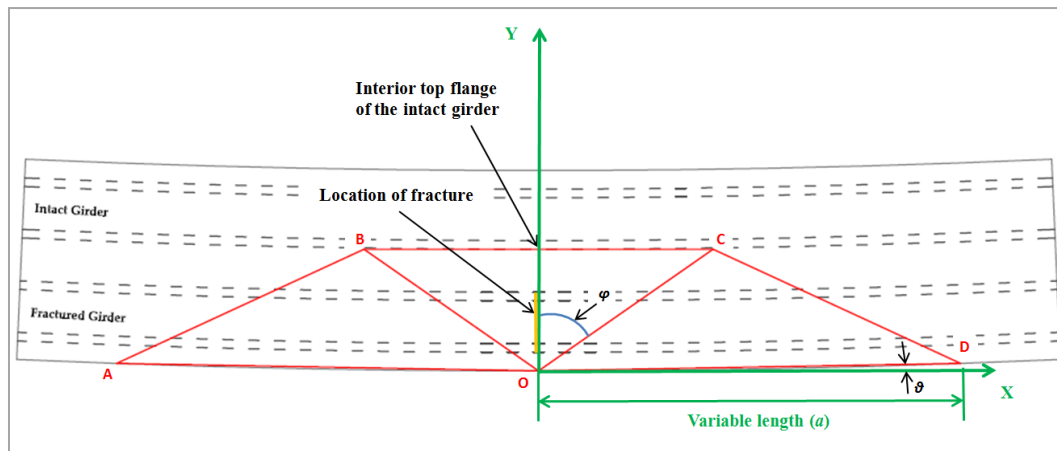


Figure 5-5: Parameters of the yield line pattern

The angle  $\theta$  is given by Equation 5-1:

$$\theta = \sin^{-1}(a / 2 \cdot R) \quad (\text{Equation 5-1})$$

where  $a$  (ft) is the horizontal distance of the point A or D from the origin, and  $R$  (ft) is the bridge's radius of curvature. Radians should be used as units when  $\sin^{-1}(a / 2 \cdot R)$  is calculated.

The bending capacity varied along the yield line due to the fact that the reinforcement in the deck was not normal to the yield line. If the yielding occurred along a line at an angle  $\alpha$  to the reinforcement mat (Figure 5-6), the resultant bending capacity ( $m_b$ ) could



be calculated by inserting the bending capacities of the two directions ( $m_x$ ,  $m_y$ ) in Equation 5-2 [Wight, MacGregor,(2008)]

$$m_b = m_x \sin^2 \alpha + m_y \cos^2 \alpha \quad (\text{Equation 5-2})$$

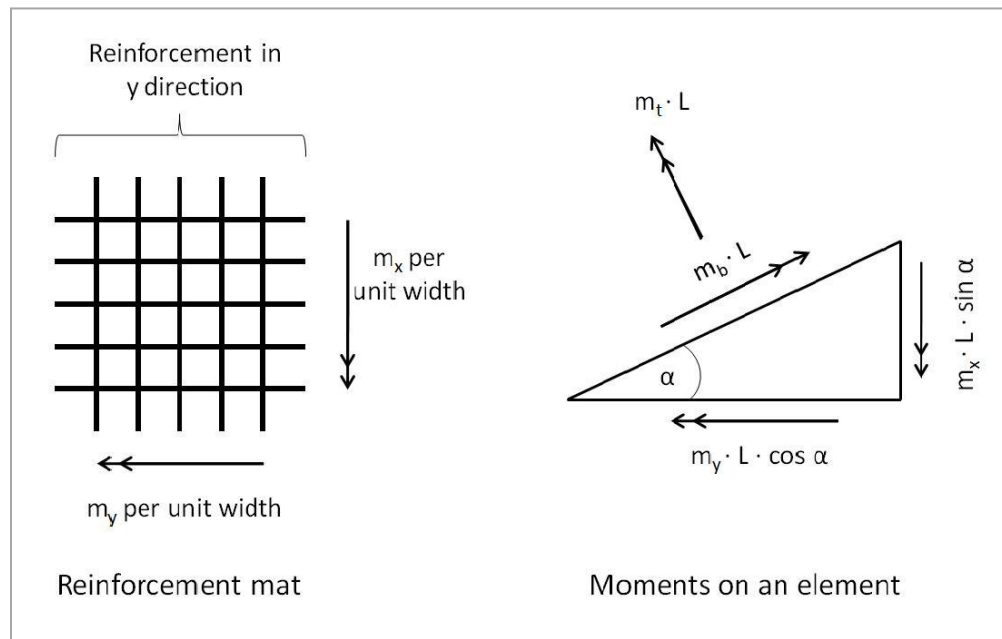


Figure 5-6: Bending moment along a yield line at an angle  $\alpha$  [Wight, MacGregor]

In the case of the straight line and the inner diagonals, the bending moment capacities can be readily calculated because the angle  $\alpha$  is equal to  $0^\circ$  and  $35^\circ$ , respectively. The bending moment capacity of the outer diagonals, however, is a function of the length  $\alpha$ ; consequently, an expression to define  $\alpha$  is needed. Equation 5-3 can be used to determine the angle  $\alpha$  of the outer diagonals.

$$\alpha = \tan^{-1}\left(\frac{X_j - X_i}{Y_j - Y_i}\right) + \frac{\pi}{2} \quad (\text{Equation 5-3})$$

where  $(X_i, Y_i)$  and  $(X_j, Y_j)$  are the coordinates of the end points of the outer diagonals. For any other case that the reinforcement is not oriented as shown in Figure 5-6, the angle  $\alpha$  should be determined based upon the orientation of the reinforcement.

In order to calculate the internal virtual work done by the concrete deck, the parameters needed are 1) the length of each line and 2) the angle of rotation of each plate. First, the length of each line can be calculated using the distance formula (Equation 5-4). Knowing the coordinates of each yield line's endpoints, the length of the line is equal to

$$l = \sqrt{(X_j - X_i)^2 + (Y_j - Y_i)^2} \quad (\text{Equation 5-4})$$

where, as before,  $(X_i, Y_i)$  and  $(X_j, Y_j)$  are the coordinates of the end points of the yield line.

Second, the angle of rotation of each plate can be calculated by evaluating the geometry of the displaced shape corresponding to the assumed yield line pattern. The angle between two planes is given by the angle between the normal vectors. For example, if  $3x - 2y + 5z = 1$  and  $4x + 2y - z = 4$  are the equations that define two planes, the angle between these planes can be determined as follows:

- i. The two normal vectors are  $n = \langle 3, -2, 5 \rangle$  and  $m = \langle 4, 2, -1 \rangle$
- ii.  $n \cdot m = 3 \cdot 4 - 2 \cdot 2 - 5 \cdot 1 = 3$
- iii.  $\|n\| = \sqrt{3^2 + (-2)^2 + 5^2} = \sqrt{38}$ ,  $\|m\| = \sqrt{4^2 + 2^2 + (-1)^2} = \sqrt{21}$
- iv. Hence, the angle is equal to  $\theta_{\text{Rotation}} = \arccos\left(\frac{3}{\sqrt{38} \cdot \sqrt{21}}\right) = 1.46 \text{rads}$

Having all the parameters defined, the internal virtual work of each line with length  $l$  can be calculated as the product of  $dIW = m_b \cdot l \cdot \theta_{Rotation}$ .

As mentioned in previous chapters, the railing plays a significant role in contributing to the redundancy of a bridge, and, for this reason, the virtual work done by the railing should be included in the total internal virtual work calculation. As the bridge deflects downwards, the railing acts as an inverted beam and tries to resist the bending of the bridge in the longitudinal direction. The moment acting on the railing will depend on the type of railing (continuous or with expansion joints) and the location that the hinge line intersects the railing. Figure 5-7 illustrates the moments acting on the railing that should be included in the calculation of internal virtual work. The work done by the railing is equal to the moment capacity of the railing times the angle of rotation. In the case of positive moment capacity, the angle of rotation of the railing is two times the angle between the ABO and CDO planes (Figure 5-5); the angle of rotation for the negative moment capacity is equal to the angle of the ABO (or the CDO) plane with the horizontal.

To ensure that the railing section can reach its moment capacity, the connection between the railing and the deck must have sufficient reinforcement to transmit the shear associated with flexure. The maximum shear force at the connection is equal to the compressive force applied to the railing section when the positive moment capacity is calculated. The positive moment capacity is calculated using the railing section and assuming that, at the level of the concrete deck below the railing, there is reinforcement equal to the reinforcement area existing in the effective deck width. The effective deck width can be computed according to Section 4.6.2.6 of the AASHTO LRFD Specification (2007). According to the specification, the effective width can be determined using Figure 4.6.2.6.2-2 (AASHTO, 2007), where  $b$  is equal to the distance from the edge of the concrete deck above the fractured girder to the interior top flange of the intact girder, and  $l_i$  is the length of railing between expansion joints. In the case that the railing is

continuous,  $l_i$  should be taken as the total length of the span. Under no circumstances can the effective width be taken as greater than  $b$ .

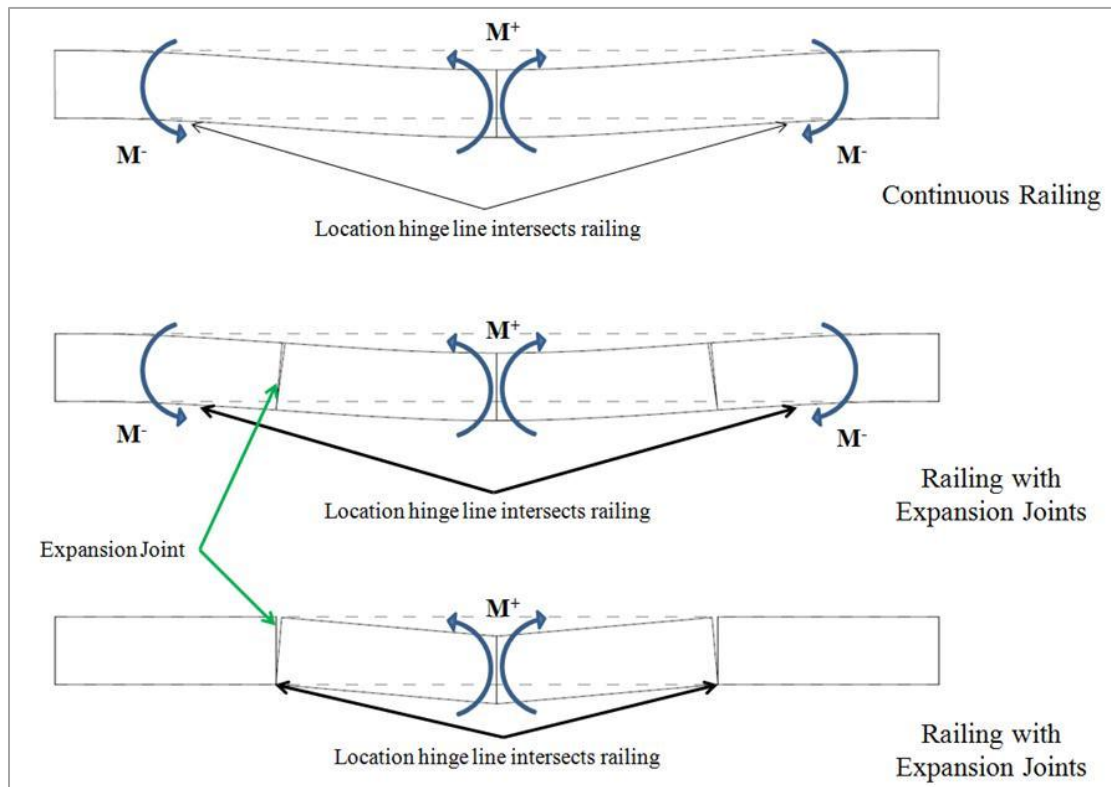


Figure 5-7: Acting moments on the railing for different cases

The assumption to include the reinforcement within the effective deck width is supported by the railing behavior observed in the full-scale bridge test conducted at FSEL. The railing failed by crushing of the concrete in a manner that is similar to the failure of an over-reinforced concrete section. It is suspected that as the deck deflected downward under increasing increments of load, catenary behavior of the concrete deck engaged more and more reinforcement over the width of the deck. Thus, the catenary behavior increased the tension in the reinforcing bars that were embedded over an

effective width, and the amount of reinforcing steel engaged in this response led to behavior representative of that corresponding to an over-reinforced section. The results of the additional tension in the deck reinforcement led to the crushing observed in the railing. The effective width of the concrete deck included in the rail strength calculation is intended to capture this behavior. However, the effective width obtained from Section 4.6.2.6 of the AASHTO LRFD Specification (2007) is smaller than the observed one. Accordingly, the effective width is computed in such a way as to ensure a conservative solution.

The external virtual work consists of the work done by the truck load and the dead load of the bridge. The truck load should be positioned at the location where it produces the largest positive bending moment. In the case of a simply supported bridge, the maximum positive bending moment can be achieved when the middle axle of an HS-20 truck is located at the mid-span of the bridge. In the case of a continuous bridge, however, the location of the middle axle should coincide with the location of the highest positive moment. The location of highest positive moment can be obtained from the moment envelope diagram for a combination of dead load and moving truck load. Moreover, the distance between the exterior and the middle axles should be kept constant and equal to 14 ft. Regarding the position of the truck across the width of the bridge, it is suggested that the wheels on one side of the truck be positioned 2 ft away from the railing. Once the position of the truck is set, the work done by the truck load can be computed. This work is equal to the summation of each point load multiplied by the deflection of each location. The deflection of each location, however, is a function of the length  $a$ . The deflection of the wheel loads of an HS-20 truck load can be determined by using the ratio of congruent triangles (Equation 5-5).

$$\delta_{load} = r_{load} \cdot \Delta / r \quad (\text{Equation 5-5})$$

In this equation,  $\delta_{load}$  is the deflection at the load location,  $r_{load}$  is the distance of the load location from the edge of the slab above the fracture,  $\Delta$  is the virtual displacement, and  $r$  is the distance of a point on the yield line with the same angle  $\beta$  from the positive  $x$ -axis as the load position (Figure 5-8). Having determined the coordinates of the truck wheels,  $r_{load}$  can be computed using the Pythagorean Theorem. All the terms of Equation 5-5 are known except for  $r$ . The length of  $r$  can be determined as follows:

- i. For a given angle  $\beta$ , the equation of the line passing through the origin and the point load can be defined.
- ii. Knowing the coordinates of the outer diagonal yield line endpoints (A and B, C and D), an equation of the line can be derived.
- iii. The  $x$ -coordinate of the intersection can be found by setting equal the  $y$ -coordinate of the two equations and then inserting the known  $x$ -coordinate into the one of the equations to obtain the  $y$ -coordinate.
- iv. Finally, the length  $r$  can be computed using the distance formula between the origin and the intersecting point.

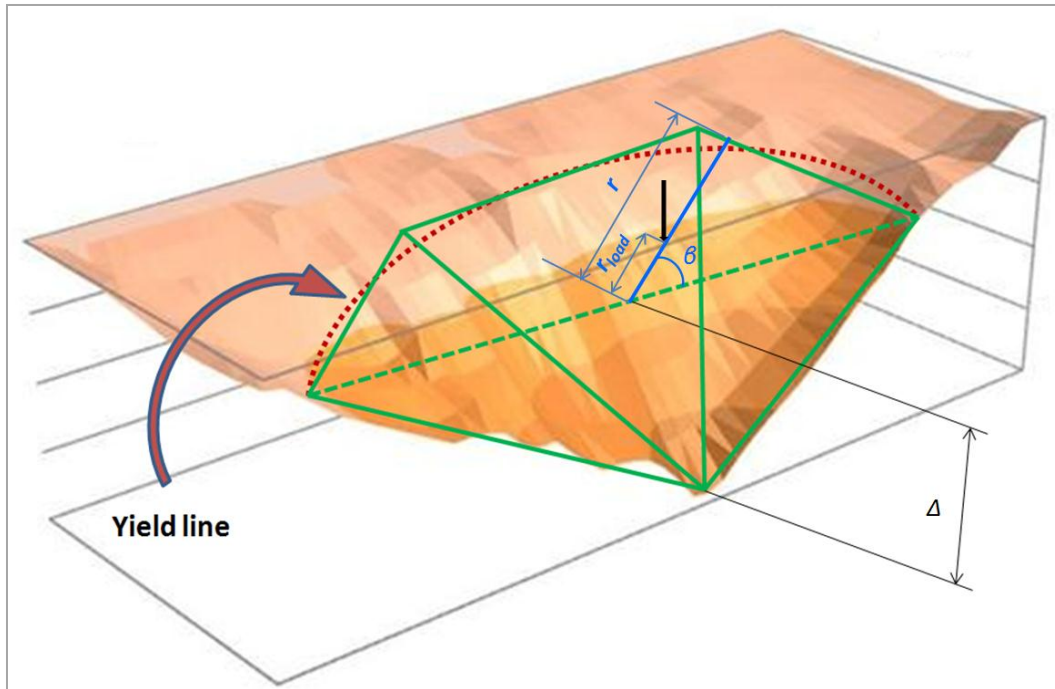


Figure 5-8: Defining the deflection at the load location

The work done by the dead load of the bridge should be included in the external virtual work calculation. Only the self-weight of the concrete deck and the railing inside the failure area should be included. As indicated previously, it is appropriate to use the Yield Line Model when the fractured girder is separated from the concrete deck. Consequently, the self-weight of the fractured girder is not included in the external virtual work calculation. The external work done by the railing is computed using (Equation 5-6):

$$EW_{RAILING} = A_{Railing} \cdot 2 \cdot a \cdot 0.15 \cdot \Delta / 2 \quad (\text{Equation 5-6})$$

where  $A_{Railing}$  (ft<sup>2</sup>) is the cross-sectional area of the railing,  $a$  (ft) is the horizontal distance from the point A or D to the origin, and  $\Delta$  is the virtual displacement. The factor 0.15 is

used to account for the assumed self-weight of reinforced concrete ( $150 \text{ lb/ft}^3 = 0.15 \text{ kips/ft}^3$ ).

In a similar way, the external work done by the concrete deck can be computed by Equation 5-7 and 5-8. Equation 5-6 is used to compute the work done by the middle triangle (i.e., BOC in Figure 5-5)

$$EW_{DECK \text{ MID-TRINGLE}} = 1/2 \cdot l \cdot h \cdot t \cdot 0.15 \cdot \Delta/3 \quad (\text{Equation 5-7})$$

where  $l$  (ft) is the length of the yield line lying above the interior top flange of the intact girder (BC),  $h$  (ft) is the height of the triangle BOC and is equal to the distance from centerline of the interior flange of the intact girder to the edge of the flange,  $t$  (ft) is the thickness of the concrete deck, and  $\Delta$  is the virtual displacement. Once again, the factor 0.15 accounts for the self-weight of reinforced concrete, which was assumed to be  $150 \text{ lb/ft}^3 = 0.15 \text{ kips/ft}^3$ . Additionally, the work done by the outer triangles (i.e., AOB and COD) can be approximated using Equation 5-8.

$$EW_{DECK \text{ OUT-TRINGLE}} = 1/2 \cdot a \cdot h \cdot t \cdot 0.15 \cdot \Delta/3 \quad (\text{Equation 5-8})$$

where  $a$  (ft), as before, is the horizontal distance from point A or D to the origin and  $\Delta$  is the virtual displacement. Equation 5-8 is accurate for a straight bridge; as the curvature and the length  $a$  increase, however, this expression overestimates the work done by the outer triangles because the areas of these triangles become smaller. An accurate expression for the work done by the outer triangles can be obtained if the term  $a$  in Equation 5-8 is replaced with  $l_{CD}$  or  $l_{AB}$  from Equation 5-4, and  $h_i$  is calculated according to Equation 5-9.



$$h_i = \left| \sqrt{X_i^2 + Y_i^2} \cdot \sin(\theta_i + \alpha_i) \right| \quad (\text{Equation 5-9})$$

where  $X_i$ ,  $Y_i$  are the coordinates of point D,  $\theta_i$  is the angle measured from the positive  $x$ -axis to line OD, and  $\alpha_i$  is the angle of the yield line DC obtained from Equation 5-3 (Figure 5-9). The heights of the outer triangles are equal due to symmetry (i.e.,  $h_{COD} = h_{AOB}$ ). Additional details of this implementation are provided in the examples that appear in the Appendix.

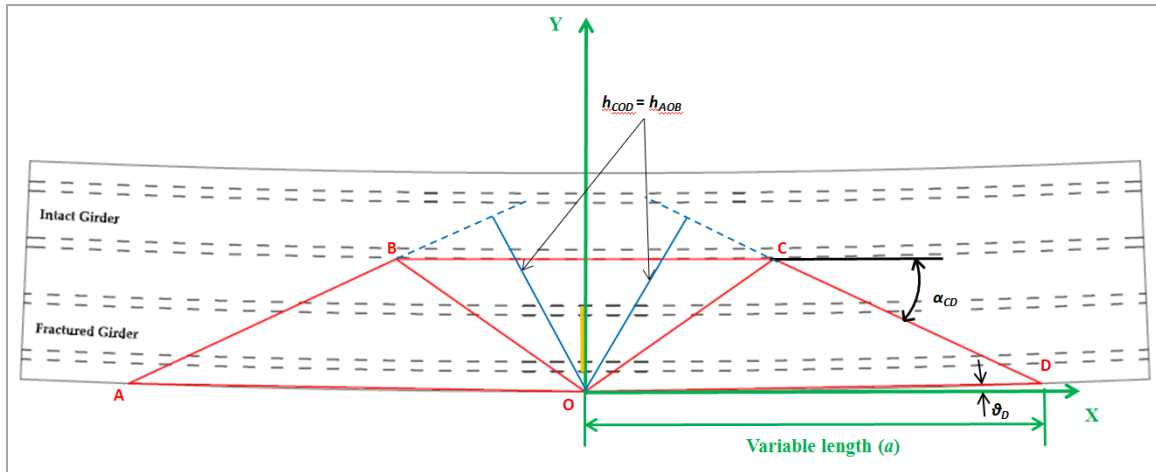


Figure 5-9: Geometric parameters of Equation 5-8

### 5.2.2 Yield Line Model analysis results of the FSEL bridge

The Yield Line Model was successfully applied to the FSEL test bridge. Applying an HS-20 truck load to the bridge at the most severe location, the ultimate load was computed to be  $3.91 \times$  HS-20 Trucks or 281.9 kips for  $f'_c = 6.26$  ksi, which was the measured strength of the deck. The ultimate load was computed to be  $3.66 \times$  HS-20 Trucks or 263.84 kips for  $f'_c = 4.00$  ksi, which was the specified design strength of the

deck. The total estimated capacity of the test bridge using an HS-20 truck loading is less than the actual load carried by the bridge—363.0 kips—for two reasons. First, the wheel loads of the truck used in the analysis produce a larger moment than that produced by the road base that was distributed over a portion of the deck during the test. Second, the positive moment capacity of the railing used in the analysis was smaller than the actual capacity due to the conservative assumption used to estimate the width of the deck participating with the railing. This approach was taken to obtain a conservative solution. The area of the tension reinforcement bars in the effective width appears to be greater than what was assumed for the analyses in order to produce the crushing failure observed in the test.

### **5.3 SUMMARY**

The underestimation of the ultimate load by the Simplified Strip Model does not make it invalid. In fact, the Simplified Strip Model serves a different purpose than the Yield Line Model, and each simple analysis procedure can provide useful information. An engineer should first analyze a bridge for redundancy using the initial strength checks to identify if the unsupported loads can be transferred to the intact girder. If failure of the shear studs is computed, the Yield Line Model should be used to estimate the ultimate load that the bridge can sustain.

All the results presented above are in a good agreement with the test results of the FSEL test bridge, which indicates that the Yield Line Model successfully estimates the ultimate load that a bridge can sustain. Nonetheless, the Yield Line Model and the Simplified Strip Model should be compared with the finite analysis results that are currently ongoing [Kim (2010)]. Depending on the outcome of the comparison, future refinement of the simple models might be needed.

## CHAPTER 6

### Conclusions and Recommendations

#### 6.1 PROJECT SUMMARY

The twin box-girder bridge is a preferable type of bridge in Texas and it is usually used at flyover intersections. This type of bridge is aesthetically pleasing due to its slenderness and the shape of the girders. However, the AASHTO Bridge Design Specifications categorize the twin box-girder bridge as a fracture critical bridge. Because there are only two bottom flanges in tension, the AASHTO Specifications assume that a failure of a component in tension (bottom flange) will result in the collapse of the bridge or the inability of the bridge to perform its function. A fracture critical bridge is required to be bi-annually inspected. The cost of an inspection is very high, especially when consideration is given to the indirect costs incurred by displaced motorists who depend on the inspected bridge. The high cost of inspection is the main drawback of an otherwise efficient and aesthetically appealing design.

Several observations of fracture critical member failures on in-service bridges have indicated, however, that the overall behavior of a fracture critical bridge is not always governed by the fracture of its critical members. These observations have made the bridge owners question the fracture critical provisions, asking for different inspection levels depending on the bridge characteristics.

The Texas Department of Transportation and the Federal Highway Administration co-sponsored a research project at the Ferguson Structural Engineering Laboratory at The University of Texas at Austin. The main goal of the research program was to investigate the behavior of twin box girder fracture critical steel bridges and to develop methods for evaluating their redundancy level in the event that a fracture occurs in a critical member. The research project included the reconstruction of a full-size twin box girder bridge, which was used as a test specimen for three destructive tests. Laboratory experiments were performed to investigate the tensile capacity of several shear stud connection

configurations between the steel girder and the concrete deck. Several analyses were performed based on simple models and computer simulations. All the information gathered from the three full-size tests as well as the laboratory tests helped the calibration of the analysis models.

## **6.2 FSEL BRIDGE BEHAVIOR DURING TESTS**

As described in earlier chapters, the performance of the FSEL test bridge was very good during all the tests. The test bridge had alternative load paths to transmit the load positioned above the fractured girder to the intact girder. Several different load paths provided a high level of redundancy to the bridge so that it could sustain very high loads while still having a full-depth fracture in one of its girders. For Test 2, when the bridge was dynamically tested with a full-depth fracture in one of its girders and a load of 75 kips placed in the most critical location, the performance of the structure was excellent. The overall damage was limited, making it possible for a driver to safely drive over the bridge. When the test-bridge was statically tested in Test 3, it was able to sustain more than four times the design truck load before collapsing.

The railing above the fractured girder played a significant role in the post-fracture behavior of the FSEL test bridge. As mentioned earlier in this thesis, the railing acted as an inverted beam and transferred a portion of the load, which was first carried by the fractured girder, back to the supports. When the expansion joint in the railing engaged, the downward deflection was arrested. During Test 3, when the railing above the fracture location reached its moment capacity, the test bridge started to deflect at a higher rate than it had prior to then until it eventually collapsed. The locations of the north and the south expansion joints were weak spots in the bridge sections, and shear failures occurred in the concrete deck at these locations.

The concrete deck acted as a shear diaphragm, and it played a major role in transferring loads away from the fracture location. A hinge line formed on the concrete deck as described in Chapter 5, which occurred due to the moment capacity being exceeded. The formation of the hinge line did not prevent the deck from continuing to transfer loads away from the fracture location.

### **6.3 SIMPLIFIED MODELS**

Simplified analytical modeling methods to evaluate the redundancy level of a bridge are proposed in this thesis. Chapter 3 and Chapter 5, respectively, contain descriptions of the initial strength checks and the Simplified Strip Model, and the Yield Line Model. These simplified methods provide a quick and conservative estimation of the ultimate load that a twin box-girder bridge can sustain.

The initial strength checks can be used to determine any possible failures and ensure that the unsupported load can be transferred away from the fracture girder. The Simplified Strip Model can be used by an engineer to determine whether or not deck failure or shear stud pullout has occurred and what is the extent of the damage. If the initial strength checks indicate a failure of shear studs, then the Yield Line Model should be used to estimate the ultimate load that a bridge could sustain. However, in the case of a hinge forming at the interior top flanges of both girders, then the Simplified Strip Model can be used to estimate the ultimate load.

### **6.4 RECOMMENDATIONS**

The major goal of this research project was to determine methods for evaluating the redundancy level of fracture critical bridges, with an emphasis on twin box-girder bridges. All the tests performed during this research program provided significant information on the performance of the FSEL test bridge. Even if the test bridge is a

representative type of bridge that is widely used in Texas, the results of these tests cannot directly be extrapolated for all twin box-girder bridges. The FSEL test bridge consisted of a single supported span, while in practice these bridges are usually multi-span, continuous bridges. Continuous-span bridges have “built in” redundancy compared to simple-span structures and are expected to perform better than these less redundant structures. Therefore, the results of the FSEL bridge are more conservative than what is expected for a multi-span bridge. Analysis of multi-span bridges was limited in this study, and further investigation of multi-span structures is recommended.

The type of railing used in the FSEL test bridge was a T501 concrete railing. This type of railing has a stocky concrete section that can act as an inverted beam in the event of a fracture. However, a large variety of traffic railings are used on existing bridges. If the contribution of the railing is taken into account, questions on the bridge behavior will be raised if a different type of railing is used. Both the simple models developed in this research indicate the importance of the railing in providing redundancy. A bridge with a continuous railing and a section similar to the T501 railing will deflect less under the same load than the same bridge with a discontinuous railing or with smaller railing section. Smaller deflections will result in less extensive failure predicted by the Simplified Strip Model than cases where larger deflections occur. It is important to note that the Yield Line Model indicates that almost one third of the internal work comes from the railing. Therefore, in the case of a railing with a smaller section, the ultimate load will be less than the ultimate load of a stocky railing section. Based on these observations, it is highly recommended that a continuous railing with a section similar to the T501 railing be used on fracture critical twin box girder bridges.

Regarding the thickness of the concrete deck and the height of the shear studs, several recommendations are given. It is recommended that shear studs having a height long enough to pass the bottom reinforcement layer of steel be used. Laboratory tests [Sutton, (2007), Mouras (2008)] have shown that if the shear studs pass the bottom reinforcement, the redundancy of the connection is improved. Moreover, the laboratory tests indicate

that by increasing the length of the shear studs, their tensile capacity increases. However, if the shear studs have enough capacity to resist the event of the fracture, the concrete deck will reach its moment capacity, and a hinge line will form at the interior top flanges of the girders. It is more desirable to form of a hinge in the concrete deck than to have a shear stud failure. The hinge formation, compared to the shear stud failure, is more ductile. Furthermore, after the formation of a hinge, loads could still be transmitted away from the fracture. Equation 6-1 determines the minimum tensile capacity of the shear studs to form hinges in the concrete deck between the girders. A higher tensile capacity of the shear studs than that calculated by Equation 6-1 will not provide any additional benefit because the moment capacity of the concrete deck will govern. Conversely, the design of a thicker deck between the two girders may result in a shear stud pull out. It is highly recommended that the design be based on a balanced section in which the shear studs will fail just after the formation of hinges at both the interior top flanges.

$$P_{min} = (M_n^+ + M_n^-)/s \quad \text{(Equation 6-1)}$$

where:  $P_{min}$  = Minimum tensile capacity of shear stud group to form a hinge at the deck

$M_n^+$  = Positive moment capacity of the concrete deck

$M_n^-$  = Negative moment capacity of the concrete deck

$s$  = Distance between the two girders

The FSEL test bridge had a very small horizontal curvature. In-service twin box-girder bridges can be designed with a significantly higher horizontal curvature than that of the test bridge. The increase of the radius of curvature increases the torsion on the bridge, which must be resisted by the intact girder in the event of a fracture of a critical tension flange. Simple equations to compute the torque applied on the intact girder were given in Chapter 3. Moreover, the result of an increase in curvature on the behavior of a twin box-girder bridge is under investigation through parametric finite element analyses,

and it will be presented in the dissertation by Kim [Kim, (2010)]. In addition to the consequences of the horizontal curvature, the effects of several variables, like number of spans, type of railing, material properties and geometry of the bridge, are currently being investigated by Kim [Kim, (2010)].



## APPENDIX A

### Analysis of bridge components

#### A.1 CALCULATION OF THE INTACT GIRDER'S MOMENT DIAGRAM

The assumed elastic section was one-half of the bridge section. Details of the elastic section, such as dimensions, based on which all the calculations were performed as well as typical strain and stress gradients (e.g. Section N3), are shown in Figure A-1.

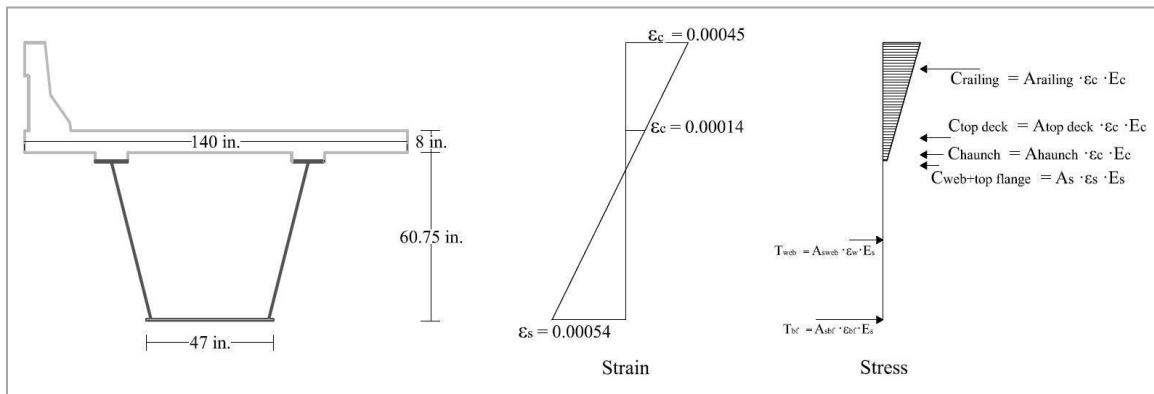


Figure A-1: Elastic section of the intact girder used for the moment diagram calculation.

Originally, the actual static strain values of Test 2 were used to calculate the forces that were applied at the section. The calculated forces, which were applied at the section, were not balanced. Due to the fact that the measured strain values contained errors, the forces of the section were not in equilibrium. To resolve this problem, it was decided on to keep the bottom flange strain constant and equal to the measured value and to change the strain values of top deck so that the forces could be balanced. As it is illustrated in Figure A-2, the recorded and the calculated strain values were close to each other ( $\epsilon_{recorded} = -0.00017$ ,  $\epsilon_{calculated} = -0.00019$ ), so the assumption was reasonable.

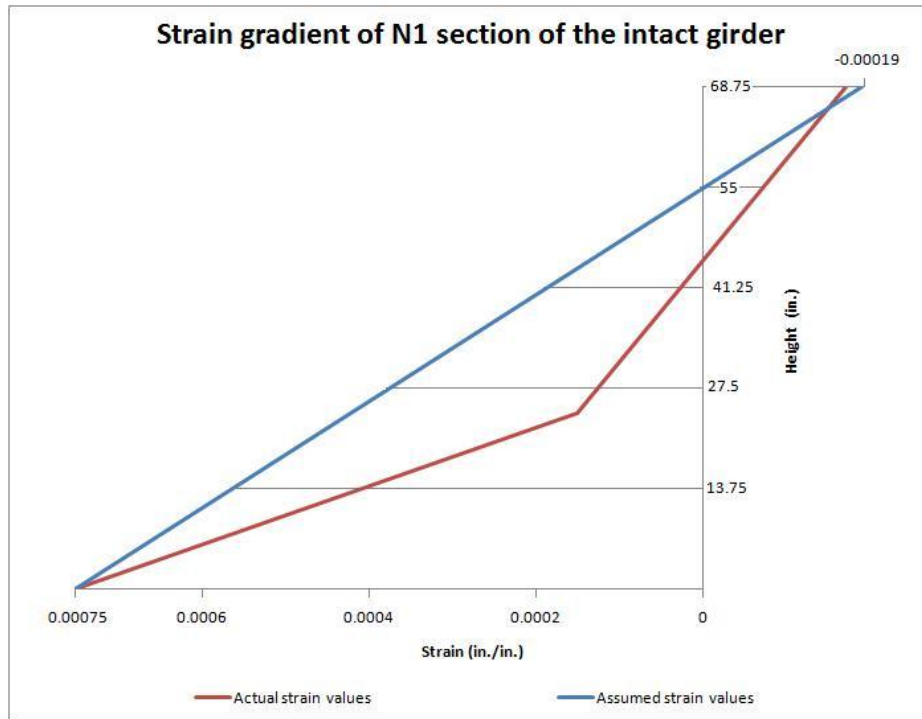


Figure A-2: Strain gradient of N1 section of the intact girder

The values at the top surface of the railing were extrapolated from the other data points. The concrete strength was taken as 6.26 ksi based on lab tests. The structural steel for the webs and flanges of the steel box girders was assumed to be ASTM A572 Grade 50 ksi based on TxDOT drawings.

The forces applied on the elastic section, after calculating the appropriate strain values so that they would be balanced, were:

$$C_{Railing} = 0.5 \cdot (\epsilon_{Railing\ Top} + \epsilon_{Railing\ Bottom}) \cdot h \cdot b \cdot E_c = 0.5 \cdot (-0.00059) \cdot 32 \cdot 9.72 \cdot 4560 = -414.88 \text{ kips}$$

$$C_{Deck} = 0.5 \cdot (\epsilon_{Deck\ Top} + \epsilon_{Deck\ Bottom}) \cdot h \cdot b \cdot E_c = 0.5 \cdot (-0.00019) \cdot 8 \cdot 140 \cdot 4560 = -490.67 \text{ kips}$$

$$C_{Reinforcement} = A_s \cdot (\epsilon_{Reinf\ Top} + \epsilon_{Reinf\ Bottom}) \cdot E_s = 2 \cdot 7.23 \cdot (-0.00009) \cdot 9000 = -38.77 \text{ kips}$$

$$C_{Haunch}=2 \cdot 0.5 \cdot (\epsilon_{Haunch Top} + \epsilon_{Haunch Bott.}) \cdot h \cdot b \cdot E_c = 2 \cdot 0.5 \cdot (-0.00009) \cdot 2.86 \cdot 12 \cdot 4560 = -13.31 \text{ kips}$$

$$C_{Top Flange}=2 \cdot \epsilon_{Top Flange} \cdot h \cdot b \cdot E_s = 2 \cdot (-0.00003) \cdot 9.625 \cdot 12 \cdot 29000 = -12.58 \text{ kips}$$

$$C_{Web}=2 \cdot 0.5 \cdot A_s \cdot \epsilon_{Web} \cdot E_s = 0.99 \cdot (-0.00002) \cdot 29000 = -0.56 \text{ kips}$$

$$T_{Web}=2 \cdot 0.5 \cdot A_s \cdot \epsilon_{Web} \cdot E_s = 27.11 \cdot (0.00053) \cdot 29000 = 418.75 \text{ kips}$$

$$T_{Bottom Flange}=A_s \cdot \epsilon_{Bottom Flange} \cdot E_s = 0.75 \cdot 47 \cdot (0.00054) \cdot 29000 = 552.02 \text{ kips}$$

Take moments about the bottom flange to calculate the moment of the specific section.

$$M = C_{Railing} \cdot 81.88 + C_{Deck} \cdot 64.2 + C_{Reinforcement} \cdot 65.13 + C_{Haunch} \cdot 59.18 + C_{Top Flange} \cdot 57.6 \\ + C_{Web} \cdot 56.29 - T_{Web} \cdot 18.82 - T_{Bottom Flange} \cdot 0.38$$

$$M = 414.88 \cdot 81.88 + 490.67 \cdot 64.2 + 38.77 \cdot 65.13 + 13.31 \cdot 59.18 + 12.58 \cdot 57.6 \\ + 0.56 \cdot 56.29 - 418.75 \cdot 18.82 - 552.02 \cdot 0.38$$

$$M = 61454.68 \text{ kips-in.} = 5121.22 \text{ kips-ft}$$

Following, a chart with a summary of all the calculations of the moment diagram values is presented.

Table A-1: Summary of calculations for the intact girder's moment diagram

N3						
	Height of N.A.	54.97			Moment Arm z (in.)	
	Total Height of Section	68.75		Force (kips)		
Top Deck	Top of Railing Strain	-0.00045		Railing	-414.88	81.88
	Top Surface Strain	-0.00014		Deck	-490.67	64.20
	Bottom Surface Strain	-0.00006		Reinforcement	-38.77	65.13
	Bottom of Haunch Strain	-0.00003		Haunch	-13.31	59.18
	Reinforcement Strain	-0.00009		Top Flange	-12.58	57.60
	Steel Section	Top Flange Strain	-0.00003		Web-	-0.56
Top of Web Strain		-0.00002		Web+	418.75	18.82
Bottom of Web Strain		0.00053		Bottom Flange	552.02	0.375
Bottom Flange Strain		0.00054		$\Sigma F_x$	0.00	
				M (kips - in.)		61454.68
				M (kips - ft)		5121.22

N2						
	Height of N.A.	54.97			Moment Arm z (in.)	
	Total Height of Section	68.75		Force (kips)		
Top Deck	Top of Railing Strain	-0.00047		Railing	-431.96	81.88
	Top Surface Strain	-0.00014		Deck	-510.87	64.20
	Bottom Surface Strain	-0.00006		Reinforcement	-40.37	65.13
	Bottom of Haunch Strain	-0.00003		Haunch	-13.86	59.18
	Reinforcement Strain	-0.00010		Top Flange	-13.10	57.60
	Steel Section	Top Flange Strain	-0.00003		Web-	-0.58
Top of Web Strain		-0.00002		Web+	435.99	18.82
Bottom of Web Strain		0.00055		Bottom Flange	574.74	0.375
Bottom Flange Strain		0.00056		$\Sigma F_x$	0.00	
				M (kips - in.)		63984.85
				M (kips - ft)		5332.07

N1					
	Height of N.A.	54.97			
	Total Height of Section	68.75			
Top Deck	Top of Railing Strain	-0.00062		Railing	Force (kips)
	Top Surface Strain	-0.00019		Deck	Moment Arm z (in.)
	Bottom Surface Strain	-0.00008		Reinforcement	
	Bottom of Haunch Strain	-0.00004		Haunch	
	Reinforcement Strain	-0.00013		Top Flange	
Steel Section	Top Flange Strain	-0.00004		Web-	
	Top of Web Strain	-0.00003		Web+	
	Bottom of Web Strain	0.00074		Bottom Flange	
	Bottom Flange Strain	0.00075		$\Sigma F_x$	
					M (kips - in.)
					M (kips - ft)

S1					
	Height of N.A.	54.97			
	Total Height of Section	68.75			
Top Deck	Top of Railing Strain	-0.00067		Railing	Force (kips)
	Top Surface Strain	-0.00020		Deck	Moment Arm z (in.)
	Bottom Surface Strain	-0.00008		Reinforcement	
	Bottom of Haunch Strain	-0.00004		Haunch	
	Reinforcement Strain	-0.00014		Top Flange	
Steel Section	Top Flange Strain	-0.00004		Web-	
	Top of Web Strain	-0.00003		Web+	
	Bottom of Web Strain	0.00079		Bottom Flange	
	Bottom Flange Strain	0.00080		$\Sigma F_x$	
					M (kips - in.)
					M (kips - ft)

S2					
	Height of N.A.	54.97			Moment Arm z (in.)
	Total Height of Section	68.75		Force (kips)	
Top Deck	Top of Railing Strain	-0.00056		Railing	-514.07
	Top Surface Strain	-0.00017		Deck	-607.98
	Bottom Surface Strain	-0.00007		Reinforcement	-48.04
	Bottom of Haunch Strain	-0.00004		Haunch	-16.49
	Reinforcement Strain	-0.00011		Top Flange	-15.59
				Web-	-0.69
Steel Section	Top Flange Strain	-0.00004		Web+	518.87
	Top of Web Strain	-0.00002		Bottom Flange	684.00
	Bottom of Web Strain	0.00066		$\Sigma F_x$	0.00
	Bottom Flange Strain	0.00067		M (kips - in.)	76147.79
			M (kips - ft)	6345.65	

S3					
	Height of N.A.	54.97			Moment Arm z (in.)
	Total Height of Section	68.75		Force (kips)	
Top Deck	Top of Railing Strain	-0.00049		Railing	-449.15
	Top Surface Strain	-0.00015		Deck	-531.21
	Bottom Surface Strain	-0.00006		Reinforcement	-41.98
	Bottom of Haunch Strain	-0.00003		Haunch	-14.41
	Reinforcement Strain	-0.00010		Top Flange	-13.62
				Web-	-0.60
Steel Section	Top Flange Strain	-0.00003		Web+	453.35
	Top of Web Strain	-0.00002		Bottom Flange	597.62
	Bottom of Web Strain	0.00058		$\Sigma F_x$	0.00
	Bottom Flange Strain	0.00058		M (kips - in.)	66531.75
			M (kips - ft)	5544.31	

## A.2 CALCULATION OF THE RAILING'S MOMENT DIAGRAM

The elastic section used for the calculation of the moment diagram consists of the typical T501 traffic rail and a part of the concrete deck (Figure A-3).

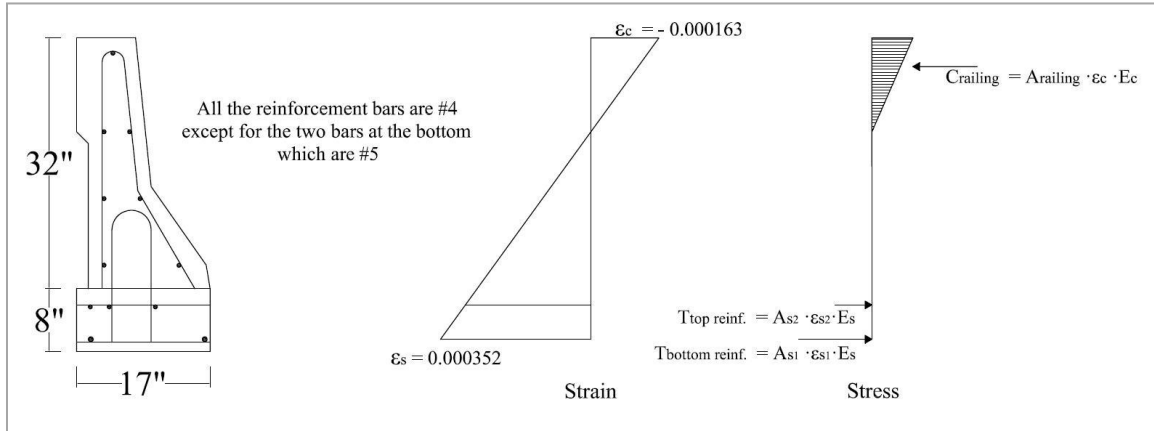


Figure A-3 Elastic section of the railing - strain & stress gradient

The static strain values were taken from the test data. Because only the top face of the railing was instrumented, it was decided to keep this value constant and calculate the strain value of the bottom reinforcement layer so that the forces applied to the section were balanced. The calculated strain values for the reinforcement layers seem reasonable and they do not diverge from any evidence that was observed after Test 2. The concrete strength was taken as 6.26 ksi based on lab tests. The reinforcement bars were tested and it was found that their strength was 60 ksi.

The forces applied on the elastic section, after calculating the appropriate strain values so that they would be balanced, were:

$$C_{Railing} = 0.5 \cdot \epsilon_{Railing\ Top} \cdot h \cdot b \cdot E_c = 0.5 \cdot (-0.0000104) \cdot 7.71 \cdot 7.50 \cdot 4560 = -1.37 \text{ kips}$$

$$T_{Top\ Reinforcement\ Layer} = A_{s2} \cdot \epsilon_{s2} \cdot E_s = 3 \cdot 0.2 \cdot (0.0000359) \cdot 29000 = 0.62 \text{ kips}$$

$$T_{Bottom\ Reinforcement\ Layer} = A_{s1} \cdot \epsilon_{s2} \cdot E_s = 2 \cdot 0.31 \cdot (0.0000414) \cdot 29000 = 0.75 \text{ kips}$$

Take moments about the bottom reinforcement layer to calculate the moment of the specific section.

$$M = C_{Railing} \cdot 35.87 - T_{Top\ Reinforcement\ Layer} \cdot 4.13$$

$$M = 1.37 \cdot 35.87 - 0.62 \cdot 4.13$$

$$M = 46.55 \text{ kips-in.} = 3.88 \text{ kips-ft}$$



A summary of all the calculations of the moment diagram values in tabular form is given below.

Table A-2: Summary of calculations for the railing's moment diagram

N3						
	Height of N.A.	32.29			Force (kips)	Moment Arm z (in.)
	Total Height of Section	40.00		Railing	-1.37	35.87
Top Deck	Top of Railing Strain	-0.0000104		Deck	0.00	0.00
	Top Surface Strain	0.0000328		Top Reinf.	0.62	4.13
	Top Reinf. Layer Strain	0.0000359		Bottom Reinf.	0.75	0.00
	Bottom Reinf. Layer Strain	0.0000414		$\Sigma F_x$	0.00	
				M (kips - in.)	46.55	
				M (kips - ft)	3.88	

N2						
	Height of N.A.	32.29			Force (kips)	Moment Arm z (in.)
	Total Height of Section	40.00		Railing	-5.23	35.87
Top Deck	Top of Railing Strain	-0.0000397		Deck	0.00	0.00
	Top Surface Strain	0.0001250		Top Reinf.	2.38	4.13
	Top Reinf. Layer Strain	0.0001369		Bottom Reinf.	2.84	0.00
	Bottom Reinf. Layer Strain	0.0001581		$\Sigma F_x$	0.00	
				M (kips - in.)	177.63	
				M (kips - ft)	14.80	

N1						
	Height of N.A.	32.29			Force (kips)	Moment Arm z (in.)
	Total Height of Section	40.00		Railing	-	35.87
Top Deck	Top of Railing Strain	-0.0001625		Deck	0.00	0.00
	Top Surface Strain	0.0005124		Top Reinf.	9.76	4.13
	Top Reinf. Layer Strain	0.0005612		Bottom Reinf.	11.65	0.00
	Bottom Reinf. Layer Strain	0.0006482		$\Sigma F_x$	0.00	
				M (kips - in.)	728.05	
				M (kips - ft)	60.67	

S1				Force (kips)	Moment Arm z (in.)
	Height of N.A.	32.29		-	
	Total Height of Section	40.00		10.50	35.87
Top Deck	Top of Railing Strain	-0.0000797		0.00	0.00
	Top Surface Strain	0.0002512		4.79	4.13
	Top Reinf. Layer Strain	0.0002751		5.71	0.00
	Bottom Reinf. Layer Strain	0.0003178		0.00	
			$\Sigma F_x$	0.00	
			M (kips - in.)		356.92
			M (kips - ft)		29.74

S2				Force (kips)	Moment Arm z (in.)
	Height of N.A.	32.29		-6.80	35.87
	Total Height of Section	40.00		0.00	0.00
Top Deck	Top of Railing Strain	-5.16E-05		3.10	4.13
	Top Surface Strain	0.0001628		3.70	0.00
	Top Reinf. Layer Strain	0.0001783		0.00	
	Bottom Reinf. Layer Strain	0.0002059			
			$\Sigma F_x$	0.00	
			M (kips - in.)		231.30
			M (kips - ft)		19.28

S3				Force (kips)	Moment Arm z (in.)
	Height of N.A.	32.29		-0.26	35.87
	Total Height of Section	40.00		0.00	0.00
Top Deck	Top of Railing Strain	-0.0000020		0.12	4.13
	Top Surface Strain	0.0000063		0.14	0.00
	Top Reinf. Layer Strain	0.0000069		0.00	
	Bottom Reinf. Layer Strain	0.0000079			
			$\Sigma F_x$	0.00	
			M (kips - in.)		8.92
			M (kips - ft)		0.74

### A.3 CALCULATION OF THE CONCRETE DECK'S MOMENT CAPACITY

The following moment capacity calculations of the concrete deck were based on a 22 in. wide transverse deck section as shown in the figure A-4.

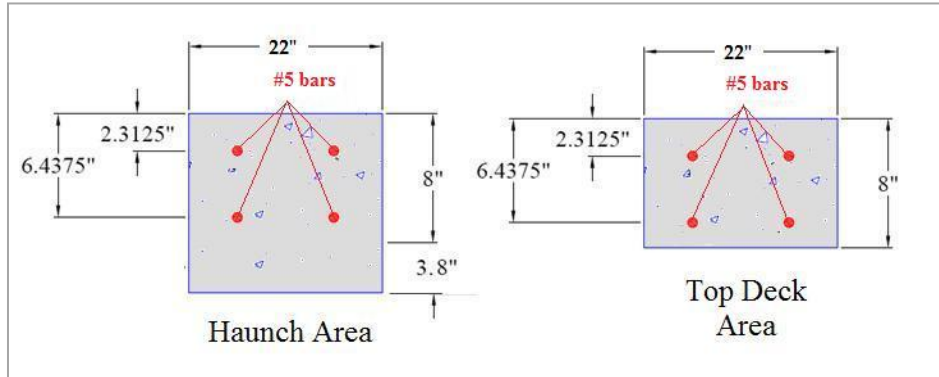


Figure A-4: Typical sections used for the moment capacity calculation

#### Positive Moment Capacity

The assumed strain and stress failure profile are shown in the figure below:

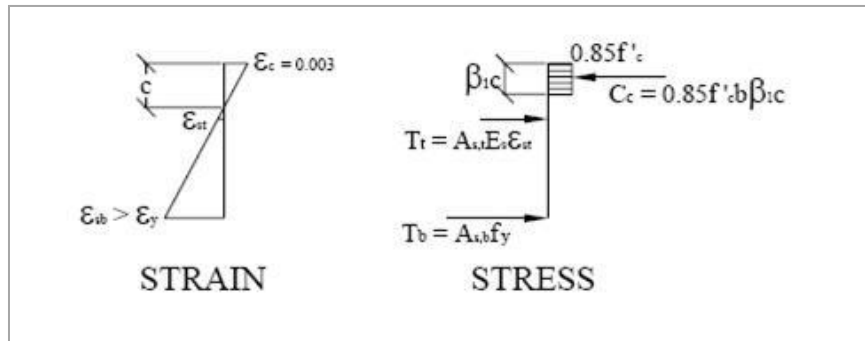


Figure A-5: Strain and stress gradients at positive moment regions

According to ACI 318-08, it was assumed that the ultimate strain of concrete was 0.003 in./in. and the bottom reinforcement has yielded prior to failure. The top reinforcement was always included in the calculations for more accurate results. Based on lab tests the concrete strength was taken as 6.26 ksi and the reinforcement strength as 60 ksi.

Let  $C = T$ :

$$C = 0.85 \cdot f_c' \cdot \beta_1 \cdot c \cdot b = 0.85 \cdot 6.26 \cdot 0.7 \cdot 22 \cdot c = 81.94 \cdot c$$

Note:  $\beta_1 = 0.70$  for 6.26 ksi concrete.

$$\varepsilon_{s, \text{bottom}} = 0.003 \cdot (6.4375 - c) / c$$

$$\varepsilon_{s, \text{top}} = 0.003 \cdot (2.3125 - c) / c$$

$$T_{\text{bottom}} = A_{s, \text{bottom}} \cdot f_y = 1.137 \cdot 60 = 68.22 \text{ kips}$$

$$T_{\text{top}} = A_{s, \text{top}} \cdot \varepsilon_{s, \text{top}} \cdot E_s = 1.137 \cdot 29,0000 \cdot \varepsilon_{s, \text{top}} = 32,973 \cdot \varepsilon_{s, \text{top}}$$

$$81.94 \cdot c = 68.22 + 32,973 \cdot \varepsilon_{s, \text{top}}$$

$$81.94 \cdot c = 68.22 + 32,973 \cdot 0.003 \cdot (2.3125 - c) / c$$

Iterate until the neutral axis depth was found. Solution:  $c = 1.494$  in.

$$\varepsilon_{s, \text{bottom}} = 0.00993 > \text{Yield strain (= 0.00207 for 60 ksi)}$$

$$\varepsilon_{s, \text{top}} = 0.001644 < \text{Yield strain (= 0.00207 for 60 ksi)}$$

$$C = 122.42 \text{ kips}$$

$$T_{\text{bottom}} = 68.22 \text{ kips}$$

$$T_{\text{top}} = 54.20 \text{ kips}$$

Take moments about the NA to solve for nominal moment capacity

$$M_n^+ = C \cdot (c - \beta_1 \cdot c / 2) + T_{top} \cdot (2.3125 - c) + T_{bottom} \cdot (6.4375 - c)$$

$$M_n^+ = 122.42 \cdot (1.494 - 0.7 \cdot 1.494/2) + 54.2 \cdot (2.3125 - 1.494) + 68.22 \cdot (6.4375 - 1.494)$$

$$M_n^+ = 500.49 \text{ kips-in.} = 41.71 \text{ kips-ft}$$

### Negative Moment Capacity

The assumed strain and stress failure profile are shown in the figure below:

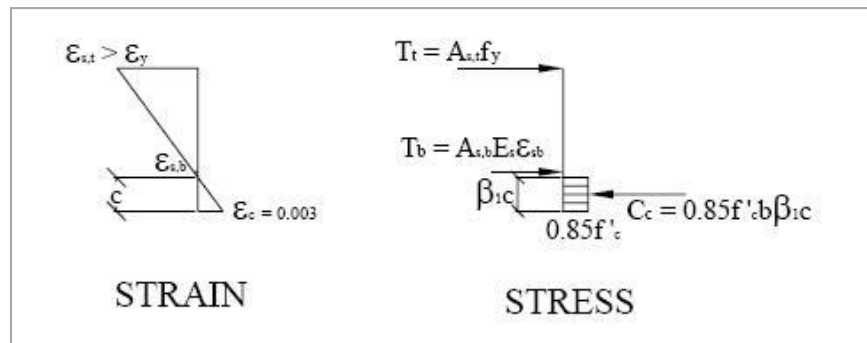


Figure A-6: Strain and stress gradients at negative moment regions

According to ACI 318-08, it was assumed that the ultimate strain of concrete was 0.003 in./in. and the top reinforcement has yielded prior to failure. The bottom reinforcement was always included in the calculations for more accurate results. Based on lab tests the concrete strength was taken as 6.26 ksi and the reinforcement strength as 60 ksi.

### Top deck area

Let  $C = T$ :

$$C = 0.85 \cdot fc' \cdot \beta_1 \cdot c \cdot b = 0.85 \cdot 6.26 \cdot 0.7 \cdot 22 \cdot c = 81.94 \cdot c$$

Note:  $\beta_1 = 0.70$  for 6.26 ksi concrete.

$$\varepsilon_{s, bottom} = 0.003 \cdot (1.5625 - c) / c$$

$$\varepsilon_{s, top} = 0.003 \cdot (5.6875 - c) / c$$

$$T_{bottom} = A_{s, bottom} \cdot \varepsilon_{s, bottom} \cdot E_s = 1.137 \cdot 29,0000 \cdot \varepsilon_{s, bottom} = 32,973 \cdot \varepsilon_{s, bottom}$$

$$T_{top} = A_{s, top} \cdot f_y = 1.137 \cdot 60 = 68.22 \text{ kips}$$

$$81.94 \cdot c = 68.22 + 32,973 \cdot \varepsilon_{s, bottom}$$

$$81.94 \cdot c = 68.22 + 32,973 \cdot 0.003 \cdot (1.5625 - c) / c$$

Iterate until the neutral axis depth was found. Solution:  $c = 1.199$  in.

$$\varepsilon_{s, bottom} = 0.00091 < \text{Yield strain (= 0.00207 for 60 ksi)}$$

$$\varepsilon_{s, top} = 0.01123 > \text{Yield strain (= 0.00207 for 60 ksi)}$$

$$C = 98.23 \text{ kips}$$

$$T_{bottom} = 30.01 \text{ kips}$$

$$T_{top} = 68.22 \text{ kips}$$

Take moments about the NA to solve for nominal moment capacity

$$M_n^- = C \cdot (c - \beta_1 \cdot c / 2) + T_{top} \cdot (5.6875 - c) + T_{bottom} \cdot (1.5625 - c)$$

$$M_n^- = 98.23 \cdot (1.199 - 0.7 \cdot 1.199/2) + 68.22 \cdot (5.6875 - 1.199) + 30.01 \cdot (1.5625 - 1.199)$$

$$M_n^- = 393.67 \text{ kips-in.} = 32.81 \text{ kips-ft}$$

### Haunch area

Let  $C = T$ :

$$C = 0.85 \cdot f_c' \cdot \beta_1 \cdot c \cdot b = 0.85 \cdot 6.26 \cdot 0.7 \cdot 22 \cdot c = 81.94 \cdot c$$

Note:  $\beta_1 = 0.70$  for 6.26 ksi concrete.

$$\varepsilon_{s, \text{bottom}} = 0.003 \cdot (5.3625 - c) / c$$

$$\varepsilon_{s, \text{top}} = 0.003 \cdot (9.4875 - c) / c$$

$$T_{\text{bottom}} = A_{s, \text{bottom}} \cdot \varepsilon_{s, \text{bottom}} \cdot E_s = 1.137 \cdot 29,0000 \cdot \varepsilon_{s, \text{bottom}} = 32,973 \cdot \varepsilon_{s, \text{bottom}}$$

$$T_{\text{top}} = A_{s, \text{top}} \cdot f_y = 1.137 \cdot 60 = 68.22 \text{ kips}$$

$$81.94 \cdot c = 68.22 + 32,973 \cdot \varepsilon_{s, \text{bottom}}$$

$$81.94 \cdot c = 68.22 + 32,973 \cdot 0.003 \cdot (5.3625 - c) / c$$

Iterate until the neutral axis depth was found. Solution:  $c = 2.3639$  in.

$$\varepsilon_{s, \text{bottom}} = 0.005403 > \text{Yield strain (= 0.00207 for 60 ksi)}$$

$$\varepsilon_{s, \text{top}} = 0.01123 > \text{Yield strain (= 0.00207 for 60 ksi)}$$

So, the assumption that the bottom reinforcement was not yielding was wrong. Transform the equilibrium equation and solve for  $c$ .

$$81.94 \cdot c = 68.22 + 68.22$$

Solution:  $c = 1.665$  in.

$$C = 136.44 \text{ kips}$$

$$T_{bottom} = 68.22 \text{ kips}$$

$$T_{top} = 68.22 \text{ kips}$$

Take moments about the NA to solve for nominal moment capacity

$$M_n^- = C \cdot (c - \beta_1 \cdot c / 2) + T_{top} \cdot (9.4875 - c) + T_{bottom} \cdot (5.3625 - c)$$

$$M_n^- = 136.44 \cdot (1.665 - 0.7 \cdot 1.665 / 2) + 68.22 \cdot (9.4875 - 1.665) + 30.01 \cdot (5.3625 - 1.665)$$

$$M_n^- = 933.55 \text{ kips-in.} = 77.80 \text{ kips-ft}$$



## APPENDIX B

### Analysis of the FSEL Test Bridge using the Strip and Yield Line Models

#### B.1 CALCULATION OF THE TRANSMITTED LOAD TO THE INTACT GIRDER

The analysis assumed that half of the entire weight of the bridge and the entire live load on the bridge needed to be resisted by the intact girder in the event of a fracture. These loads were calculated below:

##### Weight of one steel box girder:

$$W_{girder} = 1.15 \cdot (109 \text{ in}^2 / 144 \text{ ft}^2 / \text{in}^2) \cdot (0.490 \text{ kips/ft}^3) = 0.427 \text{ kip/ft}$$

Notes: This was the weight of one girder. Cross-sectional area of one girder was  $109 \text{ in}^2$ . Density of steel was taken as  $490 \text{ lb/ft}^3$ . To account for internal diaphragms, stiffeners, etc., the weight of the steel girder was multiplied by a factor of 1.15.

##### Concrete deck:

$$W_{deck} = (280 \cdot 8 / 144 \text{ ft}^2) \cdot (0.150 \text{ kip/ft}^3) = 2.33 \text{ kip/ft}$$

Notes: Width of concrete deck was 23 ft-4 in. = 280 in. Density of concrete was taken as  $150 \text{ lb/ft}^3$ . Deck thickness was 8 in.

##### T501 Railing

$$W_{railings} = 2 \cdot (311.75 / 144 \text{ ft}^2) \cdot (0.150 \text{ kip/ft}^3) = 0.65 \text{ kip/ft}$$

Notes: Multiplied by 2 to account for two rails. Cross-sectional area of one rail was calculated as  $311.75 \text{ in}^2$

##### Simulated Truck

$$W_{truck} = 76 \text{ kips}$$

### **Load to be transmitted**

$$F = (W_{girder} + W_{deck}/2 + W_{railings}/2) \cdot L + W_{truck}$$

$$F = (0.427 + 2.33/2 + 0.65/2) \cdot 120 + 76 = 306.04 \text{ kips}$$

$$F = 306.04 \text{ kips}$$

## **B.2 CALCULATION OF MAXIMUM MOMENT ON THE BRIDGE**

### **Mid-span moment due to dead load**

$$M_{DL} = (2 \cdot W_{girder} + W_{deck} + W_{railings}) \cdot L^2/8 = (2 \cdot 0.427 + 2.33 + 0.65) \cdot 120^2/8$$

$$M_{DL} = 7,063.2 \text{ kip-ft}$$

### **Moment due to truck load**

The position of the 76-kip truck load, the shear diagram and the moment diagram are shown in Figure B-1. The maximum moment was located at the mid-span of the bridge and it was equal to  $M_{max} = 9,048.6 \text{ kip-ft}$

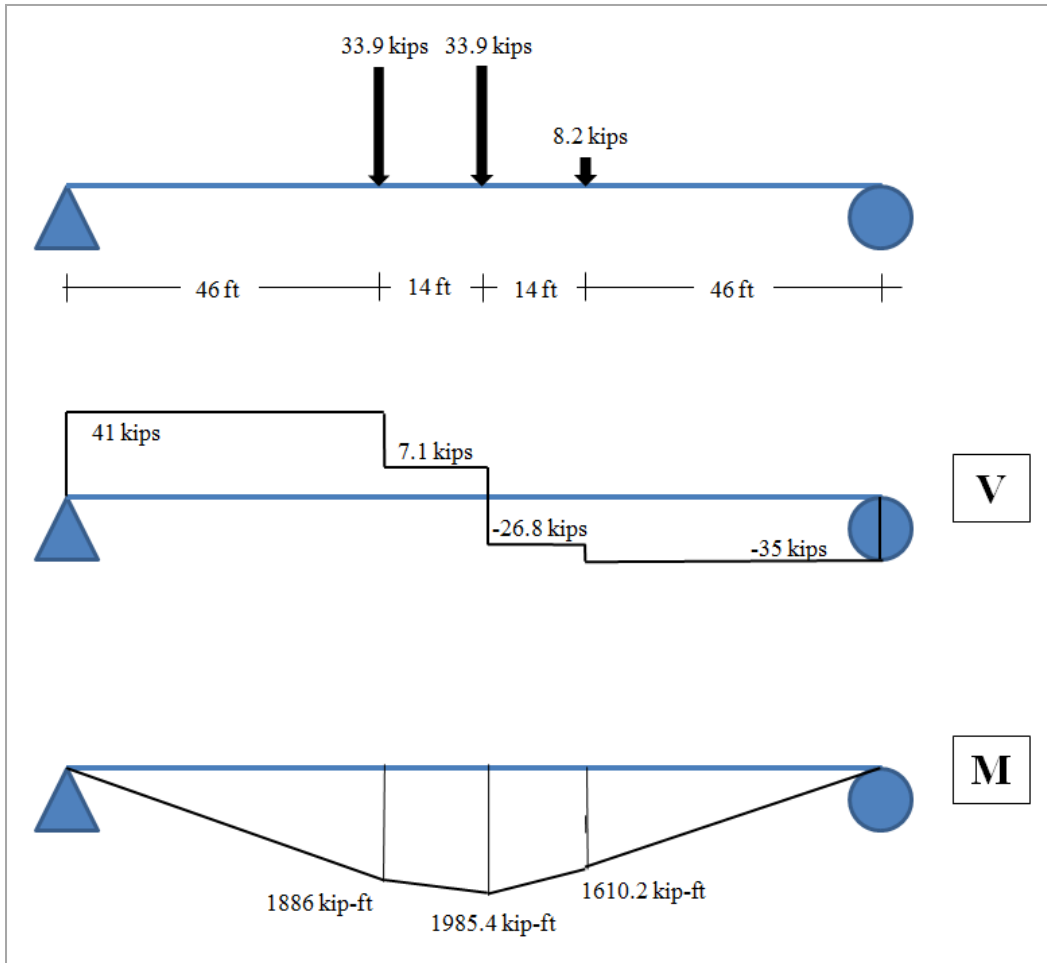


Figure B-1: Truck load location - Shear and moment diagram due to truck load

### B.3 ANALYSIS OF COMPOSITE SECTION

The plastic moment capacity of the intact girder was calculated to determine if it had sufficient capacity to sustain the total live and dead load on the bridge. The composite section based on which all the calculations were performed was shown in Figure B-2. Based on lab test, it was found that  $f_{yw} = 60$  ksi for the webs and  $f_{ybf} = 53$  ksi for the bottom flange.

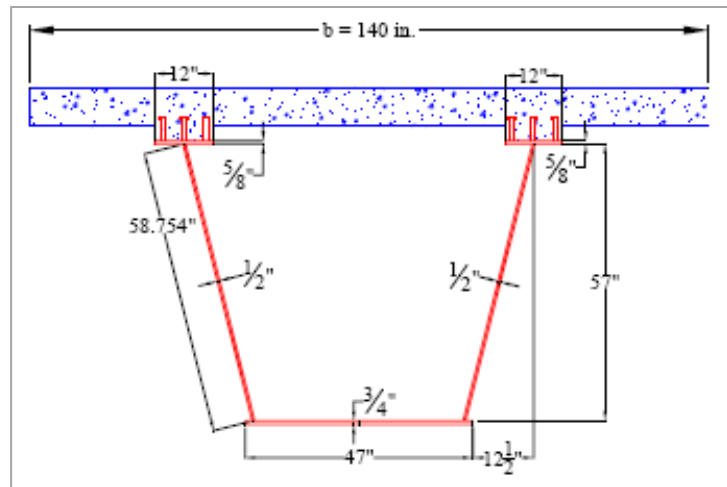


Figure B-2: Composite section [Sutton,(2007)]

Find the plastic neutral axis by setting  $T = C$ :

$$T = A_s \cdot f_y = 47 \cdot 0.75 \cdot 53 + (2 \cdot 58.754 \cdot 0.5 + 2 \cdot 12 \cdot 0.625) \cdot 60 = 6293.25 \text{ kips}$$

$$C_c = 0.85 \cdot f_c' \cdot t_s \cdot b_{eff} = 0.85 \cdot 6.26 \cdot 8 \cdot 140 = 5959.52 \text{ kips}$$

Since  $T > C$  then the plastic neutral axis was in the girder.

$$C_s = (A_s \cdot f_y - C_c) / 2 = (6293.25 - 5959.52) / 2 = 166.87 \text{ kips}$$

Using this equation, the compressive force needed to be developed in the steel section in order to achieve equilibrium ( $C = T$ ), could be determined.

$$C_{tfl} = 2 \cdot t_{tfl} \cdot b_{tfl} \cdot f_{ytf} = 2 \cdot 0.625 \cdot 12 \cdot 60 = 900 \text{ kips}$$

The top flanges could resist 900 kips in compression which was more than required to obtained equilibrium. As a result the PNA fell  $x = 166.87 / (2 \cdot 12 \cdot 60) = 0.116$  in. inside the top flange as shown in B-3.



Figure B-3: Plastic neutral axis location

So:

$$C_c = 5959.52 \text{ kips}$$

$$C_{tfl} = 166.87 \text{ kips,}$$

$$T_{tfl} = 900 - 166.87 = 733.13 \text{ kips}$$

$$T_{web} = A_{web} \cdot f_{yw} = 2 \cdot 0.5 \cdot 58.754 \cdot 60 = 3525.24 \text{ kips}$$

$$T_{bottom\ flange} = A_{bottom\ flange} \cdot f_y = 47 \cdot 0.75 \cdot 53 = 1868.25 \text{ kips}$$

By taking moments about the PNA, the nominal plastic moment capacity was calculated:

$$M_{bottom\ flange} = T_{bottom\ flange} \cdot (3/8 + 57 - 0.116) = 106,974.13 \text{ kip-in.}$$

$$M_{web} = T_{web} \cdot 57 / 2 = 100,469.34 \text{ kip-in.}$$

$$M_{T_{tfl}} = T_{tfl} \cdot (0.625 - 0.116) / 2 = 186.58 \text{ kip-in.}$$

$$M_{C_{tfl}} = C_{tfl} \cdot 0.116 / 2 = 9.68 \text{ kip-in.}$$

$$M_{C_{concrete}} = C_c \cdot (4 + 3 + 0.116) = 42,407.94 \text{ kip-in.}$$

Note: The 3-in. term added in the moment arm accounted for the average haunch height and offsets the concrete deck 3 in. above the top flange of the girder.

Thus,  $M_P = 106,974.13 + 100,469.34 + 186.58 + 9.68 + 42,407.94$

$$M_P = 250,047.67 \text{ kip-in.} = 20,837.31 \text{ kip-ft}$$

Earlier,  $M_{max}$  was found to be 9,048.6 kip-ft. The plastic moment capacity of the intact girder was adequate to sustain the dead load of the bridge plus the truck load.

#### B.4 ANALYSIS OF CONCRETE DECK

The bending and shear capacity of the concrete deck were checked to ensure that they were adequate to resist the moment and the shear produced by the unsupported load of the fractured girder. These capacities were based on a 1-ft wide transverse deck section as shown in the Figure B-4.

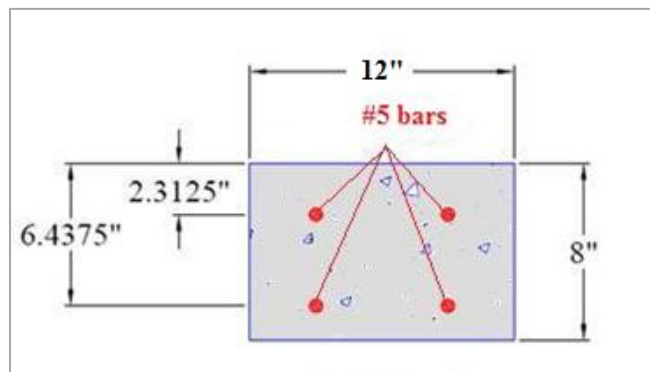


Figure B-4: Typical one foot wide section of the concrete deck

#### Positive Moment Capacity

The assumed strain and stress failure profile are shown in the figure below:

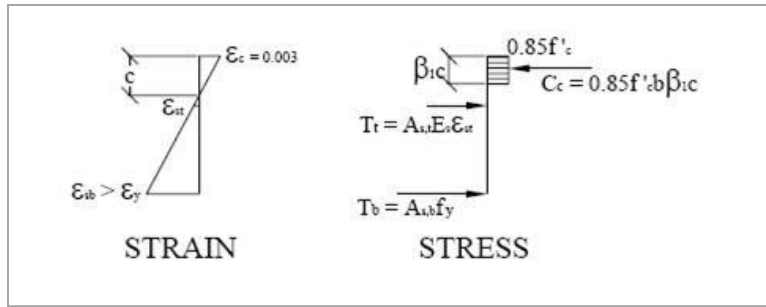


Figure B-5: Strain and stress gradients at positive moment regions

According to ACI 318-08, it was assumed that the ultimate strain of concrete was 0.003 in./in. and the bottom reinforcement had yielded prior to failure. The top reinforcement was always included in the calculations for more accurate results. Based on tests of the material the concrete strength was taken as 6.26 ksi and the reinforcement strength as 60 ksi.

Let  $C = T$ :

$$C = 0.85 \cdot f'_c \cdot \beta_1 \cdot c \cdot b = 0.85 \cdot 6.26 \cdot 0.7 \cdot 12 \cdot c = 44.70 \cdot c$$

Note:  $\beta_1 = 0.70$  for 6.26 ksi concrete.

$$\varepsilon_{s, \text{bottom}} = 0.003 \cdot (6.4375 - c) / c$$

$$\varepsilon_{s, \text{top}} = 0.003 \cdot (2.3125 - c) / c$$

$$T_{\text{bottom}} = A_{s, \text{bottom}} \cdot f_y = 0.62 \cdot 60 = 37.2 \text{ kips}$$

$$T_{\text{top}} = A_{s, \text{top}} \cdot \varepsilon_{s, \text{top}} \cdot E_s = 0.62 \cdot 29,0000 \cdot \varepsilon_{s, \text{top}} = 17,980 \cdot \varepsilon_{s, \text{top}}$$

$$44.70 \cdot c = 37.2 + 17,980 \cdot \varepsilon_{s, \text{top}}$$

$$44.70 \cdot c = 37.2 + 17,980 \cdot 0.003 \cdot (2.3125 - c) / c$$

Iterate until the neutral axis depth was found. Solution:  $c = 1.494$  in.

$$\epsilon_{s, bottom} = 0.00993 > \text{Yield strain} (= 0.00207 \text{ for } 60 \text{ ksi})$$

$$\epsilon_{s, top} = 0.001644 < \text{Yield strain} (= 0.00207 \text{ for } 60 \text{ ksi})$$

$$C = 66.78 \text{ kips}, \quad T_{bottom} = 37.2 \text{ kips}, \quad T_{top} = 29.55 \text{ kips}$$

Take moments about the NA to solve for nominal moment capacity

$$M_n^+ = C \cdot (c - \beta_1 \cdot c / 2) + T_{top} \cdot (2.3125 - c) + T_{bottom} \cdot (6.4375 - c)$$

$$M_n^+ = 66.78 \cdot (1.494 - 0.7 \cdot 1.494/2) + 29.55 \cdot (2.3125 - 1.494) + 37.2 \cdot (6.4375 - 1.494)$$

$$M_n^+ = 272.93 \text{ kips-in.} = 22.74 \text{ kips-ft}$$

### Negative Moment Capacity

The assumed strain and stress failure profile are shown in the figure below:

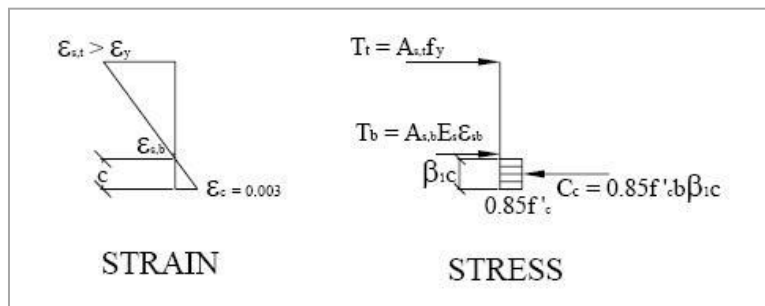


Figure B-6: Strain and stress gradients at negative moment regions



According to ACI 318-08, it was assumed that the ultimate strain of concrete was 0.003 in./in. and the top reinforcement had yielded prior to failure. The bottom reinforcement was always included in the calculations for more accurate results. Based on lab tests the concrete strength was 6.26 ksi and the reinforcement strength as 60 ksi.

Let  $C = T$ :

$$C = 0.85 \cdot f_c' \cdot \beta_1 \cdot c \cdot b = 0.85 \cdot 6.26 \cdot 0.7 \cdot 12 \cdot c = 44.70 \cdot c$$

Note:  $\beta_1 = 0.70$  for 6.26 ksi concrete.

$$\varepsilon_{s, bottom} = 0.003 \cdot (1.5625 - c) / c$$

$$\varepsilon_{s, top} = 0.003 \cdot (5.6875 - c) / c$$

$$T_{bottom} = A_{s, bottom} \cdot \varepsilon_{s, bottom} \cdot E_s = 0.62 \cdot 29,0000 \cdot \varepsilon_{s, bottom} = 17,980 \cdot \varepsilon_{s, bottom}$$

$$T_{top} = A_{s, top} \cdot f_y = 0.62 \cdot 60 = 37.2 \text{ kips}$$

$$44.70 \cdot c = 37.2 + 17,980 \cdot \varepsilon_{s, bottom}$$

$$44.70 \cdot c = 37.2 + 17,980 \cdot 0.003 \cdot (1.5625 - c) / c$$

Iterate until the neutral axis depth was found. Solution:  $c = 1.199$  in.

$$\varepsilon_{s, bottom} = 0.00091 < \text{Yield strain (= 0.00207 for 60 ksi)}$$

$$\varepsilon_{s, top} = 0.01123 > \text{Yield strain (= 0.00207 for 60 ksi)}$$

$$C = 53.60 \text{ kips}$$

$$T_{bottom} = 16.35 \text{ kips}$$

$$T_{top} = 37.2 \text{ kips}$$

Take moments about the NA to solve for nominal moment capacity

$$M_n^- = C \cdot (c - \beta_1 \cdot c / 2) + T_{top} \cdot (5.6875 - c) + T_{bottom} \cdot (1.5625 - c)$$

$$M_n^- = 53.60 \cdot (1.199 - 0.7 \cdot 1.199/2) + 37.2 \cdot (5.6875 - 1.199) + 16.35 \cdot (1.5625 - 1.199)$$

$$\boxed{M_n^- = 214.69 \text{ kips-in.} = 17.89 \text{ kips-ft}}$$

## Bending Capacity Check

The deflected shape of the concrete deck and the bending moment diagram, if it was assumed that the shear studs have enough tensile capacity, was shown in Figure B-7:

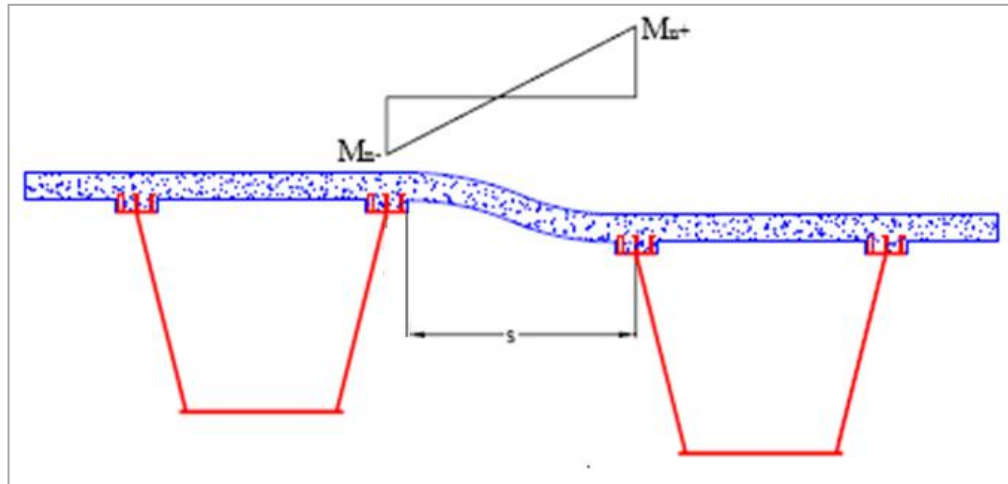


Figure B-7: Deflected shape and moment diagram before any failure of shear studs

$$V = (M_n^+ + M_n^-)/s = (22.74 \text{ kip-ft} + 17.89 \text{ kip-ft})/5.5 \text{ ft} = \mathbf{7.39 \text{ kips per foot of deck}}$$

Note: The spacing,  $s$ , is equal to the distance between the mid-width of the fractured girder's interior top flange and the edge of the interior top flange of the intact girder (5.5 ft).

The shear capacity is calculated using the ACI equation for shear shown below, which neglects the contribution of the reinforcement. The capacity is based on a 1-ft wide transverse deck section. The depth used in this equation is the depth to the centroid of the tension reinforcement (6.4375 in.).

$$V_c = 2 \cdot \sqrt{f'_c} \cdot b \cdot d = 2 \cdot \sqrt{6260} \cdot 12 \cdot 6.4375 = \mathbf{12.22 \text{ kips}}$$

Thus, the shear capacity of the deck is controlled by the shear of the plastic deck mechanism (7.39 kips/ft). Therefore, the total length required to transfer the 306.04-kip force is:

$$l_M = 306.04 / 7.39 = 41.41 \text{ ft}$$

$$41.41 / 120 = \mathbf{34.51 \% \text{ of the span length}}$$

### **B.5 SHEAR STUD CHECK**

In order to determine the tensile strength of the shear stud group, the guidelines given by Mouras (2008) are followed. The shear stud connection in the FSEL bridge consists of a group of three 5-in. tall shear studs spaced transversely. The haunch along the length of the bridge is 3 in. By using Equation B-1 and B-2 given below, the tensile capacity of the shear studs group is calculated to be 15.02 kips throughout the bridge.

$$N_b = k_c \cdot \sqrt{f'_c} \cdot h_h^{1.5} \quad \text{Equation B-1 (ACI 318-08)}$$

$$N_{cbg} = \frac{A_{NC}}{A_{NCO}} \cdot \psi_{g,N} \cdot \psi_{ec,N} \cdot \psi_{ed,N} \cdot \psi_{c,N} \cdot N_b \quad \text{Equation B-2 (modified ACI 318-08)}$$

where:

$N_b$  = concrete cone breakout strength of a single isolated stud in a continuous piece of cracked concrete (15.19 kips)

$k_c$  = 24 for cast-in-place shear studs

$f'_c$  = concrete compressive strength (6260 psi)

$h_h$  = modified height of shear stud in concrete ( $h_h = h_{ef} - d_h = 4.625 - 3 = 1.625$  in. <  $12/3 = 4 \rightarrow h_h = 4$  in.)

$h_{ef}$  = effective height of shear stud in concrete, which is equal to the length of stud less the height of the stud head ( $h_{eff} = 5 - 0.375 = 4.625$  in.)

$d_h$  = haunch height (3 in.)

$c_{a,min}$  = distance between outer stud and the edge of flange ( $c_{a,min} = 1.5$  in.)

$N_{cbg}$  = design concrete breakout strength of a stud or group of studs (33.47 kips)

$A_{Nc}$  = projected concrete cone failure area of a stud group ( $A_{Nc} = 3 h_{ef} w_h = 166.5$  in<sup>2</sup>)

Note:  $A_{Nc} = 3 h_{ef} w_h$  because haunch is confined over the full height of the projected cone failure area.

$A_{Nco}$  = projected concrete cone failure area of a single stud in continuous concrete ( $A_{Nco} = 9h_h^2 = 144$  in<sup>2</sup>)

$\Psi_{g,N}$  = group effect modification factor for studs on a bridge girder ( $\Psi_{g,N} = 0.90$  for 3 studs spaced transversely)

$\psi_{ec,N}$  = eccentric load modification factor ( $\psi_{ec,N} = 1$ )

$\psi_{ed,N}$  = edge distance modification factor ( $\psi_{ed,N} = 0.7 + 0.3 c_{a,min} / (1.5 h_{ef}) = 0.76$ )

$\psi_{c,N}$  = cracked concrete modification factor ( $\psi_{c,N} = 1.25$  for cast-in studs)

Using Equation 3-2, a determination as to whether the shear studs pull out or a hinge is formed in the concrete deck can be made. A strip width equal to the shear stud spacing of 22 inches is used to calculate the tension in the stud group.

$$N_{cbg} = T = 15.02 \text{ kips}, M_2/b + V = 22.74 \cdot (22/12) / 6 + 7.39 \cdot (22/12) = 20.50 \text{ kips}$$

Because  $T < M_2/b + V$ , the shear studs pull out, which is consistent with test observations.

### **B.6 SHEAR CHECK OF THE COMPOSITE SECTION AT THE SUPPORTS DUE TO TORSION AND BENDING**

The entire weight of the bridge and the live load were applied to the intact girder. The shear, which was developed at the end of the span, due to this loading was calculated below.

$$V = V_{DL} + V_{TRUCK} = (2 \cdot 0.427 + 2.33 + 0.65) \cdot 120 / 2 + 41$$

$$V = 271.04 \text{ kips}$$

The unsupported load, which is first carried by the fractured girder, has to be transferred to the intact girder. The eccentricity between the chord of the intact girder bearings and the center of gravity (CG) of each load leads to a torque that is applied to the intact girder in addition to all the transferred loads. Due to the large horizontal curvature of the bridge ( $R = 1365.39$  ft), the eccentricities of each load are assumed to be equal to the distance between the CG of each load and the centerline of the intact girder bearings. Table B-1 summarizes all the eccentricities.

Table B-1: Eccentricities of loads

	Live or Dead Load	Eccentricity
		(ft)
1	Fractured Girder (FG)	12
2	Railing above FG	17.17
3	Deck above FG	11.83
4	Intact Girder (IG)	0.00
5	Railing above IG	5.17
6	Deck above IG	0.17
7	Truck	11.25

Thus, the torques due to each load are equal to:

$$t_{FG} = 51.24 \cdot 12 = 614.88 \text{ kip}\cdot\text{ft}$$

$$t_{RFG} = 39 \cdot 17.17 = 669.63 \text{ kip}\cdot\text{ft}$$

$$t_{DFG} = 139.8 \cdot 11.83 = 1,653.83 \text{ kip}\cdot\text{ft}$$

$$t_{IG} = 51.24 \cdot 0 = 0 \text{ kip}\cdot\text{ft}$$

$$t_{RIG} = 39 \cdot 5.17 = 201.63 \text{ kip}\cdot\text{ft}$$

$$t_{DIG} = 139.8 \cdot 0.17 = 23.77 \text{ kip}\cdot\text{ft}$$

$$t_{TRUCK} = 76 \cdot 11.25 = 855 \text{ kip}\cdot\text{ft}$$

Assuming that half of the calculated torque is applied to each end of the intact girder, the torque developed at each end section is equal to:

$$T = (614.88 + 669.63 + 1,653.83 - 201.63 - 23.77 + 855) / 2 = 1,784 \text{ kip}\cdot\text{ft}$$

In all the above calculations for the applied torque, the curvature of the bridge is neglected due to the large radius of curvature of the test bridge. In order to include the

effect of the horizontal curvature, Equations 3-5 through 3-19 need to be used. In the case of the FSEL bridge:

1.  $R_{INT} = 1359.34$  ft,  $L_{INT} = 119.48$  ft,  $\varphi = 0.0879$
2.  $R_{FG} = 1371.2$  ft,  $\theta_{0FG} = 0$  rad,  $\theta_{IFG} = 0.0879$  rads,  $\bar{\theta}_{FG} = 0.04395$  rads
3.  $R_{IG} = 1359.34$  ft,  $\theta_{0IG} = 0$  rad,  $\theta_{IIG} = 0.0879$  rads,  $\bar{\theta}_{IG} = 0.04395$  rads
4.  $R_{TRUCK} = 1370.48$  ft,  $\theta_{0TRUCK} = 0.0204$  rad,  $\theta_{ITRUCK} = 0.03385$  rads,  $\bar{\theta}_{TRUCK} = 0.027$  rads

The center of gravity of each component is found by inserting all the above values into Equation 3-18.

$$\bar{D}_{FG} = \frac{1371.2^2 \cdot 1.96 \cdot [\sin(0.0879 - 0.04395) - \sin(-0.04395)]}{1371.2 \cdot 1.96 \cdot 0.0879} = 1370.76 \text{ ft}$$

$$\bar{D}_{IG} = \frac{1359.34^2 \cdot 1.96 \cdot [\sin(0.0879 - 0.04395) - \sin(-0.04395)]}{1359.34 \cdot 1.96 \cdot 0.0879} = 1358.90 \text{ ft}$$

$$\bar{D}_{TRUCK} = \frac{1370.48^2 \cdot 2.72 \cdot [\sin(0.03385 - 0.027) - \sin(0.0204 - 0.027)]}{1370.48 \cdot 2.72 \cdot (0.03385 - 0.0204)} = 1370.47 \text{ ft}$$

By using Equation 3-19, the eccentricity of each component can be found as follows:

$$e_{FG} = 1370.76 - 1359.34 \cdot \cos(119.48/(2 \cdot 1359.34)) = 12.73 \text{ ft}$$

$$e_{IG} = 1358.90 - 1359.34 \cdot \cos(119.48/(2 \cdot 1359.34)) = 0.87 \text{ ft}$$

$$e_{TRUCK} = 1370.47 - 1359.34 \cdot \cos(119.48/(2 \cdot 1359.34)) = 11.12 \text{ ft}$$

The calculated eccentricities are in a very good agreement with the assumed ones ( $e_{FG} = 12.73$  ft  $\approx$  12 ft,  $e_{IG} = 0.87$  ft  $\approx$  0 ft,  $e_{TRUCK} = 11.12$  ft  $\approx$  11.25 ft). As a result, if the

bridge under consideration has a large radius of curvature, the eccentricities can be measured from the centerline of the intact girder.

To compute the shear flow of the closed cross-section, Equation 3-20 is used.

$$q = T / (2 \cdot A) = 1,838.76 / (2 \cdot 3850.36/144) = 34.38 \text{ kips/ft} = 2.78 \text{ kips/in}$$

The shear stress due to torsion at every component of the composite section was calculated as:

$$\tau_{CONC. DECK} = q / t_{CONC. DECK} = 2.78 / 8 = 0.34 \text{ ksi}$$

$$\tau_{WEB} = q / t_{WEB} = 2.78 / 0.5 = 5.56 \text{ ksi}$$

$$\tau_{BOTT. FLANGE} = q / t_{BOTT. FLANGE} = 2.78 / 0.75 = 3.71 \text{ ksi}$$

The flexural shear was assumed to be carried by the webs of the composite section, since the contribution of the bottom flange and the concrete deck was small. The flexural shear stress at the webs of the composite section was calculated as:

$$\tau_{Flexural WEB} = V / (2 \cdot h_{WEB} \cdot t_{WEB} \cdot \cos(14^\circ)) = 271.04 / (2 \cdot 58.754 \cdot 0.5 \cdot 0.97) = 4.76 \text{ ksi}$$

Note: The factor 2 accounted for the fact that the composite sections consisted of two webs, which shared the total flexural shear. The  $\cos(14^\circ)$  accounted for the fact that the webs were not vertical and due to their inclination the shear which was developed was higher.

The shear stress, which was developed at the concrete deck due to torsion, was equal to 0.34 ksi. According to ACI 318-08, the shear capacity of the reinforced concrete section is,

$$V_S = A_t \cdot f_{yt} \cdot b \cdot \cot \theta / s$$



Thus,

$$V_{TORSION} = q \cdot b = 2.78 \cdot 72 = 200.16 \text{ kips} \leq V_S = A_t \cdot f_{yt} \cdot b \cdot \cot \theta / s = 0.62 \cdot 60 \cdot 72 / 6 = 446.4 \text{ kips}$$

The shear stresses in the steel girder are checked according to the AASHTO Specifications (2007). The shear stress in the webs of the end panel should be limited to either the shear-yielding or shear-buckling resistance. The nominal shear stress capacity of the web panel ( $\tau_n$ ) is computed as the shear-buckling capacity to the shear yield strength ratio ( $C$ ) multiplied by the plastic shear stress ( $\tau_p$ ) ( $\tau_n = C \cdot \tau_p$ ). The plastic shear stress is equal to  $0.58f_{yw}$ . The ratio  $C$  is determined as follows:

$$\text{If } \frac{D}{t_w} \leq 1.12 \sqrt{\frac{Ek}{f_{yw}}} \text{ then } C=1.0$$

$$\text{If } 1.12 \sqrt{\frac{Ek}{f_{yw}}} < \frac{D}{t_w} \leq 1.40 \sqrt{\frac{Ek}{f_{yw}}} \text{ then } C = \frac{1.12}{D/t_w} \sqrt{\frac{Ek}{f_{yw}}}$$

$$\text{If } \frac{D}{t_w} > 1.40 \sqrt{\frac{Ek}{f_{yw}}} \text{ then } C = \frac{1.57}{(D/t_w)^2} \left( \frac{Ek}{f_{yw}} \right)$$

For the FSEL test bridge,  $D = 58.75$  in.,  $t_w = 0.5$  in.,  $E = 29,000$  ksi,  $f_{yw} = 60$  ksi. The factor  $k$  is calculated as

$$k = 5 + \frac{5}{\left( \frac{d_0}{D} \right)^2}$$

where  $d_0$  is the spacing from the support to the first stiffener adjacent to the support (144 in.). AASHTO limits the factor  $d_0/D$  to 1.5 for end panels. In the case of the FSEL test bridge, this limit is violated because  $d_0/D = 2.45 > 1.5$ . Due to this violation, the ratio is set to its actual value (i.e.,  $d_0/D = 2.45$ ). Moreover, it is important to mention that the ratio of

$d_0/D=2.45$  provides a lower nominal shear stress than  $d_0/D=1.5$ . By inserting the value of  $d_0/D$  into the equation above,  $k$  is calculated to be 5.83. Because

$$\frac{D}{t_w} = \frac{57}{0.5} = 114 > 1.40 \sqrt{\frac{Ek}{f_{yw}}} = 74.32$$

$$C = \frac{1.57}{(D/t_w)^2} \left( \frac{Ek}{f_{yw}} \right) = 0.32 .$$

Having all the variables defined, the nominal shear stress ( $\tau_n$ ) is equal to  $\tau_n = 0.32 \cdot 0.58 \cdot f_{yw} = 11.14$  ksi.

The total shear stress in the webs includes contributions from the flexural shear stress and the torsional shear stress. As shown in Figure B-8, the shear stresses are added and subtracted in the east and west web, respectively. The east web controls because the shear from flexure and torsion add to each other. The total shear stress that develops in the east web is calculated to be  $\tau_{TOTAL} = \tau_{WEB} + \tau_{Flexural\ WEB} = 5.56 + 4.76 = 10.32$  ksi, which is less than the nominal shear stress capacity ( $\tau_n = 11.14$  ksi).

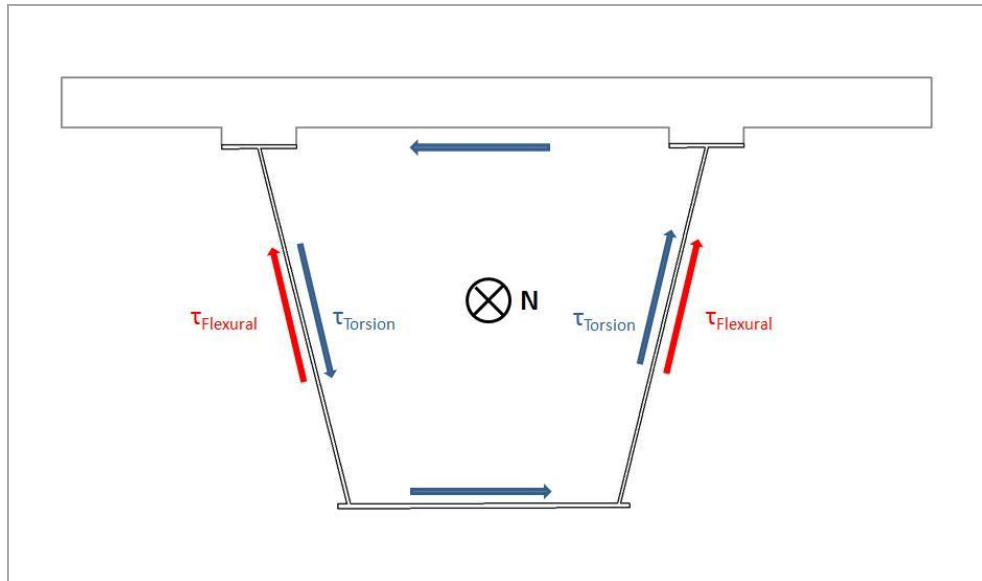


Figure B-8: Flexural and torsional shear stresses on the composite section

The end diaphragm, which connects both girders, needs to be checked to ensure that it has adequate capacity to resist the torque applied to the intact girder. The force couples at the bearings of the two girders, which are produced by the torque applied on the intact girder, causes shearing of the end diaphragm. Thus, the forces acting on each side of the end diaphragm can be calculated as follows:

$V_{ED} = T / l_b = 1,784 \text{ k-ft} / 12 \text{ ft} = 148.67 \text{ kips}$ , where  $T$  is the torque applied to the intact girder, and  $l_b$  is the distance between the two bearings.

The nominal shear strength of the end diaphragm can be computed according to AASHTO Sec. 6.10.9.2.

$$V_n = C \cdot V_P, \text{ where } V_P = 0.58 \cdot F_{yw} \cdot D \cdot t_w = 0.58 \cdot 60 \cdot 57 \cdot 0.5 = 991.8 \text{ kips}$$

and  $C$  is calculated as

$$C = \frac{1.57}{(D/t_w)^2} \left( \frac{Ek}{f_{yw}} \right) = 0.29 \text{ because } \frac{D}{t_w} = \frac{57}{0.5} = 114 > 1.40 \sqrt{\frac{Ek}{f_{yw}}} = 68.82, \text{ where } k = 5.$$

Thus, the shear strength of the end diaphragm ( $V_n = 0.29 \cdot 991.8 = 287.62$  kips) is adequate to resist the applied shearing force ( $V_{ED} = 148.67$  kips).

Summarizing the calculations, it is found that all the components of the section have adequate capacities to resist the applied load, except for the shear studs. The plastic mechanism in the deck between the girders cannot be formed due to the low tensile strength of the shear studs. As a result, a yield line analysis needs to be performed to determine the ultimate load that this bridge can sustain.

## **B.7 ANALYSIS OF FSEL BRIDGE USING THE SIMPLIFIED STRIP MODEL**

In Chapter 3, the Simplified Strip Model was described. The deflection of each support of all strips was known at any iteration based on the assumed deflected shape. By inserting these deflections in the slope deflection equations, the moment diagram of the strip was calculated. From the moment diagram, the reactions of the strip, which represent the top flanges, could be calculated. Having defined the moment and the reactions of every strip, they were checked against the moment capacity of the concrete deck and the tensile capacity of the shear studs in each strip. In the event of the moment or the tensile reaction of a support had exceeded the nominal capacity, a failure would occur as described in Chapter 3. After this point the strip model was changed according to the failure. Table B-2 shows a sample of iteration.

Table B-2: A sample iteration of the Simplified Strip Model

<b>Three span Continuous Beam</b>													
<b>Strip center (in)</b>	<b>Intact Girder (in)</b>		<b>Fractured Girder (in)</b>		<b>Units in kips-in</b>					<b>Units in kips</b>			
	West	East	West	East	Ma	Mb (haunch)	Mb (deck)	Mc	Md	Ra	Rb	Rc	Rd
<b>-682</b>	-0.26	-0.29	-0.30	-0.42	0.0	75.0	54.6	-169.1	0.0	1.04	-4.43	5.74	-2.35
<b>-660</b>	-0.42	-0.46	-0.47	-0.66	0.0	118.3	86.2	-267.0	0.0	1.64	-7.00	9.06	-3.71
<b>-638</b>	-0.57	-0.63	-0.64	-0.91	0.0	161.7	117.9	-364.9	0.0	2.25	-9.56	12.38	-5.07
<b>-616</b>	-0.72	-0.80	-0.81	-1.15	0.0	205.1	149.5	-462.7	0.0	2.85	-12.13	15.70	-6.43
<b>-594</b>	-0.88	-0.97	-0.98	-1.39	0.0	248.5	181.1	-560.6	0.0	3.45	-14.69	19.03	-7.79
<b>-572</b>	-1.02	-1.14	-1.16	-1.62	0.0	297.0	219.1	-637.4	0.0	4.12	-17.10	21.83	-8.85
<b>-550</b>	-1.14	-1.33	-1.35	-1.80	0.0	368.1	285.8	-619.3	0.0	5.11	-18.83	22.31	-8.60
<b>-528</b>	-1.25	-1.51	-1.54	-1.97	0.0	439.3	352.6	-601.1	0.0	6.10	-20.55	22.80	-8.35
<b>-506</b>	-1.36	-1.70	-1.74	-2.14	0.0	510.4	419.3	-582.9	0.0	7.09	-22.27	23.28	-8.10
<b>-484</b>	-1.48	-1.88	-1.93	-2.32	0.0	581.6	486.0	-564.8	0.0	8.08	-24.00	23.77	-7.84
<b>-462</b>	-1.59	-2.07	-2.13	-2.49	0.0	652.7	552.8	-546.6	0.0	9.07	-25.72	24.25	-7.59
<b>-440</b>	-1.71	-2.25	-2.32	-2.67	0.0	723.8	619.5	-528.4	0.0	10.05	-27.45	24.73	-7.34
<b>-418</b>	-1.82	-2.39	-2.53	-2.85	0.0	645.7	559.0	-394.7	0.0	8.97	-23.42	19.93	-5.48
<b>-396</b>	-1.93	-2.51	-2.75	-3.04	0.0	482.2	425.8	-194.9	0.0	6.70	-16.10	12.11	-2.71
<b>-374</b>	-2.03	-2.63	-2.96	-3.23	0.0	318.7	292.6	5.0	0.0	4.43	-8.78	4.29	0.07
<b>-352</b>	-2.14	-2.74	-3.18	-3.42	0.0	155.2	159.4	204.8	0.0	2.16	-1.47	-3.53	2.84
<b>-330</b>	-2.25	-2.86	-3.40	-3.61	0.0	-8.3	26.1	404.6	0.0	-0.11	5.85	-11.35	5.62
<b>-308</b>	-2.35	-2.97	-3.61	-3.80	0.0	173.4	166.2		0.0	2.41	-3.61		1.20
<b>-286</b>	-2.46	-3.09	-3.83	-3.99	0.0	150.7	144.4		0.0	2.09	-3.14		1.05

<b>-264</b>	-2.52	-3.17	-4.05	-4.18	0.0	128.0	122.6		0.0	1.78	-2.67		0.89
<b>-242</b>	-2.58	-3.26	-4.26	-4.37	0.0	105.3	100.9		0.0	1.46	-2.19		0.73
<b>-220</b>	-2.64	-3.34	-4.48	-4.56	0.0	82.6	79.1		0.0	1.15	-1.72		0.57
<b>-198</b>	-2.70	-3.43	-4.70	-4.75	0.0	59.9	57.4		0.0	0.83	-1.25		0.42
<b>-176</b>	-2.76	-3.52	-4.91	-4.93	0.0	37.2	35.6		0.0	0.52	-0.77		0.26
<b>-154</b>	-2.82	-3.60	-5.13	-5.12	0.0	14.4	13.8		0.0	0.20	-0.30		0.10
<b>-132</b>	-2.85	-3.62	-5.36	-5.35	0.0	-71.9	-68.9		0.0	-1.00	1.50		-0.50
<b>-110</b>	-2.85	-3.60	-5.59	-5.60	0.0	-211.3	-202.5		0.0	-2.93	4.40		-1.47
<b>-88</b>	-2.85	-3.57	-5.82	-5.85	0.0	-350.7	-336.1		0.0	-4.87	7.31		-2.44
<b>-66</b>	-2.85	-3.54	-6.05	-6.10	0.0	-490.1	-469.7		0.0	-4.87	7.31		-3.40
<b>-44</b>	-2.85	-3.51	-6.29	-6.35	0.0	-629.5	-603.2		0.0	-4.87	7.31		-4.37
<b>-22</b>	-2.85	-3.48	-6.52	-6.60	0.0	-768.9	-736.8		0.0	-4.87	7.31		-5.34
<b>0</b>	-2.85	-3.45	-6.75	-6.85	0.0	-908.2	-870.4		0.0	-4.87	7.31		-6.31
<b>22</b>	-2.77	-3.40	-6.46	-6.56	0.0	-789.0	-756.2		0.0	-4.87	7.31		-5.48
<b>44</b>	-2.70	-3.35	-6.18	-6.27	0.0	-669.8	-641.9		0.0	-4.87	7.31		-4.65
<b>66</b>	-2.62	-3.29	-5.89	-5.97	0.0	-550.6	-527.7		0.0	-4.87	7.31		-3.82
<b>88</b>	-2.54	-3.24	-5.60	-5.68	0.0	-431.4	-413.4		0.0	-4.87	7.31		-3.00
<b>110</b>	-2.47	-3.19	-5.31	-5.39	0.0	-312.2	-299.2		0.0	-4.34	6.50		-2.17
<b>132</b>	-2.39	-3.14	-5.03	-5.10	0.0	-193.0	-185.0		0.0	-2.68	4.02		-1.34
<b>154</b>	-2.32	-3.06	-4.77	-4.84	0.0	-128.3	-122.9		0.0	-1.78	2.67		-0.89
<b>176</b>	-2.26	-2.95	-4.56	-4.63	0.0	-128.9	-123.5		0.0	-1.79	2.69		-0.90
<b>198</b>	-2.20	-2.83	-4.35	-4.41	0.0	-129.5	-124.1		0.0	-1.80	2.70		-0.90
<b>220</b>	-2.14	-2.72	-4.14	-4.20	0.0	-130.2	-124.7		0.0	-1.81	2.71		-0.90
<b>242</b>	-2.08	-2.61	-3.93	-3.98	0.0	-130.8	-125.3		0.0	-1.82	2.72		-0.91
<b>264</b>	-2.02	-2.49	-3.72	-3.77	0.0	-131.4	-125.9		0.0	-1.83	2.74		-0.91
<b>286</b>	-1.96	-2.38	-3.51	-3.55	0.0	-132.1	-126.5		0.0	-1.83	2.75		-0.92
<b>308</b>	-1.85	-2.27	-3.31	-3.35	0.0	-95.4	-91.4		0.0	-1.33	1.99		-0.66

<b>330</b>	-1.75	-2.17	-3.10	-3.15	0.0	-55.0	-52.8		0.0	-0.76	1.15		-0.38
<b>352</b>	-1.64	-2.06	-2.90	-2.95	0.0	-14.7	-14.1		0.0	-0.20	0.31		-0.10
<b>374</b>	-1.53	-1.96	-2.70	-2.75	0.0	25.7	24.6		0.0	0.36	-0.54		0.18
<b>396</b>	-1.43	-1.85	-2.49	-2.55	0.0	66.1	63.3		0.0	0.92	-1.38		0.46
<b>418</b>	-1.32	-1.75	-2.29	-2.35	0.0	106.4	102.0		0.0	1.48	-2.22		0.74
<b>440</b>	-1.21	-1.63	-2.09	-2.16	0.0	-172.5	-114.4	524.8	0.0	-2.40	12.08	-16.97	7.29
<b>462</b>	-1.08	-1.49	-1.89	-1.99	0.0	-83.7	-43.6	396.6	0.0	-1.16	7.83	-12.18	5.51
<b>484</b>	-0.96	-1.36	-1.70	-1.82	0.0	5.1	27.1	268.4	0.0	0.07	3.59	-7.39	3.73
<b>506</b>	-0.84	-1.22	-1.50	-1.65	0.0	93.9	97.8	140.3	0.0	1.30	-0.66	-2.59	1.95
<b>528</b>	-0.72	-1.09	-1.31	-1.48	0.0	182.8	168.5	12.1	0.0	2.54	-4.91	2.20	0.17
<b>550</b>	-0.59	-0.95	-1.11	-1.31	0.0	271.6	239.3	-116.1	0.0	3.77	-9.16	7.00	-1.61
<b>572</b>	-0.47	-0.81	-0.92	-1.14	0.0	360.4	310.0	-244.2	0.0	5.01	-13.40	11.79	-3.39
<b>594</b>	-0.39	-0.69	-0.77	-0.97	0.0	329.4	282.5	-234.1	0.0	4.58	-12.40	11.08	-3.25
<b>616</b>	-0.33	-0.57	-0.64	-0.80	0.0	271.9	233.2	-193.2	0.0	3.78	-10.24	9.14	-2.68
<b>638</b>	-0.26	-0.45	-0.50	-0.63	0.0	214.4	183.8	-152.3	0.0	2.98	-8.07	7.21	-2.12
<b>660</b>	-0.19	-0.33	-0.37	-0.46	0.0	156.9	134.5	-111.5	0.0	2.18	-5.91	5.28	-1.55
<b>682</b>	-0.12	-0.21	-0.23	-0.29	0.0	99.4	85.2	-70.6	0.0	1.38	-3.74	3.34	-0.98

The empty cells of Table B-2 indicated a shear stud failure. The cells, which were shaded with green, show a hinge formation at the interior top flange of the intact girder. The hinge length was equal to eight times the width of a strip, since it was found that the moment at the interior top flange of the intact girder exceeded the nominal moment capacity of the concrete deck at eight strips. The hinge formation, following the pull out of the shear studs at the interior top flange of the fractured girder, resulted in a mechanism of the strip beam. For this reason the reactions of the top flange of the intact girder for these eight strips became constant. The analysis of the Simplified Strip model indicated that the bridge had adequate capacity to sustain the design truck load in the event of a fracture occurred at the centerline of one of its girders. The Yield Line Model was used to estimate the ultimate load that the FSEL bridge could sustain.

#### **B.8 ANALYSIS OF FSEL BRIDGE USING THE YIELD LINE MODEL**

Following the procedure of the Yield Line Model described in Chapter 5 the ultimate load was estimated. The unit moment capacity of a 1-ft strip concrete deck was calculated in a similar way as the moment capacity of the 22-in wide strip, which was described in Appendix A. Table B-3 summarizes the basic parameters of the FSEL bridge.



Table B-3: Basic parameters of the FSEL bridge

<i>Span Length</i>		
$L$	120.00	ft
<i>Outer Horizontal Curvature</i>		
$R$	1377.00	ft
<i>Distance of the deck's outer edge from the intact girder's interior top flange</i>		
$b$	14.17	ft
<i>Moment Capacity of the Deck</i>		
$m_{nT}$	17.62	kip-ft
$m_{nL}$	10.27	kip-ft
$m_{pT}$	22.74	kip-ft
$m_{pL}$	14.76	kip-ft
<i>Moment Capacity of the Railing</i>		
$M_n$	416.27	kip-ft

Following the procedure described in Chapter 5, Table B-4 can be constructed. All the variables presented in this table are defined as follows:

1.  $a$  is equal to the horizontal distance from point A or D to the origin.
2.  $\theta_i$  (radians) is the angle measured from the positive  $x$ -axis to the radial line that connects the origin with points D, C, or B (line OD, OC, OB in Figure 5-9).
3.  $X_i, Y_i$  are the coordinates of points A, B, C, and D.
4.  $l$  is the length of each yield line, and it is calculated by inserting the end point coordinates into the distance formula (Equation 5-4).
5.  $\alpha$  is the angle of each yield line with the horizontal axis (Equation 5-3)
6. The moment capacity ( $m_b$ ) of each hinge line is calculated according to Equation 5-2.

7.  $h_i$  is the height of DOC, COB, or BOA triangle.
8.  $\theta_{rotation}$  is the angle of rotation of each plane (DOC, COB, and BOA) with respect to the horizontal for yield lines along the perimeter; for diagonal yield lines,  $\theta_{rotation}$  is the angle of rotation between two adjacent planes (e.g., DOC with COB, and COB with BOA)
9. The last factors ( $dIW$ ,  $IW_{Hinge}$ ,  $IW_{Railing}$ ,  $IW_{TOTAL}$ ) are, respectively, the internal work (IW) of each hinge line, the summation of the yield lines IW, the IW of the railing, and the total IW.

Table B-4: Internal work calculation for FSEL bridge

$a$ (ft)		$\theta_i$ (rad)	$X$	$Y$	$\ell$	$\alpha$	$m_b$	$h$	$\vartheta_{rotation}$	$dIW$	$IW_{Hinge}$
41	Perimeter	0.015	41.0	0.6							116.71
		0.611	20.2	14.2	24.8	0.58	14.5	22.9	0.044	15.72	$IW_{Railing}$
		2.531	-20.2	14.2	40.5	0.00	16.6	14.2	0.071	47.50	52.54
		3.127	-41.0	0.6	24.8	2.56	14.5	22.9	0.044	15.72	$IW_{TOTAL}$
	Diagonals				24.7	0.61	18.4		0.0415	18.88	169.25
					24.7	0.61	18.4		0.0415	18.88	

As mentioned previously, the length  $a$  and the magnitude of the truck load are mutually dependent. Accordingly, one of these variables should be fixed in order to obtain the other one. It is recommended that the live load magnitude corresponding to the number of trucks be selected first; with this value set, the length  $a$  for the given load magnitude can be obtained. A good starting value is 2×HS-20 trucks. If a valid solution for the length  $a$  is computed, the given truck load is a possible failure loading. In subsequent iterations, the truck load should be decreased until a valid solution for  $a$  no

longer exists. The minimum truck load is the last one that gave a physically admissible solution for the length  $a$ . In contrast, if the initially chosen truck load does not provide a physically admissible solution for the length  $a$ , then the truck load needs to be increased in subsequent iterations.

Once the length  $a$  has been computed, all the variables associated with the Yield Line Model can be calculated. After several iterations, the minimum wheel multiplier was computed to be equal to 3.66. As a result, the front wheel and middle/rear wheel loads are equal to 14.64 kips and 58.56 kips, respectively. Table B-5 summarizes the external work calculation for the minimum truck load multiplier of 3.66.

Table B-5: External work calculation of the truck load

Truck Load	Truck Load						
	$P$	$X_{point\ Load}$	$Y_{point\ Load}$	$r_{LOAD}$	$r$	$\delta_i$	$EW$
Front Wheel	14.66	14	3.42	14.41	31.41	0.54	7.93
Front Wheel	14.66	14	9.42	16.87	24.89	0.32	4.72
Middle Wheel	58.63	0	3.42	3.42	14.17	0.76	44.48
Middle Wheel	58.63	0	9.42	9.42	14.17	0.34	19.65
Rear Wheel	58.63	-14	3.42	14.41	31.41	0.54	31.73
Rear Wheel	58.63	-14	9.42	16.87	24.89	0.32	18.89
<b>EW<sub>TRUCK</sub></b>							127.41
<b>EW<sub>DL</sub></b>							41.84
<b>EW<sub>TOTAL</sub> - IW<sub>TOTAL</sub></b>							0.00

The Yield Line Model indicated that the ultimate load capacity of the FSEL bridge was 3.66×HS-20 Trucks or 263.52 kips, which is smaller than the actual load of 363.75 kips that the bridge carried during the test. As previously mentioned, the difference between the estimated and actual load capacity is due to two reasons. First, the point

loads used in the analysis produce a larger moment than the distributed load used in the test because of the way in which the road base was distributed and positioned on the bridge. Second, the positive moment capacity of the railing used for estimating the bridge capacity is smaller than the observed one because of the assumptions made in defining the effective width of the concrete deck that contributes to the railing response. These assumptions were made to ensure a conservative estimate of the overall capacity of a bridge following the fracture of one of its girders.

The initial strength checks for the bridge, which were performed earlier, should be recalculated for the truck load of  $3.66 \times \text{HS-20}$  (263.52 kips). As before, the moment at the mid-span of the intact girder produced by this increased truck load is found to be 13,944 kip-ft, which is less than the plastic moment capacity of the intact girder section.

$$M_p = 250,047.67 \text{ kip-in.} = 20,837.31 \text{ kip-ft} > 13,944 \text{ kip-ft}$$

The force needed to be transferred is found to be:

$$F = (0.427 + 2.33/2 + 0.65/2) \cdot 120 + 263.52 = 493.56 \text{ kips}$$

$$F = 493.56 \text{ kips}$$

The length of the bridge needed to transfer the load  $F$  based on the flexural capacity of the bridge is:

$$l_M = 493.56 / 7.39 = 66.79 \text{ ft}$$

$$66.79 / 120 = \mathbf{55.66 \% \text{ of the span length}}$$

The flexural shear at the end support is found to be:

$$V = V_{DL} + V_{TRUCK} = (2 \cdot 0.427 + 2.33 + 0.65) \cdot 120 / 2 + 142$$

$$V = 372 \text{ kips}$$

The torques due to each load are equal to:

$$t_{FG} = 51.24 \cdot 12 = 614.88 \text{ kips}\cdot\text{ft}$$

$$t_{RFG} = 39 \cdot 17.17 = 669.63 \text{ kips}\cdot\text{ft}$$

$$t_{DFG} = 139.8 \cdot 11.83 = 1,653.83 \text{ kips}\cdot\text{ft}$$

$$t_{IG} = 51.24 \cdot 0 = 0 \text{ kips}\cdot\text{ft}$$

$$t_{RIG} = 39 \cdot 5.17 = 201.63 \text{ kips}\cdot\text{ft}$$

$$t_{DIG} = 139.8 \cdot 0.17 = 23.77 \text{ kips}\cdot\text{ft}$$

$$t_{TRUCK} = 263.52 \cdot 11.25 = 2,964.6 \text{ kip}\cdot\text{ft}$$

Assuming that half of the calculated torque is applied to each end of the intact girder, the torque developed at the end section is equal to:

$$T = (614.88 + 669.63 + 1,653.83 - 201.63 - 23.77 + 2,964.6) / 2 = 2,838.77 \text{ kip}\cdot\text{ft}$$

Knowing the applied torque at the end support, the shear flow of the end section is calculated to be:

$$q = T / (2 \cdot A) = 2,838.77 / (2 \cdot 3850.36/144) = 53.08 \text{ kips/ft} = 4.42 \text{ kips/in}$$

The shear stresses in the concrete deck, webs, and bottom flange are computed by following the same procedure as before.

$$\tau_{CONC. DECK} = q / t_{CONC. DECK} = 4.42 / 8 = 0.55 \text{ ksi}$$

$$\tau_{WEB} = q / t_{WEB} = 4.42 / 0.5 = 8.84 \text{ ksi}$$

$$\tau_{BOTT. FLANGE} = q / t_{BOTT. FLANGE} = 4.42 / 0.75 = 5.89 \text{ ksi}$$

$$\tau_{Flexural WEB} = V / (2 \cdot h_{WEB} \cdot t_{WEB} \cdot \cos(14^\circ)) = 372 / (2 \cdot 58.754 \cdot 0.5 \cdot 0.97) = 6.53 \text{ ksi}$$

The shear stress, which develops in the concrete deck due to torsion, is equal to 0.55 ksi. According to ACI 318-08, the shear capacity of a reinforced concrete section is  $V_S = A_t \cdot f_{yt} \cdot b \cdot \cot\theta / s$ . As a result,

$$V_{TORSION} = q \cdot b = 4.42 \cdot 72 = 318.24 \text{ kips} \leq V_S = A_t \cdot f_{yt} \cdot b \cdot \cot\theta / s = 0.62 \cdot 60 \cdot 72 / 6 = 446.4 \text{ kips}$$

The shear stress in the webs is a combination of the flexural and the torsional shear stresses. As shown in Figure B-8, the shear stresses add together in the east web, and they must be subtracted in the west web. The east web controls in this case. The total shear stress that develops in the east web is calculated to be:

$$\tau_{TOTAL} = \tau_{WEB} + \tau_{Flexural WEB} = 8.84 + 6.53 = 15.37 \text{ ksi which is bigger than } \tau_n = 11.14 \text{ ksi.}$$

Regarding the end diaphragm, the shearing forces at each edge of the end diaphragm are equal to:

$$V_{ED} = T / l_b = 2,838.77 / 12 = 236.56 \text{ kips}$$

where  $T$  is the torque applied on the intact girder, and  $l_b$  is the distance between the two bearings. Thus, the shear strength of the end diaphragm ( $V_n = 0.29 \cdot 991.8 = 287.62 \text{ kips}$ ) is adequate to resist the applied shearing force ( $V_{ED} = 236.56 \text{ kips}$ ).

Summarizing the calculations, it is found that the web stresses of the end section exceed the nominal stress before the collapse of the bridge. This result indicates that the webs would buckle under the applied load. Buckling of the webs, however, was not observed in the test. The difference between the predicted response and the observed behavior stems from some of the assumptions made in the development of the simplified

analysis procedure to compute the response of a twin steel box-girder bridge following the fracture of one of its girders. The buckling capacity of the webs in shear is based on simply supported boundary conditions. The actual boundary conditions in a box girder may approach a fixed condition. Moreover, in experimental studies of composite girders, the webs of end panels were able to reach their tension field capacity. In the calculations performed for this example, the buckling capacity of the girder webs is low due to the large stiffener spacing in the last panels, which exceed the AASHTO maximum spacing requirements. Based upon the web buckling capacity computed using the AAHTO specifications, however, the estimated bridge capacity would be 1.48 HS-20 trucks (106.56 kips). The variation in the results computed with the simplified modeling approach suggests that, in certain cases, it may be desirable to perform detailed finite element analyses to compute the stresses in critical components.

## APPENDIX C

### Analysis of the Woodway Bridge (Span 11) using the simple models

#### C.1 INTRODUCTION

This example focuses on span 11 of the Woodway exit ramp on IH 610/Katy Freeway. This bridge is simply supported and straight (i.e.,  $R=\infty$ ), and its total is 199.5 ft. Figure C-1 shows the elevation view of Woodway Bridge Span 11 and other general information. The top and bottom flange thickness changed along the span of the bridge. Table C-1 summarizes all the dimensions of both flanges along the span of the bridge. Only three steel sections were used along the length of the span. The Transition sections occurred due to different cutoff points for the top and bottom flanges. Figure C-2 and C-3 present the typical cross-section of the bridge and steel girder respectively. A typical SSTR section was used as railing. Since the bridge drawings did not provide information for the expansion joints, it was assumed that there were 0.75 in. wide expansion joints every 30 ft.

Table C-1: General information of bottom and top flange

Type of Section	Length of application measured from south (ft)	Bottom Flange		Top Flange	
		$t_{BF}$ (in)	$b_{BF}$ (in)	$t_{TF}$ (in)	$b_{BF}$ (in)
End Section	0-52	1.50	44.5	1.25	18
Transition Section	52-60	2.00	44.5	1.25	18
Middle Section	60-139.5	2.00	44.5	1.75	18
Transition Section	139.5-147.5	2.00	44.5	1.25	18
End Section	147.5-199.5	1.50	44.5	1.25	18



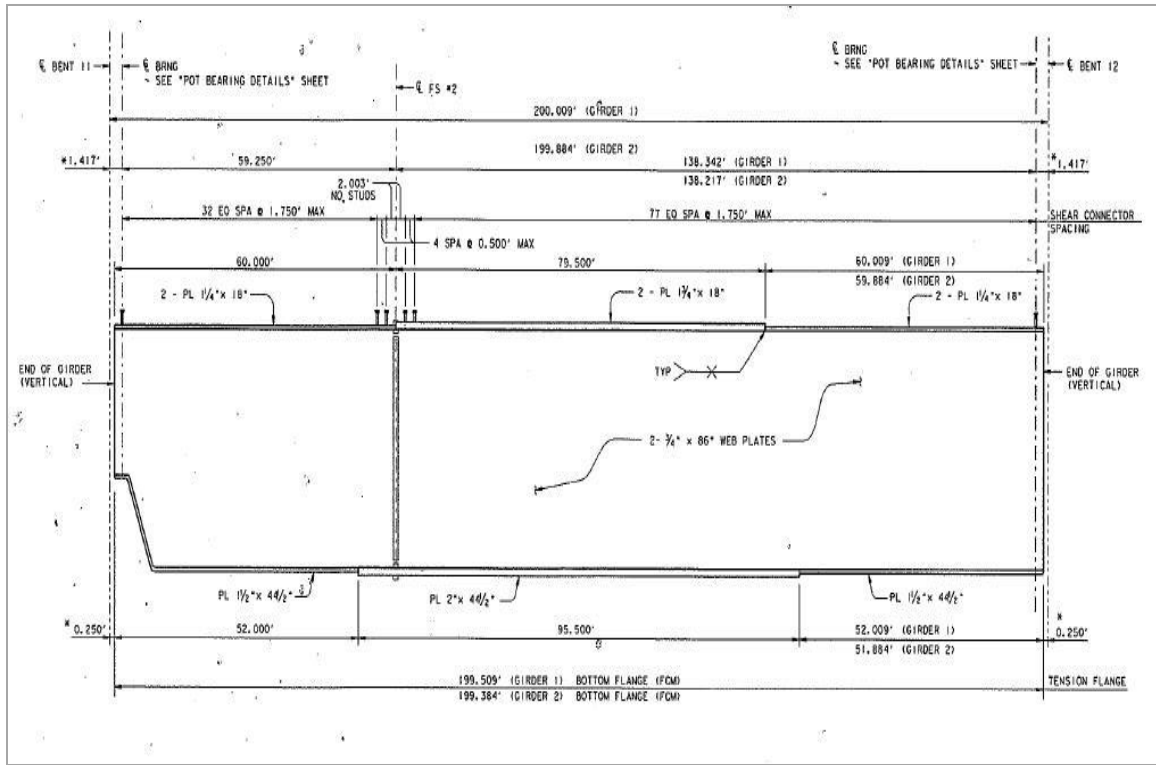


Figure C-1: Elevation view of Woodway Bridge Span 11

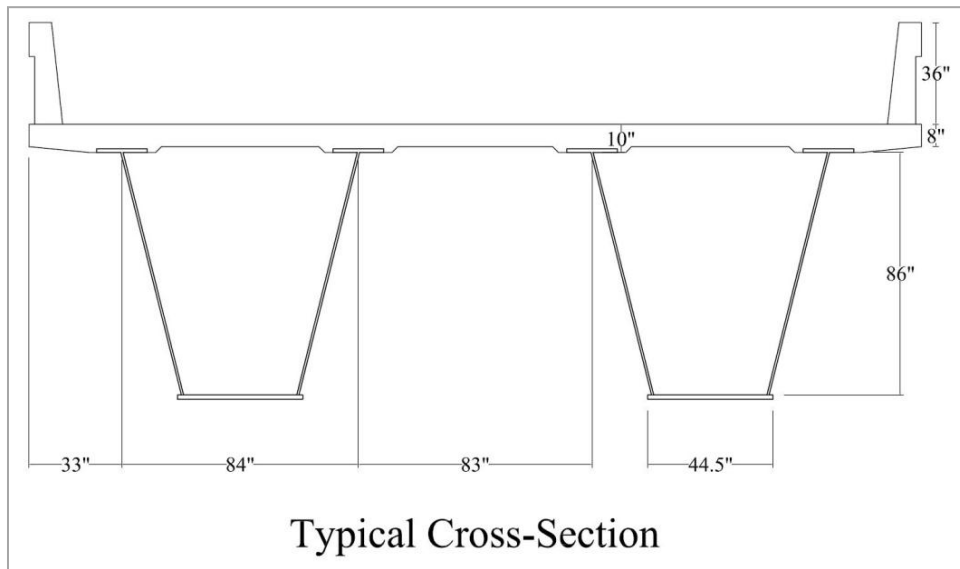


Figure C-2: Typical cross-section of the Woodway Bridge Span 11

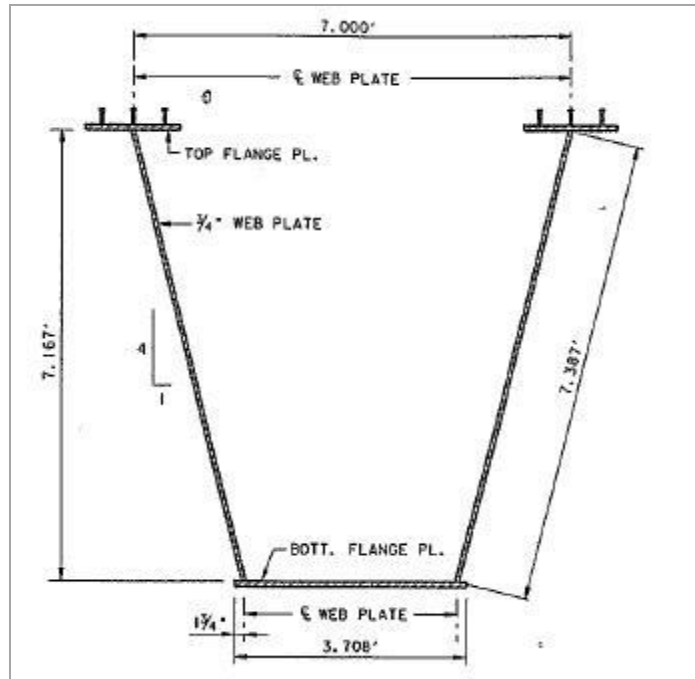


Figure C-3: Typical cross-section of the steel girder of the Woodway Bridge Span 11

## C.2 CALCULATION OF THE TRANSMITTED LOAD TO THE INTACT GIRDER

It was assumed that half of the entire weight of the bridge and the entire live load on the bridge was needed to be resisted from the intact girder at even of a fracture occurred. These loads were calculated below:

### Weight of one steel box girder:

$$W_{girder} = 1.15 \cdot (244.72/144 \text{ ft}^2) \cdot (0.490 \text{ kips/ft}^3) = 0.958 \text{ kip/ft (End Section)}$$

$$W_{girder} = 1.15 \cdot (266.95/144 \text{ ft}^2) \cdot (0.490 \text{ kips/ft}^3) = 1.044 \text{ kip/ft (Transition Section)}$$

$$W_{girder} = 1.15 \cdot (284.97/144 \text{ ft}^2) \cdot (0.490 \text{ kips/ft}^3) = 1.116 \text{ kip/ft (Middle Section)}$$

Notes: This was the weight of one girder. Cross-sectional areas of End, Transition, and Middle section were 244.72 in<sup>2</sup>, 266.95 in<sup>2</sup> and 284.97 in<sup>2</sup> respectively. Density of steel was taken as 490 lb/ft<sup>3</sup>. To account for internal diaphragms, stiffeners, etc., the weight of the steel girder was multiplied by a factor of 1.15.

**Concrete deck:**

$$W_{deck} = (317 \cdot 8 / 144 \text{ ft}^2) \cdot (0.150 \text{ kip/ft}^3) = 2.642 \text{ kip/ft}$$

Notes: Width of concrete deck was 26 ft-5 in. = 317 in. Density of concrete was taken as 150 lb/ft<sup>3</sup>. Deck thickness was 8 in.

**SSTR Railing**

$$W_{railings} = 2 \cdot (312/144 \text{ ft}^2) \cdot (0.150 \text{ kip/ft}^3) = 0.65 \text{ kip/ft}$$

Notes: Multiplied by 2 to account for two rails. Cross-sectional area of one rail was calculated to be 312 in<sup>2</sup>

**Simulated Truck (HS-20)**

$$W_{truck} = 2 \cdot 72 \text{ kips} = 144 \text{ kips (with a load factor of 2)}$$

**Load to be transmitted**

$$F = \Sigma(W_{girder\ i} \cdot L_i) + (W_{deck}/2 + W_{railings}/2) \cdot L + W_{truck}$$

$$F = (0.958 \cdot 104 + 1.044 \cdot 16 + 1.116 \cdot 79.5) + (2.642 + 0.65) \cdot 199.5/2 + 144 = 677.4 \text{ kips}$$

$$F = 677.4 \text{ kips}$$

### C.3 CALCULATION OF MAXIMUM MOMENT ON THE BRIDGE

#### Moment due to dead load

The moment at the mid-span was calculated to be  $M_{DL} = 27,102.23$  kip-ft. Moreover, it was found that  $M_{DL}(52)$  and  $M_{DL}(60)$  were 20,783.66 kip-ft and 22,720.33 kip-ft respectively.

#### Moment due to truck load

As before, the middle axle of the 144-kip truck load is positioned at the centerline of the bridge. The maximum moment at the mid-span of the bridge due to both the dead load and the truck load is calculated to be  $M_{max}=33,724$  kip-ft. By superimposing the moment diagrams for these loads, the moments at the flange transitions are  $M(52)=24,703$  kip-ft and  $M(60)=27,242$  kip-ft.

### C.4 ANALYSIS OF COMPOSITE SECTION

The plastic moment capacity of the intact girder was calculated so to be checked if the intact girder had enough flexural capacity to sustain the whole load applied on the bridge and the dead load. All the three different composite sections described above would be checked. The specified minimum yield strength of  $f_y = 50$  ksi was used in the calculations.

#### Middle Section

Find the plastic neutral axis by setting  $T = C$ :

$$T = A_s \cdot f_y = (44.5 \cdot 2 + 2 \cdot 88.644 \cdot 0.75 + 2 \cdot 18 \cdot 1.75) \cdot 50 = 14,248.3 \text{ kips}$$

$$C_c = 0.85 \cdot f_c' \cdot t_s \cdot b_{eff} = 0.85 \cdot 4 \cdot 8 \cdot 158.5 = 4,311.2 \text{ kips}$$

Since  $T > C$  then the plastic neutral axis was in the girder.

$$C_s = (A_s \cdot f_y - C_c) / 2 = (14,248.3 - 4,311.2) / 2 = 4,968.55 \text{ kips}$$

Using this equation, the compressive force needed to be developed in the steel section in order to achieve equilibrium ( $C = T$ ), was determined.

$$C_{tfl} = 2 \cdot t_{tfl} \cdot b_{tfl} \cdot f_y = 2 \cdot 1.75 \cdot 18 \cdot 50 = 3150 \text{ kips}$$

The top flanges could resist 3150 kips in compression which was less than required to obtain equilibrium. As a result the PNA fell in the web. Assume that  $x$  was the distance of the neutral axis from the bottom of the top flange (Figure C-4), then the depth of the neutral axis in the webs could be determined as a function of the depth:

$$x = (4,968.55 - 3150) / (2 \cdot 0.75 \cdot (17/16)^{0.5} \cdot 50) = 23.52 \text{ in.}$$

Note: The  $(17/16)^{0.5}$  factor was based on the slope of the web.

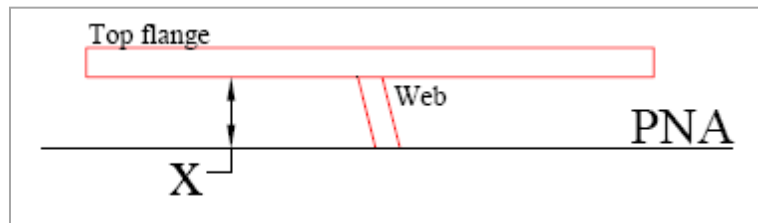


Figure C-4: Plastic neutral axis location

So:

$$C_c = 4,311.2 \text{ kips}$$

$$C_{tfl} = 3150 \text{ kips}$$

$$C_{web} = 1818.55 \text{ kips}$$

$$T_{web} = A_{web} \cdot f_y = 2 \cdot 0.75 \cdot (86-23.52) \cdot (17/16)^{0.5} \cdot 50 = 4830.22 \text{ kips}$$

$$T_{bottom\ flange} = A_{bottom\ flange} \cdot f_y = 44.5 \cdot 2 \cdot 50 = 4450 \text{ kips}$$

By taking moments about the PNA, the nominal plastic moment capacity was calculated:

$$M_{bottom\ flange} = T_{bottom\ flange} \cdot (1 + 86 - 23.52) = 282,486 \text{ kip-in.}$$

$$M_{web} = C_{web} \cdot 23.52/2 + T_{web} \cdot (86-23.52) / 2 = 172,282.22 \text{ kip-in.}$$

$$M_{C\ tfl} = C_{tfl} \cdot (1.75/2 + 23.52) = 76,844.25 \text{ kip-in.}$$

$$M_{C\ concrete} = C_c \cdot (4 + 2 + 23.52) = 127,266.62 \text{ kip-in.}$$

Note: The 2-in. term added in the moment arm accounted for distance of the bottom of the concrete deck from the bottom of the top flange.

$$\text{Thus, } M_P = 282,486 + 172,282.22 + 76,844.25 + 127,266.62$$

$$M_{P\ Middle\ Section} = 658,879.09 \text{ kip-in.} = 54,906 \text{ kip-ft}$$

Earlier,  $M_{max}$  was found to be 33,724 kip-ft. The plastic moment capacity had more than enough capacity to sustain the whole dead load of the bridge plus the live truck load.

Following the same procedure, the plastic moment capacity of the Transition and End section were calculated and found to be larger than the maximum moment which would be applied to these sections if a fracture of the outer girder occurred.

$$M_{P \text{ Transition Section}} = 633,734 \text{ kip-in.} = 52,811 \text{ kip-ft} > M(60) = 27,242 \text{ kip-ft}$$

$$M_{P \text{ End Section}} = 564,757 \text{ kip-in.} = 47,063 \text{ kip-ft} > M(52) = 24,703 \text{ kip-ft}$$

### C.5 ANALYSIS OF CONCRETE DECK

As before, the bending and shear capacity of the concrete deck were checked to ensure that they were adequate to resist the moment and the shear produced by the unsupported load of the fractured girder. These capacities were based on a 1-ft wide transverse deck section as shown in the Figure C-5.

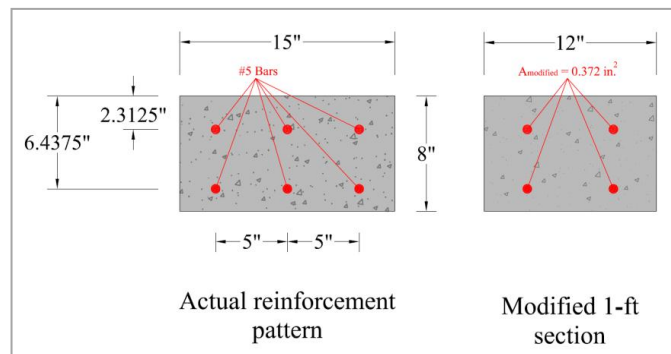


Figure C-5: Actual and modified 1-ft wide section of the concrete deck in the transverse direction

### Positive Moment Capacity

The assumed strain and stress failure profile are shown in the figure below:

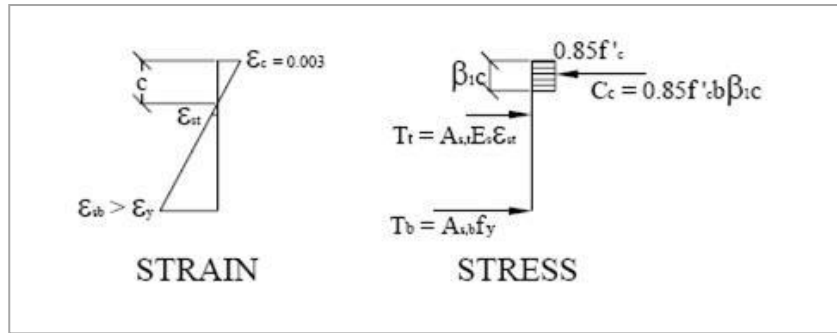


Figure C-6: Strain and stress gradients at positive moment regions

According to ACI 318-08, it was assumed that the ultimate strain of concrete was 0.003 in./in. and the bottom reinforcement had yielded prior to failure. The top reinforcement was always included in the calculations for more accurate results. The concrete strength was taken as 4 ksi and the reinforcement strength as 60 ksi, their nominal strength specified in the bridge plans.

Let  $C = T$ :

$$C = 0.85 \cdot f'_c \cdot \beta_1 \cdot c \cdot b = 0.85 \cdot 4 \cdot 0.85 \cdot 12 \cdot c = 34.68 \cdot c$$

Note:  $\beta_1 = 0.85$  for 4 ksi concrete.

$$\varepsilon_{s, \text{bottom}} = 0.003 \cdot (6.4375 - c) / c$$

$$\varepsilon_{s, \text{top}} = 0.003 \cdot (2.3125 - c) / c$$

$$T_{\text{bottom}} = A_{s, \text{bottom}} \cdot f_y = 2 \cdot 0.372 \cdot 60 = 44.64 \text{ kips}$$

$$T_{\text{top}} = A_{s, \text{top}} \cdot \varepsilon_{s, \text{top}} \cdot E_s = 2 \cdot 0.372 \cdot 29,0000 \cdot \varepsilon_{s, \text{top}} = 21,576 \cdot \varepsilon_{s, \text{top}}$$

$$34.68 \cdot c = 44.64 + 21,576 \cdot \varepsilon_{s, \text{top}}$$



$$34.68 \cdot c = 44.64 + 21,576 \cdot 0.003 \cdot (2.3125 - c) / c$$

Iterate until the neutral axis depth was found. Solution:  $c = 1.808$  in.

$$\varepsilon_{s, bottom} = 0.00768 > \text{Yield strain} (= 0.00207 \text{ for } 60 \text{ ksi})$$

$$\varepsilon_{s, top} = 0.000837 < \text{Yield strain} (= 0.00207 \text{ for } 60 \text{ ksi})$$

$$C = 80.82 \text{ kips}$$

$$T_{bottom} = 44.64 \text{ kips}$$

$$T_{top} = 18.06 \text{ kips}$$

Take moments about the NA to solve for nominal moment capacity

$$M_n^+ = C \cdot (c - \beta_1 \cdot c / 2) + T_{top} \cdot (2.3125 - c) + T_{bottom} \cdot (6.4375 - c)$$

$$M_n^+ = 80.82 \cdot (1.808 - 0.85 \cdot 1.808 / 2) + 18.06 \cdot (2.3125 - 1.808) + 44.64 \cdot (6.4375 - 1.808)$$

$$\boxed{M_n^+ = 299 \text{ kip-in.} = 24.98 \text{ kip-ft}}$$

### Negative Moment Capacity

The assumed strain and stress failure profile are shown in the figure below:

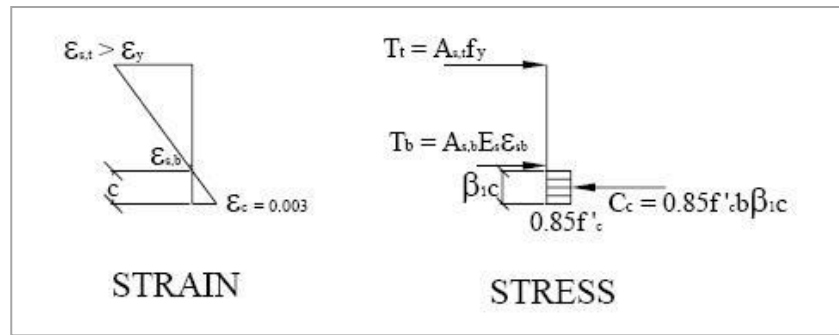


Figure C-7: Strain and stress gradients at negative moment regions

According to ACI 318-08, it was assumed that the ultimate strain of concrete was 0.003 in./in. and the top reinforcement had yielded prior to failure. The bottom reinforcement was always included in the calculations for more accurate results. The concrete strength was taken as 4 ksi and the reinforcement strength as 60 ksi.

Let  $C = T$ :

$$C = 0.85 \cdot f'_c \cdot \beta_1 \cdot c \cdot b = 0.85 \cdot 4 \cdot 0.85 \cdot 12 \cdot c = 34.68 \cdot c$$

Note:  $\beta_1 = 0.85$  for 4 ksi concrete.

$$\varepsilon_{s, \text{bottom}} = 0.003 \cdot (1.5625 - c) / c$$

$$\varepsilon_{s, \text{top}} = 0.003 \cdot (5.6875 - c) / c$$

$$T_{\text{bottom}} = A_{s, \text{bottom}} \cdot \varepsilon_{s, \text{bottom}} \cdot E_s = 2 \cdot 0.372 \cdot 29,0000 \cdot \varepsilon_{s, \text{bottom}} = 21,576 \cdot \varepsilon_{s, \text{bottom}}$$

$$T_{\text{top}} = A_{s, \text{top}} \cdot f_y = 2 \cdot 0.372 \cdot 60 = 44.64 \text{ kips}$$

$$34.68 \cdot c = 44.64 + 21,576 \cdot \varepsilon_{s, \text{bottom}}$$

$$34.68 \cdot c = 44.64 + 21,576 \cdot 0.003 \cdot (1.5625 - c) / c$$

Iterate until the neutral axis depth was found. Solution:  $c = 1.443$  in.

$$\varepsilon_{s, \text{bottom}} = 0.000248 < \text{Yield strain (= 0.00207 for 60 ksi)}$$

$$\epsilon_{s, top} = 0.008824 > \text{Yield strain} (= 0.00207 \text{ for } 60 \text{ ksi})$$

$$C = 50.04 \text{ kips}$$

$$T_{bottom} = 5.35 \text{ kips}$$

$$T_{top} = 44.64 \text{ kips}$$

Take moments about the NA to solve for nominal moment capacity

$$M_n = C \cdot (c - \beta_1 \cdot c / 2) + T_{top} \cdot (5.6875 - c) + T_{bottom} \cdot (1.5625 - c)$$

$$M_n = 50.04 \cdot (1.443 - 0.85 \cdot 1.808/2) + 44.64 \cdot (5.6875 - 1.808) + 5.35 \cdot (1.5625 - 1.808)$$

$$M_n = 205 \text{ kip-in.} = 17.13 \text{ kip-ft}$$

### Bending Capacity Check

The deflected shape of the concrete deck and the bending moment diagram, if it is assumed that the shear studs have enough tensile capacity, is shown in Figure C-8:

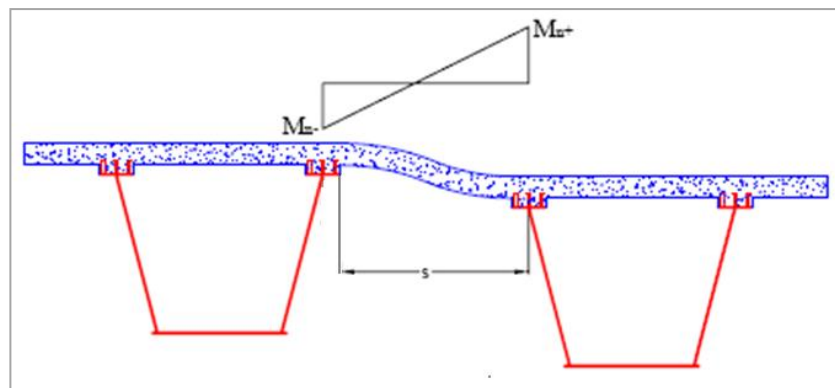


Figure C-8: Deflected shape and moment diagram before any failure of shear studs

$$V = (M_n^+ + M_n^-)/s = (24.98 \text{ kip-ft} + 17.13 \text{ kip-ft})/6.17 \text{ ft} = \mathbf{6.83 \text{ kips}}$$

Note: The spacing,  $s$ , is equal to the distance between the mid-width of the fractured girder's interior top flange and the edge of the interior top flange of the intact girder (6 ft–2 in.).

The shear capacity us calculated using the ACI 3108-08 equation for shear shown below. The capacity is again based on a 1-ft wide transverse deck section. The depth used in this equation is the depth to the centroid of the tension reinforcement (6.4375 in.).

$$V_c = 2 \cdot \sqrt{f'_c} \cdot b \cdot d = 2 \cdot \sqrt{4000} \cdot 12 \cdot 6.4375 = \mathbf{9.77 \text{ kips}}$$

Thus, the shear associated with the plastic deck mechanism controls (6.83 kips/ft), and the total length required to transfer the 677.4-kip force is:

$$l_M = 677.4 / 6.83 = 99.18 \text{ ft}$$

$$99.18 / 199.5 = \mathbf{49.71 \% \text{ of the span length}}$$

## **C.6 SHEAR STUD CHECK**

As in Appendix B, the tensile strength of a shear stud group is determined based on the guidelines recommended by Mouras (2008). The shear stud connections used in span 11 of the Woodway Bridge consist of a group of three 6-in tall shear studs spaced transversely. The haunch differs along the length of the bridge from 0.25 in. to 0.5 in. By using the modified ACI 318-08 equations presented in Appendix B (and shown again below for convenience), the tensile capacity of the shear stud group is calculated to be 19.06 kips throughout the bridge.

$$N_b = k_c \cdot \sqrt{f'_c} \cdot h_h^{1.5} \quad \text{Equation B-1 (ACI 318-08)}$$

$$N_{cbg} = \frac{A_{NC}}{A_{NCO}} \cdot \psi_{g,N} \cdot \psi_{ec,N} \cdot \psi_{ed,N} \cdot \psi_{c,N} \cdot N_b \quad \text{Equation B-2 (modified ACI 318-08)}$$

where:

$N_b$  = concrete cone breakout strength of a single isolated stud in a continuous piece of cracked concrete (22.31 kips)

$k_c = 24$  for cast-in-place shear studs

$f'_c$  = specified concrete compressive strength (4000 psi)

$h_h$  = modified height of shear stud in concrete

( $h_h = h_{ef} - d_h = 5.625 - 0.5 = 5.125$  in.  $< 18/3 = 6 \rightarrow h_h = 6$  in.)

$h_{ef}$  = effective height of shear stud in concrete, which is equal to the length of stud less the height of the stud head ( $h_{eff} = 6 - 0.375 = 5.625$  in.)

$d_h$  = haunch height (0.5 in.)

$c_{a,min}$  = distance between outer stud and the edge of flange ( $c_{a,min} = 3$  in.)

$N_{cbg}$  = design concrete breakout strength of a stud or group of studs (19.06 kips)

$A_{Nc}$  = projected concrete cone failure area of a stud group ( $A_{Nc} = 3 h_{ef} w_h = 303.75$  in<sup>2</sup>)

Note:  $A_{Nc} = 3 h_{ef} w_h$  because haunch confined full height projected cone area.

$A_{Nco}$  = projected concrete cone failure area of a single stud in continuous concrete  
( $A_{Nco} = 9h_h^2 = 324 \text{ in}^2$ )

$\Psi_{g,N}$  = group effect modification factor for studs on a bridge girder ( $\Psi_{g,N} = 0.90$  for 3 studs spaced transversely)

$\psi_{ec,N}$  = eccentric load modification factor ( $\psi_{ec,N} = 1$ )

$\psi_{ed,N}$  = edge distance modification factor ( $\psi_{ed,N} = 0.7 + 0.3 c_{a,min} / (1.5 h_{ef}) = 0.81$ )

$\psi_{c,N}$  = cracked concrete modification factor ( $\psi_{c,N} = 1.25$  for cast-in studs)

The calculated tensile capacity of the group of studs is 19.06 kips. Using Equation 3-2, it can be determined whether or not the shear studs will pull out or if a hinge will be formed in the concrete deck. A strip width equal to the shear stud spacing of 21 inches is used to calculate the tension in the stud group.

$$T = M_2/b + V = 24.98 \cdot (21/12) / 7 + 6.83 \cdot (21/12) = 18.2 \text{ kips} < 19.06 \text{ kips}$$

Because the shear stud capacity exceeds the tension generated by the deck mechanism, the shear studs do not pull out, and, as a result, hinges form in the concrete deck.

### **C.7 SHEAR CHECK OF THE COMPOSITE SECTION AT THE SUPPORTS DUE TO TORSION AND BENDING**

Once again, it was assumed that the entire weight of the bridge and live load were applied to the intact girder. The shear, which was developed at the end of the span, due to this loading was calculated below.

$$V = V_{DL} + V_{TRUCK} = 2 \cdot (0.958 \cdot 104 + 1.044 \cdot 16 + 1.116 \cdot 79.5) / 2 + (2.642 + 0.65) \cdot 199.5 / 2 + 75.4$$

$$V = 608.84 \text{ kips}$$

The unsupported load, which is first carried by the fractured girder, now has to be transferred to the intact girder. The eccentricity between the chord of the intact girder bearings and the center of gravity (CG) leads to a torque that is applied to the intact girder in addition to all the transferred loads. Due to the fact that this bridge is straight (i.e.,  $R = \infty$ ), the eccentricities of each load are equal to the distance between the CG of each load and the centerline of the intact girder. Table C-2 summarizes all the eccentricities.

Table C-2: Eccentricities of loads

	Live or Dead Load	Eccentricity
		(ft)
1	Fractured Girder (FG)	13.92
2	Railing above FG	19.83
3	Deck above FG	13.56
4	Intact Girder (IG)	0.00
5	Railing above IG	5.92
6	Deck above IG	0.35
7	Truck	11.17

Thus, the torques due to each load are equal to:

$$t_{FG} = 205.06 \cdot 13.92 = 2,854.41 \text{ kips}\cdot\text{ft}$$

$$t_{RFG} = 64.84 \cdot 19.83 = 1,285.78 \text{ kips}\cdot\text{ft}$$

$$t_{DFG} = 263.54 \cdot 13.56 = 3,573.60 \text{ kips}\cdot\text{ft}$$

$$t_{IG} = 205.06 \cdot 0 = 0 \text{ kips}\cdot\text{ft}$$

$$t_{RIG} = 64.84 \cdot 5.92 = 383.85 \text{ kips}\cdot\text{ft}$$

$$t_{DIG} = 263.54 \cdot 0.35 = 92.24 \text{ kips}\cdot\text{ft}$$

$$t_{TRUCK} = 144 \cdot 11.17 = 1,608.48 \text{ kips}\cdot\text{ft}$$

Therefore, the torque developed in the composite section at the support is equal to:

$$T = (2,854.41 + 1,285.78 + 3,573.60 - 383.85 - 92.24 + 1,608.48) / 2 = 4,423.10 \text{ kip}\cdot\text{ft}$$

To compute the shear flow of the closed section, Equation 3-20 is used.

$$q = T / (2 \cdot A) = 4,423.10 / (2 \cdot 5,923.68/144) = 53.76 \text{ kips/ft} = 4.48 \text{ kips/in}$$

The shear stress due to torsion for every component of the composite section is calculated below:

$$\tau_{CONC. DECK} = q / t_{CONC. DECK} = 4.48 / 8 = 0.56 \text{ ksi}$$

$$\tau_{WEB} = q / t_{WEB} = 4.48 / 0.75 = 5.97 \text{ ksi}$$

$$\tau_{BOTT. FLANGE} = q / t_{BOTT. FLANGE} = 4.48 / 1.25 = 3.58 \text{ ksi}$$

The flexural shear is assumed to be carried by the webs of the composite section because the contribution of the bottom flange and the concrete deck is small. The flexural shear stress in the webs of the composite section is calculated:

$$\tau_{Flexural WEB} = V / (2 \cdot h_{WEB} \cdot t_{WEB} \cdot \cos(14^\circ)) = 608.84 / (2 \cdot 88.644 \cdot 0.75 \cdot 0.97) = 4.72 \text{ ksi}$$



Note: The factor 2 accounts for the fact that the composite section consist of two webs, which share the total flexural shear. The  $\cos(14^\circ)$  accounts for the fact that the webs are not vertical.

The shear stress that is developed in the concrete deck due to torsion is equal to 0.56 ksi. According to ACI 318-08, the shear capacity of a reinforced concrete section is:

$$V_S = A_t \cdot f_{yt} \cdot b \cdot \cot\theta / s$$

As a result,

$$V_{TORSION} = q \cdot b = 4.48 \cdot 84 = 376.32 \text{ kips} \leq V_S = A_t \cdot f_{yt} \cdot b \cdot \cot\theta / s = 0.62 \cdot 60 \cdot 84 / 5 = 624.96 \text{ kips}$$

The shear stresses in the steel girder are checked according to the AASHTO Specifications. The shear stress in the webs of the end panel should be limited to either the shear-yielding or shear-buckling resistance. The nominal shear stress resistance of the web panel ( $\tau_n$ ) is computed as the product of the shear-buckling resistance to the shear yield strength ratio ( $C$ ) and the plastic shear stress ( $\tau_p$ ) (i.e.,  $\tau_n = C \cdot \tau_p$ ). The plastic shear stress is equal to  $0.58f_{yw}$ . The ratio  $C$  is determined as shown below:

$$\text{If } \frac{D}{t_w} \leq 1.12 \sqrt{\frac{Ek}{f_{yw}}} \text{ then } C=1.0$$

$$\text{If } 1.12 \sqrt{\frac{Ek}{f_{yw}}} < \frac{D}{t_w} \leq 1.40 \sqrt{\frac{Ek}{f_{yw}}} \text{ then } C = \frac{1.12}{D/t_w} \sqrt{\frac{Ek}{f_{yw}}}$$

$$\text{If } \frac{D}{t_w} > 1.40 \sqrt{\frac{Ek}{f_{yw}}} \text{ then } C = \frac{1.57}{(D/t_w)^2} \left( \frac{Ek}{f_{yw}} \right)$$

For span 11 of the Woodway Bridge  $D = 88.64$  in.,  $t_w = 0.75$  in.,  $E = 29,000$  ksi,  $f_{yw} = 50$  ksi. The buckling coefficient  $k$  is calculated as

$$k = 5 + \frac{5}{\left(d_0/D\right)^2}$$

where  $d_0$  is the spacing from the support to the first stiffener adjacent to the support (132 in.). AASHTO limits the factor  $d_0/D$  for end panels to 1.5. In the case of span 11 of the Woodway Bridge,  $d_0/D=1.49<1.5$ , so  $d_0/D=1.49$ . By inserting the value of  $d_0/D$  in the equation for  $k$ , this value is calculated to be 7.25.

$$\text{Because } \frac{D}{t_w} = \frac{88.64}{0.75} = 118.19 > 1.40 \sqrt{\frac{Ek}{f_{yw}}} = 90.78$$

$$C = \frac{1.57}{(D/t_w)^2} \left( \frac{Ek}{f_{yw}} \right) = 0.47.$$

Having all the variables defined, the nominal shear stress ( $\tau_n$ ) is equal to  $\tau_n = 0.47 \cdot 0.58 \cdot f_{yw} = 13.63$  ksi.

The shear stress in the webs is a combination of the flexural and torsional shear stresses. As shown in Figure C-9Figure , the shear stresses are added and subtracted in the east and west web, respectively. Accordingly, the east web controls because the shear from flexure and torsion add. The total shear stress that is developed in the east web is calculated to be  $\tau_{TOTAL} = \tau_{WEB} + \tau_{Flexural WEB} = 5.97 + 4.72 = 10.27$  ksi, which is less than  $\tau_n = 13.63$  ksi. Summarizing the calculations, it is found that all the components of the section have adequate capacities to sustain the applied load.

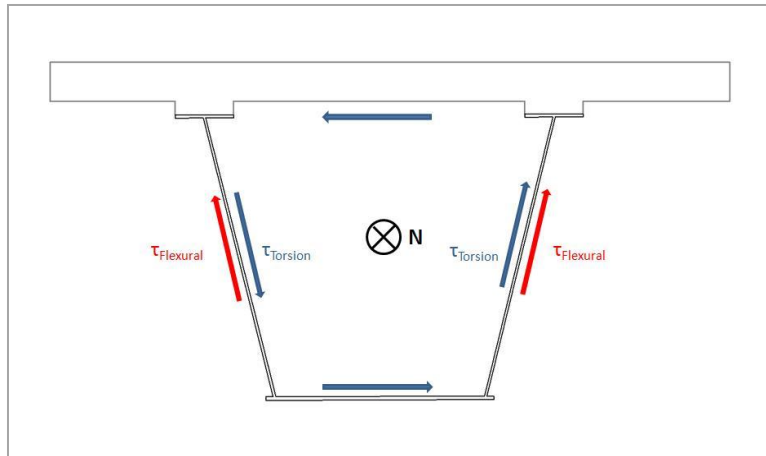


Figure C-9: Flexural and torsional shear stresses on the composite section

The end diaphragm, which connects both girders, needs to be checked to ensure that it can adequately resist the torque applied to the intact girder. The torque applied on the intact girder is equilibrated by a force couple acting at the bearings of the two girders. This force couple causes shearing of the end diaphragm. The forces acting on each side of the end diaphragm can be calculated as follows:

$V_{ED} = T / l_b = 4,423.10 / 13.92 = 317.75$  kips, where  $T$  is the torque applied on the intact girder and  $l_b$  is the distance between the two bearings. The nominal shear strength of the end diaphragm can be computed according to AASHTO Sec. 6.10.9.2:

$$V_n = C \cdot V_P$$

where  $V_P = 0.58 \cdot F_{yw} \cdot D \cdot t_w = 0.58 \cdot 50 \cdot 86 \cdot 0.75 = 1870.5$  kips, and  $C$  is calculated as:

$$C = \frac{1.57}{(D/t_w)^2} \left( \frac{Ek}{f_{yw}} \right) = 0.35 \text{ because } \frac{D}{t_w} = \frac{86}{0.75} = 114.67 > 1.40 \sqrt{\frac{Ek}{f_{yw}}} = 75.39$$

where  $k = 5$ .

Thus, the shear strength of the end diaphragm ( $V_n = 0.35 \cdot 1870.5 = 654.68$  kips) is adequate to resist the applied shearing force ( $V_{ED} = 317.75$  kips).

Summarizing the calculations, it is found that all the components of the section have adequate capacities to resist the applied load. However, because the analysis indicates that overall bridge capacity is controlled by the formation of a plastic hinge line above both interior top flanges, the ultimate load is estimated from the initial checks and not from the Yield Line Model. Following the same procedure as described above, the initial checks determine the ultimate truck load that this bridge can sustain in the event of a fracture. After several iterations, it is found that the ultimate truck load is 5.52×HS-20 (397.12 kips). The buckling shear stress in the webs of the end section controls the maximum truck load that can be sustained. The moment at the mid-span of the intact girder produced by the dead load and this 395.94 kip truck load is:

$$M_{P \text{ Middle Section}} = 54,906 \text{ kip-ft} > M_{max} = 44,824 \text{ kip-ft}$$

$$M_{P \text{ Transition Section}} = 52,811 \text{ kip-ft} > M(60) = 34,776 \text{ kip-ft}$$

$$M_{P \text{ End Section}} = 47,063 \text{ kip-ft} > M(52) = 31,229 \text{ kip-ft}$$

The force needed to be transferred is found to be:

$$F = (0.958 \cdot 104 + 1.044 \cdot 16 + 1.116 \cdot 79.5) + (2.642 + 0.65) \cdot 199.5 / 2 + 397.12 = 930.56 \text{ kips}$$

$$F = 930.56 \text{ kips}$$

The length of the bridge needed to transfer the load  $F$  based on the flexural capacity of the bridge is:

$$l_M = 930.56 / 6.83 = 136.25 \text{ ft}$$

$$136.25 / 199.5 = \mathbf{68.29 \% \text{ of the span length}}$$

The flexural shear at the end support is found to be:

$$V = V_{DL} + V_{TRUCK} = 2 \cdot (0.958 \cdot 104 + 1.044 \cdot 16 + 1.116 \cdot 79.5) / 2 + (2.642 + 0.65) \cdot 199.5 / 2 + 207.85$$

$$V = 741.28 \text{ kips}$$

The torque due to each load are equal to:

$$t_{FG} = 205.06 \cdot 13.92 = 2,854.44 \text{ kips} \cdot \text{ft}$$

$$t_{RFG} = 64.84 \cdot 19.83 = 1,285.78 \text{ kips} \cdot \text{ft}$$

$$t_{DFG} = 263.54 \cdot 13.56 = 3,573.60 \text{ kips} \cdot \text{ft}$$

$$t_{IG} = 205.06 \cdot 0 = 0 \text{ kips} \cdot \text{ft}$$

$$t_{RIG} = 64.84 \cdot 5.92 = 383.85 \text{ kips} \cdot \text{ft}$$

$$t_{DIG} = 263.54 \cdot 0.35 = 92.24 \text{ kips} \cdot \text{ft}$$

$$t_{TRUCK} = 397.12 \cdot 11.17 = 4,435.78 \text{ kips} \cdot \text{ft}$$

Therefore, the torque developed in the composite section at the support is equal to:

$$T = (2,854.44 + 1,285.78 + 3,573.60 - 383.85 - 92.24 + 4,435.78) / 2 = 5,836.75 \text{ kip} \cdot \text{ft}$$

Knowing the applied torque at the end support, the shear flow of the end section is calculated as:

$$q = T / (2 \cdot A) = 5,836.75 / (2 \cdot 5923.68 / 144) = 70.94 \text{ kips/ft} = 5.91 \text{ kips/in}$$

The shear stresses in the concrete deck, webs and bottom flange are computed by following the same procedure as before:

$$\tau_{CONC. DECK} = q / t_{CONC. DECK} = 5.91 / 8 = 0.74 \text{ ksi}$$

$$\tau_{WEB} = q / t_{WEB} = 5.91 / 0.75 = 7.88 \text{ ksi}$$

$$\tau_{BOTT. FLANGE} = q / t_{BOTT. FLANGE} = 5.91 / 1.25 = 4.73 \text{ ksi}$$

$$\tau_{Flexural WEB} = V / (2 \cdot h_{WEB} \cdot t_{WEB} \cdot \cos(14^\circ)) = 741.28 / (2 \cdot 88.644 \cdot 0.75 \cdot 0.97) = 5.75 \text{ ksi}$$

The shear stress, which is developed in the concrete deck due to torsion, is equal to 0.74 ksi. According to ACI 318-08, the shear capacity of a reinforced concrete section is:

$$V_S = A_t \cdot f_{yt} \cdot b \cdot \cot\theta / s.$$

As a result,

$$V_{TORSION} = q \cdot b = 5.91 \cdot 84 = 496.60 \text{ kips} \leq V_S = A_t \cdot f_{yt} \cdot b \cdot \cot\theta / s = 0.62 \cdot 60 \cdot 84 / 5 = 624.96 \text{ kips}$$

As indicated previously, the total shear stress in the webs is a combination of the flexural and torsional shear stresses (Figure C-9), and the east web controls because the shear from flexure and torsion add. The total shear stress that is developed in the east web is calculated to be:

$$\tau_{TOTAL} = \tau_{WEB} + \tau_{Flexural WEB} = 7.88 + 5.75 = 13.63 \text{ ksi which is equal to } \tau_n = 13.63 \text{ ksi.}$$

As before, the forces acting on each side of the end diaphragm can be calculated as follows:  $V_{ED} = T / l_b = 5,836.75 / 13.92 = 419.31$  kips, where  $T$  is the torque applied to the intact girder and  $l_b$  is the distance between the two bearings. Thus, the shear strength in the end diaphragm ( $V_n = 0.35 \cdot 1870.5 = 654.68$  kips) is adequate to resist the applied shearing force ( $V_{ED} = 419.31$  kips). Summarizing the calculations, it was found that the shear stresses developed in the webs of the end section limit the ultimate load to 5.52×HS-20 Trucks (397.12 kips).

## APPENDIX D

### Analysis of the Woodway Bridge (span 17 & 18) using the simple models

#### D.1 INTRODUCTION

This example focuses on spans 17 and 18 of the Woodway exit ramp on IH 610/Katy Freeway, which actually is a two span continuous bridge. The length of each span is 128 ft. The radius of curvature is 3,813.72 ft for span 17 and 1,903.86 ft for span 18. Figure D-1 shows the elevation view of spans 17 and 18 of the Woodway Bridge and other general information. The top and bottom flange thickness changes along the span of the bridge. Table D-1 summarizes all the dimensions of both flanges along the span of the bridge. Only three steel sections are used along the length of the span. The “Transition” sections occur due to different cutoff points for the top and bottom flanges. Figures D-2 and D-3 present the typical cross-section of the bridge and steel girder, respectively.

Table D-1: General information of bottom and top flange

Span	Type of Section	Length of application measured from south (ft)	Bottom Flange		Top Flange	
			$t_{BF}$ (in.)	$b_{BF}$ (in.)	$t_{TF}$ (in.)	$b_{BF}$ (in.)
1 (17)	End	0-80	7/8	62	0.75	14
1 (17)	Transition	80-112	1 3/8	62	1	20
1 (17)	Pier	112-128	1 3/8	62	2	20
2 (18)	Pier	128-144	1 3/8	62	2	20
2 (18)	Transition	144-176	1 3/8	62	1	20
2 (18)	End	176-256	7/8	62	0.75	14

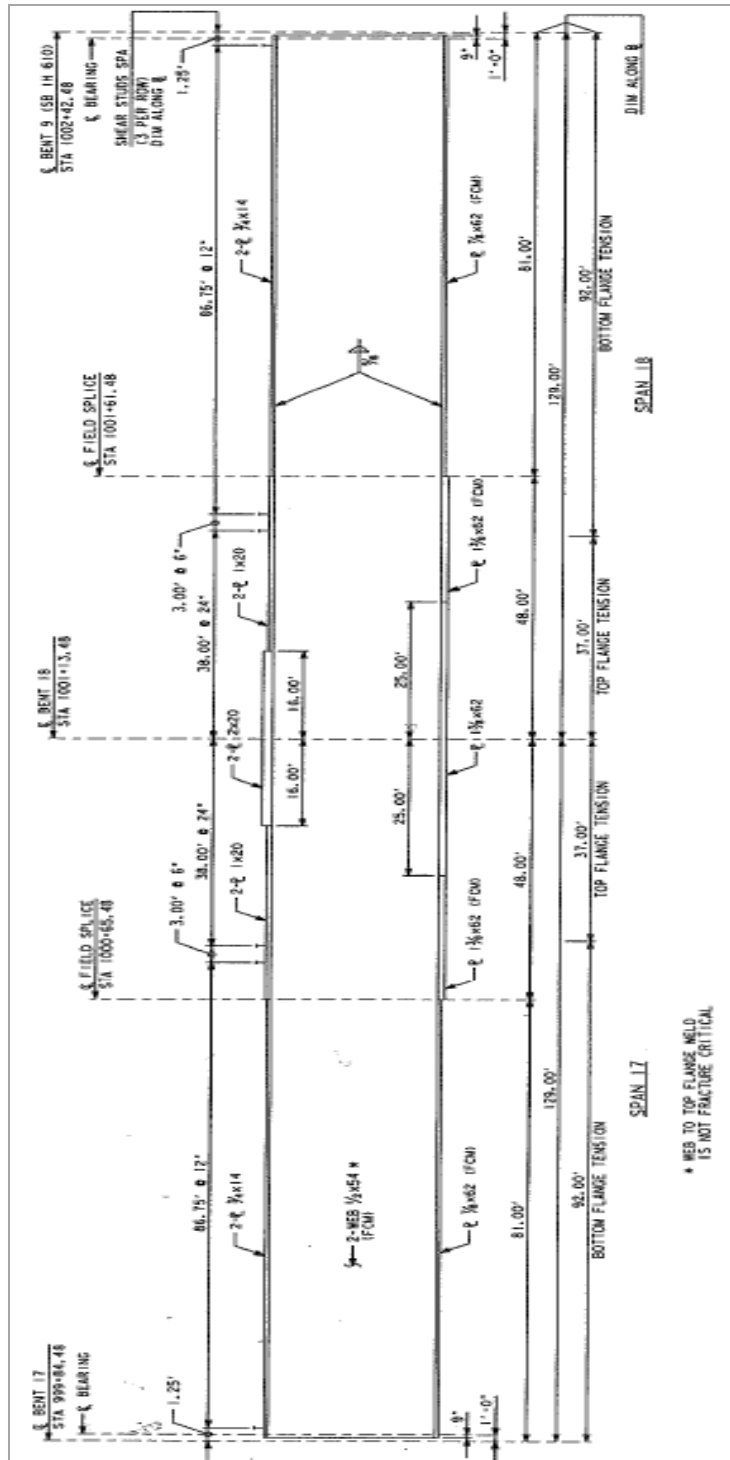


Figure D-1: Elevation view of Woodway Bridge Span 17 & 18



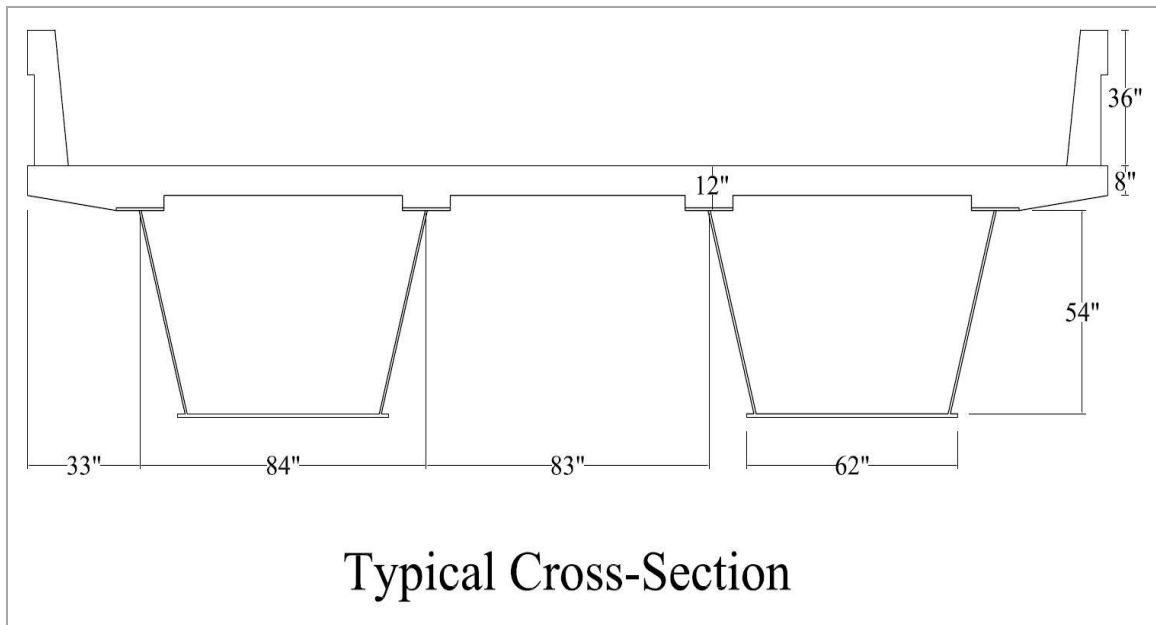


Figure D-2: Typical cross-section of the Woodway Bridge Span 17 & 18

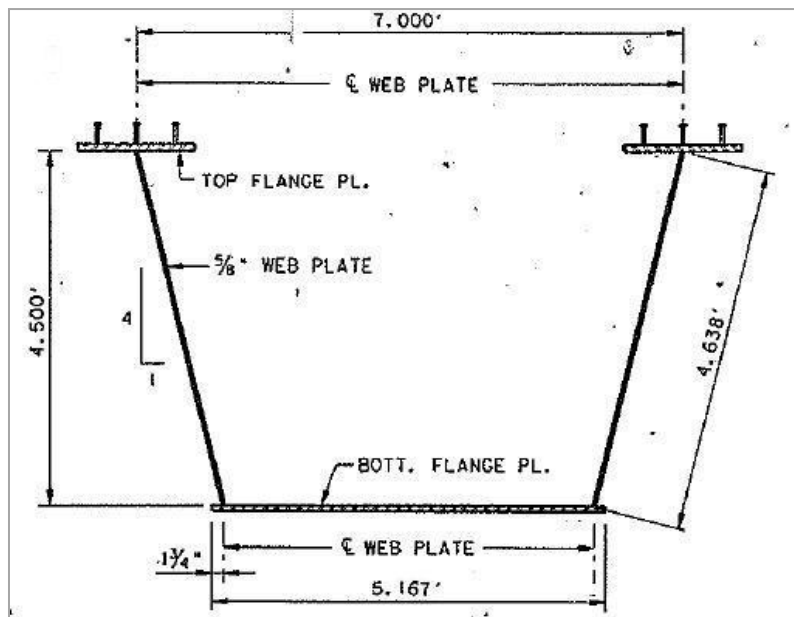


Figure D-3: Typical cross-section of the Woodway Bridge Span 17 & 18 steel girder

## **D.2 CALCULATION OF THE TRANSMITTED LOAD TO THE INTACT GIRDER**

It was assumed that half of the entire weight of the bridge and the entire live load on the bridge needed to be resisted from the intact girder at the event of a fracture occurred. These loads were calculated below:

### **Weight of one steel box girder:**

$$W_{girder} = 1.15 \cdot (144.83/144 \text{ ft}^2) \cdot (0.490 \text{ kips/ft}^3) = 0.567 \text{ kip/ft (End Section)}$$

$$W_{girder} = 1.15 \cdot (194.83/144 \text{ ft}^2) \cdot (0.490 \text{ kips/ft}^3) = 0.763 \text{ kip/ft (Transitioning Section)}$$

$$W_{girder} = 1.15 \cdot (234.83/144 \text{ ft}^2) \cdot (0.490 \text{ kips/ft}^3) = 0.919 \text{ kip/ft (Middle Section)}$$

Notes: This was the weight of one girder. Cross-sectional areas of End, Transitioning and Middle section were 144.83 in<sup>2</sup>, 194.83 in<sup>2</sup> and 234.83 in<sup>2</sup> respectively. Density of steel was taken as 490 lb/ft<sup>3</sup>. To account for internal diaphragms, stiffeners, etc., the weight of the steel girder was multiplied by a factor of 1.15.

### **Concrete deck:**

$$W_{deck} = (317 \cdot 8 / 144 \text{ ft}^2) \cdot (0.150 \text{ kip/ft}^3) = 2.642 \text{ kip/ft}$$

Notes: Width of concrete deck was 26 ft-5 in. = 317 in. Density of concrete was taken as 150 lb/ft<sup>3</sup>. Deck thickness was 8 in.

### **SSTR Railing**

$$W_{railings} = 2 \cdot (312/144 \text{ ft}^2) \cdot (0.150 \text{ kip/ft}^3) = 0.65 \text{ kip/ft}$$

Notes: Multiplied by 2 to account for two rails. Cross-sectional area of one rail was calculated to be 312 in<sup>2</sup>

### **Simulated Truck (HS-20)**

$$W_{truck} = 2 \cdot 72 \text{ kips} = 144 \text{ kips (with a load factor of 2)}$$

### **Load to be transmitted**

$$F = \Sigma(W_{girder\ i} \cdot L_i) + (W_{deck}/2 + W_{railings}/2) \cdot L + W_{truck}$$

$$F = (0.567 \cdot 80 + 0.763 \cdot 32 + 0.919 \cdot 16) + (2.642 + 0.65) \cdot 128/2 + 144 = 439.17 \text{ kips}$$

$$F = 439.17 \text{ kips}$$

### **D.3 CALCULATION OF MAXIMUM MOMENT ON THE BRIDGE**

Spans 17 and 18 of the Woodway Bridge were analyzed in SAP 2009 in order to identify the location of the maximum positive bending moment. This location is where the fracture would take place. The bridge was analyzed using one moving HS-20 truck; thus, the fracture location results from the most critical location of the truck. Due to symmetrical geometry, the moment diagram envelope of the dead load and one moving load is symmetrical about the interior support. Figure D-4 illustrates the first half of the moment diagram envelope (Span 17). It is found that the maximum positive moment occurs at 50 ft from the south end of span 17, and its magnitude is 8448.42 kip-ft. The maximum negative moment at the inner pier is -11125.61 kip-ft.

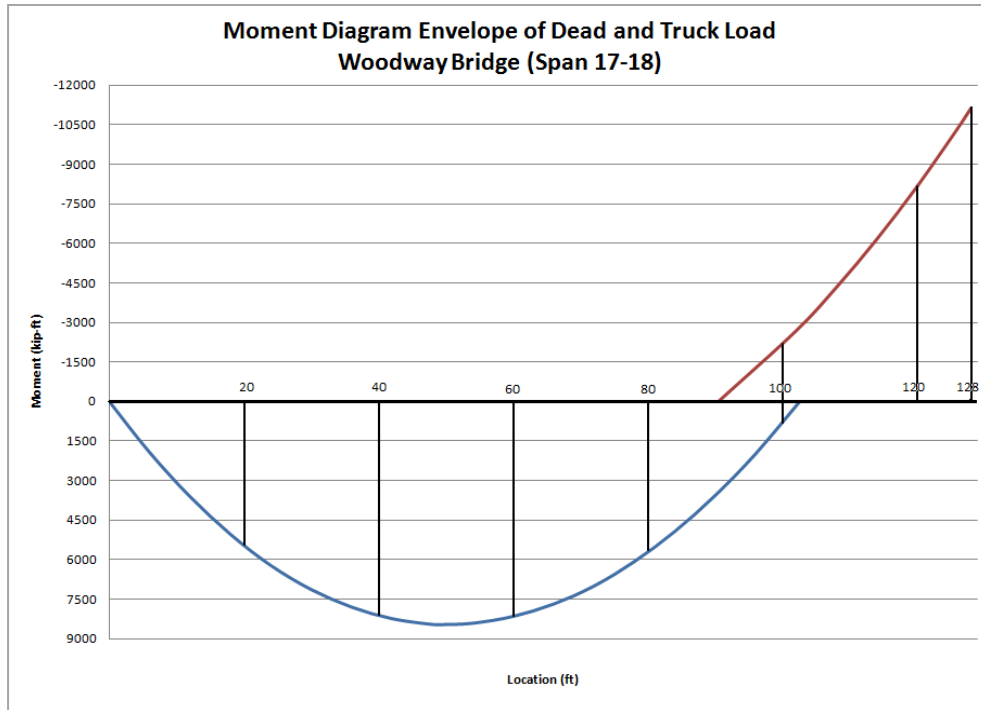


Figure D-4: Moment envelope of dead and one truck load on spans 17 and 18 of the Woodway Bridge

#### D.4 ANALYSIS OF COMPOSITE SECTION

The plastic moment capacity of the intact girder is calculated to determine if the intact girder has sufficient flexural capacity to sustain the entire truck and dead load applied to the bridge. The positive plastic moment capacities of the End section as well as the negative moment capacity of the Pier section are checked. Based on TxDOT minimum requirements,  $f_y = 50$  ksi is used for the components of the steel girder.

##### Positive Plastic Moment Capacity of End Section:

Find the plastic neutral axis by setting  $T = C$ :

$$T = A_s \cdot f_y = (62 \cdot 7/8 + 2 \cdot 55.66 \cdot 5/8 + 2 \cdot 14 \cdot 3/4) \cdot 50 = 7,241.25 \text{ kips}$$

$$C_c = 0.85 \cdot f_c' \cdot t_s \cdot b_{eff} = 0.85 \cdot 4 \cdot 8 \cdot 158.5 = 4,311.2 \text{ kips}$$

Because  $T > C$ , the plastic neutral axis (PNA) is in the girder.

$$C_s = (A_s \cdot f_y - C_c) / 2 = (7,241.25 - 4,311.2) / 2 = 1,465.03 \text{ kips}$$

Using this equation, the compressive force needed to be developed in the steel section for equilibrium ( $C = T$ ) can be determined.

$$C_{tfl} = 2 \cdot t_{tfl} \cdot b_{tfl} \cdot f_y = 2 \cdot 3/4 \cdot 14 \cdot 50 = 1,050 \text{ kips}$$

The top flanges can resist 1,050 kips in compression, which is less than what is needed to obtain equilibrium. As a result, the PNA falls in the web. Assuming that  $x$  is the distance from the neutral axis to the bottom of the top flange (Figure D-5), the depth of the neutral axis can be found:

$$x = (1,465.03 - 1,050) / (2 \cdot 5/8 \cdot (17/16)^{0.5} \cdot 50) = 6.44 \text{ in.}$$

Note: The  $(17/16)^{0.5}$  factor is based on the slope of the web.

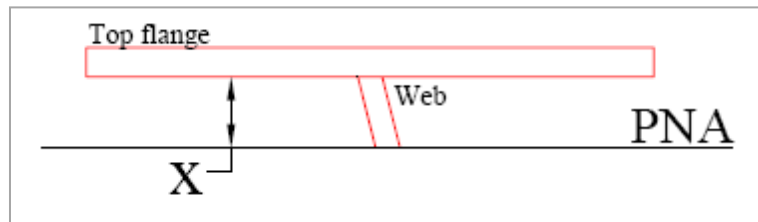


Figure D-5: Plastic neutral axis location

Thus:

$$C_c = 4,311.2 \text{ kips}$$

$$C_{tfl} = 1,050 \text{ kips}$$

$$C_{web} = 415.03 \text{ kips}$$

$$T_{web} = A_{web} \cdot f_y = 2 \cdot 5/8 \cdot (54 - 6.44) \cdot (17/16)^{0.5} \cdot 50 = 3,063.98 \text{ kips}$$

$$T_{bottom\ flange} = A_{bottom\ flange} \cdot f_y = 62 \cdot 7/8 \cdot 50 = 2,712.5 \text{ kips}$$

By taking moments about the PNA, the nominal plastic moment capacity can be calculated:

$$M_{bottom\ flange} = T_{bottom\ flange} \cdot (7/16 + 54 - 6.44) = 130,193.22 \text{ kip-in.}$$

$$M_{web} = C_{web} \cdot 6.44/2 + T_{web} \cdot (54 - 6.44) / 2 = 74,197.84 \text{ kip-in.}$$

$$M_{C\ tfl} = C_{tfl} \cdot (3/8 + 6.44) = 7,155.75 \text{ kip-in.}$$

$$M_{C\ concrete} = C_c \cdot (8/2 + 4 + 6.44) = 62,253.73 \text{ kip-in.}$$

Note: The 4-in. term added in the moment arm accounts for distance from the bottom of the concrete deck to the bottom of the top flange.

Therefore,  $M_p = 130,193.22 + 74,197.84 + 7,155.75 + 62,253.73$

$$M_{P\ End\ Section} = 273,800.54 \text{ kip-in.} = 22,816.71 \text{ kip-ft}$$

Previously,  $M_{max}^+$  was found to be 8,562.79 kip-ft. Therefore, the positive plastic moment capacity is sufficient to sustain the entire dead load of the bridge plus the truck live load.

### Negative Plastic Moment Capacity of Pier Section:

According to AASHTO Sec. 6.11.8.2.2, the bottom flange at the pier should be checked for combined shear and compression as follows:

The slenderness ratio for the compression flange  $\lambda_f = b_{fc} / t_{fc} = 57.75 / 1.375 = 42$

For  $F_{yc} = 50$  ksi,  $f_v = 3.23$  ksi,  $E = 29,000$  ksi,  $k = 4$  and  $k_s = 5.34$

$$\Delta = \sqrt{1 - 3 \cdot \left( \frac{f_v}{F_{yc}} \right)^2} = 0.994$$

$$R_1 = \frac{0.57}{\sqrt{\frac{1}{2} \cdot \left[ \Delta + \sqrt{\Delta^2 + 4 \cdot \left( \frac{f_v}{F_{yc}} \right)^2 \cdot \left( \frac{k}{k_s} \right)^2} \right]}} = 0.571$$

$$R_2 = \frac{1.23}{\sqrt{\frac{1}{2} \cdot \left[ \frac{F_{yr}}{F_{yc}} + \sqrt{\left( \frac{F_{yr}}{F_{yc}} \right)^2 + 4 \cdot \left( \frac{f_v}{F_{yc}} \right)^2 \cdot \left( \frac{k}{k_s} \right)^2} \right]}} = 1.59$$

Because  $R_1 \cdot \sqrt{\frac{k \cdot E}{F_{yc}}} = 27.5 < \lambda_f = 42 < R_2 \cdot \sqrt{\frac{k \cdot E}{F_{yc}}} = 76.58$ ,

$$F_{nc} = R_b \cdot R_h \cdot F_{yc} \left[ \Delta - \left( \Delta - \frac{F_{yr}}{R_h \cdot F_{yc}} \right) \left\{ 1 - \sin \left[ \frac{\pi}{2} \left( \frac{R_2 - \frac{b_{fc}}{t_{fc}} \cdot \sqrt{\frac{F_{yc}}{k \cdot E}}}{R_2 - R_1} \right) \right] \right\} \right] = 47.58 \text{ ksi}$$

In order to compute the moment capacity of the pier section, the elastic section modulus of the composite cross section must be calculated. Because the contribution of concrete is negligible in the negative moment region, only the area of the reinforcing bars and the steel girder section is included in the calculation of the elastic section modulus. By using AutoCAD 2010, the moment of inertia of the pier section, neglecting the concrete portion, is calculated to be:

$$I = 154,035.85 \text{ in}^4 = 7.43 \text{ ft}^4$$

Similarly, the distance from the extreme compressive fiber to the neutral axis is found to be:

$$y_b = 28.96 \text{ in} = 2.41 \text{ ft}$$

As a result, the elastic section modulus can be computed as the ratio of  $I / y_b$

$$S = I / y_b = 5,318.92 \text{ in}^3 = 3.08 \text{ ft}^3$$

According to the shear-axial stress interaction equation (AASHTO Sec. 6.11.8.2.2), the allowable stress in the bottom flange is equal to 47.58 ksi. The product of the allowable stress and the elastic section modulus for the bottom flange gives the moment capacity of the pier section. Thus,

$$M_{Pier\ Section} = 253,074.21 \text{ kip-in.} = 21,089.52 \text{ kip-ft}$$

Previously,  $M_{max}$  was found to be -11125.61 kip-ft. Thus, the negative moment capacity is sufficient to sustain the entire dead load of the bridge plus the truck live load.



## D.5 ANALYSIS OF CONCRETE DECK

As before, the bending and shear capacity of the concrete deck were checked to ensure that they were adequate to resist the moment and the shear produced by the unsupported load of the fractured girder. These capacities were based on a 1-ft wide transverse deck section as shown in the Figure D-6.

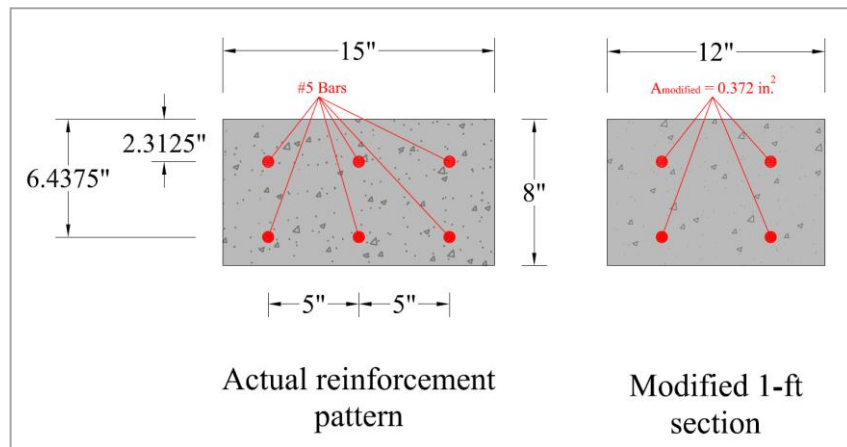


Figure D-6: Actual and modified 1-ft wide section of the concrete deck in the transverse direction

### Positive Moment Capacity

The assumed strain and stress failure profile are shown in the figure below:

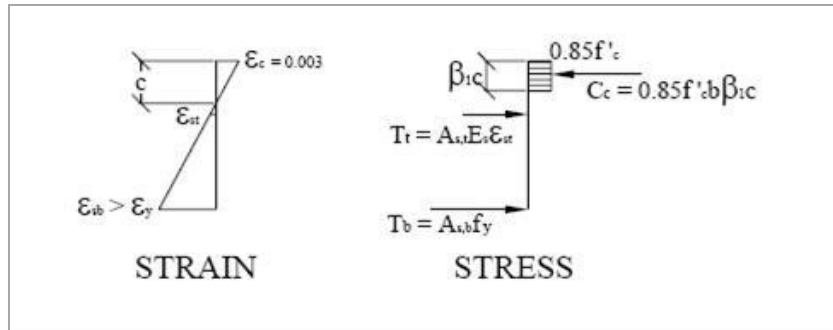


Figure D-7: Strain and stress gradients at positive moment regions

According to ACI 318-08, it was assumed that the ultimate strain of concrete was 0.003 in./in. and the bottom reinforcement had yielded prior to failure. The top reinforcement was always included in the calculations for more accurate results. The concrete strength was taken as 4 ksi and the reinforcement strength as 60 ksi.

Let  $C = T$ :

$$C = 0.85 \cdot f'_c \cdot \beta_1 \cdot c \cdot b = 0.85 \cdot 4 \cdot 0.85 \cdot 12 \cdot c = 34.68 \cdot c$$

Note:  $\beta_1 = 0.85$  for 4 ksi concrete.

$$\varepsilon_{s, \text{bottom}} = 0.003 \cdot (6.4375 - c) / c$$

$$\varepsilon_{s, \text{top}} = 0.003 \cdot (2.3125 - c) / c$$

$$T_{\text{bottom}} = A_{s, \text{bottom}} \cdot f_y = 2 \cdot 0.372 \cdot 60 = 44.64 \text{ kips}$$

$$T_{\text{top}} = A_{s, \text{top}} \cdot \varepsilon_{s, \text{top}} \cdot E_s = 2 \cdot 0.372 \cdot 29,0000 \cdot \varepsilon_{s, \text{top}} = 21,576 \cdot \varepsilon_{s, \text{top}}$$

$$34.68 \cdot c = 44.64 + 21,576 \cdot \varepsilon_{s, \text{top}}$$

$$34.68 \cdot c = 44.64 + 21,576 \cdot 0.003 \cdot (2.3125 - c) / c$$

Iterate until the neutral axis depth was found. Solution:  $c = 1.808$  in.

$$\varepsilon_{s, \text{bottom}} = 0.00768 > \text{Yield strain (} = 0.00207 \text{ for 60 ksi)}$$

$$\varepsilon_{s, \text{top}} = 0.000837 < \text{Yield strain (} = 0.00207 \text{ for 60 ksi)}$$

$$C = 80.82 \text{ kips}$$

$$T_{bottom} = 44.64 \text{ kips}$$

$$T_{top} = 18.06 \text{ kips}$$

Take moments about the NA to solve for nominal moment capacity

$$M_n^+ = C \cdot (c - \beta_1 \cdot c / 2) + T_{top} \cdot (2.3125 - c) + T_{bottom} \cdot (6.4375 - c)$$

$$M_n^+ = 80.82 \cdot (1.808 - 0.85 \cdot 1.808 / 2) + 18.06 \cdot (2.3125 - 1.808) + 44.64 \cdot (6.4375 - 1.808)$$

$$M_n^+ = 299.79 \text{ kips-in.} = 24.98 \text{ kips-ft}$$

### Negative Moment Capacity

The assumed strain and stress failure profile are shown in the figure below:

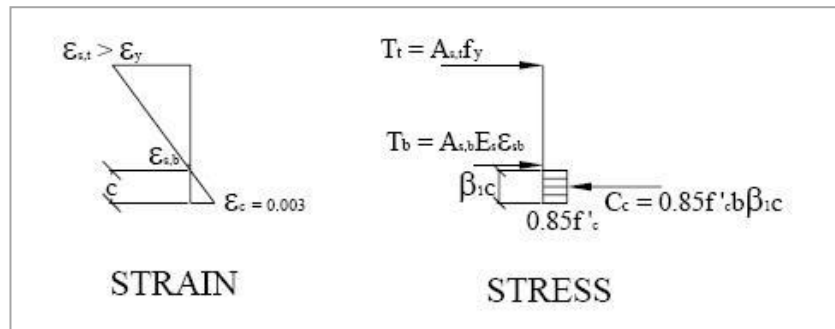


Figure D-8: Strain and stress gradients at negative moment regions

According to ACI 318-08, it was assumed that the ultimate strain of concrete was 0.003 in./in. and the top reinforcement had yielded prior to failure. The bottom reinforcement was always included in the calculations for more accurate results. The concrete strength was taken as 4 ksi and the reinforcement strength as 60 ksi.

Let  $C = T$ :

$$C = 0.85 \cdot f_c' \cdot \beta_1 \cdot c \cdot b = 0.85 \cdot 4 \cdot 0.85 \cdot 12 \cdot c = 34.68 \cdot c$$

Note:  $\beta_1 = 0.85$  for 4 ksi concrete.

$$\varepsilon_{s, \text{bottom}} = 0.003 \cdot (1.5625 - c) / c$$

$$\varepsilon_{s, \text{top}} = 0.003 \cdot (5.6875 - c) / c$$

$$T_{\text{bottom}} = A_{s, \text{bottom}} \cdot \varepsilon_{s, \text{bottom}} \cdot E_s = 2 \cdot 0.372 \cdot 29,0000 \cdot \varepsilon_{s, \text{bottom}} = 21,576 \cdot \varepsilon_{s, \text{bottom}}$$

$$T_{\text{top}} = A_{s, \text{top}} \cdot f_y = 2 \cdot 0.372 \cdot 60 = 44.64 \text{ kips}$$

$$34.68 \cdot c = 44.64 + 21,576 \cdot \varepsilon_{s, \text{bottom}}$$

$$34.68 \cdot c = 44.64 + 21,576 \cdot 0.003 \cdot (1.5625 - c) / c$$

Iterate until the neutral axis depth was found. Solution:  $c = 1.443$  in.

$$\varepsilon_{s, \text{bottom}} = 0.000248 < \text{Yield strain} (= 0.00207 \text{ for } 60 \text{ ksi})$$

$$\varepsilon_{s, \text{top}} = 0.008824 > \text{Yield strain} (= 0.00207 \text{ for } 60 \text{ ksi})$$

$$C = 50.04 \text{ kips}$$

$$T_{\text{bottom}} = 5.35 \text{ kips}$$

$$T_{\text{top}} = 44.64 \text{ kips}$$

Take moments about the NA to solve for nominal moment capacity

$$M_n^- = C \cdot (c - \beta_1 \cdot c / 2) + T_{\text{top}} \cdot (5.6875 - c) + T_{\text{bottom}} \cdot (1.5625 - c)$$

$$M_n^- = 50.04 \cdot (1.443 - 0.85 \cdot 1.808/2) + 44.64 \cdot (5.6875 - 1.808) + 5.35 \cdot (1.5625 - 1.808)$$

$$M_n^- = 205.62 \text{ kips-in.} = 17.13 \text{ kips-ft}$$

## Bending Capacity Check

The deflected shape of the concrete deck and the bending moment diagram, if it is assumed that the shear studs have enough tensile capacity, is shown in Figure D-9:

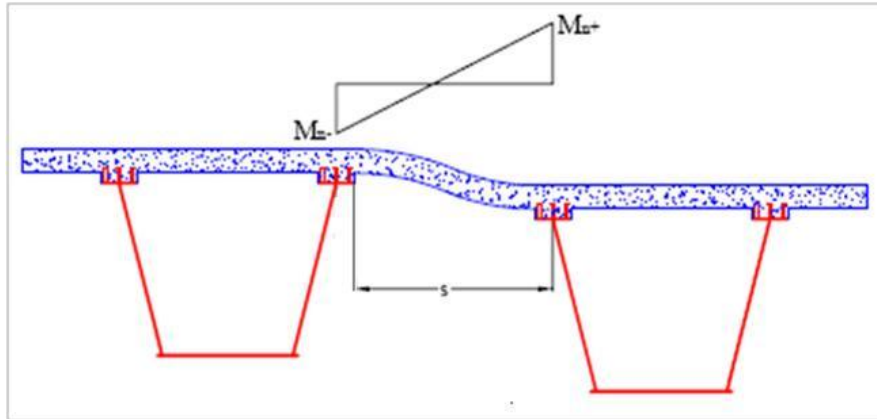


Figure D-9: Deflected shape and moment diagram before any failure of shear studs

$$V = (M_n^+ + M_n^-)/s = (24.98 \text{ kip-ft} + 17.13 \text{ kip-ft})/6.17 \text{ ft} = \mathbf{6.82 \text{ kips}}$$

Note: The spacing,  $s$ , is equal to the distance between the mid-width of the fractured girder's interior top flange and the edge of the interior top flange of the intact girder (6ft 2in.).

The shear capacity is calculated using the ACI 318-08 equation for shear shown below. The capacity is based on a 1-ft wide transverse deck section. The depth used in this equation is the depth to the centroid of the tension reinforcement (6.4375 in.).

$$V_c = 2 \cdot \sqrt{f'_c} \cdot b \cdot d = 2 \cdot \sqrt{4000} \cdot 12 \cdot 6.4375 = \mathbf{9.77 \text{ kips}}$$

Thus the maximum shear capacity of the deck is equal to the shear associated with the plastic deck mechanism (6.82 kips/ft). Therefore, the total length required to transfer the 439.17-kip force is:

$$l_M = 439.17 / 6.82 = 64.39 \text{ ft}$$

$$64.72 / 128 = \mathbf{50.30 \% \text{ of the span length}}$$

#### D.6 SHEAR STUD CHECK

In order to determine the tensile strength of a shear stud group, the guidelines recommended by Mouras (2008) are followed. The shear stud connections used in spans 17 and 18 of the Woodway Bridge consist of a group of three 6-in tall shear studs spaced transversely. The haunch differs along the length of the bridge from 3.25 in. to 2 in. By using the modified ACI 318-08 equations presented in Appendix B (and shown again below for convenience), the tensile capacity of the shear stud group is calculated to be 16.8 kips throughout the bridge.

$$N_b = k_c \cdot \sqrt{f'_c} \cdot h_h^{1.5} \quad \text{Equation B-1 (ACI 318-08)}$$

$$N_{cbg} = \frac{A_{NC}}{A_{NCO}} \cdot \psi_{g,N} \cdot \psi_{ec,N} \cdot \psi_{ed,N} \cdot \psi_{c,N} \cdot N_b \quad \text{Equation B-2 (modified ACI 318-08)}$$

where:

$N_b$  = concrete cone breakout strength of a single isolated stud in a continuous piece of cracked concrete (15.32 kips)

$k_c = 24$  for cast-in-place shear studs

$f'_c$  = specified concrete compressive strength (4000 psi)

$h_h$  = modified height of shear stud in concrete ( $h_h = h_{ef} - d_h = 5.625 - 3.25 = 2.375$  in.  $< 14/3 = 4.67$  in.  $\rightarrow h_h = 4.67$  in.)

$h_{ef}$  = effective height of shear stud in concrete, which is equal to the length of stud less the height of the stud head ( $h_{eff} = 6 - 0.375 = 5.625$  in.)

$d_h$  = haunch height (3.25 in.)

$c_{a,min}$  = distance between outer stud and the edge of flange ( $c_{a,min} = 3$  in.)

$N_{cbg}$  = design concrete breakout strength of a stud or group of studs (16.8 kips)

$A_{Nc}$  = projected concrete cone failure area of a stud group ( $A_{Nc} = 3 h_{ef} w_h = 236.25$  in<sup>2</sup>)

Note:  $A_{Nc} = 3 h_{ef} w_h$  because haunch confined full height projected cone area.

$A_{Nco}$  = projected concrete cone failure area of a single stud in continuous concrete ( $A_{Nco} = 9h_h^2 = 196.28$  in<sup>2</sup>)

$\Psi_{g,N}$  = group effect modification factor for studs on a bridge girder ( $\Psi_{g,N} = 0.90$  for 3 studs spaced transversely)

$\psi_{ec,N}$  = eccentric load modification factor ( $\psi_{ec,N} = 1$ )

$\psi_{ed,N}$  = edge distance modification factor ( $\psi_{ed,N} = 0.7 + 0.3 c_{a,min} / (1.5 h_{ef}) = 0.81$ )

$\psi_{c,N}$  = cracked concrete modification factor ( $\psi_{c,N} = 1.25$  for cast-in studs)

The calculated tensile capacity of the group of studs is 16.8 kips. Using Equation 3-2, the controlling failure mechanism (i.e., pull out of the shear studs or formation of a plastic hinge in the concrete deck) can be determined. A strip width equal to the shear stud spacing of 12 inches is used to calculate the tension in the stud group.

$$T = 16.8 \text{ kips}, M_2/b + V = 24.98 \cdot (12/12) / 7 + 6.82 \cdot (12/12) = 10.39 \text{ kips}$$

Because  $T > M_2/b + V$  (i.e., shear stud capacity exceeds the tension generated by the deck mechanism), the shear studs do not pull out; as a result, hinges form in the concrete deck.

#### **D.7 SHEAR CHECK OF THE COMPOSITE SECTION AT THE SUPPORTS DUE TO TORSION AND BENDING**

As stated previously, it is assumed that the entire weight of the bridge and live load are applied to the intact girder. The shear at the abutments and at the interior pier of the bridge are 335.69 kips and 514.75 kips, respectively.

The unsupported load, which is first carried by the fractured girder, has to be transferred to the intact girder. In addition to all the transferred loads, a torque is applied to the intact girder due to the eccentricity between the chord of the intact girder bearings and the center of gravity (CG) of each load. The eccentricities of each load can be computed using Equation 3-5 through Equation 3-19. This bridge has the following geometric characteristics:

1.  $R_{INT} = 1,896.9 \text{ ft}$ ,  $L_{INT} = 127 \text{ ft}$ ,  $\varphi = 0.06695 \text{ rad}$
2.  $R_{FG} = 1,910.82 \text{ ft}$ ,  $\theta_{0FG} = 0 \text{ rad}$ ,  $\theta_{1FG} = 0.0084 \text{ rad}$ ,  $\theta_{2FG} = 0.0251 \text{ rad}$ ,  $\theta_{3FG} = 0.067 \text{ rad}$ ,  $\bar{\theta}_{FG} = 0.0303 \text{ rads}$
3.  $R_{RFG} = 1,917.07 \text{ ft}$ ,  $\theta_{0FG} = 0 \text{ rad}$ ,  $\theta_{1FG} = 0.067 \text{ rad}$ ,  $\bar{\theta}_{FG} = 0.0335 \text{ rad}$



4.  $R_{DFG} = 1,910.72 \text{ ft}$  ,  $\theta_{0FG} = 0 \text{ rad}$ ,  $\theta_{1FG} = 0.067 \text{ rad}$ ,  $\bar{\theta}_{FG} = 0.0335 \text{ rad}$
5.  $R_{IG} = 1,896.9 \text{ ft}$  ,  $\theta_{0IG} = 0 \text{ rad}$ ,  $\theta_{1IG} = 0.0084 \text{ rad}$ ,  $\theta_{2IG} = 0.0251 \text{ rad}$ ,  $\theta_{3IG} = 0.067 \text{ rad}$ ,  
 $\bar{\theta}_{IG} = 0.0303 \text{ rad}$
6.  $R_{RIG} = 1,890.65 \text{ ft}$  ,  $\theta_{0FG} = 0 \text{ rad}$ ,  $\theta_{1FG} = 0.067 \text{ rad}$ ,  $\bar{\theta}_{FG} = 0.0335 \text{ rad}$
7.  $R_{DIG} = 1,897 \text{ ft}$  ,  $\theta_{0FG} = 0 \text{ rad}$ ,  $\theta_{1FG} = 0.067 \text{ rad}$ ,  $\bar{\theta}_{FG} = 0.0335 \text{ rad}$
8.  $R_{TRUCK} = 1,911 \text{ ft}$ ,  $\theta_{0TRUCK} = 0.0335 \text{ rad}$ ,  $\theta_{1TRUCK} = 0.0482 \text{ rad}$ ,  $\bar{\theta}_{TRUCK} = 0.04085 \text{ rad}$

The center of gravity of each component is found by inserting the above values in Equation 3-18.

$$\bar{D}_{FG} = 1910.45 \text{ ft}$$

$$\bar{D}_{RFG} = 1916.71 \text{ ft}$$

$$\bar{D}_{DFG} = 1910.36 \text{ ft}$$

$$\bar{D}_{IG} = 1896.53 \text{ ft}$$

$$\bar{D}_{RIG} = 1890.30 \text{ ft}$$

$$\bar{D}_{DIG} = 1896.65 \text{ ft}$$

$$\bar{D}_{TRUCK} = 1910.98 \text{ ft}$$

By using Equation 3-19, the eccentricity of each component can be found as follows:

$$e_{FG} = 1,910.45 - 1,890.65 \cdot \cos(0.06691/2) = 14.61 \text{ ft}$$

$$e_{RFG} = 1,916.71 - 1,890.65 \cdot \cos(0.06691/2) = 20.87 \text{ ft}$$

$$e_{DFG} = 1,910.36 - 1,890.65 \cdot \cos(0.06691/2) = 14.52 \text{ ft}$$

$$e_{IG} = 1,896.53 - 1,890.65 \cdot \cos(0.06691/2) = 0.69 \text{ ft}$$

$$e_{RIG} = 1,890.3 - 1,890.65 \cdot \cos(0.06691/2) = -5.54 \text{ ft}$$

$$e_{DIG} = 1,896.65 - 1,890.65 \cdot \cos(0.06691/2) = 0.81 \text{ ft}$$

$$e_{TRUCK} = 1,910.98 - 1,890.65 \cdot \cos(0.06691/2) = 15.14 \text{ ft}$$

As a result, the torques due to each load are computed to be:

$$t_{FG} = 84.48 \cdot 14.61 = 1,234.25 \text{ kips}\cdot\text{ft}$$

$$t_{RFG} = 41.6 \cdot 20.87 = 868.19 \text{ kips}\cdot\text{ft}$$

$$t_{DFG} = 169.09 \cdot 14.52 = 2,455.19 \text{ kips}\cdot\text{ft}$$

$$t_{IG} = 84.48 \cdot 0.69 = 58.29 \text{ kips}\cdot\text{ft}$$

$$t_{RIG} = 41.6 \cdot -5.54 = -230.46 \text{ kips}\cdot\text{ft}$$

$$t_{DIG} = 169.09 \cdot 0.81 = 136.96 \text{ kips}\cdot\text{ft}$$

$$t_{TRUCK} = 144 \cdot 15.14 = 2,180.16 \text{ kips}\cdot\text{ft}$$

Therefore, the torque developed in the composite section at the support is equal to:

$$T = (1,234.25 + 868.19 + 2,455.19 + 58.29 - 230.46 + 136.96 + 2,180.16) / 2 = 3,351.29 \text{ kip}\cdot\text{ft}$$

To compute the shear flow of the closed section, Equation 3-20 is used.

$$q = T / (2 \cdot A) = 3,351.29 / (2 \cdot 4,534.07/144) = 53.22 \text{ kips/ft} = 4.44 \text{ kips/in}$$

The shear stress due to torsion in every component of the composite section is calculated as:

$$\tau_{CONC. DECK} = q / t_{CONC. DECK} = 4.44 / 8 = 0.56 \text{ ksi}$$

$$\tau_{WEB} = q / t_{WEB} = 4.44 / 0.625 = 7.1 \text{ ksi}$$

$$\tau_{BOTT. FLANGE} = q / t_{BOTT. FLANGE} = 4.44 / 1.375 = 3.23 \text{ ksi}$$

The flexural shear is assumed to be carried by the webs of the composite section because the contribution of the bottom flange and the concrete deck is small. The flexural shear stress in the webs of the composite section is calculated below:

$$\tau_{Flexural WEB Abutm.} = V_1 / (2 \cdot h_{WEB} \cdot t_{WEB} \cdot \cos(14^\circ)) = 335.69 / (2 \cdot 55.656 \cdot 5/8 \cdot 0.97) = 4.97 \text{ ksi}$$

$$\tau_{Flexural WEB Pier} = V_2 / (2 \cdot h_{WEB} \cdot t_{WEB} \cdot \cos(14^\circ)) = 514.75 / (2 \cdot 55.656 \cdot 5/8 \cdot 0.97) = 7.63 \text{ ksi}$$

Note: The factor 2 accounts for the fact that the composite sections consist of two webs, which share the total flexural shear. The  $\cos(14^\circ)$  accounts for the fact that the webs are inclined.

The shear stress that develops in the concrete deck due to torsion is equal to 0.56 ksi. According to ACI 318-08, the shear capacity of a reinforced concrete section is:

$$V_S = A_t \cdot f_{yt} \cdot b \cdot \cot\theta / s.$$

Consequently,

$$V_{TORSION} = q \cdot b = 4.44 \cdot 84 = 372.96 \text{ kips} \leq V_S = A_t \cdot f_{yt} \cdot b \cdot \cot\theta / s = 0.62 \cdot 60 \cdot 84 / 5 = 624.96 \text{ kips}$$

The shear stresses in the steel girder are checked according to the AASHTO Specifications. The shear stress in the webs of the end panel should be limited to either

the shear-yielding or shear-buckling resistance. The nominal shear stress resistance of the web panel ( $\tau_n$ ) is computed as the product of the shear-buckling resistance to the shear yield strength ratio ( $C$ ) times the plastic shear stress ( $\tau_p$ ) (i.e.,  $\tau_n=C\cdot\tau_p$ ). The plastic shear stress is equal to  $0.58f_{yw}$ . The ratio  $C$  is determined as below:

$$\text{If } \frac{D}{t_w} \leq 1.12 \sqrt{\frac{Ek}{f_{yw}}} \text{ then } C=1.0$$

$$\text{If } 1.12 \sqrt{\frac{Ek}{f_{yw}}} < \frac{D}{t_w} \leq 1.40 \sqrt{\frac{Ek}{f_{yw}}} \text{ then } C = \frac{1.12}{D/t_w} \sqrt{\frac{Ek}{f_{yw}}}$$

$$\text{If } \frac{D}{t_w} > 1.40 \sqrt{\frac{Ek}{f_{yw}}} \text{ then } C = \frac{1.57}{(D/t_w)^2} \left( \frac{Ek}{f_{yw}} \right)$$

For spans 17 and 18 of the Woodway Bridge,  $D = 55.66$  in.,  $t_w = 5/8$  in.,  $E = 29,000$  ksi,  $f_{yw} = 50$  ksi. The factor  $k$  is calculated as

$$k = 5 + \frac{5}{\left( \frac{d_0}{D} \right)^2}$$

where  $d_0$  is the spacing from the support to the first stiffener adjacent to the support (128 in.). AASHTO limits the factor  $d_0/D$  for end panels to 1.5. The end panel of the bridge considered in this example is located at the end of the girder, and  $d_0/D=2.30>1.5$ ; thus,  $d_0/D=2.30$ . By inserting the value of  $d_0/D$  in the equation for  $k$ , this value is calculated to be 5.95.

$$\text{Because } \frac{D}{t_w} = \frac{55.66}{5/8} = 89.06 > 1.40 \sqrt{\frac{Ek}{f_{yw}}} = 82.24$$

$$C = \frac{1.57}{(D/t_w)^2} \left( \frac{Ek}{f_{yw}} \right) = 0.68$$

Having all the variables defined, the nominal shear stress ( $\tau_n$ ) is computed to be  $\tau_n = 0.68 \cdot 0.58 \cdot f_{yw} = 19.72$  ksi.

The total shear stress in the webs is due to a combination of the flexural and torsional shear stresses. As shown in Figure D-10, the shear stresses are added and subtracted in the east and west web, respectively. The east web controls because the shear from flexure and torsion add. The total shear stress that develops in the end panel of the east web is calculated to be  $\tau_{TOTAL} = \tau_{WEB} + \tau_{Flexural\ WEB} = 7.1 + 7.63 = 14.73$  ksi at the abutment and  $\tau_{TOTAL} = \tau_{WEB} + \tau_{Flexural\ WEB} = 7.1 + 4.97 = 12.07$  ksi at the interior pier. Both values are less than  $\tau_n = 19.72$  ksi based on AASHTO Specifications. Summarizing the calculations, it is found that all the components of the section have adequate capacities to sustain the applied load.

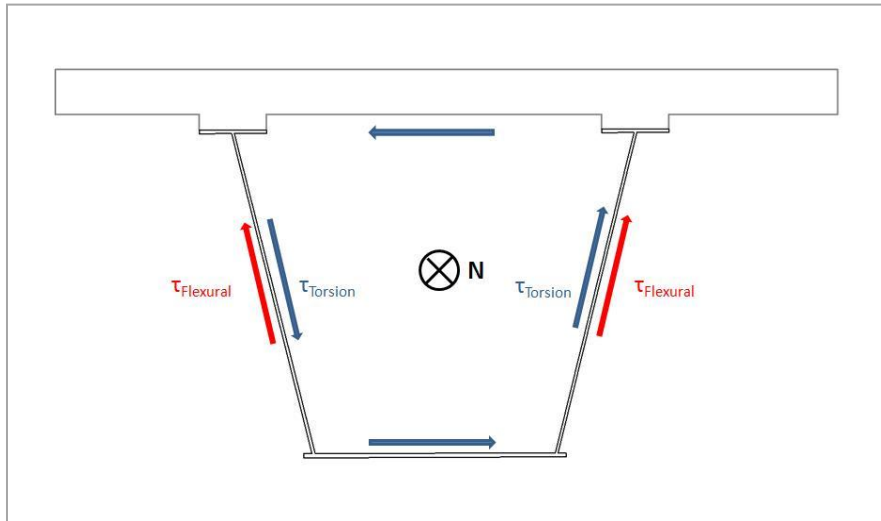


Figure D-10: Flexural and torsional shear stresses on the composite section

The end diaphragm, which connects both girders, must be checked to ensure that it has adequate capacity to resist the torque applied to the intact girder. This torque is equilibrated through the reaction forces acting at the bearings, and these reaction forces cause shearing in the end diaphragm. The forces acting on each side of the end diaphragm can be calculated as follows:

$V_{ED} = T / l_b = 3,351.29 / 13.92 = 240.75$  kips, where  $T$  is the torque applied on the intact girder and  $l_b$  is the distance between the two bearings. The nominal shear strength of the end diaphragm can be computed according to AASHTO Sec. 6.10.9.2.

$V_n = C \cdot V_P$ , where  $V_P = 0.58 \cdot F_{yw} \cdot D \cdot t_w = 0.58 \cdot 50 \cdot 52.38 \cdot 0.75 = 1139.27$  kips,  $k=5$ , and  $C$  is calculated as:

$$C = \frac{1.12}{D/t_w} \sqrt{\frac{Ek}{f_{yw}}} = 0.86$$

because

$$1.12 \sqrt{\frac{Ek}{f_{yw}}} = 60.31 < \frac{D}{t_w} = \frac{52.38}{0.75} = 69.84 < 1.40 \sqrt{\frac{Ek}{f_{yw}}} = 75.39$$

Thus, the shear strength of the end diaphragm ( $V_n = 0.86 \cdot 1139.27 = 979.77$  kips) is adequate to resist the applied shearing force ( $V_{ED} = 240.75$  kips).

Because the analysis presented above indicates that the capacity of this bridge is controlled by the formation of a plastic hinge line above both interior top flanges, the ultimate load is estimated from the initial checks and not from the Yield Line Model. Following the same procedure as described in the example of Appendix C, the initial checks determine the ultimate truck load that this bridge will sustain in the event of a fracture. After several iterations, it is found that the ultimate truck load is 4.30×HS-20

(309.6 kips). The buckling shear stress in the webs of the end section controls the maximum truck load that this bridge can sustain. The moment at the mid-span of the intact girder produced by the dead load and this 309.6-kip truck load is:

$$M_{P \text{ End Section}} = 22,816.71 \text{ kip-ft} > M_{max}^+ = 12,211 \text{ kip-ft}$$

The bottom flange at the pier section needs to be checked for torsion and bending. According to AASHTO Sec. 6.11.8.2.2, the slenderness ratio for the compression flange is

$$\lambda_f = b_{fc} / t_{fc} = 57.75 / 1.375 = 42$$

For  $F_{yc} = 50$  ksi,  $f_v = 4.43$  ksi,  $E = 29,000$  ksi,  $k = 4$  and  $k_s = 5.34$

$$\Delta = \sqrt{1 - 3 \cdot \left( \frac{f_v}{F_{yc}} \right)^2} = 0.988$$

$$R_1 = \frac{0.57}{\sqrt{\frac{1}{2} \cdot \left[ \Delta + \sqrt{\Delta^2 + 4 \cdot \left( \frac{f_v}{F_{yc}} \right)^2 \cdot \left( \frac{k}{k_s} \right)^2} \right]}} = 0.572$$

$$R_2 = \frac{1.23}{\sqrt{\frac{1}{2} \cdot \left[ \frac{F_{yr}}{F_{yc}} + \sqrt{\left( \frac{F_{yr}}{F_{yc}} \right)^2 + 4 \cdot \left( \frac{f_v}{F_{yc}} \right)^2 \cdot \left( \frac{k}{k_s} \right)^2} \right]}} = 1.594$$

$$\text{Because } R_1 \cdot \sqrt{\frac{k \cdot E}{F_{yc}}} = 27.55 < \lambda_f = 42 < R_2 \cdot \sqrt{\frac{k \cdot E}{F_{yc}}} = 76.78,$$

$$F_{nc} = R_b \cdot R_h \cdot F_{yc} \left[ \Delta - \left( \Delta - \frac{F_{yr}}{R_h \cdot F_{yc}} \right) \left\{ 1 - \sin \left[ \frac{\pi}{2} \left( \frac{R_2 - \frac{b_{fc}}{t_{fc}} \cdot \sqrt{\frac{F_{yc}}{k \cdot E}}}{R_2 - R_1} \right) \right] \right\} \right] = 47.31 \text{ksi}$$

As before, the moment capacity of the pier section is equal to the product of the elastic section modulus and the allowable stress. The elastic section modulus remains constant and is equal to:

$$S = I / y_b = 5,318.92 \text{ in}^3 = 3.08 \text{ ft}^3$$

According to AASHTO Sec. 6.11.8.2.2, the allowable stress in the bottom flange is equal to 47.31 ksi. Thus, the moment capacity of the pier section is equal to:

$$M_{Pier\ Section} = 251,638.10 \text{ kip-in.} = 20,969.84 \text{ kip-ft} > M_{max} = 13,107 \text{ kip-ft}$$

Thus, the negative plastic moment capacity has sufficient capacity to sustain the entire dead load of the bridge plus the truck live load.

The force needed to be transferred is found to be:

$$F = (0.567 \cdot 80 + 0.763 \cdot 32 + 0.919 \cdot 16) + (2.642 + 0.65) \cdot 128/2 + 309.6 = 604.77 \text{ kips}$$

$$F = 604.77 \text{ kips}$$

The length of the bridge needed to transfer the load  $F$  based on the flexural capacity of the bridge is:

$$l_M = 604.77 / 6.82 = 88.68 \text{ ft}$$

$$88.68 / 128 = \mathbf{69.28 \% \text{ of the span length}}$$



The flexural shear at the abutment and the interior support is found to be:

$$V_{Abutm} = V_{DL} + V_{TRUCK} = 214.63 + 260.27, \quad V_{Abutm} = 474.9 \text{ kips}$$

$$V_{Pier} = V_{DL} + V_{TRUCK} = 377.14 + 295.86, \quad V_{Pier} = 673 \text{ kips}$$

The torques associated with each load are:

$$t_{FG} = 84.48 \cdot 14.61 = 1,234.25 \text{ kips}\cdot\text{ft}$$

$$t_{RFG} = 41.6 \cdot 20.87 = 868.19 \text{ kips}\cdot\text{ft}$$

$$t_{DFG} = 169.09 \cdot 14.52 = 2,455.19 \text{ kips}\cdot\text{ft}$$

$$t_{IG} = 84.48 \cdot 0.69 = 58.29 \text{ kips}\cdot\text{ft}$$

$$t_{RIG} = 41.6 \cdot -5.54 = -230.46 \text{ kips}\cdot\text{ft}$$

$$t_{DIG} = 169.09 \cdot 0.81 = 136.96 \text{ kips}\cdot\text{ft}$$

$$t_{TRUCK} = 309.6 \cdot 15.14 = 4,687.34 \text{ kips}\cdot\text{ft}$$

Therefore, the torque developed in the composite section at the support is equal to:

$$T = (1,234.25 + 868.19 + 2,455.19 + 58.29 - 230.46 + 136.96 + 4,687.34) / 2 = 4,604.88 \text{ kip}\cdot\text{ft}$$

To compute the shear flow of the closed section, Equation 3-20 is used.

$$q = T / (2 \cdot A) = 4,604.88 / (2 \cdot 4,534.07/144) = 73.12 \text{ kips/ft} = 6.09 \text{ kips/in}$$

The shear stresses in the concrete deck, webs, and bottom flange are computed by following the same procedure as before:

$$\tau_{CONC. DECK} = q / t_{CONC. DECK} = 6.09 / 8 = 0.76 \text{ ksi}$$

$$\tau_{WEB} = q / t_{WEB} = 6.09 / 0.625 = 9.74 \text{ ksi}$$

$$\tau_{BOTT. FLANGE} = q / t_{BOTT. FLANGE} = 6.09 / 1.375 = 4.43 \text{ ksi}$$

$$\tau_{FlexuralWEB Abutm.} = V_{Abutm} / (2 \cdot h_{WEB} \cdot t_{WEB} \cdot \cos(14^\circ)) = 474.9 / (2 \cdot 55.656 \cdot 5/8 \cdot 0.97) = 7.04 \text{ ksi}$$

$$\tau_{FlexuralWEB Pier} = V_{Pier} / (2 \cdot h_{WEB} \cdot t_{WEB} \cdot \cos(14^\circ)) = 673 / (2 \cdot 55.656 \cdot 5/8 \cdot 0.97) = 9.98 \text{ ksi}$$

The shear stress that develops in the concrete deck due to torsion is equal to 0.76 ksi. According to ACI 318-08, the shear capacity of a reinforced concrete section is:

$$V_S = A_t \cdot f_{yt} \cdot b \cdot \cot\theta / s.$$

Thus,

$$V_{TORSION} = q \cdot b = 6.09 \cdot 84 = 511.56 \text{ kips} \leq V_S = A_t \cdot f_{yt} \cdot b \cdot \cot\theta / s = 0.62 \cdot 60 \cdot 84 / 5 = 624.96 \text{ kips}$$

As stated previously, the shear stress in the webs is a combination of the flexural and torsional shear stress, and the response of the east web controls because the shear from flexure and torsion add. The total shear stress that develops in the east web is calculated to be:

$$\tau_{TOTAL Abutm} = \tau_{WEB} + \tau_{FlexuralWEB Abutm} = 9.74 + 7.04 = 16.78 \text{ ksi} < \tau_n = 23.49 \text{ ksi.}$$

$$\tau_{TOTAL Pier} = \tau_{WEB} + \tau_{FlexuralWEB Pier} = 9.74 + 9.98 = 19.72 \text{ ksi} = \tau_n = 19.72 \text{ ksi.}$$

The end diaphragm, which connects both girders, has adequate capacity to resist the torque applied to the intact girder.

$V_{ED} = T / l_b = 4,604.88 / 13.92 = 330.81 \text{ kips}$ , where  $T$  is the torque applied on the intact girder and  $l_b$  is the distance between the two bearings. Thus, the shear strength of the end diaphragm ( $V_n = 0.86 \cdot 1139.27 = 979.77 \text{ kips}$ ) is adequate to resist the applied

shearing force ( $V_{ED} = 330.81$  kips). Finally, it is found that the ultimate load is equal to 4.30×HS-20 Trucks (309.6 kips).

## APPENDIX E

### Instrumentation

#### E.1 GLOSSARY OF INSTRUMENTATION GAGES

Table E-1: Glossary of instrumentation codes

Code	Description
N4, N3.5, ... S4	Location of the gage according to the defined sections
WG	West Girder (Intact Girder)
WG1	West Girder (Western Edge of Bottom Flange)
WG2	West Girder (Eastern Edge of Bottom Flange)
RA, RB, RC	1st, 2nd and 3rd Component of the Rosette
OND	Outside North Diaphragm
IND	Inside North Diaphragm
OSD	Outside South Diaphragm
ISD	Inside South Diaphragm
EG	East Girder (Fractured Girder)
EG1	East Girder (Western Edge of Bottom Flange)
EG2	East Girder (Eastern Edge of Bottom Flange)
NCL or SCL	Just North or South of the CL
IEW	Inside East Web
OEW	Outside East Web
IWW	Inside West Web
OWW	Outside West Web
IBF	Inside Bottom Flange
OBF	Outside Bottom Flange
IF	Interior Top Flange of the Fractured Girder
TF	Exterior Top Flange of the Fractured Girder
ITF or InteriorTF	Interior Top Flange of the Fractured Girder
LP	Linear Potentiometer
SD	South Diaphragm
SP	String Potentiometer
TD	Top Deck
TC1	Transverse Concrete Gage (Western one)

TC5	Transverse Concrete Gage (Eastern one)
LC	Longitudinal Concrete Gage
ER	East Railing
WR	West Railing
MH	Middle Height of the Railing for sections N2, N1, S1, S2
MH	6 in. from Top Surface of the Railing for sections NCL, SCL
MH2	12 in. from Top Surface of the Railing for sections NCL, SCL

Table E-2: Typical gage models

<b>Gage Type</b>	<b>Manufacturer</b>	<b>Model #</b>	<b>Gage Length</b>
Bolt / Shear Stud	TML/Texas Measurements	BTM-6C	6 mm
Uni-axial steel	Vishay	CEA-06-250UN-350/P2	0.25 in.
Rosette steel	Vishay	CEA-06-250UR-350/P2	0.25 in.
Uni-axial concrete	TML/Texas Measurements	PL-60-120-11-3LT	60 mm

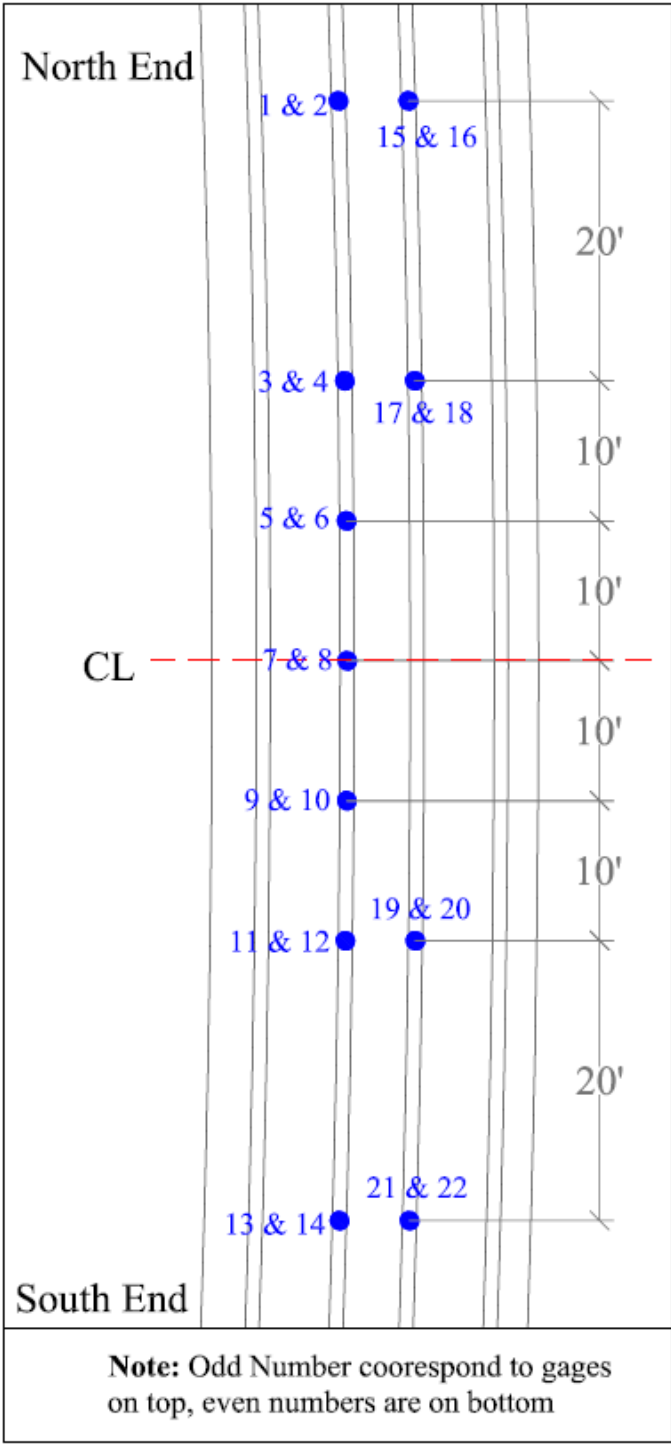


Figure E-1: Reinforcing bar foil gage locations

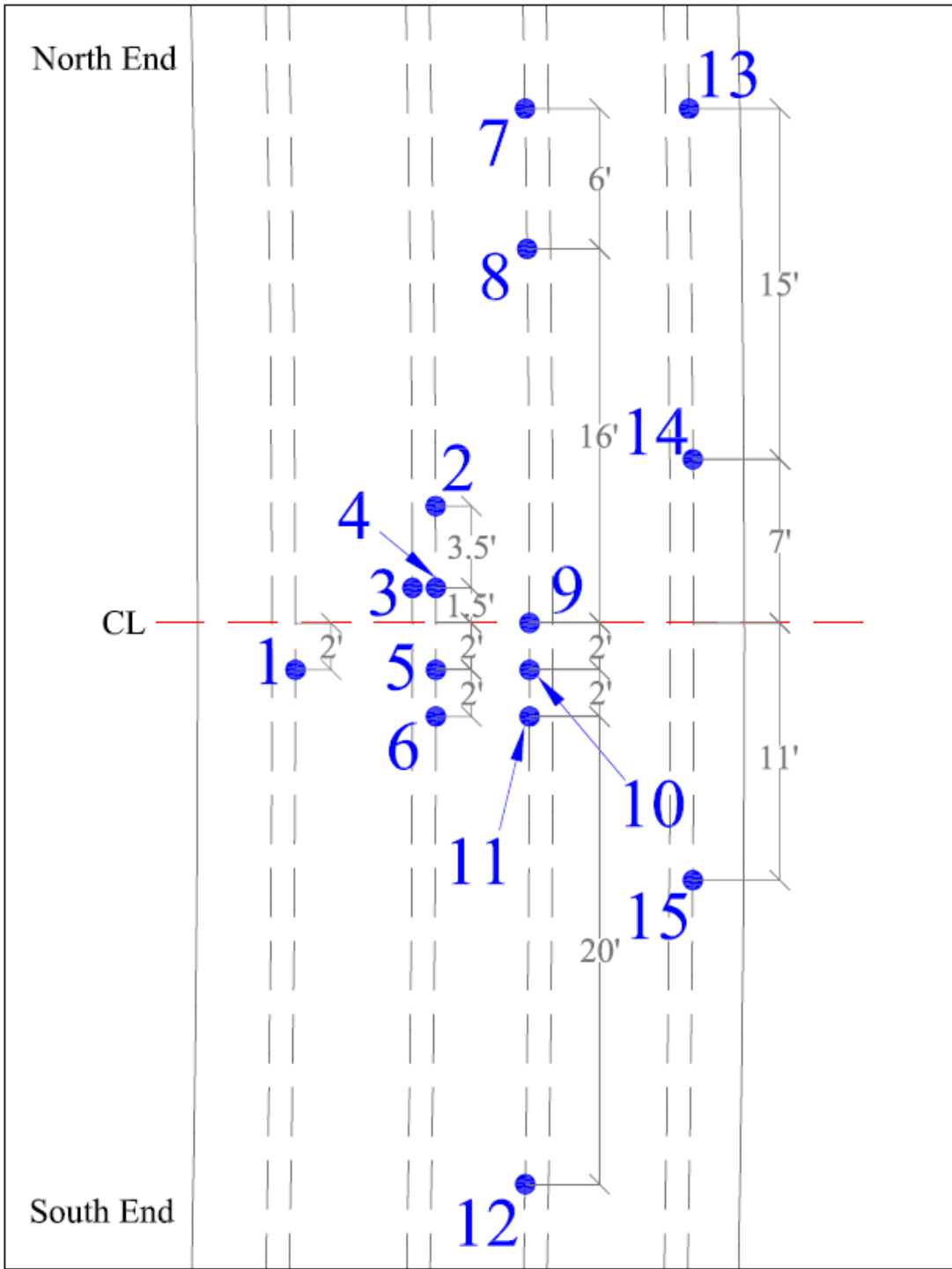


Figure E-2: Shear stud foil gage locations

## E.2 FULL-SCALE TEST 2

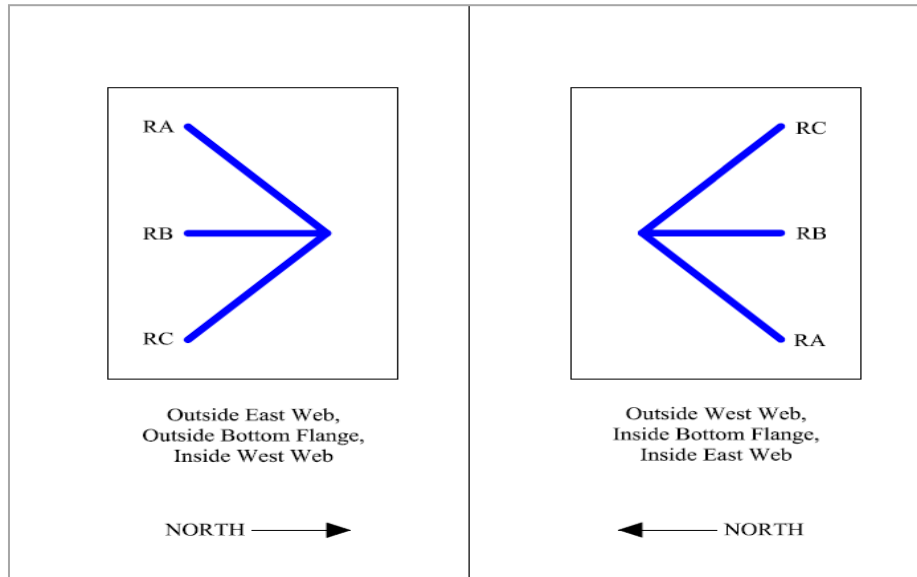


Figure E-3: Intact girder rosette orientation Full-Scale Test 2 and 3

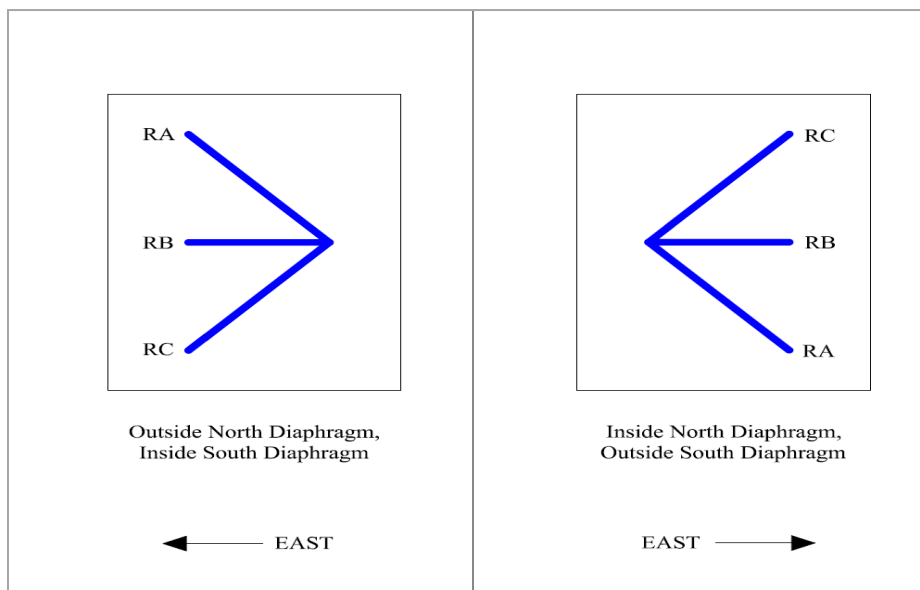
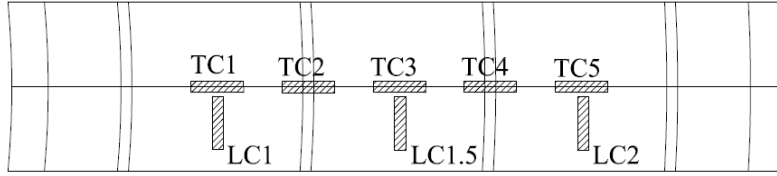


Figure E-4: End diaphragm rosette orientation Full-Scale Test 2 and 3

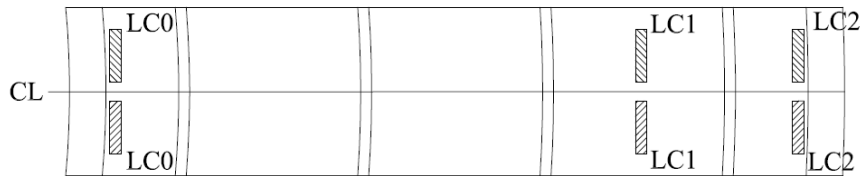


Typical Formation of TD Gages for all sections except CL



EAST →

Typical Formation of TD Gages at CL



EAST →

Figure E-5: Typical concrete deck gage locations Full-Scale Test 2 and 3

Table E-3: Index of instrumentation channels Full-Scale Test 2

Index	Gage Name	Description
0	FR1	Foil Rebar Strain Gage
1	FR2	Foil Rebar Strain Gage
2	FR3	Foil Rebar Strain Gage
3	FR4	Foil Rebar Strain Gage
4	FR5	Foil Rebar Strain Gage
5	FR6	Foil Rebar Strain Gage
6	FR7	Foil Rebar Strain Gage
7	FR8	Foil Rebar Strain Gage
8	FR9	Foil Rebar Strain Gage

9	FR10	Foil Rebar Strain Gage
10	FR11	Foil Rebar Strain Gage
11	FR12	Foil Rebar Strain Gage
12	FR13	Foil Rebar Strain Gage
13	FR14	Foil Rebar Strain Gage
14	FR15	Foil Rebar Strain Gage
15	FR16	Foil Rebar Strain Gage
16	FR17	Foil Rebar Strain Gage
17	FR18	Foil Rebar Strain Gage
18	FR19	Foil Rebar Strain Gage
19	FR20	Foil Rebar Strain Gage
20	FR21	Foil Rebar Strain Gage
21	FR22	Foil Rebar Strain Gage
22	FS1	Shear Stud Strain Gage
23	FS2	Shear Stud Strain Gage
24	FS3	Shear Stud Strain Gage
25	FS4	Shear Stud Strain Gage
26	FS5	Shear Stud Strain Gage
27	FS6	Shear Stud Strain Gage
28	FS14	Shear Stud Strain Gage
29	FS9	Shear Stud Strain Gage
30	FS10	Shear Stud Strain Gage
31	FS11	Shear Stud Strain Gage
32	FS12	Shear Stud Strain Gage
33	FS15	Shear Stud Strain Gage
34	FS7	Shear Stud Strain Gage
35	WG-S1-IEW-RA	West Girder-Section S1-Inside East Web- Component A of the Rosette
36	WG-S1-IEW-RB	West Girder-Section S1-Inside East Web- Component B of the Rosette
37	WG-S1-IEW-RC	West Girder-Section S1-Inside East Web- Component C of the Rosette
38	WG-S1-IBF-RA	West Girder-Section S1-Inside Bottom Flange- Component A of the Rosette
39	FS13	Shear Stud Strain Gage
40	WG-S1-IBF-RB	West Girder-Section S1-Inside Bottom Flange- Component B of the Rosette
41	WG-S1-IBF-RC	West Girder-Section S1-Inside Bottom Flange- Component C of the Rosette

42	WG-S1-IWW-RA	West Girder-Section S1-Inside West Web-Component A of the Rosette
43	WG-S1-IWW-RB	West Girder-Section S1-Inside West Web-Component B of the Rosette
44	WG-S1-IWW-RC	West Girder-Section S1-Inside West Web-Component C of the Rosette
45	WG-S1-OEW-RA	West Girder-Section S1-Outside East Web-Component A of the Rosette
46	WG-S1-OEW-RB	West Girder-Section S1-Outside East Web-Component B of the Rosette
47	WG-S1-OEW-RC	West Girder-Section S1-Outside East Web-Component C of the Rosette
48	WG-S1-OBF-RA	West Girder-Section S1-Outside Bottom Flange-Component A of the Rosette
49	WG-S1-OBF-RB	West Girder-Section S1-Outside Bottom Flange-Component B of the Rosette
50	WG-S1-OBF-RC	West Girder-Section S1-Outside Bottom Flange-Component C of the Rosette
51	WG-S1-OWW-RA	West Girder-Section S1-Outside West Web-Component A of the Rosette
52	WG-S1-OWW-RB	West Girder-Section S1-Outside West Web-Component B of the Rosette
53	WG-S1-OWW-RC	West Girder-Section S1-Outside West Web-Component C of the Rosette
54	WG-N1-IEW-RA	West Girder-Section N1-Inside East Web-Component A of the Rosette
55	WG-N1-IEW-RB	West Girder-Section N1-Inside East Web-Component B of the Rosette
56	WG-N1-IEW-RC	West Girder-Section N1-Inside East Web-Component C of the Rosette
57	WG-N1-IBF-RA	West Girder-Section N1-Inside Bottom Flange-Component A of the Rosette
58	WG-N1-IBF-RB	West Girder-Section N1-Inside Bottom Flange-Component B of the Rosette
59	WG-N1-IBF-RC	West Girder-Section N1-Inside Bottom Flange-Component C of the Rosette
60	WG-N1-IWW-RA	West Girder-Section N1-Inside West Web-Component A of the Rosette
61	WG-N1-IWW-RB	West Girder-Section N1-Inside West Web-Component B of the Rosette
62	GO TO 172	

63	WG-N1-OEW-RA	West Girder-Section N1-Outside East Web-Component A of the Rosette
64	WG-N1-OEW-RB	West Girder-Section N1-Outside East Web-Component B of the Rosette
65	WG-N1-OEW-RC	West Girder-Section N1-Outside East Web-Component C of the Rosette
66	WG-N1-OBF-RA	West Girder-Section N1-Outside Bottom Flange-Component A of the Rosette
67	WG-N1-OBF-RB	West Girder-Section N1-Outside Bottom Flange-Component B of the Rosette
68	WG-N1-OBF-RC	West Girder-Section N1-Outside Bottom Flange-Component C of the Rosette
69	WG-N1-OWW-RA	West Girder-Section N1-Outside West Web-Component A of the Rosette
70	WG-N1-OWW-RB	West Girder-Section N1-Outside West Web-Component B of the Rosette
71	WG-N1-OWW-RC	West Girder-Section N1-Outside West Web-Component C of the Rosette
72	OND-RA	Outside North Diaphragm-Component A of the Rosette
73	OND-RB	Outside North Diaphragm-Component B of the Rosette
74	OND-RC	Outside North Diaphragm-Component C of the Rosette
75	IND-RA	Inside North Diaphragm-Component A of the Rosette
76	IND-RB	Inside North Diaphragm-Component B of the Rosette
77	IND-RC	Inside North Diaphragm-Component C of the Rosette
78	OSD-RA	Outside South Diaphragm-Component A of the Rosette
79	OSD-RB	Outside South Diaphragm-Component B of the Rosette
80	OSD-RC	Outside South Diaphragm-Component C of the Rosette
81	ISD-RA	Inside South Diaphragm-Component A of the Rosette
82	ISD-RB	Inside South Diaphragm-Component B of the Rosette
83	ISD-RC	Inside South Diaphragm-Component C of the Rosette
84	EG-N3-OBF-F	East Girder-Section N3-Outside Bottom Flange- Foil Gage
85	EG-N3-IBF-F	East Girder-Section N3-Inside Bottom Flange- Foil Gage
86	WG-N3-OEW-RA	West Girder-Section N3-Outside East Web-Component A of the Rosette
87	WG-N3-OEW-RB	West Girder-Section N3-Outside East Web-Component B of the Rosette

88	WG-N3-OEW-RC	West Girder-Section N3-Outside East Web-Component C of the Rosette
89	WG-N3-OBF-RA	West Girder-Section N3-Outside Bottom Flange-Component A of the Rosette
90	WG-N3-OBF-RB	West Girder-Section N3-Outside Bottom Flange-Component B of the Rosette
91	WG-N3-OBF-RC	West Girder-Section N3-Outside Bottom Flange-Component C of the Rosette
92	WG-N3-OWW-RA	West Girder-Section N3-Outside West Web-Component A of the Rosette
93	WG-N3-OWW-RB	West Girder-Section N3-Outside West Web-Component B of the Rosette
94	WG-N3-OWW-RC	West Girder-Section N3-Outside West Web-Component C of the Rosette
95	WG-N3-IEW-RA	West Girder-Section N3-Inside East Web-Component A of the Rosette
96	WG-N3-IEW-RB	West Girder-Section N3-Inside East Web-Component B of the Rosette
97	WG-N3-IEW-RC	West Girder-Section N3-Inside East Web-Component C of the Rosette
98	WG-N3-IBF-RA	West Girder-Section N3-Inside Bottom Flange-Component A of the Rosette
99	WG-N3-IBF-RB	West Girder-Section N3-Inside Bottom Flange-Component B of the Rosette
100	WG-N3-IBF-RC	West Girder-Section N3-Inside Bottom Flange-Component C of the Rosette
101	WG-N3-IWW-RA	West Girder-Section N3-Inside West Web-Component A of the Rosette
102	WG-N3-IWW-RB	West Girder-Section N3-Inside West Web-Component B of the Rosette
103	WG-N3-IWW-RC	West Girder-Section N3-Inside West Web-Component C of the Rosette
104	EG-N2-OBF-F	East Girder-Section N2-Outside Bottom Flange- Foil Gage
105	EG-N2-IBF-F	East Girder-Section N2-Inside Bottom Flange- Foil Gage
106	WG-N2-OEW-RA	West Girder-Section N2-Outside East Web-Component A of the Rosette
107	WG-N2-OEW-RB	West Girder-Section N2-Outside East Web-Component B of the Rosette
108	WG-N2-OEW-RC	West Girder-Section N2-Outside East Web-

		Component C of the Rosette
109	WG-N2-OBF-RA	West Girder-Section N2-Outside Bottom Flange- Component A of the Rosette
110	WG-N2-OBF-RB	West Girder-Section N2-Outside Bottom Flange- Component B of the Rosette
111	WG-N2-OBF-RC	West Girder-Section N2-Outside Bottom Flange- Component C of the Rosette
112	WG-N2-OWW-RA	West Girder-Section N2-Outside West Web- Component A of the Rosette
113	WG-N2-OWW-RB	West Girder-Section N2-Outside West Web- Component B of the Rosette
114	WG-N2-OWW-RC	West Girder-Section N2-Outside West Web- Component C of the Rosette
115	WG-N2-IEW-RA	West Girder-Section N2-Inside East Web- Component A of the Rosette
116	WG-N2-IEW-RB	West Girder-Section N2-Inside East Web- Component B of the Rosette
117	WG-N2-IEW-RC	West Girder-Section N2-Inside East Web- Component C of the Rosette
118	WG-N2-IBF-RA	West Girder-Section N2-Inside Bottom Flange- Component A of the Rosette
119	WG-N2-IBF-RB	West Girder-Section N2-Inside Bottom Flange- Component B of the Rosette
120	WG-N2-IBF-RC	West Girder-Section N2-Inside Bottom Flange- Component C of the Rosette
121	WG-N2-IWW-RA	West Girder-Section N2-Inside West Web- Component A of the Rosette
122	WG-N2-IWW-RB	West Girder-Section N2-Inside West Web- Component B of the Rosette
123	WG-N2-IWW-RC	West Girder-Section N2-Inside West Web- Component C of the Rosette
124	EG-N1-OBF-F	East Girder-Section N1-Outside Bottom Flange- Foil Gage
125	EG-N1-IBF-F	East Girder-Section N1-Inside Bottom Flange- Foil Gage
126	EG-S1-OBF-F	East Girder-Section S2-Outside Bottom Flange- Foil Gage
127	EG-S1-IBF-F	East Girder-Section S2-Inside Bottom Flange- Foil Gage
128	EG-S2-OBF-F	East Girder-Section S2-Outside Bottom Flange- Foil Gage

129	EG-S2-IBF-F	East Girder-Section S2-Inside Bottom Flange- Foil Gage
130	WG-S2-OEW-RA	West Girder-Section S2-Outside East Web-Component A of the Rosette
131	WG-S2-OEW-RB	West Girder-Section S2-Outside East Web-Component B of the Rosette
132	WG-S2-OEW-RC	West Girder-Section S2-Outside East Web-Component C of the Rosette
133	WG-S2-OBF-RA	West Girder-Section S2-Outside Bottom Flange-Component A of the Rosette
134	WG-S2-OBF-RB	West Girder-Section S2-Outside Bottom Flange-Component B of the Rosette
135	WG-S2-OBF-RC	West Girder-Section S2-Outside Bottom Flange-Component C of the Rosette
136	WG-S2-OWW-RA	West Girder-Section S2-Outside West Web-Component A of the Rosette
137	WG-S2-OWW-RB	West Girder-Section S2-Outside West Web-Component B of the Rosette
138	WG-S2-OWW-RC	West Girder-Section S2-Outside West Web-Component C of the Rosette
139	WG-S2-IEW-RA	West Girder-Section S2-Inside East Web-Component A of the Rosette
140	WG-S2-IEW-RB	West Girder-Section S2-Inside East Web-Component B of the Rosette
141	WG-S2-IEW-RC	West Girder-Section S2-Inside East Web-Component C of the Rosette
142	WG-S2-IBF-RA	West Girder-Section S2-Inside Bottom Flange-Component A of the Rosette
143	WG-S2-IBF-RB	West Girder-Section S2-Inside Bottom Flange-Component B of the Rosette
144	WG-S2-IBF-RC	West Girder-Section S2-Inside Bottom Flange-Component C of the Rosette
145	WG-S2-IWW-RA	West Girder-Section S2-Inside West Web-Component A of the Rosette
146	WG-S2-IWW-RB	West Girder-Section S2-Inside West Web-Component B of the Rosette
147	WG-S2-IWW-RC	West Girder-Section S2-Inside West Web-Component C of the Rosette
148	EG-S3-OBF-F	East Girder-Section S3-Outside Bottom Flange- Foil Gage
149	EG-S3-IBF-F	East Girder-Section S3-Inside Bottom Flange- Foil

		Gage
150	WG-S3-OEW-RA	West Girder-Section S3-Outside East Web-Component A of the Rosette
151	WG-S3-OEW-RB	West Girder-Section S3-Outside East Web-Component B of the Rosette
152	WG-S3-OEW-RC	West Girder-Section S3-Outside East Web-Component C of the Rosette
153	WG-S3-OBF-RA	West Girder-Section S3-Outside Bottom Flange-Component A of the Rosette
154	WG-S3-OBF-RB	West Girder-Section S3-Outside Bottom Flange-Component B of the Rosette
155	WG-S3-OBF-RC	West Girder-Section S3-Outside Bottom Flange-Component C of the Rosette
156	WG-S3-OWW-RA	West Girder-Section S3-Outside West Web-Component A of the Rosette
157	WG-S3-OWW-RB	West Girder-Section S3-Outside West Web-Component B of the Rosette
158	WG-S3-OWW-RC	West Girder-Section S3-Outside West Web-Component C of the Rosette
159	WG-S3-IEW-RA	West Girder-Section S3-Inside East Web-Component A of the Rosette
160	WG-S3-IEW-RB	West Girder-Section S3-Inside East Web-Component B of the Rosette
161	WG-S3-IEW-RC	West Girder-Section S3-Inside East Web-Component C of the Rosette
162	WG-S3-IBF-RA	West Girder-Section S3-Inside Bottom Flange-Component A of the Rosette
163	WG-S3-IBF-RB	West Girder-Section S3-Inside Bottom Flange-Component B of the Rosette
164	WG-S3-IBF-RC	West Girder-Section S3-Inside Bottom Flange-Component C of the Rosette
165	WG-S3-IWW-RA	West Girder-Section S3-Inside West Web-Component A of the Rosette
166	WG-S3-IWW-RB	West Girder-Section S3-Inside West Web-Component B of the Rosette
167	WG-S3-IWW-RC	West Girder-Section S3-Inside West Web-Component C of the Rosette
168	CD-F1	Inner Center Diaphragm of the Intact Girder-Foil Strain Gage
169	CD-F2	Inner Center Diaphragm of the Intact Girder-Foil Strain Gage



170	CD-F3	Inner Center Diaphragm of the Intact Girder-Foil Strain Gage
171	CD-F4	Inner Center Diaphragm of the Intact Girder-Foil Strain Gage
172	WG-N1-IWW-RC	West Girder-Section N1-Inside West Web-Component C of the Rosette
173	TD-N3-TC2	Top Deck-Section N3-Transverse Concrete Gage
174	TD-N3-TC3	Top Deck-Section N3-Transverse Concrete Gage
175	TD-N3-TC4	Top Deck-Section N3-Transverse Concrete Gage
176	TD-N3-TC5	Top Deck-Section N3-Transverse Concrete Gage
177	TD-N2-TC1	Top Deck-Section N2-Transverse Concrete Gage
178	TD-N2-TC2	Top Deck-Section N2-Transverse Concrete Gage
179	TD-N2-TC3	Top Deck-Section N2-Transverse Concrete Gage
180	TD-N2-TC4	Top Deck-Section N2-Transverse Concrete Gage
181	TD-N2-TC5	Top Deck-Section N2-Transverse Concrete Gage
182	TD-N1.5-TC1	Top Deck-Section N1.5-Transverse Concrete Gage
183	TD-N1.5-TC2	Top Deck-Section N1.5-Transverse Concrete Gage
184	TD-N1.5-TC3	Top Deck-Section N1.5-Transverse Concrete Gage
185	TD-N1.5-TC4	Top Deck-Section N1.5-Transverse Concrete Gage
186	TD-N1.5-TC5	Top Deck-Section N1.5-Transverse Concrete Gage
187	TD-N1-TC1	Top Deck-Section N1-Transverse Concrete Gage
188	TD-N1-TC2	Top Deck-Section N1-Transverse Concrete Gage
189	TD-N1-TC3	Top Deck-Section N1-Transverse Concrete Gage
190	TD-N1-TC4	Top Deck-Section N1-Transverse Concrete Gage
191	TD-N1-TC5	Top Deck-Section N1-Transverse Concrete Gage
192	TD-S1-TC1	Top Deck-Section S1-Transverse Concrete Gage
193	TD-S1-TC2	Top Deck-Section S1-Transverse Concrete Gage
194	TD-S1-TC3	Top Deck-Section S1-Transverse Concrete Gage
195	TD-S1-TC4	Top Deck-Section S1-Transverse Concrete Gage
196	TD-S1-TC5	Top Deck-Section S1-Transverse Concrete Gage
197	TD-S1.5-TC1	Top Deck-Section S1.5-Transverse Concrete Gage
198	TD-S1.5-TC2	Top Deck-Section S1.5-Transverse Concrete Gage
199	TD-S1.5-TC3	Top Deck-Section S1.5-Transverse Concrete Gage
200	TD-S1.5-TC4	Top Deck-Section S1.5-Transverse Concrete Gage
201	TD-S1.5-TC5	Top Deck-Section S1.5-Transverse Concrete Gage
202	TD-S2-TC1	Top Deck-Section S2-Transverse Concrete Gage
203	TD-S2-TC2	Top Deck-Section S2-Transverse Concrete Gage
204	TD-S2-TC3	Top Deck-Section S2-Transverse Concrete Gage

205	TD-S2-TC4	Top Deck-Section S2-Transverse Concrete Gage
206	TD-S2-TC5	Top Deck-Section S2-Transverse Concrete Gage
207	TD-S3-TC1	Top Deck-Section S3-Transverse Concrete Gage
208	TD-S3-TC2	Top Deck-Section S3-Transverse Concrete Gage
209	TD-S3-TC3	Top Deck-Section S3-Transverse Concrete Gage
210	TD-S3-TC4	Top Deck-Section S3-Transverse Concrete Gage
211	TD-S3-TC5	Top Deck-Section S3-Transverse Concrete Gage
212	TD-N2-LC1	Top Deck-Section N2-Longitudinal Concrete Gage
213	TD-N2-LC2	Top Deck-Section N2-Longitudinal Concrete Gage
214	TD-N1.5-LC1	Top Deck-Section N1.5-Longitudinal Concrete Gage
215	TD-N1-LC0	Top Deck-Section N1-Longitudinal Concrete Gage
216	TD-N1-LC1	Top Deck-Section N1-Longitudinal Concrete Gage
217	TD-N1-LC2	Top Deck-Section N1-Longitudinal Concrete Gage
218	TD-S1-LC0	Top Deck-Section S1-Longitudinal Concrete Gage
219	TD-S1-LC1	Top Deck-Section S1-Longitudinal Concrete Gage
220	TD-S1-LC2	Top Deck-Section S1-Longitudinal Concrete Gage
221	TD-S1.5-LC1	Top Deck-Section S1.5-Longitudinal Concrete Gage
222	TD-S2-LC1	Top Deck-Section S2-Longitudinal Concrete Gage
223	TD-S2-LC2	Top Deck-Section S2-Longitudinal Concrete Gage
224	ER-N3	East Railing-Section N3
225	ER-N2	East Railing-Section N2
226	ER-N1	East Railing-Section N1
227	ER-S1	East Railing-Section S1
228	ER-S2	East Railing-Section S2
229	ER-S3	East Railing-Section S3
230	LP-N3	Linear Potentiometer-Section N3
231	LP-N2	Linear Potentiometer-Section N2
232	LP-N1	Linear Potentiometer-Section N1
233	LP-CL	Linear Potentiometer-Section CL
234	LP-CL1	Linear Potentiometer-Across the fracture (West)
235	LP-CL2	Linear Potentiometer-Across the fracture (East)
236	LP-S1	Linear Potentiometer-Section S1
237	LP-S2	Linear Potentiometer-Section S2
238	LP-S3	Linear Potentiometer-Section S3
239	LP-SD1	Linear Potentiometer-South Diaphragm Exterior Tip of Bottom Flange (FG)
240	LP-SD2	Linear Potentiometer-South Diaphragm Interior Tip of Bottom Flange (FG)

241	LP-SD3	Linear Potentiometer-South Diaphragm Interior Tip of Bottom Flange (IG)
242	LP-SD4	Linear Potentiometer-South Diaphragm Exterior Tip of Bottom Flange (IG)
243	SP-CL	String Potentiometer-Mid-Width of Bottom Flange at CL of the Fracture Girder

### E.3 FULL-SCALE TEST 3

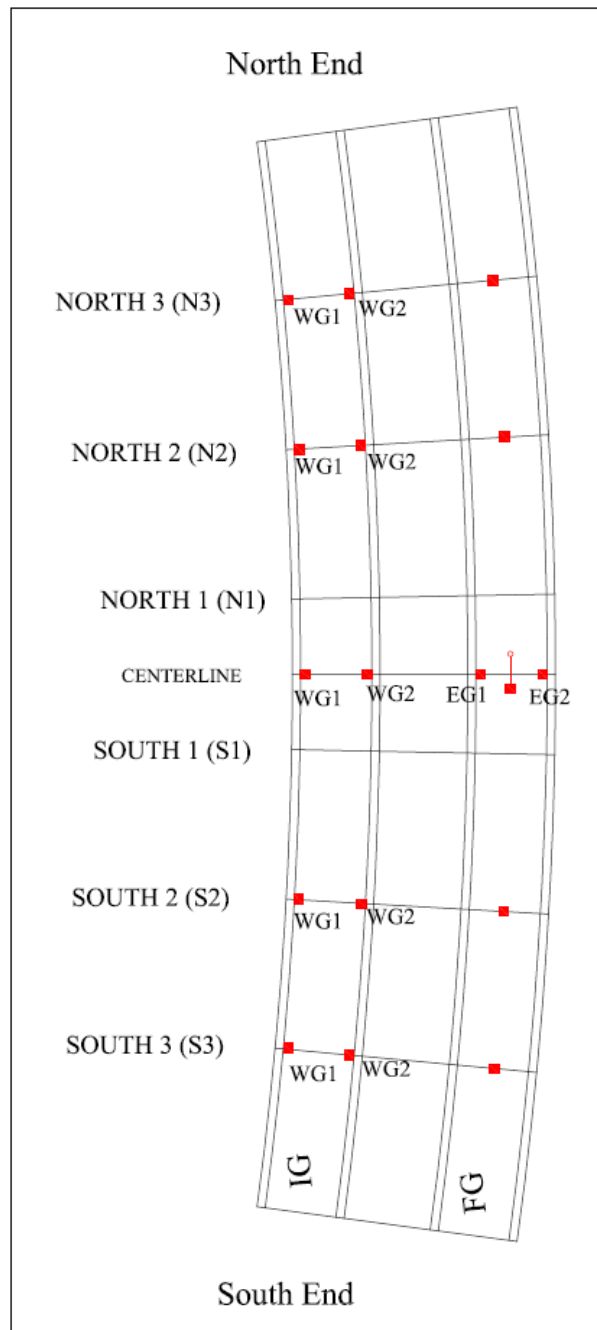


Figure E-6: String potentiometer locations between girder bottom flanges and ground  
Full-Scale Test 3

Table E-4: Index of instrumentation channels Full-Scale Test 3

<b>National Instruments System</b>		
<b>Index</b>	<b>Gage Name</b>	<b>Description</b>
0	FR1	Foil Rebar Strain Gage
1	FR2	Foil Rebar Strain Gage
2	FR3	Foil Rebar Strain Gage
3	FR4	Foil Rebar Strain Gage
4	FR5	Foil Rebar Strain Gage
5	FR6	Foil Rebar Strain Gage
6	FR7	Foil Rebar Strain Gage
7	FR8	Foil Rebar Strain Gage
8	FR9	Foil Rebar Strain Gage
9	FR10	Foil Rebar Strain Gage
10	FR11	Foil Rebar Strain Gage
11	FR12	Foil Rebar Strain Gage
12	FR13	Foil Rebar Strain Gage
13	FR14	Foil Rebar Strain Gage
14	FR15	Foil Rebar Strain Gage
15	FR16	Foil Rebar Strain Gage
16	FR17	Foil Rebar Strain Gage
17	FR19	Foil Rebar Strain Gage
18	FR20	Foil Rebar Strain Gage
19	FR21	Foil Rebar Strain Gage
20	FR22	Foil Rebar Strain Gage
21	FS1	Shear Stud Strain Gage
22	FS2	Shear Stud Strain Gage
23	FS13	Shear Stud Strain Gage
24	FS3	Shear Stud Strain Gage
25	FS4	Shear Stud Strain Gage
26	FS5	Shear Stud Strain Gage
27	FS6	Shear Stud Strain Gage
28	FS14	Shear Stud Strain Gage
29	WG-S1-IEW-RA	West Girder-Section S1-Inside East Web- Component A of the Rosette
30	WG-S1-IEW-RB	West Girder-Section S1-Inside East Web- Component B of the Rosette
31	WG-S1-IEW-RC	West Girder-Section S1-Inside East Web- Component C of the Rosette
32	WG-S1-IBF-RA	West Girder-Section S1-Inside Bottom Flange- Component A of the Rosette

33	WG-S1-IBF-RB	West Girder-Section S1-Inside Bottom Flange- Component B of the Rosette
34	WG-S1-IBF-RC	West Girder-Section S1-Inside Bottom Flange- Component C of the Rosette
35	WG-S1-IWW-RA	West Girder-Section S1-Inside West Web- Component A of the Rosette
36	WG-S1-IWW-RB	West Girder-Section S1-Inside West Web- Component B of the Rosette
37	WG-S1-IWW-RC	West Girder-Section S1-Inside West Web- Component C of the Rosette
38	EG-N3-TF-F	East Girder-Section N3-Exterior Top Flange- Foil Gage
39	EG-N2-TF-F	East Girder-Section N2-Exterior Top Flange- Foil Gage
40	EG-N1-TF-F	East Girder-Section N1-Exterior Top Flange- Foil Gage
41	EG-S2-InteriorTF-F	East Girder-Section S2-Interior Top Flange- Foil Gage
42	EG-S4-InteriorTF-F	East Girder-Section S4-Interior Top Flange- Foil Gage
43	WG-CL-IBF-F	West Girder-Section CL-Inside Bottom Flange-Foil Gage
44	WG-CL-OBF-F	West Girder-Section CL-Outside Bottom Flange-Foil Gage
45	WG-S1-OEW-RA	West Girder-Section S1-Outside East Web- Component A of the Rosette
46	WG-S1-OEW-RB	West Girder-Section S1-Outside East Web- Component B of the Rosette
47	WG-S1-OEW-RC	West Girder-Section S1-Outside East Web- Component C of the Rosette
48	WG-S1-OBF-RA	West Girder-Section S1-Outside Bottom Flange- Component A of the Rosette
49	WG-S1-OBF-RB	West Girder-Section S1-Outside Bottom Flange- Component B of the Rosette
50	WG-S1-OBF-RC	West Girder-Section S1-Outside Bottom Flange- Component C of the Rosette
51	WG-S1-OWW-RA	West Girder-Section S1-Outside West Web- Component A of the Rosette
52	WG-S1-OWW-RB	West Girder-Section S1-Outside West Web- Component B of the Rosette
53	WG-S1-OWW-RC	West Girder-Section S1-Outside West Web-

		Component C of the Rosette
54	WG-N1-IEW-RA	West Girder-Section N1-Inside East Web-Component A of the Rosette
55	WG-N1-IEW-RB	West Girder-Section N1-Inside East Web-Component B of the Rosette
56	WG-N1-IEW-RC	West Girder-Section N1-Inside East Web-Component C of the Rosette
57	WG-N1-IBF-RA	West Girder-Section N1-Inside Bottom Flange-Component A of the Rosette
58	WG-N1-IBF-RB	West Girder-Section N1-Inside Bottom Flange-Component B of the Rosette
59	WG-N1-IBF-RC	West Girder-Section N1-Inside Bottom Flange-Component C of the Rosette
60	WG-N1-IWW-RA	West Girder-Section N1-Inside West Web-Component A of the Rosette
61	WG-N1-IWW-RB	West Girder-Section N1-Inside West Web-Component B of the Rosette
62	WG-N1-IWW-RC	West Girder-Section N1-Inside West Web-Component C of the Rosette
63	WG-N1-OEW-RA	West Girder-Section N1-Outside East Web-Component A of the Rosette
64	WG-N1-OEW-RB	West Girder-Section N1-Outside East Web-Component B of the Rosette
65	WG-N1-OEW-RC	West Girder-Section N1-Outside East Web-Component C of the Rosette
66	WG-N1-OBF-RA	West Girder-Section N1-Outside Bottom Flange-Component A of the Rosette
67	WG-N1-OBF-RB	West Girder-Section N1-Outside Bottom Flange-Component B of the Rosette
68	WG-N1-OBF-RC	West Girder-Section N1-Outside Bottom Flange-Component C of the Rosette
69	WG-N1-OWW-RA	West Girder-Section N1-Outside West Web-Component A of the Rosette
70	WG-N1-OWW-RB	West Girder-Section N1-Outside West Web-Component B of the Rosette
71	WG-N1-OWW-RC	West Girder-Section N1-Outside West Web-Component C of the Rosette
72	OND-RA	Outside North Diaphragm-Component A of the Rosette
73	OND-RB	Outside North Diaphragm-Component B of the Rosette

74	OND-RC	Outside North Diaphragm-Component C of the Rosette
75	IND-RA	Inside North Diaphragm-Component A of the Rosette
76	IND-RB	Inside North Diaphragm-Component B of the Rosette
77	IND-RC	Inside North Diaphragm-Component C of the Rosette
78	OSD-RA	Outside South Diaphragm-Component A of the Rosette
79	OSD-RB	Outside South Diaphragm-Component B of the Rosette
80	OSD-RC	Outside South Diaphragm-Component C of the Rosette
81	ISD-RA	Inside South Diaphragm-Component A of the Rosette
82	ISD-RB	Inside South Diaphragm-Component B of the Rosette
83	ISD-RC	Inside South Diaphragm-Component C of the Rosette
84	EG-N3-OBF-F	East Girder-Section N3-Outside Bottom Flange- Foil Gage
85	EG-N3-IBF-F	East Girder-Section N3-Inside Bottom Flange- Foil Gage
86	WG-N3-OEW-RA	West Girder-Section N3-Outside East Web-Component A of the Rosette
87	WG-N3-OEW-RB	West Girder-Section N3-Outside East Web-Component B of the Rosette
88	WG-N3-OEW-RC	West Girder-Section N3-Outside East Web-Component C of the Rosette
89	WG-N3-OBF-RA	West Girder-Section N3-Outside Bottom Flange-Component A of the Rosette
90	WG-N3-OBF-RB	West Girder-Section N3-Outside Bottom Flange-Component B of the Rosette
91	WG-N3-OBF-RC	West Girder-Section N3-Outside Bottom Flange-Component C of the Rosette
92	WG-N3-OWW-RA	West Girder-Section N3-Outside West Web-Component A of the Rosette
93	WG-N3-OWW-RB	West Girder-Section N3-Outside West Web-Component B of the Rosette
94	WG-N3-OWW-RC	West Girder-Section N3-Outside West Web-Component C of the Rosette
95	WG-N3-IEW-RA	West Girder-Section N3-Inside East Web-Component A of the Rosette
96	WG-N3-IEW-RB	West Girder-Section N3-Inside East Web-Component B of the Rosette



97	WG-N3-IEW-RC	West Girder-Section N3-Inside East Web-Component C of the Rosette
98	WG-N3-IBF-RA	West Girder-Section N3-Inside Bottom Flange-Component A of the Rosette
99	WG-N3-IBF-RB	West Girder-Section N3-Inside Bottom Flange-Component B of the Rosette
100	WG-N3-IBF-RC	West Girder-Section N3-Inside Bottom Flange-Component C of the Rosette
101	WG-N3-IWW-RA	West Girder-Section N3-Inside West Web-Component A of the Rosette
102	WG-N3-IWW-RB	West Girder-Section N3-Inside West Web-Component B of the Rosette
103	WG-N3-IWW-RC	West Girder-Section N3-Inside West Web-Component C of the Rosette
104	EG-N2-OBF-F	East Girder-Section N2-Outside Bottom Flange- Foil Gage
105	EG-N2-IBF-F	East Girder-Section N2-Inside Bottom Flange- Foil Gage
106	WG-N2-OEW-RA	West Girder-Section N2-Outside East Web-Component A of the Rosette
107	WG-N2-OEW-RB	West Girder-Section N2-Outside East Web-Component B of the Rosette
108	WG-N2-OEW-RC	West Girder-Section N2-Outside East Web-Component C of the Rosette
109	WG-N2-OBF-RA	West Girder-Section N2-Outside Bottom Flange-Component A of the Rosette
110	WG-N2-OBF-RB	West Girder-Section N2-Outside Bottom Flange-Component B of the Rosette
111	WG-N2-OBF-RC	West Girder-Section N2-Outside Bottom Flange-Component C of the Rosette
112	WG-N2-OWW-RA	West Girder-Section N2-Outside West Web-Component A of the Rosette
113	WG-N2-OWW-RB	West Girder-Section N2-Outside West Web-Component B of the Rosette
114	WG-N2-OWW-RC	West Girder-Section N2-Outside West Web-Component C of the Rosette
115	WG-N2-IEW-RA	West Girder-Section N2-Inside East Web-Component A of the Rosette
116	WG-N2-IEW-RB	West Girder-Section N2-Inside East Web-Component B of the Rosette
117	WG-N2-IEW-RC	West Girder-Section N2-Inside East Web-

		Component C of the Rosette
118	WG-N2-IBF-RA	West Girder-Section N2-Inside Bottom Flange- Component A of the Rosette
119	WG-N2-IBF-RB	West Girder-Section N2-Inside Bottom Flange- Component B of the Rosette
120	WG-N2-IBF-RC	West Girder-Section N2-Inside Bottom Flange- Component C of the Rosette
121	WG-N2-IWW-RA	West Girder-Section N2-Inside West Web- Component A of the Rosette
122	WG-N2-IWW-RB	West Girder-Section N2-Inside West Web- Component B of the Rosette
123	WG-N2-IWW-RC	West Girder-Section N2-Inside West Web- Component C of the Rosette
124	EG-NCL-TF-F	East Girder-Section NCL-Exterior Top Flange- Foil Gage
125	EG-SCL-TF-F	East Girder-Section SCL-Exterior Top Flange- Foil Gage
126	EG-S1-TF-F	East Girder-Section S1-Exterior Top Flange- Foil Gage
127	EG-S2-TF-F	East Girder-Section S2-Exterior Top Flange- Foil Gage
128	EG-S2-OBF-F	East Girder-Section S2-Outside Bottom Flange- Foil Gage
129	EG-S2-IBF-F	East Girder-Section S2-Inside Bottom Flange- Foil Gage
130	WG-S2-OEW-RA	West Girder-Section S2-Outside East Web- Component A of the Rosette
131	WG-S2-OEW-RB	West Girder-Section S2-Outside East Web- Component B of the Rosette
132	WG-S2-OEW-RC	West Girder-Section S2-Outside East Web- Component C of the Rosette
133	WG-S2-OBF-RA	West Girder-Section S2-Outside Bottom Flange- Component A of the Rosette
134	WG-S2-OBF-RB	West Girder-Section S2-Outside Bottom Flange- Component B of the Rosette
135	WG-S2-OBF-RC	West Girder-Section S2-Outside Bottom Flange- Component C of the Rosette
136	WG-S2-OWW-RA	West Girder-Section S2-Outside West Web- Component A of the Rosette
137	WG-S2-OWW-RB	West Girder-Section S2-Outside West Web- Component B of the Rosette

138	WG-S2-OWW-RC	West Girder-Section S2-Outside West Web-Component C of the Rosette
139	WG-S2-IEW-RA	West Girder-Section S2-Inside East Web-Component A of the Rosette
140	WG-S2-IEW-RB	West Girder-Section S2-Inside East Web-Component B of the Rosette
141	WG-S2-IEW-RC	West Girder-Section S2-Inside East Web-Component C of the Rosette
142	WG-S2-IBF-RA	West Girder-Section S2-Inside Bottom Flange-Component A of the Rosette
143	WG-S2-IBF-RB	West Girder-Section S2-Inside Bottom Flange-Component B of the Rosette
144	WG-S2-IBF-RC	West Girder-Section S2-Inside Bottom Flange-Component C of the Rosette
145	WG-S2-IWW-RA	West Girder-Section S2-Inside West Web-Component A of the Rosette
146	WG-S2-IWW-RB	West Girder-Section S2-Inside West Web-Component B of the Rosette
147	WG-S2-IWW-RC	West Girder-Section S2-Inside West Web-Component C of the Rosette
148	EG-S3-OBF-F	East Girder-Section S3-Outside Bottom Flange- Foil Gage
149	EG-S3-IBF-F	East Girder-Section S3-Inside Bottom Flange- Foil Gage
150	WG-S3-OEW-RA	West Girder-Section S3-Outside East Web-Component A of the Rosette
151	WG-S3-OEW-RB	West Girder-Section S3-Outside East Web-Component B of the Rosette
152	WG-S3-OEW-RC	West Girder-Section S3-Outside East Web-Component C of the Rosette
153	WG-S3-OBF-RA	West Girder-Section S3-Outside Bottom Flange-Component A of the Rosette
154	WG-S3-OBF-RB	West Girder-Section S3-Outside Bottom Flange-Component B of the Rosette
155	WG-S3-OBF-RC	West Girder-Section S3-Outside Bottom Flange-Component C of the Rosette
156	WG-S3-OWW-RA	West Girder-Section S3-Outside West Web-Component A of the Rosette
157	WG-S3-OWW-RB	West Girder-Section S3-Outside West Web-Component B of the Rosette
158	WG-S3-OWW-RC	West Girder-Section S3-Outside West Web-

		Component C of the Rosette
159	WG-S3-IEW-RA	West Girder-Section S3-Inside East Web-Component A of the Rosette
160	WG-S3-IEW-RB	West Girder-Section S3-Inside East Web-Component B of the Rosette
161	WG-S3-IEW-RC	West Girder-Section S3-Inside East Web-Component C of the Rosette
162	WG-S3-IBF-RA	West Girder-Section S3-Inside Bottom Flange-Component A of the Rosette
163	WG-S3-IBF-RB	West Girder-Section S3-Inside Bottom Flange-Component B of the Rosette
164	WG-S3-IBF-RC	West Girder-Section S3-Inside Bottom Flange-Component C of the Rosette
165	WG-S3-IWW-RA	West Girder-Section S3-Inside West Web-Component A of the Rosette
166	WG-S3-IWW-RB	West Girder-Section S3-Inside West Web-Component B of the Rosette
167	WG-S3-IWW-RC	West Girder-Section S3-Inside West Web-Component C of the Rosette
168	EG-N4-InteriorTF-F	East Girder-Section N4-Interior Top Flange- Foil Gage
169	EG-N2-InteriorTF-F	East Girder-Section N2-Interior Top Flange- Foil Gage
170	TD-N3-LC1	Top Deck-Section N3-Longitudinal Concrete Gage
171	TD-N3-LC1.5	Top Deck-Section N3-Longitudinal Concrete Gage
172	TD-N3-LC2	Top Deck-Section N3-Longitudinal Concrete Gage
173	TD-N3-TC1	Top Deck-Section N3-Transverse Concrete Gage
174	TD-N3-TC2	Top Deck-Section N3-Transverse Concrete Gage
175	TD-N3-TC3	Top Deck-Section N3-Transverse Concrete Gage
176	TD-N3-TC4	Top Deck-Section N3-Transverse Concrete Gage
177	TD-N3-TC5	Top Deck-Section N3-Transverse Concrete Gage
178	TD-N2-TC1	Top Deck-Section N2-Transverse Concrete Gage
179	TD-N2-TC2	Top Deck-Section N2-Transverse Concrete Gage
180	TD-N2-TC3	Top Deck-Section N2-Transverse Concrete Gage
181	TD-N2-TC4	Top Deck-Section N2-Transverse Concrete Gage
182	TD-N2-TC5	Top Deck-Section N2-Transverse Concrete Gage
183	TD-N1.5-TC1	Top Deck-Section N1.5-Transverse Concrete Gage
184	TD-N1.5-TC3	Top Deck-Section N1.5-Transverse Concrete Gage
185	TD-N1.5-TC4	Top Deck-Section N1.5-Transverse Concrete Gage
186	TD-N1.5-TC5	Top Deck-Section N1.5-Transverse Concrete Gage

187	TD-N1-TC1	Top Deck-Section N1-Transverse Concrete Gage
188	TD-N1-TC3	Top Deck-Section N1-Transverse Concrete Gage
189	TD-N1-TC4	Top Deck-Section N1-Transverse Concrete Gage
190	TD-N1-TC5	Top Deck-Section N1-Transverse Concrete Gage
191	TD-S1-TC1	Top Deck-Section S1-Transverse Concrete Gage
192	TD-S1-TC3	Top Deck-Section S1-Transverse Concrete Gage
193	TD-S1-TC4	Top Deck-Section S1-Transverse Concrete Gage
194	TD-S1-TC5	Top Deck-Section S1-Transverse Concrete Gage
195	TD-S1.5-TC1	Top Deck-Section S1.5-Transverse Concrete Gage
196	TD-S1.5-TC3	Top Deck-Section S1.5-Transverse Concrete Gage
197	TD-N4-TC2	Top Deck-Section N4-Transverse Concrete Gage
198	TD-N4-TC4	Top Deck-Section N4-Transverse Concrete Gage
199	TD-N3.5-TC1	Top Deck-Section N3.5-Transverse Concrete Gage
200	TD-N3.5-TC2	Top Deck-Section N3.5-Transverse Concrete Gage
201	TD-S1.5-TC4	Top Deck-Section S1.5-Transverse Concrete Gage
202	TD-S1.5-TC5	Top Deck-Section S1.5-Transverse Concrete Gage
203	TD-S2-TC1	Top Deck-Section S2-Transverse Concrete Gage
204	TD-S2-TC2	Top Deck-Section S2-Transverse Concrete Gage
205	TD-S2-TC3	Top Deck-Section S2-Transverse Concrete Gage
206	TD-S2-TC4	Top Deck-Section S2-Transverse Concrete Gage
207	TD-S2-TC5	Top Deck-Section S2-Transverse Concrete Gage
208	TD-S3-TC1	Top Deck-Section S3-Transverse Concrete Gage
209	TD-S3-TC2	Top Deck-Section S3-Transverse Concrete Gage
210	TD-S3-TC3	Top Deck-Section S3-Transverse Concrete Gage
211	TD-S3-TC4	Top Deck-Section S3-Transverse Concrete Gage
212	TD-S3-TC5	Top Deck-Section S3-Transverse Concrete Gage
213	TD-N2-LC1	Top Deck-Section N2-Longitudinal Concrete Gage
214	TD-N2-LC2	Top Deck-Section N2-Longitudinal Concrete Gage
215	TD-N1-LC1	Top Deck-Section N1-Longitudinal Concrete Gage
216	TD-N1-LC2	Top Deck-Section N1-Longitudinal Concrete Gage
217	TD-S1-LC1	Top Deck-Section S1-Longitudinal Concrete Gage
218	TD-S1-LC2	Top Deck-Section S1-Longitudinal Concrete Gage
219	TD-S2-LC1	Top Deck-Section S2-Longitudinal Concrete Gage
220	TD-S2-LC2	Top Deck-Section S2-Longitudinal Concrete Gage
221	TD-N3.5-TC4	Top Deck-Section N3.5-Transverse Concrete Gage
222	TD-N3.5-TC5	Top Deck-Section N3.5-Transverse Concrete Gage
223	ER-N2	East Railing-Section N2
224	ER-N1	East Railing-Section N1
225	ER-S1	East Railing-Section S1
226	ER-S2	East Railing-Section S2
227	ER-N2-MH	East Railing-Section N2-Middle Height

228	LP-N3-ER	Linear Potentiometer-Section N3-East Railing
229	LP-S3-ER	Linear Potentiometer-Section S3-East Railing
230	LP-N3	Linear Potentiometer-Section N3
231	LP-N2	Linear Potentiometer-Section N2
232	LP-N1	Linear Potentiometer-Section N1
233	LP-CL	Linear Potentiometer-Section CL
234	SP-CL-EG1	String Potentiometer-Section CL-East Girder (Western Tip of Bottom Flange)
235	SP-CL-EG2	String Potentiometer-Section CL-East Girder (Eastern Tip of Bottom Flange)
236	LP-S1	Linear Potentiometer-Section S1
237	LP-S2	Linear Potentiometer-Section S2
238	LP-S3	Linear Potentiometer-Section S3
239	LP-N4-IF	Linear Potentiometer-Section N4-Interior Top Flange of the Fractured Girder
240	LP-N3-IF	Linear Potentiometer-Section N3-Interior Top Flange of the Fractured Girder
241	LP-S3-IF	Linear Potentiometer-Section S3-Interior Top Flange of the Fractured Girder
242	LP-S4-IF	Linear Potentiometer-Section S4-Interior Top Flange of the Fractured Girder
243	SP-CL	String Potentiometer-Across the Fracture

<b>Agilent Systems System</b>		
<b>Index</b>	<b>Gage Name</b>	<b>Description</b>
0	ER-N1-MH	East Railing-Section N1-Middle Height
1	ER-NCL-MH	East Railing-Section NCL-6in. from the Top Surface
2	ER-NCL-MH2	East Railing-Section NCL-12in. from the Top Surface
3	ER-SCL-MH	East Railing-Section SCL-6in. from the Top Surface
4	ER-SCL-MH2	East Railing-Section SCL-12in. from the Top Surface
5	ER-S1-MH	East Railing-Section S1-Middle Height
6	ER-S2-MH	East Railing-Section S2-Middle Height
7	ER-NCL	East Railing-Section NCL
8	ER-SCL	East Railing-Section SCL
9	WR-N2	West Railing-Section N2
10	WR-N1	West Railing-Section N1
11	WR-NCL	West Railing-Section NCL
12	WR-SCL	West Railing-Section SCL
13	WR-S1	West Railing-Section S1

14	WR-S2	West Railing-Section S2
15	LP-N2-IF	Linear Potentiometer-Section N2-Interior Top Flange of the Fractured Girder
16	LP-N1-IF	Linear Potentiometer-Section N1-Interior Top Flange of the Fractured Girder
17	LP-CL-IF	Linear Potentiometer-Section CL-Interior Top Flange of the Fractured Girder
18	LP-S1-IF	Linear Potentiometer-Section S1-Interior Top Flange of the Fractured Girder
19	LP-S2-IF	Linear Potentiometer-Section S2-Interior Top Flange of the Fractured Girder
20	SP-N3-WG1	String Potentiometer-Section N3-West Girder (Western Tip of Bottom Flange)
21	SP-N3-WG2	String Potentiometer-Section N3-West Girder (Eastern Tip of Bottom Flange)
22	SP-N2-WG1	String Potentiometer-Section N2-West Girder (Western Tip of Bottom Flange)
23	SP-N2-WG2	String Potentiometer-Section N2-West Girder (Eastern Tip of Bottom Flange)
24	SP-CL-WG1	String Potentiometer-Section CL-West Girder (Western Tip of Bottom Flange)
25	SP-CL-WG2	String Potentiometer-Section CL-West Girder (Eastern Tip of Bottom Flange)
26	SP-S2-WG1	String Potentiometer-Section S2-West Girder (Western Tip of Bottom Flange)
27	SP-S2-WG2	String Potentiometer-Section S2-West Girder (Eastern Tip of Bottom Flange)
28	SP-S3-WG1	String Potentiometer-Section S3-West Girder (Western Tip of Bottom Flange)
29	SP-S3-WG2	String Potentiometer-Section S3-West Girder (Eastern Tip of Bottom Flange)
30	SP-N3-EG	String Potentiometer-Section N3-East Girder (Mid-width of Bottom Flange)
31	SP-N2-EG	String Potentiometer-Section N2-East Girder (Mid-width of Bottom Flange)
32	SP-S2-EG	String Potentiometer-Section S2-East Girder (Mid-width of Bottom Flange)
33	SP-S3-EG	String Potentiometer-Section S3-East Girder (Mid-width of Bottom Flange)
34	EG-S3-TF-F	East Girder-Section S3-Exterior Top Flange-Foil Gage

35	TD-N2.5-TC1	Top Deck-Section N2.5-Transverse Concrete Gage
36	TD-N2.5-TC2	Top Deck-Section N2.5-Transverse Concrete Gage
37	TD-N2.5-TC4	Top Deck-Section N2.5-Transverse Concrete Gage
38	TD-N2.5-TC5	Top Deck-Section N2.5-Transverse Concrete Gage
39	TD-N2-LC1.5	Top Deck-Section N2-Longitudinal Concrete Gage
40	TD-N1-LC1.5	Top Deck-Section N1-Longitudinal Concrete Gage
41	TD-NCL-LC0	Top Deck-Section NCL-Longitudinal Concrete Gage
42	TD-NCL-LC1	Top Deck-Section NCL-Longitudinal Concrete Gage
43	TD-NCL-LC2	Top Deck-Section NCL-Longitudinal Concrete Gage
44	TD-SCL-LC0	Top Deck-Section SCL-Longitudinal Concrete Gage
45	TD-SCL-LC1	Top Deck-Section SCL-Longitudinal Concrete Gage
46	TD-SCL-LC2	Top Deck-Section SCL-Longitudinal Concrete Gage
47	TD-S1-LC1.5	Top Deck-Section S1-Longitudinal Concrete Gage
48	TD-S2-LC1.5	Top Deck-Section S2-Longitudinal Concrete Gage
49	TD-S2.5-TC1	Top Deck-Section S2.5-Transverse Concrete Gage
50	TD-S2.5-TC2	Top Deck-Section S2.5-Transverse Concrete Gage
51	TD-S2.5-TC4	Top Deck-Section S2.5-Transverse Concrete Gage
52	TD-S2.5-TC5	Top Deck-Section S2.5-Transverse Concrete Gage
53	TD-S3-LC1	Top Deck-Section S3-Longitudinal Concrete Gage
54	TD-S3-LC1.5	Top Deck-Section S3-Longitudinal Concrete Gage
55	TD-S3-LC2	Top Deck-Section S3-Longitudinal Concrete Gage
56	TD-S3.5-TC1	Top Deck-Section S3.5-Transverse Concrete Gage
57	TD-S3.5-TC2	Top Deck-Section S3.5-Transverse Concrete Gage
58	TD-S3.5-TC4	Top Deck-Section S3.5-Transverse Concrete Gage
59	TD-S3.5-TC5	Top Deck-Section S3.5-Transverse Concrete Gage
60	TD-S4-TC2	Top Deck-Section S4-Transverse Concrete Gage
61	TD-S4-TC4	Top Deck-Section S4-Transverse Concrete Gage



## BIBLIOGRAPHY

- American Association of State Highway and Transportation Officials (AASHTO), (2004) “LRFD Bridge Design Specifications”. Washington, D.C.
- American Concrete Institute (ACI) (2008) “ACI 318-08 Building Code Requirements for Structural Concrete & Commentary”
- AE 3145 Strain Gage Notes, (2000). “Strain Transformation and Rosette Gage Theory”  
<http://www.ae.gatech.edu/people/jcraig/classes/ae3145/Lab2/strain-gages.html>
- Barnard, Timothy, (2006). “Constructing a Full-Scale Horizontally-Curved Twin Steel Trapezoidal Box Girder Bridge Segment to Determine Redundancies in Fracture Critical Bridges.” Departmental Report, The University of Texas at Austin.
- Dally, James W., Riley, William F., (1965). “Experimental Stress Analysis”. IIT Research Institute, Chicago.
- Hovell, Catherine, (2007). “Evaluation of Redundancy in Trapezoidal Box-Girder Bridges Using Finite Element Analysis.” Master’s Thesis, The University of Texas at Austin.
- Kim, Janghwan, (2010). “Finite Element Modeling of Twin Steel Box-Girder Bridges for Redundancy Evaluation.” Doctoral Dissertation, The University of Texas at Austin.
- Mouras, Joshua, (2008). “Evaluating the Redundancy of Steel Bridges: Improving the Strength and Behavior of Shear Stud Connections under Tensile Loading.” Master’s Thesis, The University of Texas at Austin.
- Norris, Charles H., Wilbur, John B., (1960). “Elementary structural analysis”. McGraw-Hill Book Company Inc.
- Olson, Dan (2008). “I-35W Engineer Answers Concerns about the New Bridge,” Minnesota Public Radio.  
[http://minnesota.publicradio.org/display/web/2008/07/30/issues\\_2004/](http://minnesota.publicradio.org/display/web/2008/07/30/issues_2004/)
- Stith, Jason (2010). *UT Lift User’s Guide*. The University of Texas at Austin, Austin, TX.

Sutton, James P., (2007). "Evaluating the Redundancy of Steel Bridges: Effect of a Bridge Haunch on the Strength and Behavior of Shear Studs under Tensile Loading". Master's Thesis, The University of Texas at Austin.

VISHAY Micro-Measurements, (2008). "Strain Gage Rosettes: Selection, Application and Data Reduction", Tech Note TN-515.

Wight, James K., MacGregor, James G., (2009) "Reinforced Concrete: Mechanics and Design, 5th Edition".

## VITA

Vasileios Athanasiou Samaras was born in Athens, Greece on April 17, 1984, the son of Athanasiou and Evdokias Samaras. He is the brother of Artemis Samara. He attend 2<sup>nd</sup> Unified High School of Chalandri, Athens, from which he graduated in 2002. He obtained his Diploma in Civil Engineering from the University of Thessaly at Volos in July 2007, having written a thesis on non linear analysis of cold-formed thin-walled scaffolding boards. In August, 2007, he entered the Graduate School at The University of Texas at Austin. While completing his Master's Degree in The University of Texas, he worked as a Graduate Research Assistant at the Phil M. Ferguson Structural Engineering Laboratory. He received his Master of Science in Structural Engineering degree in August 2009.

Permanent address: Lefkon Oreon 34 Chalandri, Athens

GREECE, GR 152-34

This thesis was typed by the author